The Aerodynamics of a Modern Warship

Thesis submitted in accordance with the requirements of the University of Liverpool for the degree of Doctor in Philosophy

By

Rebecca Mateer

School of Engineering

University of Liverpool

January 2020

Abstract

Although modern warships routinely operate with on-board helicopters, the effect of the ship superstructure aerodynamics on the flying environment around the ship is generally not considered in the design process. The modern warship is now well designed for stealth in warfare, but the now bulkier, smooth-sided and sharp-edged superstructures create a significant disturbance to the oncoming wind, resulting in turbulent flow features in the lee of the ship, most often across the stern where the ship's flight deck is located. Such conditions, coupled with hot exhaust gases from the ship's gas turbine engines, ever-changing weather resulting in various sea-states, sea-spray, rain, fog, etc. create a potentially very hazardous operational environment. In addition, as the launch of unmanned aircraft (UA) vehicles from the flight deck is becoming commonplace, their successful launch and recovery is also directly impacted by the scale of the turbulent flow features in the vicinity of the flight deck.

Through the use of time-accurate Computational Fluid Dynamics (CFD), this thesis addresses the impact of modern warship aerodynamics on helicopter and UAV operations. Full-scale, time-accurate, unsteady airwakes have been produced for an early design of the UK Royal Navy's new Global Combat Ship (GCS), the Type 26 City-Class, and its predecessor, the Type 23 Duke-Class. The larger, stealthier design of the GCS has been shown to produce a more aggressive airwake compared with its predecessor, resulting in higher turbulence levels across the flight deck and greater aerodynamic loading on a helicopter. The larger main mast of the GCS also has a clear effect on the accuracy of the ship's anemometer readings when compared with Type 23 thereby making it difficult to determine if the wind conditions are safe for helicopter launch and recovery. Simulation of the Type 23 and GCS exhaust gas efflux has shown that the more turbulent airwake of the GCS aids the cooling and dispersion of the ship's exhaust gases with air temperatures above the flight deck being comparatively lower for the GCS in headwind and Green 30 wind-over-deck (WOD) conditions. As such, the dispersing engine exhaust plume of Type 23 presents a greater threat to the helicopter.

Detailed analysis of the air flow around the GCS main mast has shown how CFD can be used to predict flow distortion at the ship's anemometers. Issues with current practice for positioning anemometers on bulky main mast structures, detailed in the defence standard, DEFSTAN 00-133 Part 2, have been highlighted. Findings show that the defence standard should be modified to take account of the new ship geometries that are emerging; at the least, anemometers should be placed as high up the mast structure as possible on yard arms of suitable length. Additionally, an appropriately placed aft anemometer is recommended to yield more accurate wind measurements from astern.

Analysis of the exhaust gas dispersion from the GCS has shown that significant cooling of the plume is achieved through the hot exhaust gases mixing with the ship's turbulent airwake, but elevated, unsteady temperatures are present in the vicinity of the flight deck, particularly in the port side hover position in a Green 30 WOD, that can adversely affect an operating helicopter. The addition of an eductor to the exhaust outlet does reduce temperatures above the flight deck, but the temperatures remain elevated and unsteady.

A new method for simulating the launch of lightweight unmanned aircraft into the turbulent CFD-generated ship airwake has been also developed. The simulation environment has shown potential for developing Unmanned Aircraft (UA) for maritime applications, for developing appropriate flight controllers, and for developing appropriate launch and recovery operational procedures.

Acknowledgements

Following on from a thoroughly enjoyable undergraduate degree at the University of Liverpool, the opportunity to continue my studies and embark upon a PhD journey was one that I could not pass upon, and for that opportunity, Prof Ieuan Owen and Prof Mark White, I am so grateful. I would like to thank you both for your endless patience, selflessness and encouragement throughout what has been a difficult but rewarding few years. Very early on in my studies, I coined the term, 'Work-Dads', for you both, at first light-heartedly for your wise words and ever worsening Dad jokes, but reflecting upon the past few years, in the most endearing of ways you have at many times been more than just supervisors, and for that, I will always be so grateful. Thank you.

Having the opportunity to work with BAE Systems Surface Ships, in particular, Niven McDowell, Kevin Brown and Geoff Roach, on the Royal Navy's Type 26 City-Class frigate, was a highlight and is the contribution to which I am most proud of. Working alongside such a well-established industrial partner, learning so much in the process and providing a little bit of that expertise gained along the way has been a pleasure. Thank you.

Particular thanks also go to Dr Linghai Lu for his expert help in producing a FlightLab model of a UAV system for a part of my research and Neil Cameron for his assistance in adding an automated control system – you have both been invaluable, thank you. Another special mention must also go to Denise Stewart, for her wise words, encouragement, always being there to talk to when needed, and never failing to make me laugh, even on a bad day – thank you!

For all of the wonderful people I have had the pleasure of navigating PhD life with, firstly, Sarah Scott and Michael Kelly, for showing me the ropes and imparting your wisdoms at the beginning of my studies, you were both so patient and nothing was ever too much, thank you. Wajih Memon, for all of your help with everything sim related, you have been integral to the completion of my studies, thank you so very much. To you three and to the rest of my PhD team; Jade Adams-White, Chris Dadswell, Neale Watson, Josie Roscoe, Matt Hudson, Nick Fernandez and Isaac Stephens, thank you so much for the hours of thought-provoking conversation, hugs and support when they were needed, countless laughs and all the AJ trips in between! This whole experience was made by you.

Finally, to my parents, Yvonne and Darren, who have always encouraged me to push myself to achieve whatever I have set out to, I would not have gotten to where I am today without the unconditional love and support you both continue to give me. I love you. Thank you.

Table of Contents

Nomenclature

Roman Notation		
A	Cross-sectional area	m^2
Azi_{WOD}	Angle of WOD relative to ship bow	°
C	Courant number	-
C_{DES}	DES calibration constant	-
C_{max}	Maximum courant number	-
c	Specific heat capacity	$Jkg^{-1}K^{-1}$
D	Diameter	m
d	Depth of domain	m
e	Internal energy	J
F_{DES}	DES blending function	-
f	Frequency	Hz
f_b	Body force per unit mass	Nkg^{-1}
g	Acceleration due to gravity	ms^{-2}
h	Heat transfer coefficient	$Wm^{-2}K^{-1}$
J	Momentum flux ratio	-
k	Turbulent kinetic energy	m^2s^{-2}
L	Characteristic length	m
L_t	Turbulent length scale	m
l	Length	m
$\dot{m}$	Mass flow rate	kgs^{-1}
Nu	Nusselt number	-
p	Pressure	Nm^{-2}
Q	Q-criterion	-
$\dot{q}$	Heat flux	Wm^{-2}
Re	Reynolds number	-
Ri	Richardson number	-
r	Radius	m
$\boldsymbol{S}$	Rate-of-strain tensor	s^{-1}
S_t	Strouhal number	-
T	Temperature	$°K$ or °C
T_a	Temperature after change	$°K$ or °C

T_i	Initial temperature	$°K$ or ℃
t_a	Time array	s
t_{set}	Settling time	s
U	Freestream velocity magnitude	ms^{-1}
U_a	Airwake longitudinal velocity magnitude	ms^{-1}
U_c	Crossflow velocity magnitude	ms^{-1}
U_e	Exhaust velocity magnitude	ms^{-1}
U_{pert}	Longitudinal velocity perturbations	ms^{-1}
u	Velocity in x dimension	ms^{-1}
V	Velocity magnitude	ms^{-1}
V_a	Airwake lateral velocity magnitude	ms^{-1}
V_{pert}	Lateral velocity perturbations	ms^{-1}
V_{ref}	Velocity magnitude at reference height	ms^{-1}
V_{WOD}	Velocity magnitude of WOD condition	ms^{-1}
v	Velocity in y dimension	ms^{-1}
W_a	Airwake vertical velocity magnitude	ms^{-1}
w	Velocity in z dimension	ms^{-1}
X_a	CFD/airwake co-ordinate system, longitudinal	m
X_{sim}	Simulator co-ordinate system, longitudinal	m
X_{sim2a}	Simulator to CFD/airwake co-ordinate system conversion, longitudinal	m
x	Longitudinal dimension (+'ve to stern)	m
Y_a	CFD/airwake co-ordinate system, lateral	m
Y_{sim}	Simulator co-ordinate system, lateral	m
Y_{sim2a}	Simulator to CFD/airwake co-ordinate system conversion, lateral	m
y	Lateral dimension (+'ve to starboard)	m
y^+	Dimensionless wall distance	-
Z_a	CFD/airwake co-ordinate system, vertical	m
Z_{sim}	Simulator co-ordinate system, vertical	m
Z_{sim2a}	Simulator to CFD/airwake co-ordinate system conversion, vertical	m
z	Vertical dimension (+'ve upwards)	m

z_{asl}	Height above sea surface	m
z_{ref}	Reference height	m
Greek Notation		
α	Surface roughness constant	-
Δ_t	Time step	s
Δ_x	Computational cell size in x dimension	m
Δ_y	Computational cell size in y dimension	m
Δ_z	Computational cell size in z dimension	m
ε	Turbulent dissipation rate	$m^2 s^{-3}$
μ	Dynamic viscosity	$kgm^{-1}s^{-1}$
ν	Kinematic viscosity	$m^2 s^{-1}$
ρ	Density	kgm^{-3}
τ	Thermocouple response time	s
τ_{ii}	Shear stress at face in i plane, i direction	Nm^{-2}
$\mathbf{\Omega}$	Vorticity tensor	s^{-1}
ω	Specific turbulent dissipation rate	s^{-1}

Abbreviations

ABL	Atmospheric boundary layer
ACP	Airload Computation Point
AEM	Advanced Enclosed Mast
AFAP	Air Flow Air Pattern
AFCS	Automatic Flight Control System
ASTOVL	Advanced Short Take-Off Vertical Landing
ASW	Anti-Submarine Warfare
ATM	Advanced Technology Mast
CAA	Civil Aviation Authority
CAD	Computer Aided Design
CAP	Civil Aviation Publication
CFD	Computational Fluid Dynamics
CFL	Courant-Friedrichs-Lewy
CODLOG	Combined Diesel or Gas
CSGE	Control System Graphical Editor
DDES	Delayed Detached Eddy Simulation
DEFSTAN	Defence Standard
DES	Detached Eddy Simulation
DG	Diesel Generator
DoD	Department of Defense
FFT	Fast Fourier Transform
FLME	FLIGHTLAB Model Editor
FlyCo	Flying Control
FOCFT	First of Class Flight Trial
FSC	Future Surface Combatant
FSS	Frequency Selective Material
GCS	Global Combat Ship
GT	Gas Turbine
HH	Hangar Height
HMS	Her Majesty's Ship
I-Mast	Integrated Mast
IAS	Indicated Airspeed
IRSS	Infrared Signature Suppression

ISA	International Standard Atmosphere
LES	Large Eddy Simulation
LIDAR	Light Imaging Detection and Ranging
M&S	Modelling and Simulation
MoD	UK Ministry of Defence
MUSCL	Monotonic Upwind Scheme for Conservation Laws
NAS	Naval Air Squadron
NATO	North Atlantic Treaty Organization
NIREUS	NATO Interoperability and Re-Use Study
NRC	National Research Council
PfP	Partnership for Peace
PSD	Power Spectral Density
RANS	Reynolds-Averaged Navier-Stokes
RMS	Root Mean Square
RTF	Ready-to-fly
RWUAS	Rotary Wing Unmanned Air System
SHOL	Ship Helicopter Operational Limit
SRGPS	Ship Relative Global Positioning System
SRS	Scale Resolving Simulation
SST	Shear Stress Transport
TTCP	The Technical Cooperation Programme
UA	Unmanned Aircraft
UAS	Unmanned Aircraft System
UoL	University of Liverpool
USS	United States Ship
VAD	Virtual AirDyn
WAT	Weight Altitude and Temperature
WOD	Wind-over-deck

Chapter 1. Introduction

This thesis describes a detailed computational study of the superstructure aerodynamics of a modern warship. While it is widely understood that the performance and stability of a ship is largely dependent upon the hydrodynamics of its hull below the waterline, the importance of the aerodynamics of the ship above the waterline, particularly the superstructure (the ship structure above the hull and the main deck), is less obvious. However, for helicopter-enabled ships, such as naval frigates, destroyers or support vessels, the air flow over the ship is critical for the helicopter's operational envelope and safety. It is now standard that such naval platforms operate with a maritime helicopter; the UK, for example, operates AW101 Merlin and AW159 Wildcat helicopters to both the Type 23 Duke class frigate and the Type 45 Daring class destroyer that are currently in service. The helicopter is arguably the most potent system on the ship, but its operational envelope is significantly affected by the ship's aerodynamics.

The motivation for this study is the advent of "stealthy" ships which are less detectable by radar. The characteristics of a stealth ship is a superstructure that is continuous and non-fragmented; has sloping flat surfaces instead of vertical sides; and few, if any, curved surfaces. The research that will be presented in the following chapters was funded by BAE Systems Surface Ships, and was undertaken in support of the design of the new UK Type 26 City class frigate, the first of which, HMS Glasgow, is currently under construction.

1.1. Background

A warship, or combatant ship, is a military ship that is designed primarily for naval warfare; it is armed with weapon systems and is designed to be resilient to damage. It is also faster and more manoeuvrable than a non-combatant ship. Warships are generally divided into seven main categories: aircraft carriers, cruisers, destroyers, frigates, corvettes, submarines and amphibious assault ships. In addition there are support vessels, often known as Auxiliary ships, that have limited offensive capabilities and which provide at-sea replenishment of fuel and other stores that are required to keep the warships operational.

The research reported in this thesis is concerned with ships that are in the categories of frigates and destroyers and which operate a maritime helicopter from a landing deck situated

towards the stern of the ship. The helicopter's main uses are anti-submarine and surface warfare, surveillance, troop transfer and supply replenishment at sea. Traditionally, frigates were considered to be smaller and less well armed than destroyers, with a mainly protective role for other ships. Destroyers, on the other hand were considered to be more capable warships with a wide range of offensive armaments. Nowadays the distinction is becoming blurred as frigates, notably the Type 26, are armed with the most advanced systems available.

While the research was initially concerned with the air flow over a modern warship and how it might impact the helicopter in the vicinity of the flight deck, it soon became apparent that there were two other important aspects of the ship's aerodynamics which affect the helicopter's operational envelope. The first is the ship's anemometers, which measure wind speed and direction relative to the ship, and which define the limiting conditions under which the helicopter can take off and land. The anemometers are themselves within the disturbed air flow over the ship and so the ship's aerodynamics affect their accuracy. The second issue is that of the dispersion of the hot exhaust gases from the ship's gas turbine engine(s), if the helicopter is exposed to heated air this can affect the lift from the main rotor, as well as the power output of the helicopter's engines. The mixing of the exhaust gases with the turbulent air flow over the ship will affect both the trajectory and temperature of the exhaust plume, and these too will be influenced by the ship's aerodynamics.

The thesis will describe how these aspects of the ship's aerodynamics was investigated using Computational Fluid Dynamics (CFD). Although the research is specifically concerned with a modern warship, the following sections begin with some historical background and context.

1.1.1. Historical Context

Warships can be traced back in time to ancient civilisations, but a landmark event in British naval history was in 1660 when the British navy became the Royal Navy after the restoration of the monarchy under Charles II. In 1661 Sir William Penn and Samuel Pepys established the Naval Discipline Act, which included the articles of war and founded the Royal Navy by statute [1]. The ships of this era, and until steam-powered ships were introduced from the mid-19th century, were sailing ships and a famous historical victory of that period was at the Battle of Trafalgar in 1805. The principal warships of that period were known as "ships of the line". Figure 1.1 is an image of a painting by Thomas Butterworth (ca. 1805) of a ship of the line; the painting is called "Return from Trafalgar" and it dramatically illustrates how these ships were at the mercy of the wind, both from the forces created by their sails, and from

the tumultuous waves on the sea surface. It is unclear what scientific aerodynamic theory there was at the time, but clearly the ship designers were extremely competent at capturing the benefits of the wind while maintaining stability in the rough seas.

Figure 1.1: A Ship of the Line, depicted in Thomas Buttersworth's painting "Return from Trafalgar" ca. 1805

Figure 1.2 shows a cross-section of Nelson's flagship, HMS Victory [2]. The waterline is at the widest beam of the section and above there are three gun decks housing 104 cannons. It can be seen that the width of the superstructure gets narrower as the height increases above the waterline. This feature is called the "tumblehome" and is thought to serve two purposes: to bring the weight of the higher guns closer to the ship centreline to improve stability, and to create a gap between two such ships when closing broadside so the cannon can still be deployed and marines cannot easily board the opposing ship [3].

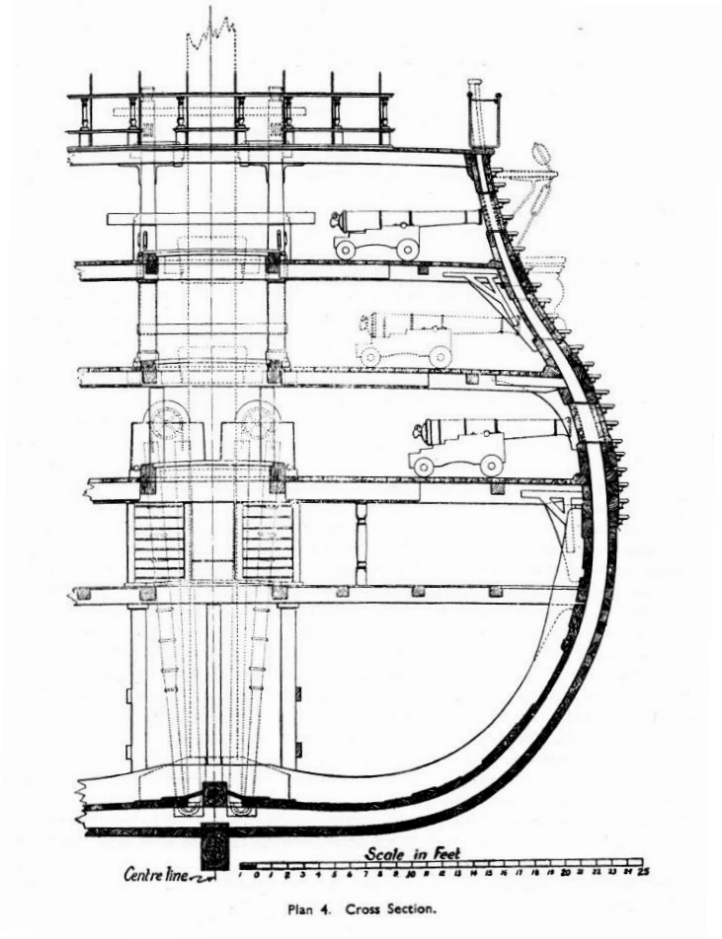

Figure 1.2: A diagrammatic cross section of HMS Victory showing the tumblehome and cannons [2]

1.1.2. Naval Aviation

Whilst the operation of fixed-wing aircraft from aircraft carriers can be traced to World War 1, rotary-wing aircraft, autogiros and then helicopters, were not developed until some years later. The first operational landing of a helicopter on a ship was a Sikorsky Hoverfly flown by Stewart R Graham, an American Coast Guard pilot, to a British bulk freighter MV Daghestan in 1944. The first landing of a helicopter to a naval frigate was conducted by a British lieutenant, Alan Bristow, who flew a Sikorsky Hoverfly to a specially constructed platform on the aft deck of HMS Helmsdale in 1946, pictured in Figure 1.3 [4].

Figure 1.3: Lieutenant Alan Bristow landing a Sikorsky Dragonfly on HMS Helmsdale in September 1946 [4]

The first non-carrier ship specifically designed to carry a helicopter was HMS Vidal, a Royal Navy survey ship which was launched in 1951 and which operated a Sikorsky Dragonfly. The first British frigate especially designed to operate a helicopter was HMS Ashanti, a Tribal class frigate launched in 1961 and which trialled the Westland Wasp helicopter which came into active service with the Royal Navy in 1964; Figure 1.4 shows a Westland Wasp aboard a Tribal class frigate. A concise history of British naval history can be found at [5] while an historical review of helicopters in the Royal Navy can be found at [6].

Figure 1.4: A Tribal class frigate with a Westland Wasp helicopter, ca. 1965 [7]

1.1.3. Wind Measurement

For sailing warships, wind was a crucial factor for the ships' design and operation. To this day, mariners have quantified 'wind strength', but it was in 1806 that a working scale of wind strength was developed by Commander Francis Beaufort of HMS Woolwich [8]. As well as quantifying the wind speed, mariners of the day were also concerned with the effect of the wind on the sea surface, and so in 1810 Beaufort added descriptions of the sea surface characteristics to each point on a 12 point wind scale. The sea state is itself a subjective measure, and sea states in a given wind will change if close to land, if the wind is on or off-shore, and if there are marine currents. It is not surprising therefore that the Beaufort scale, which is still widely used today, is largely descriptive, as seen in Table 1.1.

Table 1.1: Beaufort wind force scale

Beaufort wind scale	**Wind speed**		**Wind descriptor**	**Probable wave height** m	**Sea state**	**Sea descriptor**
	m/s	knots				
0	<1	<1	Calm	0	0	Glassy
1	1-2	1-3	Light air	0.1	1	Rippled
2	2-3	4-6	Light breeze	0.2	2	Wavelets
3	4-5	7-10	Gentle breeze	0.6	3	Slight
4	6-8	11-16	Moderate breeze	1.0	3-4	Slight-moderate
5	9-11	17-21	Fresh breeze	2.0	4	Moderate
6	11-14	22-27	Strong breeze	3.0	5	Rough
7	14-17	28-33	Near gale	4.0	5-6	Rough-very rough
8	17-21	34-40	Gale	5.5	6-7	Very rough-high
9	21-24	41-47	Strong gale	7.0	7	High
10	25-28	48-55	Storm	9.0	8	Very high
11	29-32	56-63	Violent storm	11.5	8	Very high
12	33+	64+	Hurricane	14+	9	Phenomenal

While it was a pragmatic solution in 1810 to assess the wind strength from judgements of whether the wind was a gentle breeze or a strong gale, or whether the sea was moderate or high, a more precise measurement system was required. Wind speeds are measured using anemometers, one of the earliest of which, designed by Thomas Romney Robinson in 1846 [9], comprised four hemispherical cups that were connected to a spindle and rotated in the wind. In the following years the cup anemometer was improved upon by various people until the design converged on the three-cup design that is widely used today and shown, together with a directional weather vane, in Figure 1.5(a). Modern naval ships use ultrasonic anemometers which have no moving parts; the ultrasonic anemometer shown Figure 1.5(b) measures two components of velocity in the horizontal plane, thereby giving horizontal wind

speed and direction. Figure 1.5(c) shows a three-component ultrasonic anemometer which is now coming into use and which also measures the vertical component of velocity.

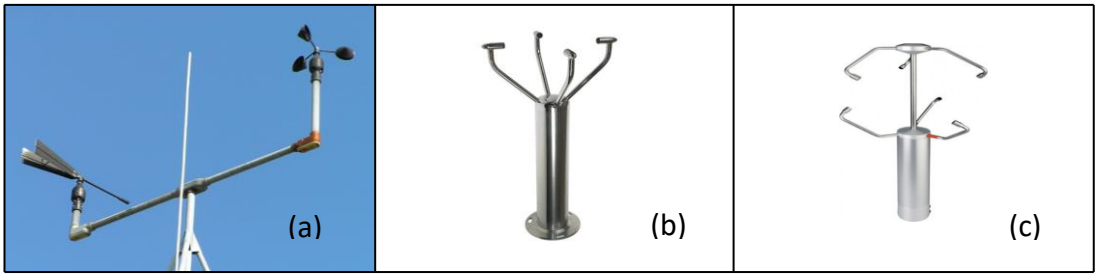

Figure 1.5: Examples of ships' anemometers: (a) cup and vane [10]*; (b) 2-D ultrasonic* [11]*; (c) 3-D ultrasonic* [12].

However, while ships' anemometers are widely used to provide a reading of wind speed and direction, they can be inaccurate due the distortion of the air flow as it passes over the ship's superstructure. The unreliable measurements by ships' anemometers is also an issue for the collection of marine meteorological data by research vessels and by merchant vessels that act as Voluntary Observing Ships [13]. The disturbed air flow over the superstructure is known as the ship's airwake, and it is how the airwake is affected by the design of a modern warship that is the principal subject of this thesis. Figure 1.6 shows a CFD calculation of a ship's airwake in a headwind, presented as normalised mean horizontal streamwise velocity. The velocity contours are shown in the vertical plane through the centre of the ship and illustrate the substantial reduction in velocity over the superstructure, including reverse flow behind significant structures such as the mast, funnel and the helicopter hangar ahead of the aft helicopter deck. The air flow approaching the ship has been given a vertical velocity profile that is representative of an oceanic boundary layer, also incorporated into Figure 1.6.

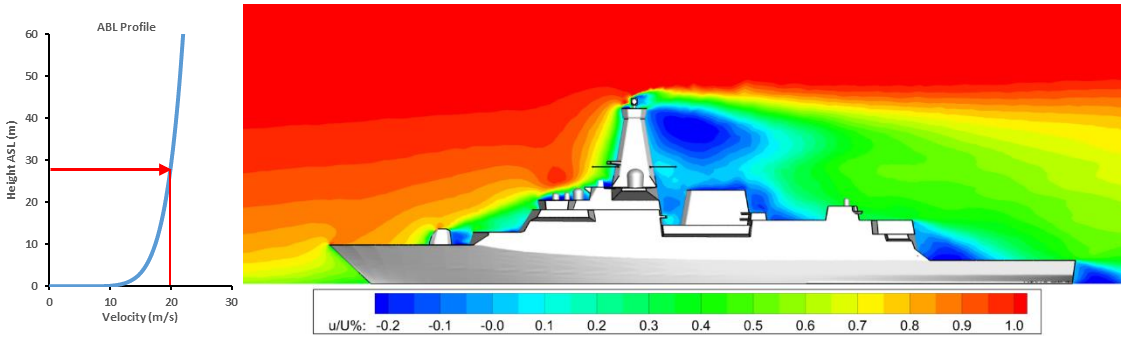

Figure 1.6: Disturbed air flow of the ship's airwake in a headwind, contours are of mean horizontal streamwise velocity component; also shown is the oceanic atmospheric boundary layer

1.1.4. Characteristics of a Modern Warship

The ship shown in Figure 1.6 is typical of a modern frigate or destroyer. The superstructure is not unduly cluttered and it is slab-sided; the mast is solid and bulky, the funnel is relatively low and discharges hot exhaust gases from a marine gas turbine; the helicopter deck is at the stern of the ship and for winds from the fore is in the lee of the superstructure.

The greatest above-water vulnerability of a ship comes from enemy radar beams originating near or slightly above the horizon coming from distant patrol aircraft, other ships or sea-skimming anti-ship missiles with active radar seekers. It is important that incoming radar waves are not reflected back to their source and so the sides of the ships are sloped inwards, hence the modern reappearance of the tumblehome seen earlier in Figure 1.2. Curved surfaces on the superstructure are minimised since they will scatter incoming beams in all directions, including back to their source. Internal corners are also to be avoided since they enable incoming beams to be reflected off two or more surfaces and back to their source. Therefore, the shape of the modern warship is becoming more "stealthy" [14], drawing on the stealth technology more commonly associated with sophisticated warplanes. The surface of the ship's superstructure can also be coated with radar absorbing materials, or even constructed from composite materials which absorb or attenuate radar signals, rather than simply reflecting them. The amount of radar energy that is reflected back to the radar receiver, usually co-located with the source, is known as its Radar Cross Section (RCS). A ship's stealth is concerned with not just radar invisibility, but also the avoidance of emitting its own electronic and infra-red (thermal) radiation, as well as underwater noise emission from the propulsion system.

The Swedish Visby class ship in Figure 1.7 is an example of a modern stealth ship. Because it is a small ship, being only 73m long and weighing about 640 tonnes, it has been constructed entirely from composite radar absorbing material. It is not only the sloping sides of the tumblehome that prevents the reflection of near-surface radar beams, but even the gun is facetted and the barrel is retractable. There are no curved surfaces, and there are no internal corners. The multitude of radomes and other sensors and instrumentation that are normally seen on warships are also missing, instead they are embedded in the composite outer skin of the vessel or are contained within and are capable of "seeing" through the non-metallic shell of the superstructure. What deck clutter and antennae there are can be stored away or retracted if necessary. The engine exhaust gases are concealed in hidden outlets near the waterline at the stern of the ship and mix with the spray emitted from the jet propulsion system, thereby eliminating the major source of infra-red emissions. The jet propulsion

system also emits less noise than a cavitating propeller. Another stealth feature of the Visby is its paintwork, which is known as dazzle camouflage, whose purpose is to break up the outline of the ship and was first introduced in World War 1 [14].

Figure 1.7: Swedish Visby class corvette [15]

The US Zumwalt class of destroyer, Figure 1.8, is another ship whose design is dominated by stealth requirements. At 180m long and 14,500 tonnes it is a large ship, even by destroyer standards. Its most obvious characteristic is its flat sloping surfaces, the lack of deck clutter and other protruding sensors and antennae. The guns on the foredeck are encased in facetted covers and there are no curved surfaces. The ship's hull and the lower section of the deckhouse are constructed from steel for structural strength. The helicopter hangar and the upper section of the deckhouse are constructed from composite material, and sensors and antennae are embedded in the composite outer surface or are contained within the composite structure. The engine exhausts are at the top of the deckhouse but are only visible from above the ship. The Zumwalt class ship was hailed as the replacement for the US navy's long-serving destroyer, the Arleigh-Burke class, and originally 32 vessels were anticipated; however, spiralling costs and questions over its defensive capabilities meant that only three were ordered [16].

Figure 1.8: US Zumwalt class destroyer [17]

While the designs of the two ships discussed above have been heavily influenced by stealth requirements, there are good reasons, not least cost and practicality, which has meant that most modern warship designs have taken a more pragmatic approach to stealth technology. The British Type 45 Daring class destroyer is a good example of a modern warship with stealth features which affect the ship's aerodynamics. The principle adopted in this design is not to make the ship invisible, but to considerably reduce its RCS so that it appears on radar as a much smaller ship, i.e. the tactic is one of disguise, not invisibility. The Type 45 came into service in 2009, replacing the Type 42 which came into service in 1975. Comparing the two ships in Figures 1.9 and 1.10 illustrates how the design of modern warships is evolving; although the two ships are British, similar developments can be seen in the ships of other navies. The older Type 42 is 132m long, compared with the newer Type 45 at 152m long; the Type 42 was a much lighter ship with a displacement of 3500 tonnes, compared with 8000 tonnes for the Type 45. As can be seen, the superstructures of the two ships are very different, and this difference is mostly driven by the reduction in RCS.

Figure 1.9: British Type 42 Sheffield class destroyer, HMS Liverpool [18]

Figure 1.10: British Type 45 Daring class destroyer, HMS Daring [19]

1.1.5. Helicopter-enabled Warships

Modern warships routinely operate with maritime helicopters. The flying environment is a challenging one: limited deck space, close proximity of superstructure, deck motion, possible visual degradation due to spray and rain, and the unsteady air flow in the vicinity of the flight deck. Figure 1.11 is a picture of a Danish Seahawk helicopter attempting to land to an offshore patrol vessel in the rough seas of the North Atlantic [20]. The unsteady air flow, or ship airwake as it is known (see Figure 1.6), is due to the combination of the ship's forward speed and the prevailing wind and is often cited by pilots as being the most challenging factor when recovering to a ship in strong winds [21]. The safe operational envelope for a particular helicopter/ship combination is defined by the Ship-Helicopter Operational Limits, or SHOL, which is specified in terms of maximum allowable wind speed for different wind directions. The combination of wind speed and direction, relative to the ship, is referred to as a wind-over-deck (WOD) condition. A typical SHOL envelope is shown in Figure 1.12 where it can be seen, for example, that it is deemed safe to land the helicopter for wind speeds from ahead of up to 50 knots, while for winds coming from a relative direction of 45° off the starboard (Green 45) the maximum wind speed is 30 knots. In naval terminology, winds approaching the ship from the starboard side are called Green winds, and winds approaching from the port side are known as Red winds. For clarity, when standing on the ship and facing the bow, starboard is to the right and port is to the left.

Figure 1.11: Danish Seahawk helicopter landing to an offshore patrol vessel in rough seas [22]

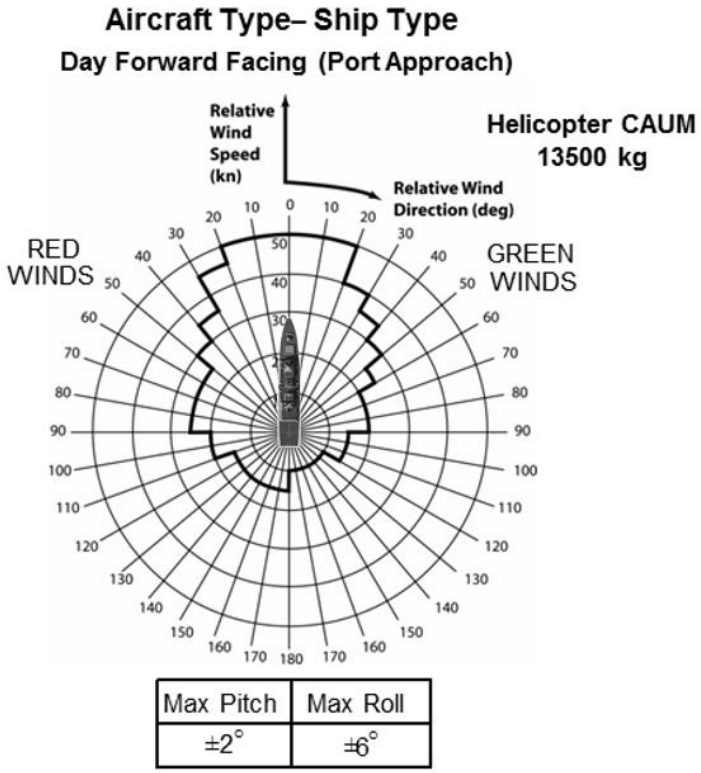

Figure 1.12: Representation of typical SHOL diagram [23]

The SHOL is determined by helicopter test pilots conducting launch and recovery (take-off and landing) trials at sea in as wide a range of wind speeds and directions as possible, to determine the safe conditions for an average fleet pilot [24]. The SHOL is more important for

the helicopter's recovery, since the pilot will not take off if the conditions are outside of the operational envelope, but if the helicopter has already been deployed it is important that the wind conditions are safe on landing. The ship's captain will have some control of the relative wind through the ship's speed and heading, but not total control.

The standard helicopter recovery procedure used in the Royal Navy is known as the port-side landing manoeuvre, which is illustrated in Figure 1.13, where the pilot first positions the helicopter parallel to and alongside the port side of the ship, matching the ship's speed. The aircraft is then translated sideways across the deck, with the pilot's eye-line at about hangar height until positioned above the landing spot; during a quiescent period in the ship's motion, the pilot will descend to the deck and land the aircraft. The landing begins from the port side because the pilot, who sits in the right-hand seat, will have a clear view of the deck. The turbulent air flow cascading over the ship's superstructure impacts upon the helicopter and will make the landing task more difficult, particularly as the pilot is trying to land on a moving deck while being in close proximity to the superstructure.

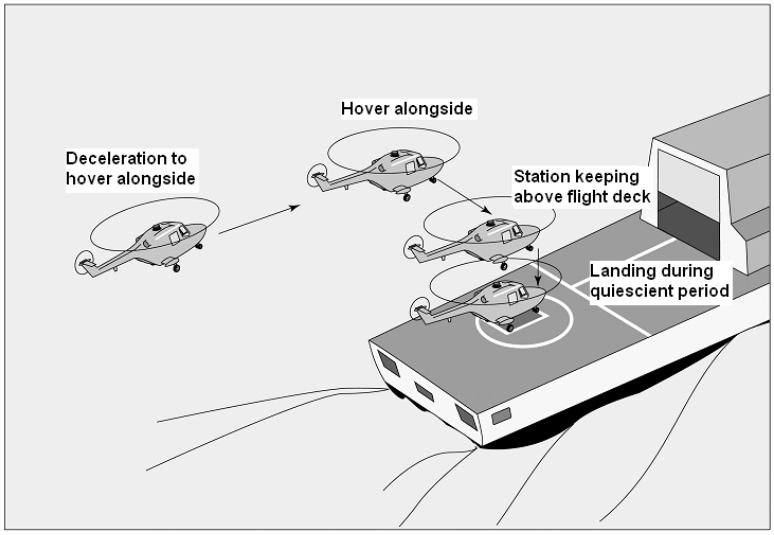

Figure 1.13: Final stages of the recovery of a Royal Navy helicopter to a single spot frigate/destroyer [23]

The engineering design of a modern helicopter-enabled warship takes into account the flight deck, hangar, and other aviation services [25]; however, consideration of the ship superstructure aerodynamics is not so prominent. Traditionally, once the ship design has been finalised, wind tunnel models have been made and used to examine the air flow over the ship, possibly including an assessment of exhaust gas dispersion and flow distortion at the locations identified for placement of the ship's anemometers. However, the effect of the

ship's aerodynamics on the helicopter will not be known until the ship is built and undergoes at-sea flight trials.

In recent years there has been significant research into the use of CFD to model the air flow over naval ships, and into the use of mathematical flight dynamics models of a helicopter to assess how that air flow will affect the aircraft and pilot workload. These technological advances have enabled helicopter launch and recovery operations to be simulated in motion-base flight simulators where piloted deck landings have been conducted to create simulated SHOLs and to inform the sea trials [23], [26], [27]. However, while CFD has been contributing towards these modelling and simulation techniques, there is still little understanding of how the stealthy designs of the modern warship is affecting its aerodynamics and, more specifically, how it affects the ship's helicopter.

1.1.5.1. Superstructure Aerodynamics: Stealth vs. Aviation?

The Type 26 City class ship will be the latest generation of frigate and is due to enter service with the Royal Navy in the mid-2020s, replacing the Type 23 Duke class. The Type 26 will operate with Merlin and Wildcat maritime helicopters. Images of the two ships are shown in Figure 1.14. As can be seen, there are significant differences in the superstructures of the two ships, much as there was in the generational change between the Type 42 and 45 destroyers shown earlier in Figures 1.9 and 1.10. Compared with the Type 23, the future Type 26 has a much cleaner uninterrupted superstructure with sloping sides and much reduced equipment and systems. The Type 26 also has a bulky enclosed main mast, aft of which is the funnel from which the gas turbine exhaust gases are discharged. Much of the design characteristics are driven by the requirements for reduced RCS, but the geometry of the superstructure will also affect its aerodynamics and therefore the operational envelope of the ship's helicopter.

This thesis will describe, in detail, how CFD has been used during the design phase of the Type 26 to predict the air flow over the ship, and how this affects the flow distortion at the anemometer positions, and the dispersion of the exhaust gases from the gas turbine, all of which have a bearing upon helicopter operations. Selected comparisons will also be made with the computed aerodynamics of the older Type 23 frigate. A short outline of the research has been presented by the Author in [19] (available in the Appendix); however; even though some of the work has been published in the public domain, there are still aspects of the research that is sensitive and so the data included in this thesis is drawn from earlier design evolutions of the ship, not the final design. In its early design stages the ship was known as

the Global Combat Ship (GCS), therefore the ship will henceforth be referred to in the thesis as the GCS.

Figure 1.14: Comparison of Type 23 Duke class (HMS Argyll) [28] *(top) and Type 26 City class* [29] *(bottom)*

Chapter 2 will give an overview of the Computational Fluid Dynamics methodology used for analysing the air flow over a warship while Chapter 3 will apply the methodology to compare the aerodynamics of the GCS and the Type 23, including an assessment of how the air flow over the flight deck will affect the aerodynamic loads on a helicopter. In Chapter 3 there is also a comparison of the air flow at the anemometer locations of the two ships and of how the exhaust efflux from the engines of the two ships are dispersed by the airwakes. Chapters 5 and 6 will give a more detailed analysis of the effect of the GCS airwake on the expected anemometer performance and on the exhaust gas dispersion, respectively. Chapter 6 presents a novel analysis of the launch of a small fixed-wing unmanned aircraft from the deck

of the GCS into an airwake; although only an initial analysis, the procedure has potential to inform the way that such craft could be operated in the future. Finally, Chapter 7 will draw together the main conclusions from the research and will make recommendations for future research

Chapter 2. Computational Fluid Dynamics for Ship Airwake Modelling

As mentioned in Chapter 1, Computational Fluid Dynamics (CFD) has been used in this research project to simulate the airwakes of the GCS and Type 23 frigates for the analysis of the turbulent flow field above each ship's flight deck. CFD has also been used to analyse the local flow in the vicinity of the ships' anemometers and the dispersion of the engine exhaust efflux, all with respect to helicopter operations. This chapter outlines the general methodological approach for all of the unsteady CFD simulations presented in this thesis. The subtleties of producing the computational mesh for "standard" ship airwakes, compared with airwakes inclusive of exhaust gas dispersion, are explained, along with the specific types of inlet conditions used for the injection of hot exhaust gases into the computational domain.

2.1. Modelling of Ship Airwakes with CFD

The ability to predict, at full-scale, the time-accurate characteristics of the turbulent air flow over a ship is becoming a powerful tool for the assessment of a ship's topside aerodynamics, and a viable alternative to wind tunnel testing. Of particular interest to the research being reported in this thesis is how the air flow impacts on the operation of the ship's helicopter. CFD simulations of the prevailing wind interacting with a ship's superstructure can provide a comprehensive data-set of the air flow characteristics over the ship, aspects of which can be used during the design cycle before a ship is built or enters service. The ability to assess a ship's topside aerodynamic characteristics during the design cycle can provide a number of opportunities to inform positive design changes, which can ultimately benefit the ship's helicopter [30]. Most innovatively, the simulated ship airwake can be used in the analysis of ship-helicopter operations prior to first of class flight trials (FOCFT), with the potential to identify key flying conditions of interest and provide simulated preparation for the flight trial programme. This potential was demonstrated in the recent flight trials of the UK's new F-35B Lightning ASTOVL (Advanced Short Take-Off Vertical Landing) aircraft to HMS Queen Elizabeth, the UK's new aircraft carrier. Piloted flight simulation, including CFD-generated airwakes, was extensively used to prepare crews for the trials [31].

The application of CFD in the simulation of ship airwakes has been actively researched since the early 2000s and has evolved significantly over the succeeding 20 years [32]–[42]. At the University of Liverpool (henceforth referred to as UoL), the use of CFD for the prediction of ship airwakes has been the subject of research since 2005 [43], from initial steady-state and inviscid flow simulations [44], to the unsteady time-accurate viscous flow computations that have been used to generate airwakes for various flight simulation research projects [45]. The process of modelling and simulating ship airwakes at the UoL has been successively improved, refined and validated [46]–[50], notably through internationally collaborative research on the Simple Frigate Shape 2 (SFS2) (Fig. 2.1), used as a baseline model for ship airwake modelling validation. The SFS2 was devised by the Technical Co-operation Programme (TTCP), to advance research on the modelling and simulation of the helicopter-ship dynamic interface by removing the difficulties faced in sharing sensitive data between its member countries [51]. Experimental SFS2 airwake data produced by the National Research Council (NRC) in Canada [52], was used by Forrest et al. [45] at the UoL to validate their developed CFD methodology for simulating ship airwakes. As presented in a recent review paper by Shukla et al. [53], the SFS2 experimental data from NRC Canada and the CFD analysis by Forrest et al., is still regarded as the benchmark data for ship airwake CFD validation [34], [41], [42]. The same CFD methodology has recently been extensively validated through experimentation by Watson et. al. [54] at the UoL for the simulation of the Queen Elizabeth Class (QEC) carrier airwakes.

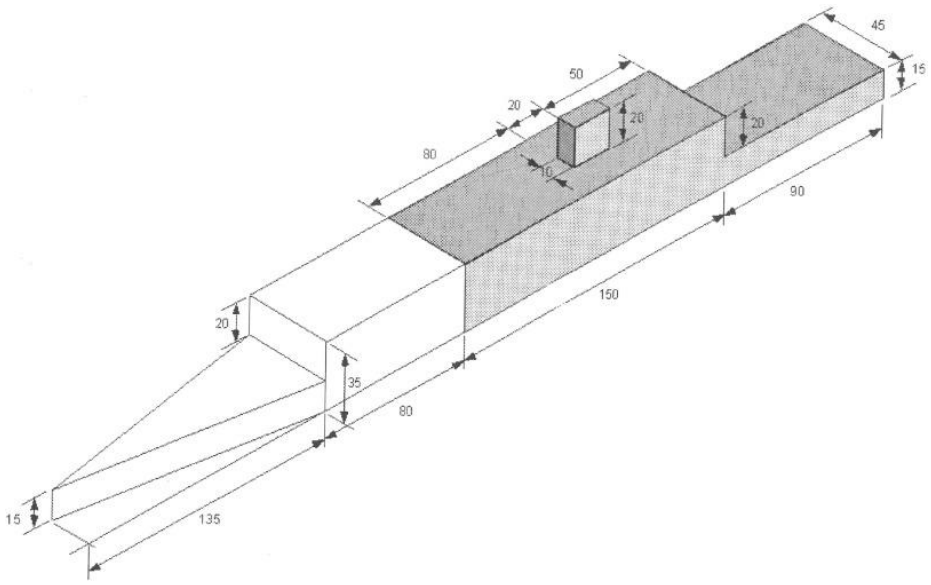

Figure 2.1: Simple Frigate Shape 2 (SFS2) [52]

The CFD methodology developed at the UoL was therefore used as the foundation for the ship airwake simulations produced during this PhD study. The additional complexity of modelling the ship's exhaust gas dispersion within the airwake has also been examined in this thesis. For ship airwakes with and without exhaust gas dispersion modelling, the production of a ship airwake CFD simulation typically involves the following key stages:-

- Geometry CAD preparation
- Mesh generation
- Solver setup/Solution approach
- Solving the governing equations of CFD
- Post-CFD analysis

For the work undertaken in this thesis, ANSYS ICEM CFD v16.2 was used for mesh generation and the ANSYS Fluent v16.2 flow solver was used for all CFD computations [55]. The following sections present an overview of the CFD methodology and an explanation of the fundamental equations which form the basis of the CFD simulations. The process of preparing the CAD (digital drawings of the ship), creating a computational grid, and the solver setup used to produce the CFD cases discussed in this thesis will also be explained.

2.2. CFD Methodology

2.2.1. The Governing Equations

The governing equations of CFD are based upon three fundamental physical principles that describe fluid dynamics: the conservation of mass, conservation of momentum (Newton's second law) and the conservation of energy. Through applying these three physical principles to a model of the fluid, three sets of coupled non-linear partial differential equations can be derived. These fundamental equations of fluid mechanics can be expressed in various forms; the following formulations are for viscous flows without chemical reactions or mass transfer as presented by Anderson [56].

Continuity equation:-

$$\frac{D\rho}{Dt} + \rho\nabla.V = 0 \tag{2.1}$$

Momentum equations (Navier-Stokes):-

$$\rho\frac{Du}{Dt} = -\frac{\partial p}{\partial x} + \frac{\partial \tau_{xx}}{\partial x} + \frac{\partial \tau_{yx}}{\partial y} + \frac{\partial \tau_{zx}}{\partial z} + \rho f_{b,x}$$

$$\rho\frac{Dv}{Dt} = -\frac{\partial p}{\partial y} + \frac{\partial \tau_{xy}}{\partial x} + \frac{\partial \tau_{yy}}{\partial y} + \frac{\partial \tau_{zy}}{\partial z} + \rho f_{b,y} \tag{2.2}$$

$$\rho\frac{Dw}{Dt} = -\frac{\partial p}{\partial z} + \frac{\partial \tau_{xz}}{\partial x} + \frac{\partial \tau_{yz}}{\partial y} + \frac{\partial \tau_{zz}}{\partial z} + \rho f_{b,z}$$

Energy equation:-

$$\begin{aligned}\rho\frac{D}{Dt}\left(e + \frac{V^2}{2}\right) = \rho\dot{q} + \frac{\partial}{\partial x}\left(k\frac{\partial T}{\partial x}\right) + \frac{\partial}{\partial y}\left(k\frac{\partial T}{\partial y}\right) + \frac{\partial}{\partial z}\left(k\frac{\partial T}{\partial z}\right) - \frac{\partial (up)}{\partial x} \\ - \frac{\partial (vp)}{\partial y} - \frac{\partial (wp)}{\partial z} + \frac{\partial (u\tau_{xx})}{\partial x} + \frac{\partial (u\tau_{yx})}{\partial y} + \frac{\partial (u\tau_{zx})}{\partial z} \\ + \frac{\partial (v\tau_{xy})}{\partial x} + \frac{\partial (v\tau_{yy})}{\partial y} + \frac{\partial (v\tau_{zy})}{\partial z} + \frac{\partial (w\tau_{xz})}{\partial x} \\ + \frac{\partial (w\tau_{yz})}{\partial y} + \frac{\partial (w\tau_{zz})}{\partial z} + \rho f_b . V\end{aligned} \tag{2.3}$$

In the form written above, the equations cannot be directly solved. CFD is the process by which an iterative solution to the equations can be obtained through the discretization of the partial differential equations onto a computational grid. Discretization replaces the partial differential equations with a system of algebraic equations which can be solved at discrete point locations. The flow field is therefore simulated in space and time through obtaining solutions at these points – the nodes of the computational grid.

2.2.2. Turbulence Modelling

When the unsteady variables in the Navier-Stokes equations are decomposed, e.g. $u_i = \bar{u}_i + u'_i$, and the equations are time-averaged, it is seen that additional terms appear in the equations due to their non-linearity. These terms, which can be written as $-\rho u'_i u'_j$ are called Reynolds Stresses and need to be accounted for when solving the equations. This is commonly called a closure problem, and it is addressed by modelling their effects using one of a range of turbulence models [57]–[59].

Employing the correct turbulence model for ship airwake calculations is essential for ensuring accurate prediction of the turbulent flow created as a result of the separation of

the freestream airflow from the ship's superstructure. Detached Eddy Simulation (DES), with a Shear-Stress-Transport (SST) k-ω turbulence model for closure, was the chosen turbulence modelling methodology for this project. The method is well-suited to ship airwake generation and, in addition, it was shown by Forrest et al. [45] to agree well with experimental data, also more recently confirmed by Yuan et al. [41]. DES is a hybrid model, employing Reynolds Averaged Navier Stokes (RANS) in the boundary layer regions and Large Eddy Simulation (LES) away from the walls, explicitly resolving turbulent structures where the flow is separated. The application of DES with an SST k-ω turbulence model occurs through the parameter, F_{DES}. The switch between RANS and LES modelling schemes is determined through this parameter which links local turbulent length scale, L_t, the calibration constant, $C_{DES} = 0.61$, and the maximum local grid spacing, Δ, (Eq. 1.4) [60].

$$F_{DES} = \max\left(\frac{L_t}{C_{DES}\Delta}, 1\right) \tag{2.4}$$

The benefits of DES are well documented for large scale, high Reynolds number, wall bounded turbulent flows, where a pure LES solution would be exceptionally computationally expensive as a result of the need to resolve the fluid flow right down to the wall. Significant mesh refinement would therefore be required to resolve the flow, unlike DES where RANS modelling in the boundary region allows for the use of a wall function to approximate the boundary layer flow condition, requiring a significantly coarser mesh (explained in more detail in Section 2.4.2).

More recently, DES has evolved to the Delayed Detached Eddy Simulation (DDES) approach for turbulence modelling, however, at the time of commencement of this project, DES turbulence modelling was successively validated for the production of unsteady time-accurate frigate airwakes by Forrest et. al. [45]. Furthermore, it has been demonstrated in recent paper by Yuan et al. [41] that for bluff body flows DES and DDES results are very closely matched, with the DDES simulation data from Yuan et al. and DES simulation data from Forrest et al. of the SFS2 both agreeing to within 5% of SFS2 experimental data. As a result, DES was used for the entirety of the project for consistency.

2.2.3. Thermal Energy Modelling

In Fluent, turbulent heat transport is modelled using the concept of the Reynolds analogy. In a laminar flow with a velocity gradient, momentum is transferred between a faster moving

fluid layer and a slower one due to the viscosity of the fluid. In a laminar fluid with a temperature gradient, thermal energy is transferred between the hotter layer of fluid and the cooler one due to the thermal conductivity of the fluid. The Reynolds analogy recognises the similarity of the transport mechanisms and if the ratio of momentum diffusivity (ν) and thermal diffusivity (α), i.e. the Prandtl number Pr, is unity then the transport mechanisms are identical. The concept is equally applicable in turbulent flow, where the turbulent mixing of the fluid transports both momentum and energy by the same mechanism, but greatly enhanced over those in the laminar flow. Therefore in turbulent flow the analogy is characterised by the turbulent Prandtl number, which is the ratio of the momentum and thermal turbulent eddy diffusivities.

Fluent uses the Reynolds analogy to model turbulent heat transfer via equation 2.5, using Fluent's nomenclature [61]:

$$\frac{\partial}{\partial t}(\rho E) + \frac{\partial}{\partial x_i}[u_i(\rho E + p)] = \frac{\partial}{\partial x_j}\left[\left(k + \frac{c_p \mu_t}{Pr_t}\right)\frac{\partial T}{\partial x_j} + u_i(\tau_{ij})\right] \qquad (2.5)$$

Experiments show the turbulent Prandtl number, Pr_t, has an average value of 0.85, but ranges from 0.7 to 0.9 [62]. In the present study the default value of 0.85 was adopted.

2.2.4. Discretization Schemes

While the governing equations are the fundamental flow physics behind CFD, the discretization of these equations is, in essence, the 'CFD part'. Various discretization methods can be used to allow the flow field to be approximated numerically at a finite number of discrete points within the fluid domain [56].

As an unstructured tetrahedral grid was used, and therefore can never be totally aligned with the freestream flow, second-order discretization is necessary to improve the accuracy of the solution by minimising the numerical discretization error. The initial steady-state solution used for each unsteady CFD case was run with first-order discretization to achieve good convergence in a short period of time; this is acceptable as this solution is purely for the purpose of flow field initialisation. Upon initialising the unsteady solver from the steady-state solution, second-order discretization was then used for pressure and third order Monotonic Upwind Scheme for Conservation Laws (MUSCL) for momentum [63]. Temporal discretization was achieved with a second-order implicit time advancement scheme.

Pressure-velocity coupling was solved with the coupled algorithm where the momentum and pressure corrections are solved together.

2.3. CAD Geometry

Any CFD simulation requires a CAD model of the physical structures over and/or through which the fluid flow will be simulated. The CAD model also encompasses the domain that is built around the structure in which the solution is enclosed. The process of refining a CAD geometry for CFD can often become an iterative process, along with mesh generation (Section 2.4). The quality of the CAD most often directly affects the quality of the mesh.

The following section will discuss the process of preparing a CAD model for ship airwake simulation.

2.3.1. Preparation of CAD

A CAD model can either be generated from scratch specifically for the CFD case to be computed, or can be supplied from an outside source in one of many CAD formats. The latter may require modification to the model to make the mesh generation process more efficient. If the geometry to be modelled is not particularly complex, generating a geometric model from scratch does not pose much difficulty and will ensure that the geometry is designed to be meshed easily and is watertight i.e. the meshing algorithm will not penetrate the solid surfaces (just as fluid would not 'leak' into a sealed structure in the real world). However, large, complex models, such as that of the GCS would take a long time to generate from drawings. In this study, a model of the GCS was therefore procured from BAE Systems in '.igs' format. A detailed image of the complete original CAD cannot be shown due to the sensitive nature of some of the equipment present within the model; however, a press-released computer rendered image of the GCS is shown in Figures 2.2 and 2.3 to illustrate the complexity of the geometric features initially present on the CAD model received.

Figure 2.2: Computer generated image of the Global Combat Ship (GCS) [64] *[Bow view]*

Figure 2.3: Computer generated image of the Global Combat Ship (GCS) [Stern View] [64]

When a CAD model is obtained from an outside source, it can arrive in one of many formats that will have to be translated into the software used for CAD preparation and mesh generation – in this case Ansys ICEM. The translation of the CAD from one software package to another can sometimes give rise to errors, such as missing parts, the physical displacement of parts, holes between facets across large surfaces, etc. If parts are missing or displaced, they can often be easily identified and corrected through the comparison of the CAD model to drawings and rendered images. Holes in the surfaces of the CAD can pose more difficulty. In the case of the GCS, the large, complex, curved hull surface did have some small holes, as shown in Figure 2.4 where the thin horizontal line in the enlarged image is a gap between panels. Due to the nature of the surface, these gaps were very difficult to fix in Ansys ICEM. In the same way that a 'fluid' body is defined between the ship's surfaces and the domain

boundaries, the behaviour of a watertight, solid structure can be enforced by placing a body of material inside the ship. By naming this body 'orfn' - named as such by Ansys ICEM to describe an orphaned body of material that does not belong to any defined parts of the CAD - the meshing algorithm in Ansys ICEM will seemingly 'walk-over' small gaps in surfaces when it detects the 'orfn' body. This occurs as a result of ICEM detecting mesh elements that penetrate a surface into an 'orfn' defined region and effectively removing them, seeing them as not belonging to any defined 'parts' – effectively orphaned elements – and hence leaks into a solid structure are prevented.

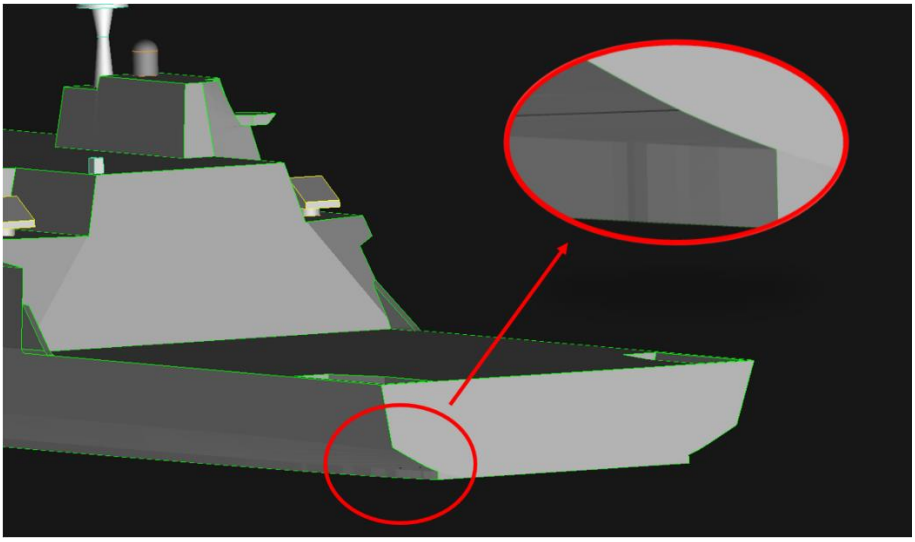

Figure 2.4: Example of CAD errors in procured model of the GCS showing a hole in rear of the hull

When optimising a CAD model for CFD it is also wise to consider the characteristics of the likely flow phenomena to be observed in the region of particular interest, or focal region, of the simulation. In the present study, the focal region for ship CFD simulations was initially the region above the flight deck and in the immediate vicinity. The turbulent structures shed from the sharp edges of the superstructure will pass across the flight deck and impose unsteady moments and forces on a helicopter flying in that region. Work by Lee and Zan [65] deemed that shedding frequencies, and therefore unsteady aerodynamic loads, in the region of 0.2-2Hz have a recognizable impact on pilot workload. As a result, any geometric features in the vicinity of the flight deck that are small enough so as to produce shedding frequencies outside of this range are removed. Such small geometric features would only increase total computational grid size and therefore computation time for no increase in simulation fidelity.

2.3.2. Domain Shape and Sizing

Following the successful modification of the CAD geometry, the ship model must then be enclosed within a domain of solid boundaries to define the region for fluid flow computation, known as the computational domain. The approach to determining the size and shape of the computational domain is that recommended by Forrest [47] whereby a cylindrical domain is employed. Only one computational grid need be generated and used for all computations through a 360° azimuth as the cylindrical walls allow fluid flow to be initialised from any specified direction.

The domain boundaries must be of adequate distance from the ship to ensure that no wall effects from the boundaries are present in the focal region of the CFD computation. Forrest [47] determined a generic approach to domain sizing according to the length of the ship to be modelled, l, as shown in Figure 2.5 where the radius of the cylinder, $r = 4.5l$, and the height of the cylinder, $d = 0.9l$.

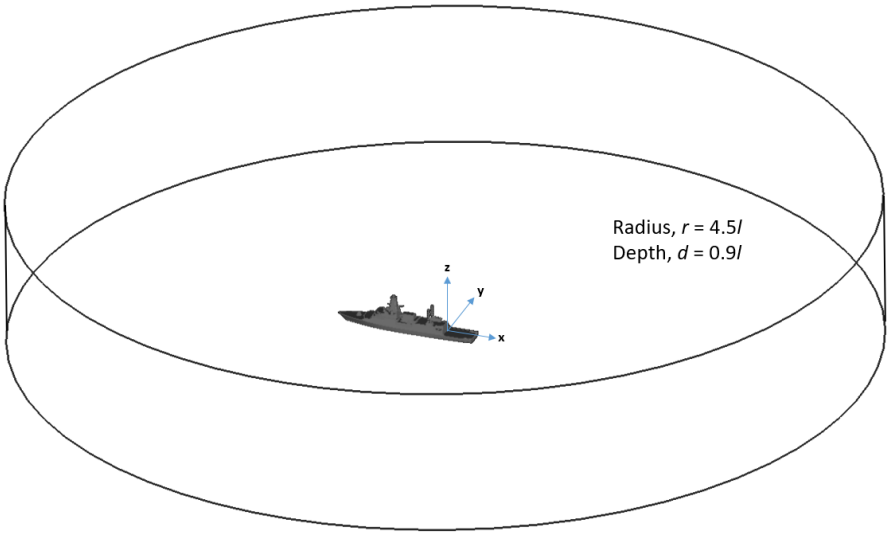

Figure 2.5: Computational fluid domain shape and sizing

The GCS was placed centrally within the cylindrical domain, whose axis coincided with the origin of the ship's axes which is on the ship's longitudinal centreline at the point where the hangar face meets the flight deck (Figure 2.6). The bottom surface of the cylindrical domain represents the waterline, therefore the origin location sits a few metres above the bottom surface. Positive x runs longitudinally from the origin toward the stern, positive y runs laterally from the origin toward starboard and positive z runs vertically upward from the origin, away from the flight deck.

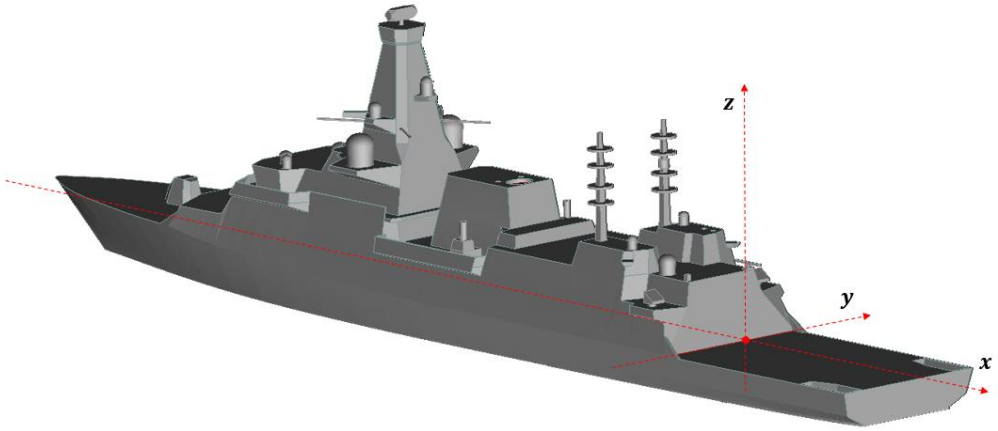

Figure 2.6: GCS axis reference

The flow direction of the fluid entering the domain is specified using unit vectors (Equation 2.6) in relation to the ship's axes. For all of the CFD simulations produced in this thesis, the prevailing wind condition, V_{WOD}, (Figure 2.7) was directly specified as a wind speed and direction and not as combination of forward ship speed with oncoming wind condition.

$$\begin{aligned} \hat{v}_x &= cos\psi \\ \hat{v}_y &= sin\psi \\ \hat{v}_z &= 0 \end{aligned} \tag{2.6}$$

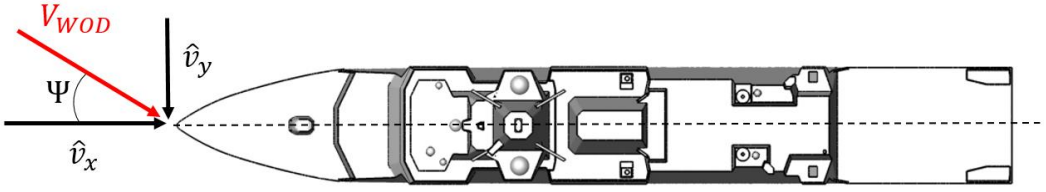

Figure 2.7: Unit vector formation to determine the wind-over-deck (WOD) condition

2.4. Mesh Generation

In order for the governing equations of CFD to be solved throughout the fluid domain, the domain needs to be discretized into small volumes, or cells. In the present study the number of cells were 11-12 million for standard airwakes and 14-15 million for airwakes inclusive of ship exhaust gas dispersion modelling.

As previously mentioned in Section 2.3, the generation of a computational grid (mesh) is directly affected by the quality of the CAD geometry that the meshing algorithm is applied

to, therefore the processes described in Sections 2.3 and 2.4 are often interdependent and iterative.

2.4.1. General Meshing Process for Ship Applications

An unstructured (i.e. irregular) meshing technique has been employed, using tetrahedral cells. Unstructured meshes are quicker and easier to generate compared with structured grids, particularly when dealing with complex geometries such as the GCS. There are a few key stages to producing a good mesh, and the success of each stage is dependent on the preceding one:-

1) The generation of an unstructured volume mesh using the Robust (Octree) method
2) Deletion of the volume elements and the retention of the unstructured surface mesh only
3) The application of the Laplacian smoothing algorithm to attain a smooth growth transition away from the ship geometry
4) The generation of an unstructured volume using the Quick (Delaunay) method from the smoothed unstructured surface mesh
5) Smoothing of the unstructured Delaunay volume mesh
6) The generation of initial prism layers using the post-inflation method to capture boundary layer flows
7) The splitting and redistribution of prism cell layers to ensure correct wall distance
8) The exportation of the final mesh with correct boundary conditions defined

The first stage of mesh production is to create a good quality surface mesh from which a volume mesh can later be grown. The surface mesh is produced by growing a robust octree volume mesh. Mesh sizing is important at this stage to ensure the correct surface mesh size in focal areas, as this will inform the size of the cell growth away from surfaces. The tetrahedral volume elements of the octree mesh are removed and the triangular surface elements are then smoothed using the Laplacian algorithm. Octree mesh generation does not produce a smooth growth transition away from surfaces due to cell growth being defined by powers of 2. This creates defined ‘jumps’ in mesh size away from surfaces. The Laplacian smoothing algorithm blends the defined lines of cell growth by working to make the ‘tri’ surface elements more equilateral, as seen in Figure 2.8.

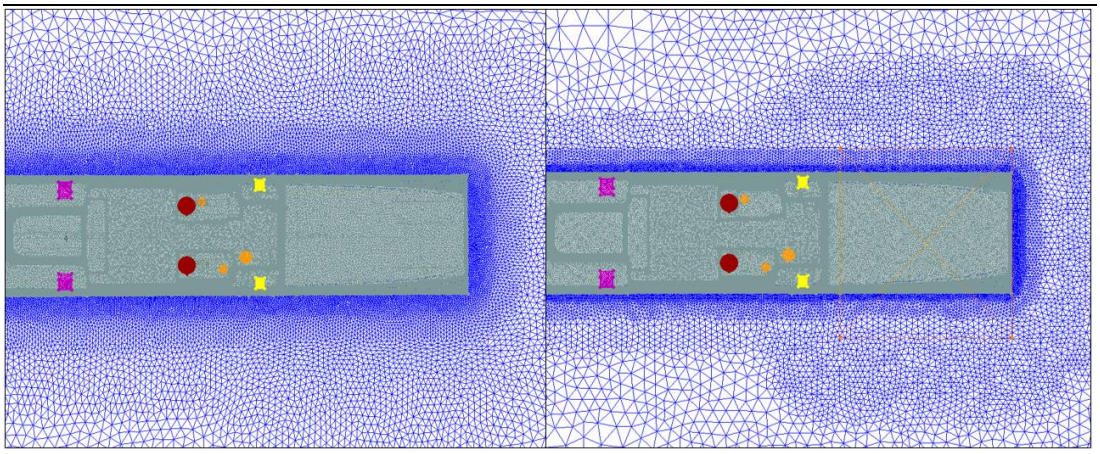

Figure 2.8: Example of a smoothed surface mesh (left) derived from a robust octree surface mesh (right)

2.4.2. Boundary Layer Meshing for Bluff Body Aerodynamics

Although bluff body aerodynamics is not as heavily concerned with boundary layer flows as, for example, the flow over an aircraft wing, the resolving of the boundary layer across the ship's surfaces is nonetheless important for accurately predicting key flow phenomena. When modelling the airwakes of a modern warship, the sharp edges of the ship's superstructure are the prime source of flow separation. Correctly modelling the boundary layer is necessary to ensure that flow reattachment across the large flat surfaces of the ship's geometry is captured accurately. An example of this would be the recirculation zone that is present in the lee of the ship's hangar in a headwind [32]; i.e. an area of low pressure, recirculating fluid that is present over the landing deck as a result of the backward facing step created by the hangar.

A key parameter in ensuring the accurate capture of the boundary layer for a specific flow problem is the y^+ value (Eqn. 2.7), known as the dimensionless wall distance. The y^+ value describes the relationship between fluid velocity and the absolute distance from a wall, y, as a result of the friction velocity, u_τ, and the kinematic viscosity, υ.

$$y^+ = \frac{y u_\tau}{\upsilon} \tag{2.7}$$

Where the friction velocity is defined using the wall shear stress, τ_w,

$$u_\tau = \sqrt{\frac{\tau_w}{\rho}} \tag{2.8}$$

Additionally, velocity can be made dimensionless with, u_τ, to give the dimensionless velocity,

$$u^+ = \frac{u}{u_\tau} \tag{2.9}$$

Figure 2.9 plots y^+ against u^+ highlighting the three distinct regions of the boundary layer: the viscous sub-layer, the buffer layer and the log-law region, which all physically behave differently. The near-wall region, $y^+ < 300$, can be modelled by one of two approaches: employing the use of a wall function or through the near-wall model (Figure 2.10). To employ the near-wall model, the mesh must be refined to allow the viscous sub-layer and buffer layer to be resolved, dramatically increasing cell count and therefore computational effort required. The viscous sub-layer and buffer layer are, by definition, within $y^+ < 30$; therefore by ensuring that the first cell node is situated at a larger value of y^+, within the log layer, $30 < y^+ < 300$, which reflects the approximate region away from the wall at which the log-law holds [66]. The log-law wall function can then be applied to estimate the boundary layer which allows for a more computationally efficient solution, as a result of only one cell being required for the log-law region.

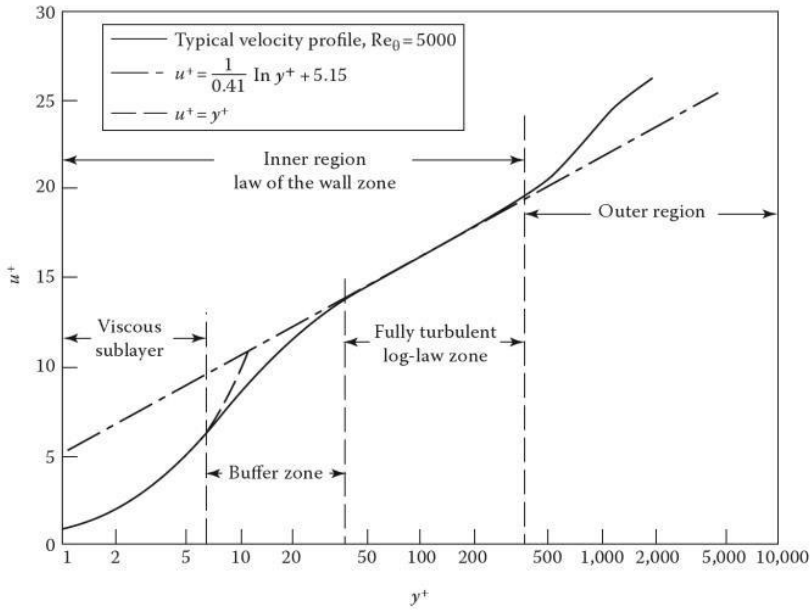

Figure 2.9: Graph depicting the presence of each boundary layer zone according to dimensionless wall distance [67]

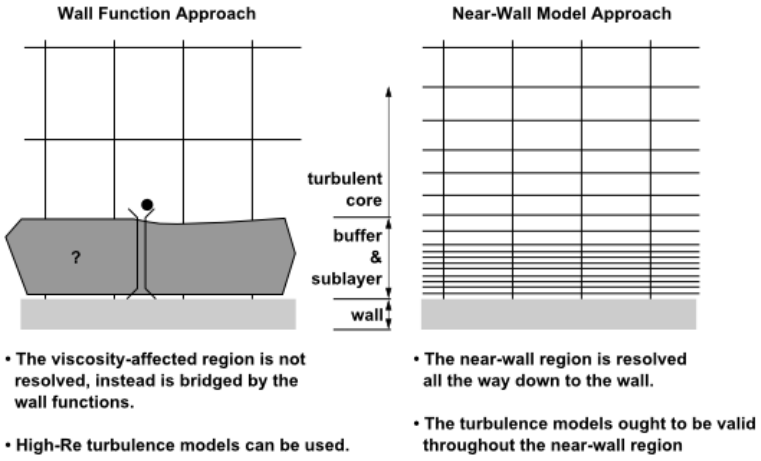

Figure 2.10: Visual explanation of the two wall modelling approaches; Wall Function Approach and Near-Wall Model Approach [68]

2.4.3. Defining Focal Regions

Every CFD simulation is designed to model specific conditions and may therefore have a focal region of interest for which the mesh is refined. In the case of the ship airwakes produced in this study, the flow analysis has been focussed predominantly on the effect of topside aerodynamics on helicopter operations, thus a focal region for mesh refinement has been above the ship's flight deck.

The mesh sizing in the focal regions of the simulation can be controlled and refined through the use of density boxes. The meshing algorithm will control cell growth within the density boxes to the specified sizing, overruling the global and part mesh parameters.

2.4.3.1. 'Standard' Airwake

For ship airwake simulations that do not include exhaust gas from the ship's engines, the focal region for mesh refinement is the area above the flight deck. The dimensions of the density region were chosen to reflect the likely operational space occupied by the helicopter during launch and recovery manoeuvres and are shown in Figure 2.11. Naval pilots often use the top of the ship's hangar as a line of sight when hovering above the flight deck, therefore the top of the density region was defined as 1.75 x hangar height. The multiplication factor accounts for the rotor plane that sits a few metres above the pilot's eyeline and allows for fluctuations in hover height whilst station-keeping. The bottom surface and the hangar-facing surface of the density region, or box, were positioned 2m above the flight deck and 2m away from the hangar face respectively. The rear surface of the density box was

positioned at the end of the flight deck. In the density region meshing criteria, a width parameter of 5 was set; this retains the minimum cell dimensions for 5 cell layers away from the density region and therefore prevents an increase and decrease in cell size as the mesh grows away from the ship surfaces and into the density region.

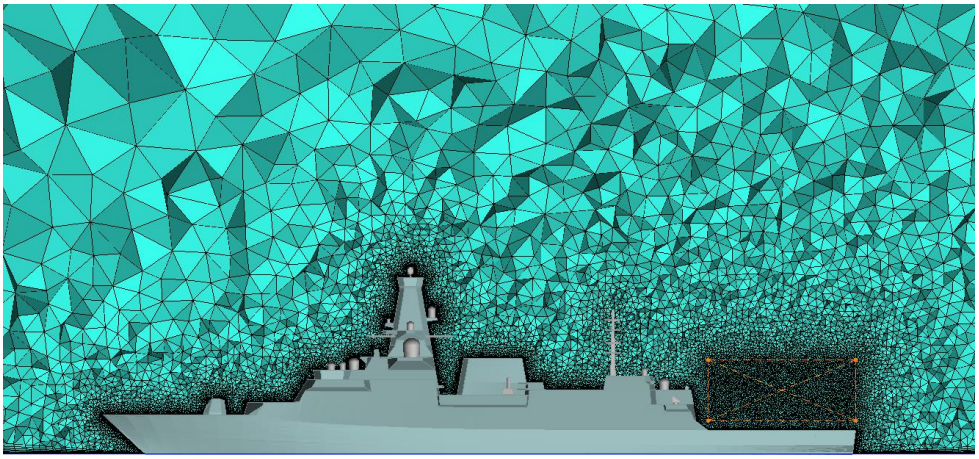

Figure 2.11: Slice through longitudinal centreline of the GCS depicting the density region over the flight deck and mesh growth away from the ship surfaces

2.4.3.2. Airwake Inclusive of Ship Engine Exhaust Gas

When additionally modelling the trajectory and dispersion of the exhaust gases from the ship's engines, the focal region of the simulation also encompasses the trajectory of the hot gas as it mixes and disperses within the ship's airwake. As a result, the mesh was refined along the trajectory of the exhaust plume to improve the modelling of the heat and momentum transfer between the exhaust gas and the airwake. Density regions were therefore constructed along the predicted trajectory to retain the minimum cell size of the mesh within this mixing region (Figure 2.12). Furthermore, as the ship's exhaust gas trajectory is dependent upon the wind strength and direction, a new mesh was required for each case with the density regions adjusted accordingly to enclose the dispersed exhaust gases. In this study the exhaust gases were modelled as air, which is a good representation as the exhaust gases, particularly from the ship's gas turbine, have a similar composition to that of air.

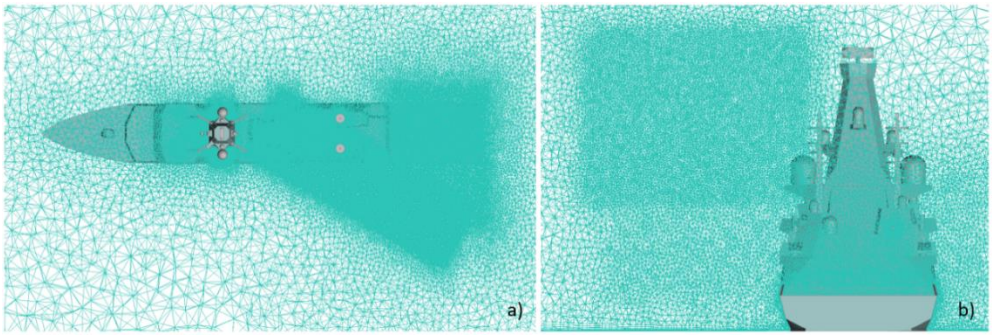

Figure 2.12: Slices through the mesh for an exhaust case of acute WOD angle depicting the necessity to adjust density regions to ensure the capture of thermal diffusion along the plume trajectory, in the a) horizontal plane and b) lateral vertical plane

2.4.4. Determination of a Successful Mesh

There are a number of metrics available within Ansys ICEM to assess the quality of the computational mesh that has been produced. The unstructured meshing technique which has been applied uses a tetrahedral mesh structure and therefore the optimal tetrahedral cell should have triangular faces of equilateral proportions. Naturally, as the mesh is grown around the complex geometry of the GCS, cells will have to deform away from equilateral proportions to accommodate various geometric features. Further deformity occurs when a prism mesh is generated after a Delaunay volume has been grown. As a guideline, the following checkpoint process was adhered to for each mesh produced to improve the success of the meshing procedure:

1) Run a mesh check to ensure there are no significant issues with the elements within the mesh
2) Check the mesh quality at various stages of the meshing process ensuring
    a. Surface mesh of quality > 0.3
    b. Surface mesh and Delaunay volume of quality > 0.3
    c. Complete mesh with prism layers with < 100 elements that are of quality < 0.05
    d. Visually scan the mesh at each stage to check for any signs of holes

Ultimately, the success of the mesh will be determined through initial solver computation attempts.

2.5. Computational Setup

2.5.1. Boundary Conditions

The application of appropriate boundary conditions is essential in ensuring effective computation of the flow field. In essence, the boundary conditions create the specifics of the fluid flow environment that is to be simulated by ensuring that the fluid interacts with its surroundings as it would in the real-world environment. Each of the surfaces in the computational domain has to be carefully defined to reflect these interactions.

2.5.1.1. Wall Effects

It is well known that the physics describing fluid flow close to a wall differs from the physics of fluid flow in the freestream at a significant distance away from the wall. The physical difference arises as an effect of friction imposed on the fluid flow as a result of its interaction with the wall, resulting in the formation of a boundary layer. It is essential that the appropriate wall conditions are applied to accurately capture the boundary layer and therefore a 'no-slip' wall function was applied to the surfaces of the ship. This wall function ensures the fluid molecules immediately adjacent to the wall surface assume the velocity of the wall, effectively becoming stationary relative to the wall.

$$u = v = w = 0 \tag{2.8}$$

The 'sea surface' of the domain was also defined as a wall but the boundary condition applied was, in contrast, a 'slip' wall. A natural boundary layer exists as the freestream flow interacts with the sea surface; however, the definition of this boundary layer was enforced through the application of an Atmospheric Boundary Layer (ABL) profile which will be discussed in section 2.5.2. For this boundary layer profile to be applied correctly, no additional frictional effects through viscosity need be calculated at the sea surface wall.

2.5.1.2. Symmetry

Due to the nature of CFD, the fluid flow problem has to be confined spatially with set boundaries; i.e. it cannot be computed to infinity. The real world problem does not have such solid boundaries - apart from the interaction of the fluid with solid surfaces e.g. a ship, buildings, etc., it is free to move in any direction, indefinitely within the Earth's atmosphere. In the case of the ship airwake CFD simulations, the domain boundaries as described in section 2.3.2. retain the ship within a cylinder of fluid. The far walls of the cylinder define the inlet and outlet for the freestream flow and will be described in more detail in the next section. The bottom of the cylinder represents the sea surface, described in the previous

section. The top face of the cylinder exists purely to enclose the simulation and as such must not impart any physical effects on the fluid flow. A symmetry boundary condition is therefore applied on this face for which ANSYS FLUENT will assume zero flux of all quantities across the surface. As such, for viscous flows, the symmetry boundary acts like a 'slip' wall as shear stress is zero [69].

2.5.1.3. Inlet Conditions

Specific to the CFD simulations produced during this study, there have been three different types of inlet condition used: pressure-far-field, mass-flow inlet and velocity inlet.

A pressure-far-field has been used as the main inlet condition for the freestream flow over the ship. This condition was chosen to complement the use of a cylindrical domain, as the inlet condition in this case can be defined in any direction relative to the ship's geometric axis by velocity unit vectors.

When modelling ship airwakes inclusive of exhaust gas effects, further inlet conditions must be specified at the ship's exhaust locations (the ship exhaust outlet is an inlet to the computational domain). Two inlet conditions for the exhausts have been used during this study: mass-flow inlet and velocity inlet. The mass-flow inlet enables the exhaust gas flow into the domain so be specified as a single value of mass flow rate, along with associated flow characteristics such as temperature, turbulence, etc. Similarly, the velocity inlet condition specifies exhaust gas flow with time-averaged three-component velocity data and associated flow characteristics.

As will be seen in Chapter 5, in the initial stages of the exhaust gas analysis, data was provided for the mass flow rate and temperature of the exhaust efflux from the GCS gas turbine engine; the exhaust outlet was circular with a diameter of 2.8m. For this case it was decided that since little was known about the exhaust flow distribution at the exit of the exhaust ducting, the duct would be extended backwards into the geometry of the ship for a distance of 5 diameters to allow a representative velocity profile to develop (Figure 2.13 [70]). Although 5 diameters is insufficient for the flow to be fully developed, it is a representative distance of the ducting length from the engine room to the exhaust outlet. Therefore, in the initial CFD analysis the inlet to the CFD domain was the inlet to the circular duct, and the boundary condition was that of a mass flow with a uniform temperature and velocity profile. It will also be shown in Chapter 5 that during the course of the project more detailed information on the detail of the exhaust system became available, which showed that the temperature and velocity profiles at the exhaust outlet were not uniform, and that the

exhaust duct exit was not circular. For this case the inlet boundary condition was therefore specified at the exhaust duct outlet as a planar distribution of temperature and of three-dimensional velocity components.

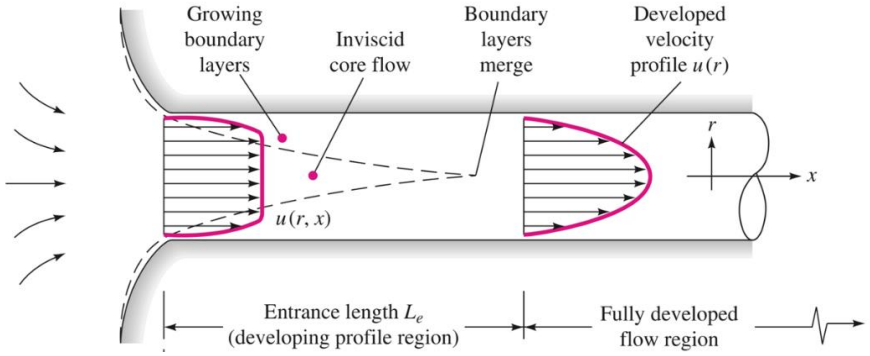

Figure 2.13: Schematic of the velocity profile that develops as fluid flows through a circular duct [70]

2.5.2. Atmospheric Boundary Layer Profile

Given the nature of the CFD problem posed, the application of a no-slip wall condition alone would not be sufficient to represent the effects of the boundary layer produced at sea as a result of the freestream flow interacting with the sea surface. To increase the fidelity of the CFD simulation in this maritime environment an Atmospheric Boundary Layer (ABL) was applied at the pressure-far-field inlet. The ABL was calculated according to the following power law:

$$V = V_{ref}\left(\frac{z_{asl}}{z_{ref}}\right)^{\alpha} \tag{2.9}$$

Where, V_{ref}, is the velocity at a reference height, z_{ref}, which calculates a wind velocity, V, at various heights above sea level, z_{asl}, and α is a constant describing the roughness of the surface. The reference height was conveniently taken as the height of the ship's anemometer and, according to Counihan [71], a value of 0.13 was used for α to represent a sea surface. An example of the boundary layer used for a 40 knot airwake in international standard atmosphere (ISA) conditions can be seen in Figure 2.14.

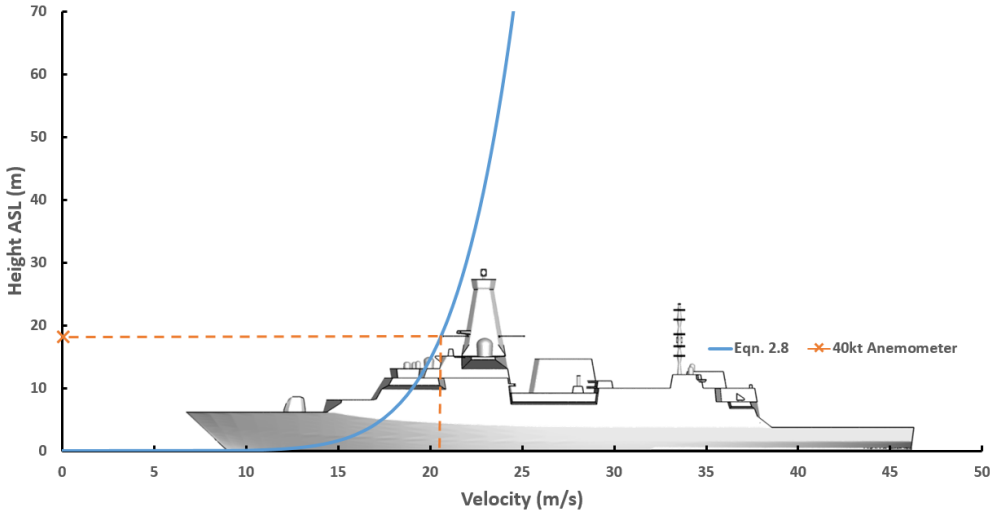

Figure 2.14: Graphical representation of the Atmospheric Boundary Layer (ABL) profile used for all CFD computations

2.5.3. Defining the Time Step

Careful consideration has to be given to the choice of time step for any time-accurate CFD simulation to ensure the stability of the solution and to prevent divergence. The speed at which the time-marching simulation passes through each computational cell within the fluid domain is a key factor in maintaining stability of the solution. The Courant Fredlichs Lewy (CFL) condition describes this relationship between cell size, Δ_n, fluid velocity, u_n, and time step, Δ_t, resulting in the Courant number, C.

$$C = \frac{u_x \Delta_t}{\Delta_x} + \frac{u_y \Delta_t}{\Delta_y} + \frac{u_z \Delta_t}{\Delta_z} \leq C_{max} \qquad (2.10)$$

The cell size, Δ_n, is taken as the minimum cell size within the domain, usually this would be located within the focal region as described in section 2.4.3. The flow velocity, u_n, through a cell of size, Δ_n, in the focal region was taken as 1.5 times the freestream flow velocity to account for any flow accelerations that may occur. Generally, $C \approx 1$, should be sought to ensure solution stability.

In addition to ensuring solution stability through the CFL condition, it was important that the solution was able to compute unsteady flow features, such as vortices being shed from the superstructure. As previously mentioned in Section 2.3.1, research has shown that frequencies of turbulent flow shedding in the region of 0.2-2 Hz are of significance to the workload of helicopter pilots operating in ship airwakes [65] so the minimum time period to be captured within this frequency band is therefore 0.5 seconds. All the simulations detailed

in this thesis were computed at a time step of 0.01 seconds, so the frequency of computation comfortably encompassed the desired range.

2.5.4. Settling Time

To ensure an accurate and reliable solution, the computed fluid flow must be allowed to settle prior to any solution data sampling. A common approach for determining the length of settling time required is to ensure a defined volume of fluid has passed through the computational domain, enabling periodic turbulent flow features to become prominent.

A simple approach was defined by Kelly [50] through the following equation:-

$$t_{set} \approx \frac{2.5L}{V_{wod}} \tag{2.11}$$

Where t_{set} is the approximate settling time, L, is the characteristic ship length, and, V_{wod}, is the relative freestream flow velocity. The multiplication factor of 2.5 serves to ensure that enough fluid has passed over the object within the domain to obtain settled periodic flow features.

2.6. Chapter Summary

This chapter has described in detail the methodical approach to the production of the unsteady time-accurate ship airwakes that will be presented in this thesis. The intricacies in preparing a high fidelity CAD model of a warship for CFD simulation have been explained, along with the necessary meshing processes that must be adhered to in order to produce a computational domain that will yield a good quality CFD solution of a ship's airwake. Particular detail has been given with regard to the difference in the meshing process required for ship airwake simulations inclusive of ship exhaust gas dispersion modelling. The following chapters will present four studies of warship aerodynamic analysis in which the CFD methodologies discussed in this chapter have generated the airwake data. Chapter 3 will start with an overall aerodynamic comparison of the GCS and its predecessor, the Type 23 Duke-class frigate.

Three publications have so far been produced from the research and are included in the Appendix.

Chapter 3. Aerodynamic Comparison of Evolving Warship Superstructure Designs

Chapter 1 illustrated how the superstructures of modern warships have evolved to become more RCS-compliant. Figures 1.9 and 1.10 compared the UK's Type 42 destroyer with its current replacement, the Type 45, while Figure 1.14 compared the Type 23 with its future replacement, the Type 26, or GCS. This chapter presents an overview of how the air flow over the GCS, the subject of this thesis, compares with that of its predecessor the Type 23; of particular interest is the air flow over the flight deck and how it could affect the ship's helicopter. The air flow distortion at the anemometer locations on the ships' masts, and the dispersion of the ships' engine exhausts will also be compared and will form an introduction to the more detailed studies of the anemometers and exhaust gas dispersion that will be presented in Chapters 4 and 5, respectively.

3.1. The Type 23 Duke-Class and Global Combat Ship

As discussed in Chapter 1, the Type 26 city-class frigate is to be brought into service by the Royal Navy in the mid-2020s as a replacement for the current Type 23 Duke-class frigate. Since the commissioning in 1990 of the Type 23 first of class, HMS Norfolk, nearly 30 years of technological advancement in maritime warfare and warship technology has led to the design of the GCS, including changes in the superstructures for the reduction of RCS. The modern warships, with their continuous, flat, less-fragmented superstructure with minimal curved surfaces will have different aerodynamic characteristics to their predecessors. Such an evolution in design is clearly apparent between the Type 23 and the GCS, as seen earlier in Figure 1.14.

The interaction of the freestream wind with the ship's geometry above the waterline creates the ship's airwake as the air flow is forced around the superstructure, shedding off sharp edges and producing areas of turbulence in the airwake that can both directly and indirectly impact upon helicopter operations. The unsteady CFD methodology described in the previous chapter has been used to examine how the RCS design concept has affected the air flow over the ship so that general observations can be made on how the more stealth-like

superstructure geometry will affect the air flow and what impact this may have for the ship's helicopter.

3.1.1. The Type 23 and GCS Superstructures

The Type 23 frigate was originally conceived as anti-submarine warfare (ASW) vessel for defence against Soviet submarines operating in the North Atlantic. As such, the ship was designed to accommodate Westland Lynx helicopters that were to be used in ASW to locate and attack submarines, which can often manoeuvre more quickly than a typical warship. Since the commissioning of HMS Norfolk, the 16 Type 23 vessels - of which 13 are still in active service - have been utilised in many missions beyond the Soviet submarine threat, demonstrating their wide-ranging capabilities in operations around the world [72].

It is essential that the UK's naval fleet is continually modernised to keep pace with international naval warfare capabilities. So, just eight years after the first Type 23 was commissioned, a plan was initiated to develop a concept for its successor through the Future Surface Combatant (FSC) programme, aimed at replacing the (then) Type 22 and 23 frigates. The programme evolved over the next decade and by 2010 resulted in the early design concept of the Global Combat Ship, i.e. the GCS. The early design of the GCS eventually became the Type 26 City-class, which is presently being built in Govan, Glasgow.

The Type 23 fleet, like all naval vessels, has undergone mid-life upgrades to help keep them current, but these are rarely so significant that they will affect the overall geometry of the ship. As a point of interest, in relation to RCS reduction, Figure 3.1 show how the cover on the Type 23's 4.5" main gun was changed from the original rounded shape to the facetted RCS-compliant shape (nick-named the Kryton gun) when the ships were upgraded between 2005 and 2012.

Figure 3.1: RCS-compliant cover (right) on the upgraded 4.5" main gun [73]

The overall design of the GCS incorporates the significant advances that have occurred in naval architecture and on-board systems for maritime warfare, which is driven by the need for the modern warship to be consistently more versatile, as well as effective. The result is a multi-purpose frigate designed beyond its primary role of ASW, to support air defence and general purpose operations around the globe [74]. The GCS is larger than its predecessor with a displacement of 6900 tonnes, compared with the Type 23 at 4900 tonnes. The GCS is longer and broader at approximately 150m in length with a beam width of approximately 20m, whilst the Type 23 is approximately 130m long with a 16m beam. As already discussed, the superstructure designs of the two ships are geometrically very different. It can therefore be expected that the new geometry will affect the ship's aerodynamics and change the flow features of the ship's airwake as the oncoming wind interacts with the smoother, less cluttered and more angular superstructure of the GCS. As the ship's helicopters are so vital to its primary ASW role, and their safe launch and recovery to the vessel is affected by the ship's airwake, the question arises as to how much of an impact the RCS-driven architecture of the GCS superstructure will have on the ship's helicopter when flying in the turbulent airwake close to the ship's flight deck. Also, the ship's airwake can affect the accuracy of the wind measurement systems which are used to determine the relative wind-over-deck (WOD) for safe helicopter launch and recovery. Furthermore, the interaction of the ship's airwake with its engine exhaust gases leads to a trajectory of dispersion that, more often than not, causes unsteady air temperatures above ambient in the vicinity of the flight deck.

Figure 3.2, which is approximately to scale, shows the larger superstructure of the GCS compared with the Type 23. The helicopter on the deck of the Type 23 in Figure 3.2 is a Lynx, while that approaching the Type 26 is a Merlin. The Type 23 was designed to operate with the Lynx, whose overall length is 15.2m. The larger Merlin, whose overall length is 22.8m, has been cleared to land on the Type 23, but it does not fit into the hangar. The GCS is designed to operate with the latest version of the Lynx, known as the Wildcat, and with the Merlin; the flight deck is also big enough for a Chinook to land, but it will not fit into the hangar. Referring to Figure 3.2, from the viewpoint of an approaching helicopter the GCS has a broader and higher superstructure and there are equipment housings, gun platforms and radomes just ahead of the flight deck, all of which will generate turbulence when the winds are from the fore. Forrest and Owen [45] showed, by considering pilot workload when landing a helicopter in a simulator to a Type 23 and to a Wave class tanker, that larger ships have more aggressive airwakes due to the larger, slower vortical structures being shed from the superstructure. It can therefore be expected, based on superstructure size alone, that

the GCS will produce a more aggressive airwake than the Type 23. The GCS also has a larger, bulkier, RCS-compliant main mast compared with the more slender mast structure of the Type 23, which can be seen from astern in Figure 3.2 and is further highlighted in Figure 3.3. The bulkier mast may also affect the air flow over the flight deck, as well as at the anemometer locations; it may also affect the dispersion of the engine exhaust gases which are discharged from the exhaust uptakes located aft of the mast.

Figure 3.2: Comparative images (approximately to scale) of Type 23 Duke Class (HMS Argyll) with 6m high hangar and Lynx on deck [28] *(top) and computer-rendered image of GCS with 8m hangar and Merlin recovering to flight deck* [74] *(bottom)*

Figure 3.4 shows aerial views of the two ships' exhaust funnel housings. The two black outlets from the Type 23's gas turbines are seen with raised exhaust outlets, compared with the flush single gas turbine exhaust outlet of the GCS. The round elevated exhaust outlets on the Type 23 are undesirable from the point of view of both RCS and IR (thermal) radiation. Exhaust stacks have traditionally been designed to direct the exhaust gases up and away from the ship to prevent their ingestion into ventilation systems and engine intakes as well as the undesirable heating of sensitive equipment installed on the superstructure. By

ensuring that the hot exhaust gases are dispersed high above the ship, this also prevents them being drawn down across the flight deck, raising the local air temperatures above ambient.

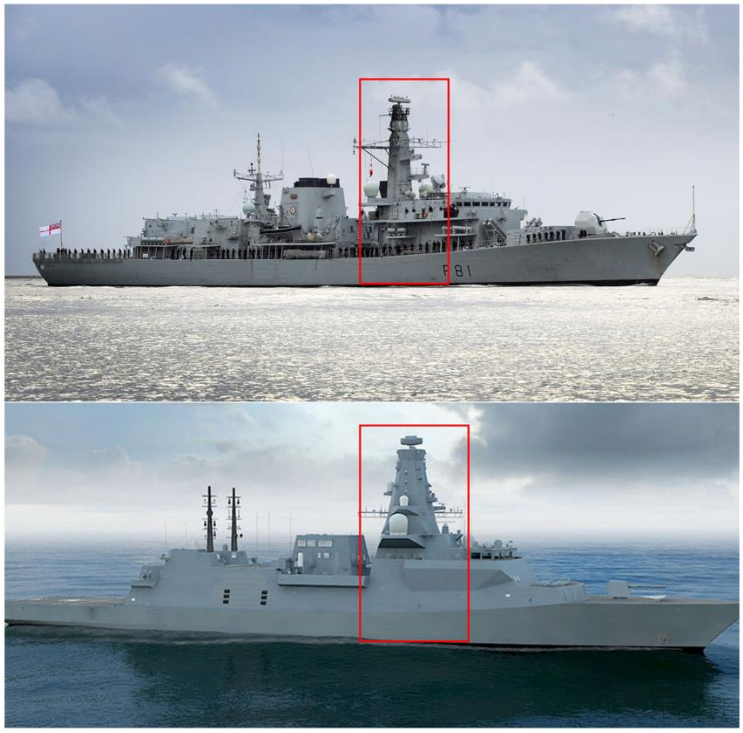

Figure 3.3: Comparative images (approximately to scale) of Type 23 Duke Class with slender main mast [75] *(top) and computer-rendered image of GCS with larger RCS-compliant main mast* [74] *(bottom)*

Figure 3.4: Comparative images of Type 23 Duke Class with raised exhaust stacks [76] *(left) and early computer-rendered image of GCS with flush exhaust stacks* [77] *(right)*

In general, as shown in Figures 3.2 to 3.4, the Type 23 superstructure is more segmented compared with the cleaner, flat-surfaced GCS, and will create different flow phenomena along the length of the ship as the relative wind sheds off the sharp edges of different sized structures. The GCS with its smooth, flat, slab-sided, tumblehome design does not offer as much opportunity for the break-up of the flow along the length of the ship's side, until the air flow reaches the hangar edge, from which it separates and cascades across the helicopter flight deck.

3.1.2. CFD Assessment of Type 23 and GCS

The following sections will illustrate how CFD has been used to predict the air flow over the two ships, including an assessment of how the differences in the superstructure geometry are expected to impact on a helicopter. They will also show how the air flow over the two ships creates flow distortion at the anemometer locations, and affects the dispersion of the exhaust gases from the gas turbines, both of which have a bearing upon helicopter operations. For the general assessment of the airwakes and their effects on the helicopter and the anemometers, the airwakes were computed without engine exhaust efflux.

As discussed in Chapter 2, when using CFD to create ship airwakes for use in flight simulation it is important to use what are known as time-accurate or Scale-Resolving Simulation (SRS) methods which compute the three-dimensional velocity components throughout the computational domain at different time steps. Although piloted flight simulation has not been used in the project being reported in this thesis, the unsteady flow field was used to impose unsteady aerodynamic loads onto a mathematical model of the helicopter flight dynamics, as will be discussed later in this chapter, and to investigate the flight of a ship-launched small unmanned vehicle in the airwake, to be discussed in Chapter 6. The time-accurate CFD can also be used to provide a record of unsteady velocities at the anemometer positions and can illustrate the time-varying air temperatures due to the ship's engine exhaust gases, both of which will be discussed in Chapters 4 and 5, respectively.

The first requirement for the CFD is a geometry of the ship. Figure 3.5 shows the Type 23 and GCS geometries, both of which were produced from general arrangement CAD data provided by BAE Systems. While it is important that the geometry is an accurate representation of the ship, surface features that are typically less than 0.3m in size have little effect on the air flow but have a significant effect on the computational effort, and were therefore removed.

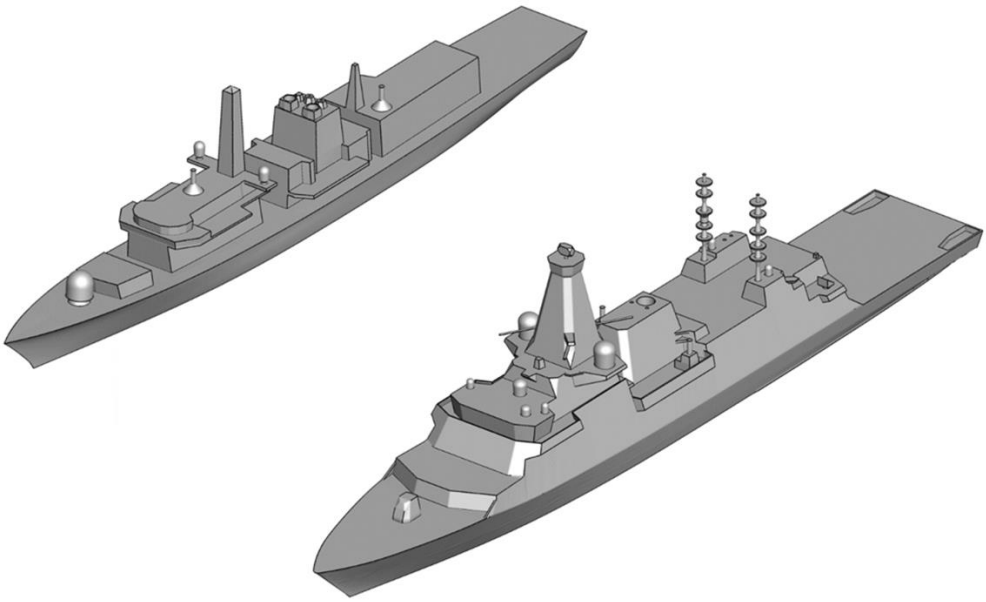

Figure 3.5: CAD geometries used for CFD simulations: Type 23 (top) and GCS (bottom)

The geometries were given surface meshes and these were then grown into the cylindrical domain, as described in Chapter 2. Boundary conditions were applied and the flow approaching the ship was profiled to represent an oceanic boundary layer. To create the unsteady airwakes it was first necessary to compute a steady state solution, before initiating the unsteady solution with a time step of 0.01 seconds. The CFD solutions require a period of time to settle to a repeatable unsteady solution, typically 15 seconds (of airwake), which allows periodic flow features to develop. A fully-developed unsteady solution was then run to produce a further 30 seconds of unsteady airwake data, while the previous 15 seconds of data was discarded. The overall solution time for a single airwake was typically about 3 days using 128 processors.

3.2. The Type 23 and GCS Airwakes

Figure 3.6 shows side-on views of the ship airwakes in a headwind, illustrated by contours of normalised total velocity, V (i.e. vector sum of u, v and w divided by freestream velocity U), and of turbulence intensity, on a vertical plane on the centrelines of the two ships. In this study turbulence intensity is defined as the root mean square of the fluctuating velocity component divided by the freestream velocity, i.e. not divided by the local mean velocity. The effect of the imposed Atmospheric Boundary Layer (ABL) can be seen by the layers of velocity contours in the left-hand images. The airwakes were computed for a wind speed of 40 knots measured at the height of the anemometer, so the contour V/U = 1 ahead of the

ships is at the height of their anemometers. The main mast of the GCS creates a bigger and more turbulent wake than the more slender Type 23 mast, although the flow over the two flight decks does not look significantly different in these views.

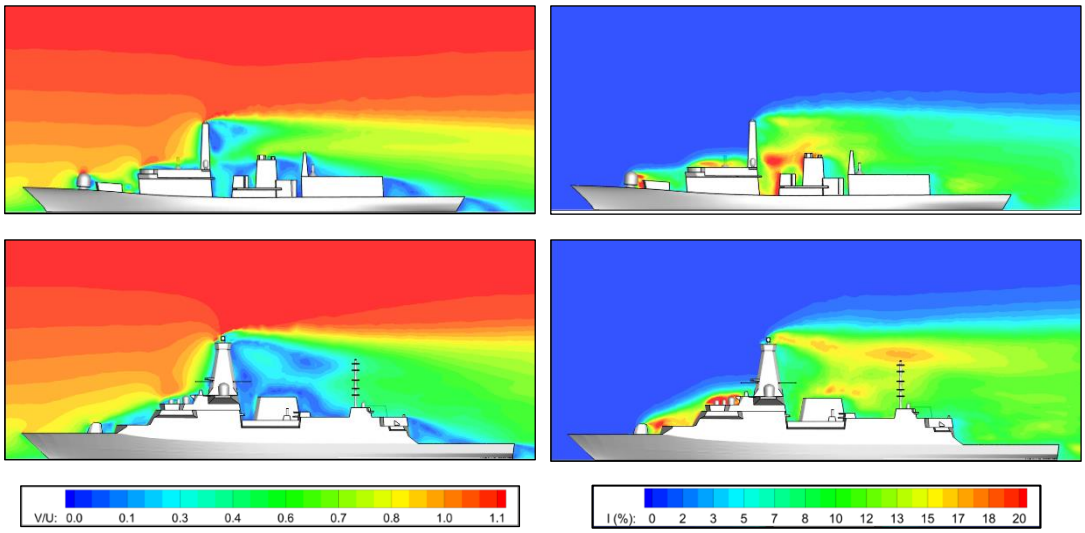

Figure 3.6: Ship airwakes in a headwind for Type 23 (top) and GCS (bottom) illustrated by normalised total velocity (left) and turbulence intensity (right)

Figure 3.7 shows the flow over the landing deck in a headwind, again as contours of normalised total velocity and turbulence intensity, but this time on a horizontal plane at half hangar height on each ship (i.e. 3m above Type 23 deck and 4m above GCS deck). It can be seen that the air flow along the sides of the smoother GCS is less disturbed than that along the more fragmented Type 23; i.e. compared to the beam of the ship, the Type 23 has a wider airwake. The velocity contours show a much larger wake behind the hangar of the larger GCS and the contours of turbulence intensity show that the high-speed air flow shedding from the hangar edges of the GCS create regions of increased turbulence either side of the landing deck. The slightly higher turbulence on the port side of the GCS deck may be due to the difference between the port and starboard equipment housings on the hangar roof, which are the only non-symmetrical features nearby. The relative size of the airwakes is even more evident in Figure 3.8, which shows the contours of velocity and turbulence on a vertical plane half way along the landing deck of each ship. The horizontal layers of velocity contours either side of the two ships are again the result of the ABL. The areas of higher (and slightly asymmetric) turbulence on the port and starboard side of the GCS's landing deck can also be seen in these views.

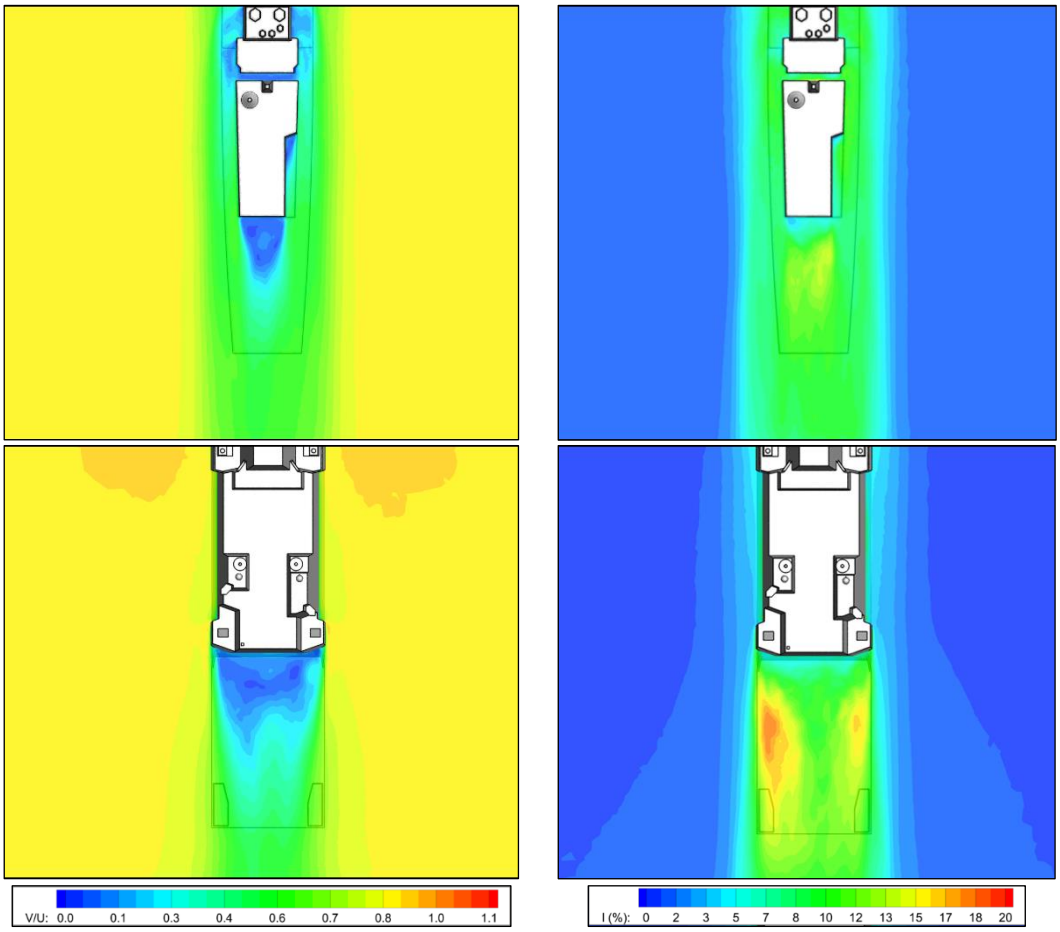

Figure 3.7: Air flow over landing deck in a headwind at half-hangar height for Type 23 (top) and GCS (bottom) illustrated by normalised total velocity (left) and turbulence intensity (right)

The airwake in a headwind is usually the least problematic for the helicopter due to it being "sheltered" by the hangar when over the landing spot, as seen earlier in the SHOL in Figure 1.12. However when translating from the undisturbed air off the port side of the ship, across the deck edge to the landing spot, the steep gradients of velocity and turbulence impose significant unsteady forces and moments on the aircraft just as the pilot is manoeuvring close to the superstructure; i.e. the headwind still presents a significant challenge to the pilot.

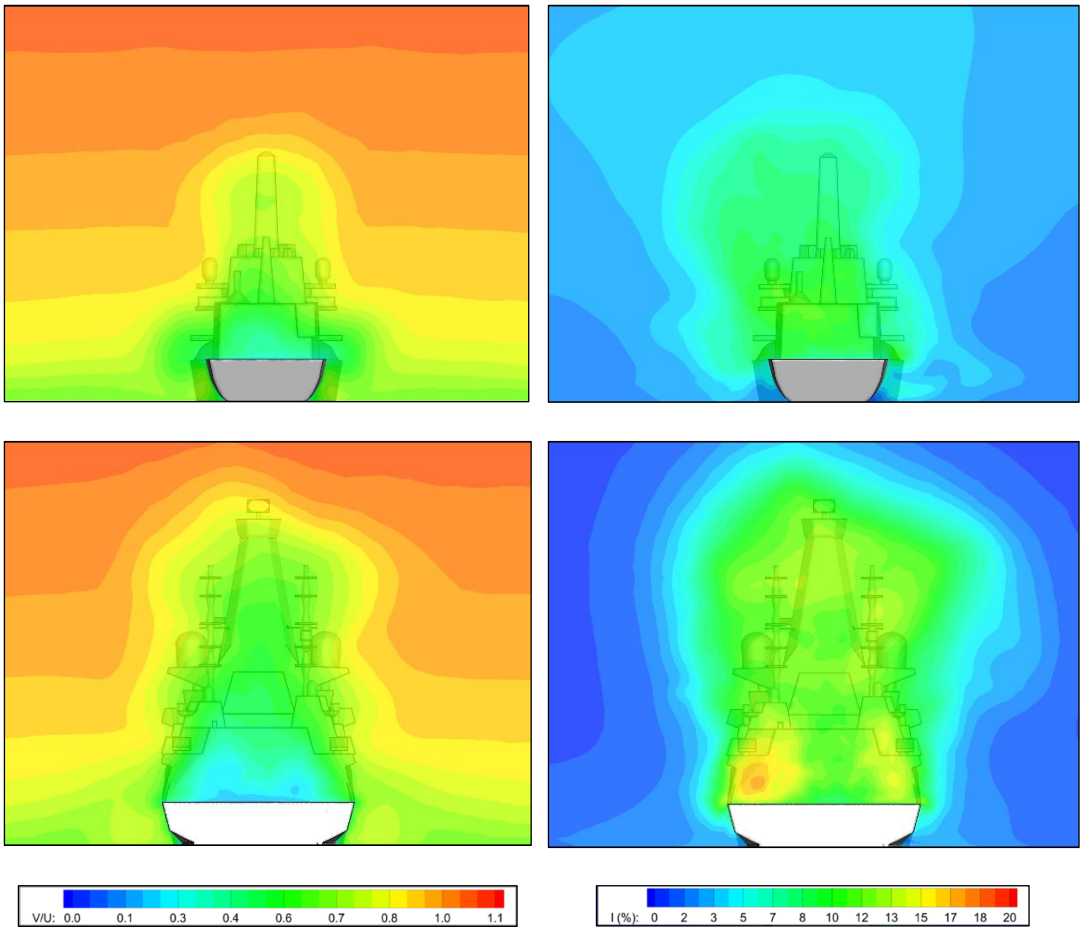

Figure 3.8: Air flow over landing deck in a headwind on vertical plane half way along flight deck for Type 23 (top) and GCS (bottom) illustrated by normalised total velocity (left) and turbulence intensity (right)

Oblique winds from the starboard, i.e. Green winds, are even more problematic as they infringe even more on the area off the port side of the ship, where the helicopter begins its landing manoeuvre, and create a very strong shear layer across the flight deck. Airwakes were therefore also created for Green 30 winds, as presented and discussed below. Figure 3.9 shows a side-on view of the airflow over the ships for a Green 30 wind, again on a vertical plane on the centreline of the two ships. The flow distortion over the landing deck is more apparent in this view than it was for the headwind and it can be seen that the size of the wake behind the hangar is bigger on the GCS, and is significantly more turbulent. Looking at the plan view in Figure 3.10, the significantly larger and more turbulent wake over the GCS landing deck is again very clear. The bright red area over the starboard side of both decks is the shear layer that forms when the flow breaks away from the vertical hangar edge; it is unsteady, i.e. it is flapping, and it separates the faster oncoming wind from the slower recirculating air flow in the lee of the hangar. The difference in the wakes of the two ships is even more apparent in the view from astern in Figure 3.11, which shows a much larger turbulent area over the deck of the GCS. From the perspective of the ship's helicopter, the flow over the GCS presents the greater challenge.

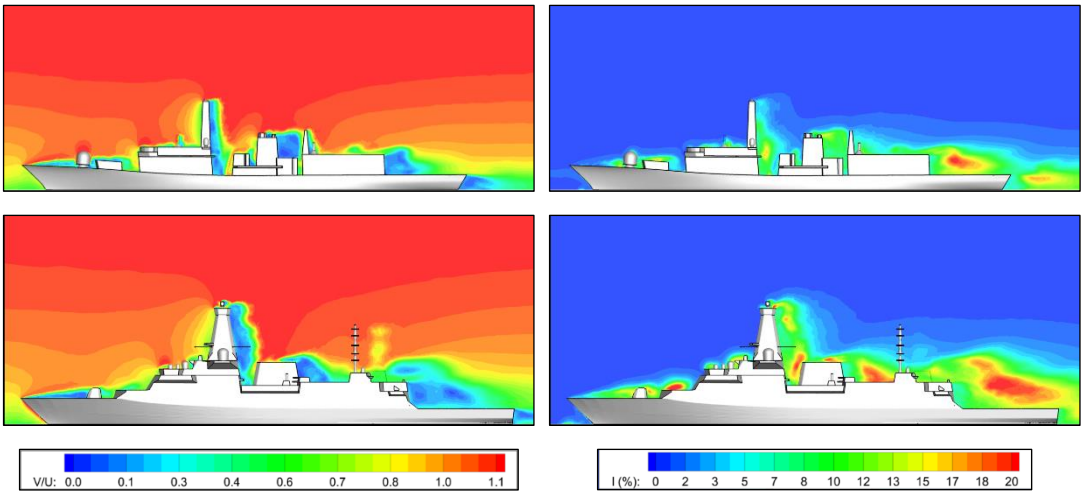

Figure 3.9: Ship airwakes in Green 30 WOD for Type 23 (top) and GCS (bottom) illustrated by normalised total velocity (left) and turbulence intensity (right)

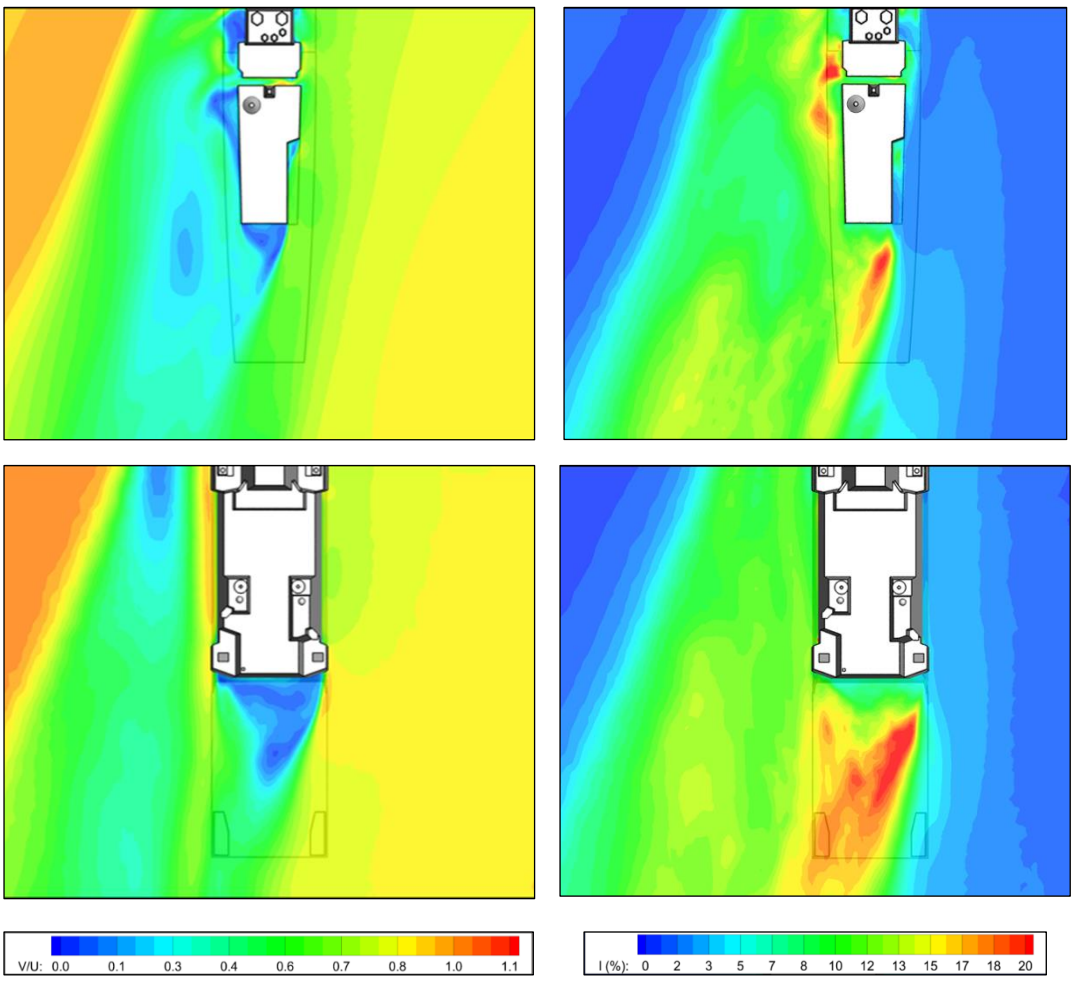

Figure 3.10: Air flow over landing deck in Green 30 WOD at half-hangar height for Type 23 (top) and GCS (bottom) illustrated by normalised total velocity (left) and turbulence intensity (right)

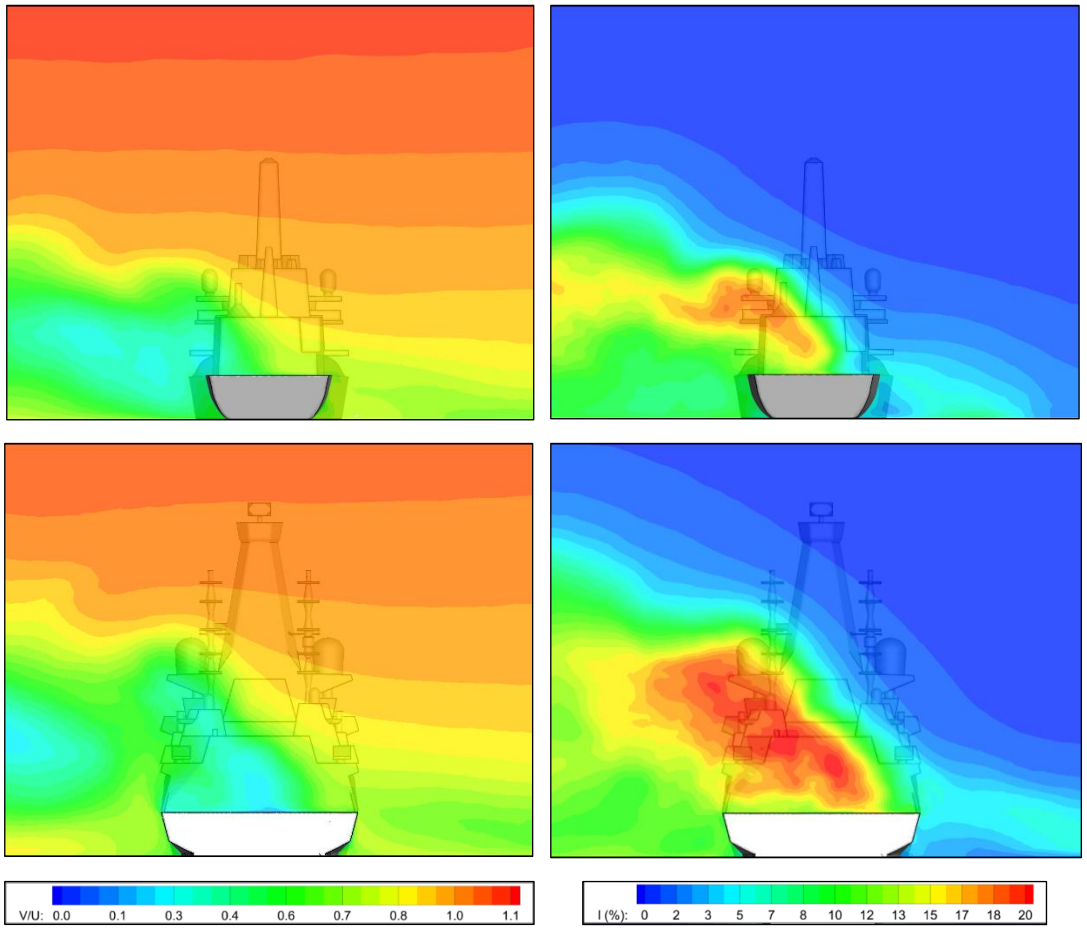

Figure 3.11: Air flow over landing deck in a Green 30 WOD on vertical plane half way along flight deck for Type 23 (top) and GCS (bottom) illustrated by normalised total velocity (left) and turbulence intensity (right)

Finally, for the discussion on the differences between the airwakes of the Type 23 and the GCS, Figure 3.12 shows the time-averaged air flow over the two ships for a Green 30 WOD, where the airwake is presented as Q-criterion isosurfaces. Q criterion is a vortex identification method that defines vortices as spatial regions in the flow where the vorticity tensor, $\mathbf{\Omega}$, dominates the rate of strain tensor, $\mathbf{S}$, using Eqn. 3.1, in addition to the pressure at the centre of the spatial region being lower than ambient [78].

$$Q = \frac{1}{2}(|\mathbf{\Omega}|^2 - |\mathbf{S}|^2) > 0 \qquad (3.1)$$

The isosurfaces of Q criterion help to illustrate the vortical structures being shed from the edges of the superstructure, and protruding features such as the masts. It can be seen how the air flow along the side of the fragmented Type 23 is broken up, compared with that along the flat, smooth sides of the GCS, which is mostly unhindered. Therefore, in the oblique wind,

when the air flowing along the side of the GCS reaches the vertical hangar edge it does so with a higher velocity than for the Type 23, as can be seen in Figure 3.10 above, leading to the more turbulent structures seen in Figure 3.12, and the turbulence intensities seen in Figure 3.11. It can also be seen in Figures 3.11 and 3.12 that the turbulent air flow over the flight deck extends to a height that is above the hangar and will therefore be above the helicopter main rotor when it is over the flight deck. The unsteady flow being drawn into the main rotor will create unsteady moments and lift, making the aircraft more difficult to control.

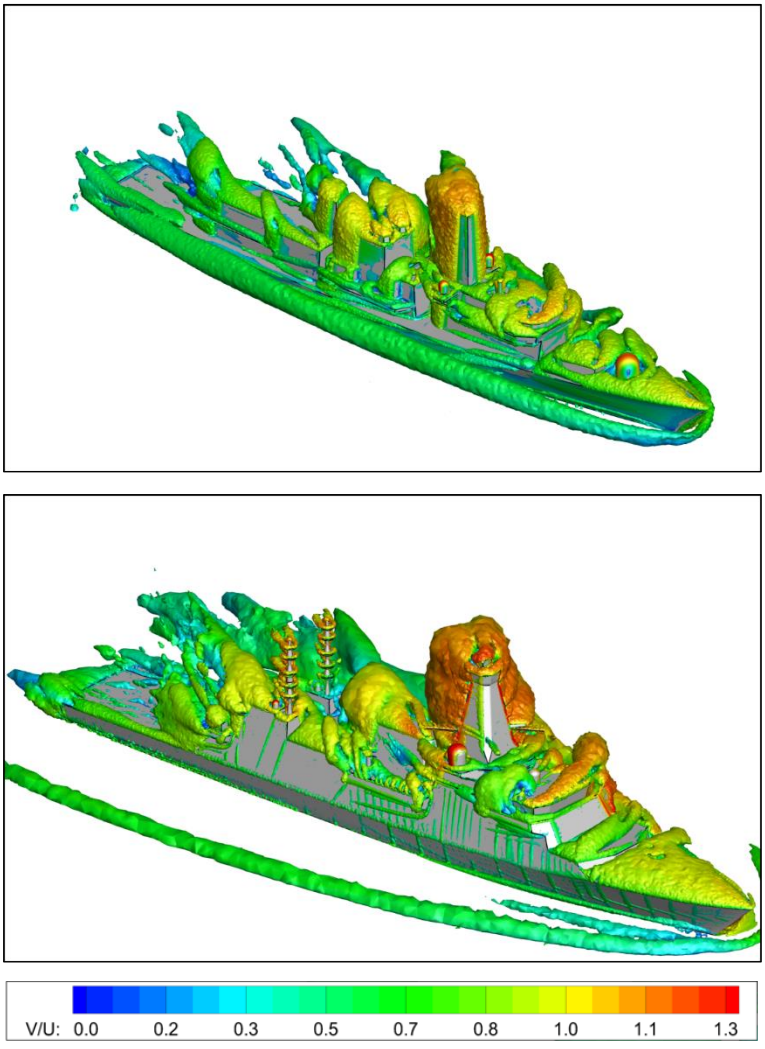

Figure 3.12: Isosurfaces of Q criterion coloured by normalised velocity magnitude for Type 23 (top) and GCS (bottom) in a Green 30 WOD

3.2.1. The Effect of an Open Mission Bay Door on the GCS Airwake

A particular feature of the GCS is a versatile Mission Bay just forward of the ship's hangar. In service this will be used for the launch and recovery of small water craft as well as additional storage space, useful for carrying stores and equipment for various missions and disaster relief. The Mission Bay has external access at both port and starboard via two large doors, wide enough to pass small water craft through, as indicated on the ship's CAD in Figures 3.13 and 3.14. In operation, with both doors fully open, a large cavity will exist through which the oncoming wind could flow, particularly an oblique wind, thus potentially altering the airwake. It was therefore decided to explore the effect on the air flow over the flight deck of having the two Mission Bay doors open, i.e. to take the opportunity to further examine the effect of segmentation of the superstructure on the characteristics of the ship's airwake. Further modification to the CAD model of GCS was required to build the Mission Bay into the superstructure, as seen in Figure 3.15, and a new computational mesh was generated and airwakes were computed for a headwind and Green 30 WOD condition.

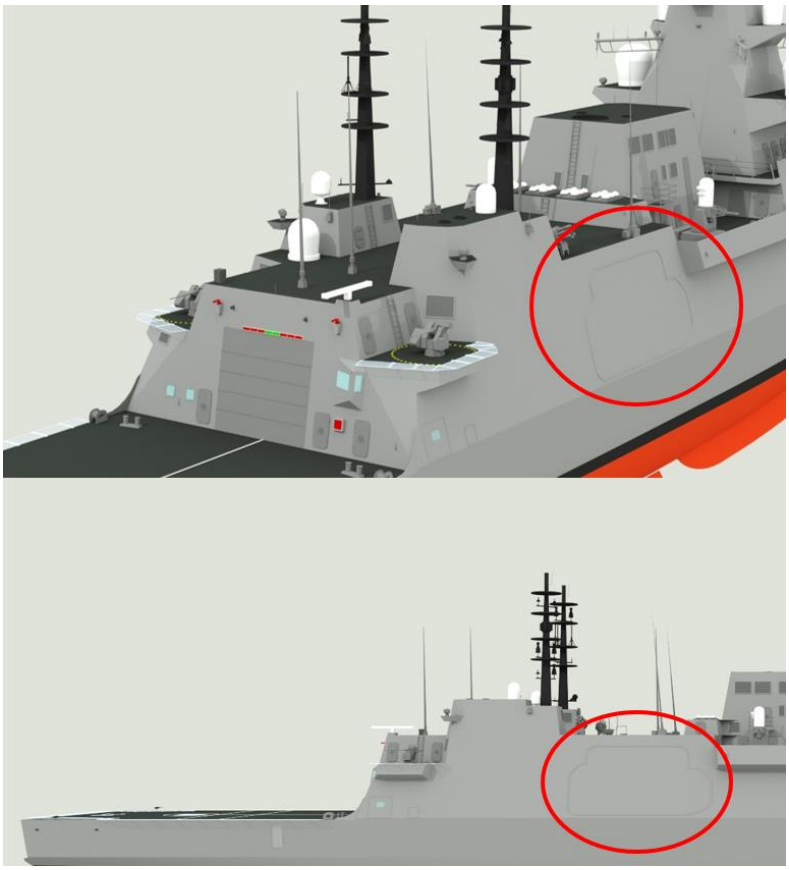

Figure 3.13: GCS Mission Bay Doors (doors are symmetrical at port and starboard) [79]

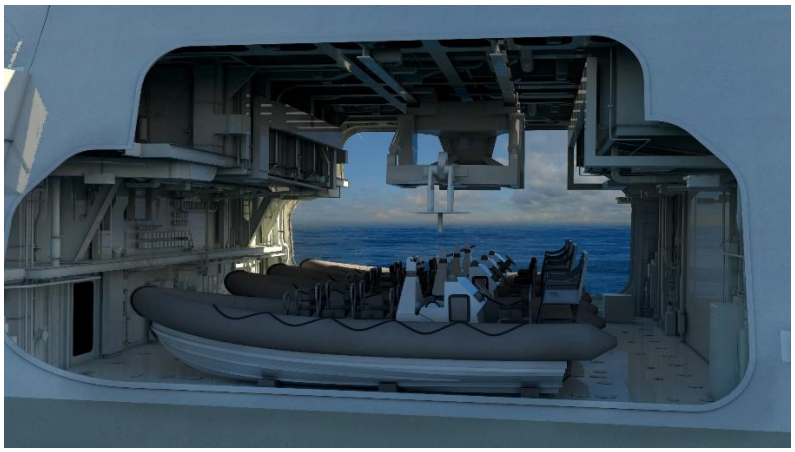

Figure 3.14: Computer-rendered image of GCS's fully opened Mission Bay [80]

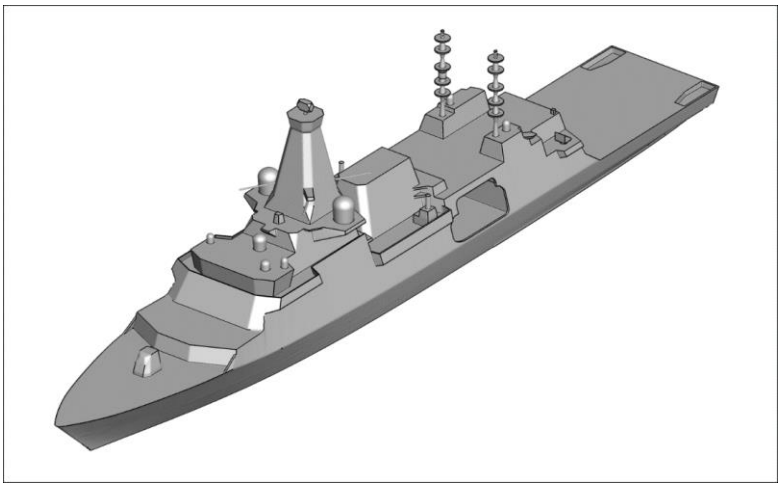

Figure 3.15: GCS CAD with open Mission Bay doors

The results of the CFD analysis showed that when the wind was from ahead the Mission Bay, not surprisingly, had little effect on the flow over the flight deck. Figure 3.16 shows the turbulence intensity on a vertical plane through the centre of the deck, viewed from astern. With the doors open there is slightly less turbulence above the deck, including above the height of the hangar, and the turbulence seen in the small area on the port side of the deck has increased. Overall though, the effect of having the Mission Bay doors open is not significant.

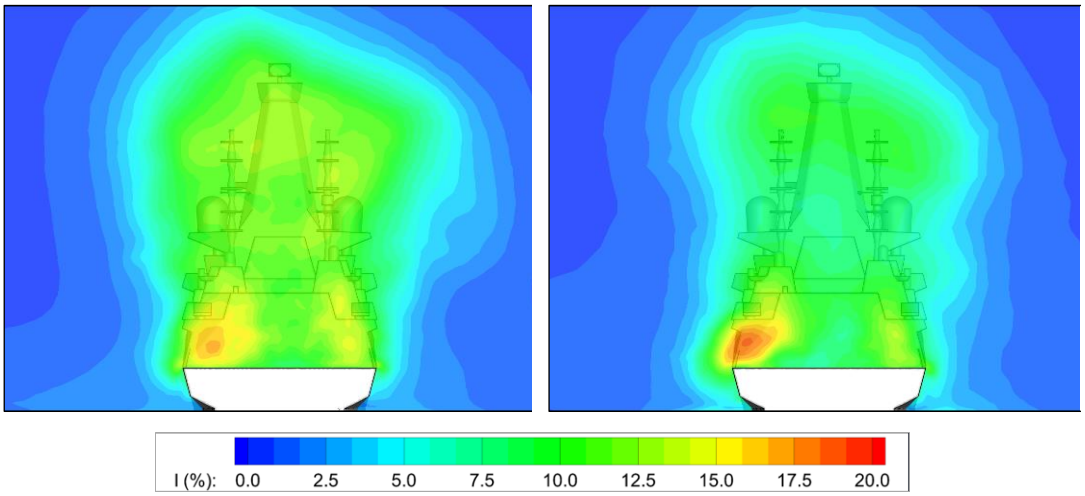

Figure 3.16: Contours of turbulent intensity on vertical plane across the landing spot in a headwind for the GCS with (left) Mission Bay Doors closed and (right) open

When the relative wind moves off the bow toward starboard to a Green 30 WOD condition, the effect of a large cavity along the length of the superstructure becomes more apparent. Figure 3.17, which shows contours of turbulence intensity on a plane at half hangar height, illustrates the effect of having the Mission Bay doors open and closed; also shown is the equivalent image for the Type 23. Comparing first the top two images of the GCS with the doors open and closed, the air flow coming through the mission bay is highlighted by the red turbulence contour. Although the distribution of the turbulent air flow over the flight deck is different with the doors open, the levels of turbulence are similar even though some of the flow that would have passed along the starboard side of the ship is diverted to flow through the Mission Bay. The image for the Type 23 also shows how, in the oblique wind, the air flows through the gap between the mast and the funnel casing, supporting the notion that the fragmented superstructure in an oblique wind affects the severity of the airwake over the flight deck.

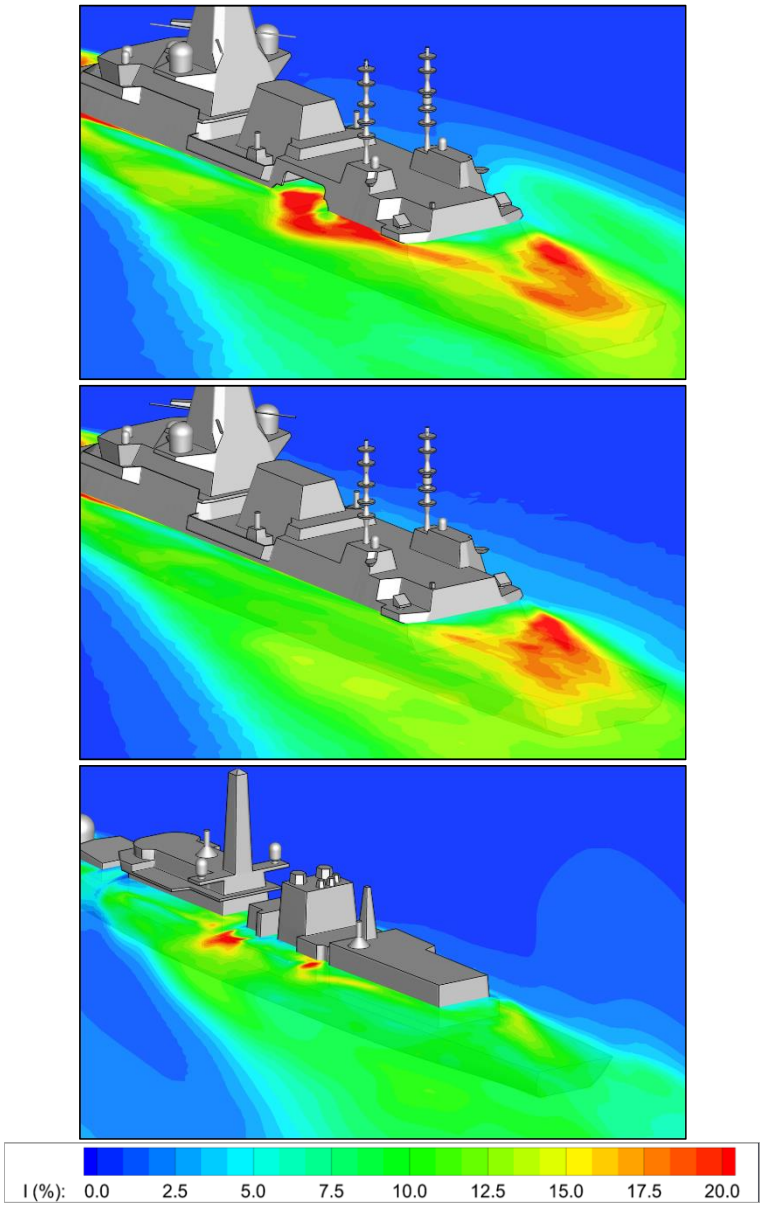

Figure 3.17: Contours of turbulence intensity across a plane through half hangar height of the GCS with Mission Bay open (top) and closed (middle), and the Type 23 (bottom)

Figure 3.18 shows the air flow as contours of turbulence intensity on a vertical plane through the centre of the landing deck of the GCS, viewed from astern with the doors open and closed. In this plane the area of turbulent flow has significantly reduced when the doors are open, mainly in the area above the height of the hangar which, during the lateral translation of a recovering helicopter, would create unsteady loads on the main rotor.

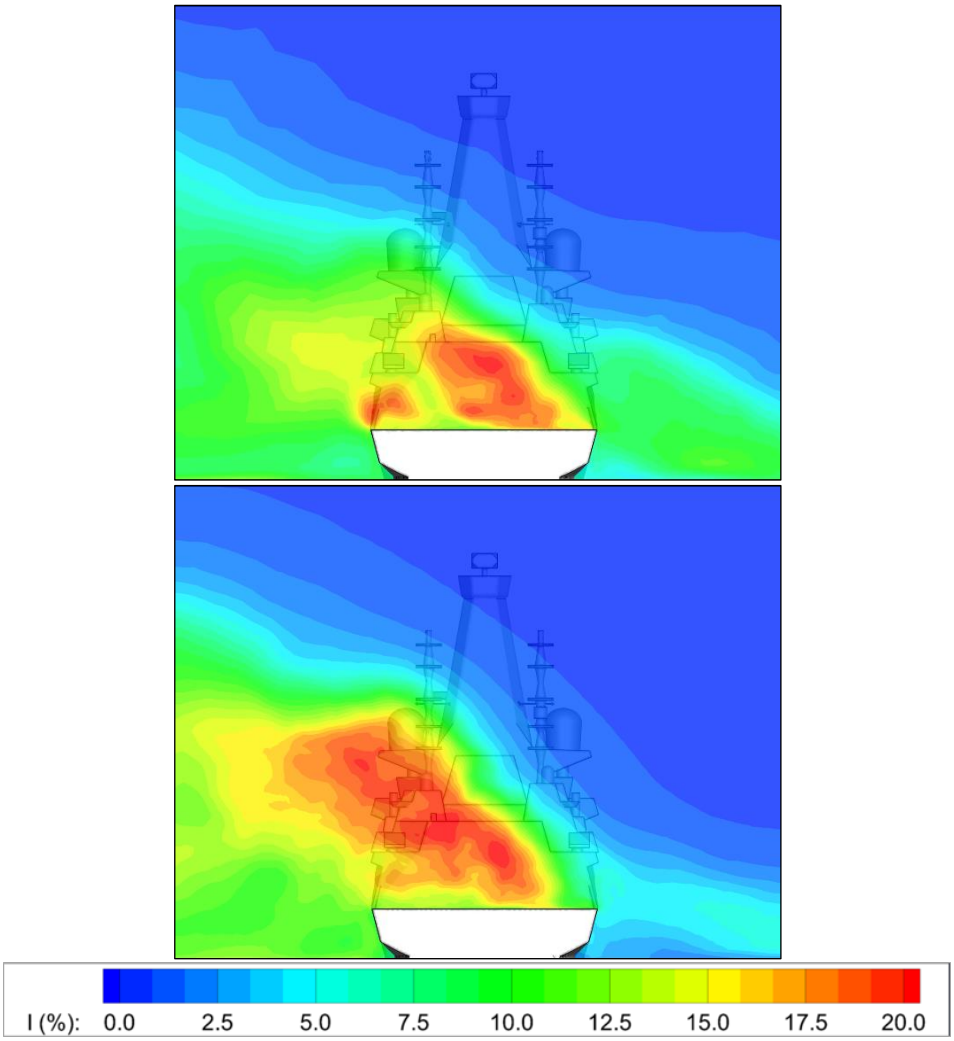

Figure 3.18: Contours of turbulence intensity across the landing spot of the GCS with Mission Bay doors open (top) and closed (bottom) in a Green 30 WOD condition

A 3-D perspective of the flow with and without the Mission Bay doors open is shown in Figure 3.19 where isosurfaces of Q criterion have been used to visualise the flow. As can be seen in the top image with the doors open, flow enters the enclosure and as a consequence, compared with the lower figure with the doors closed, there are significantly fewer vortical structures being shed across the flight deck from the vertical hangar edge. Also, comparing the two figures, there is less shedding from the top of the starboard equipment housing immediately ahead of the flight deck, i.e. the turbulent area above the hangar height referred to in Figure 3.18 above.

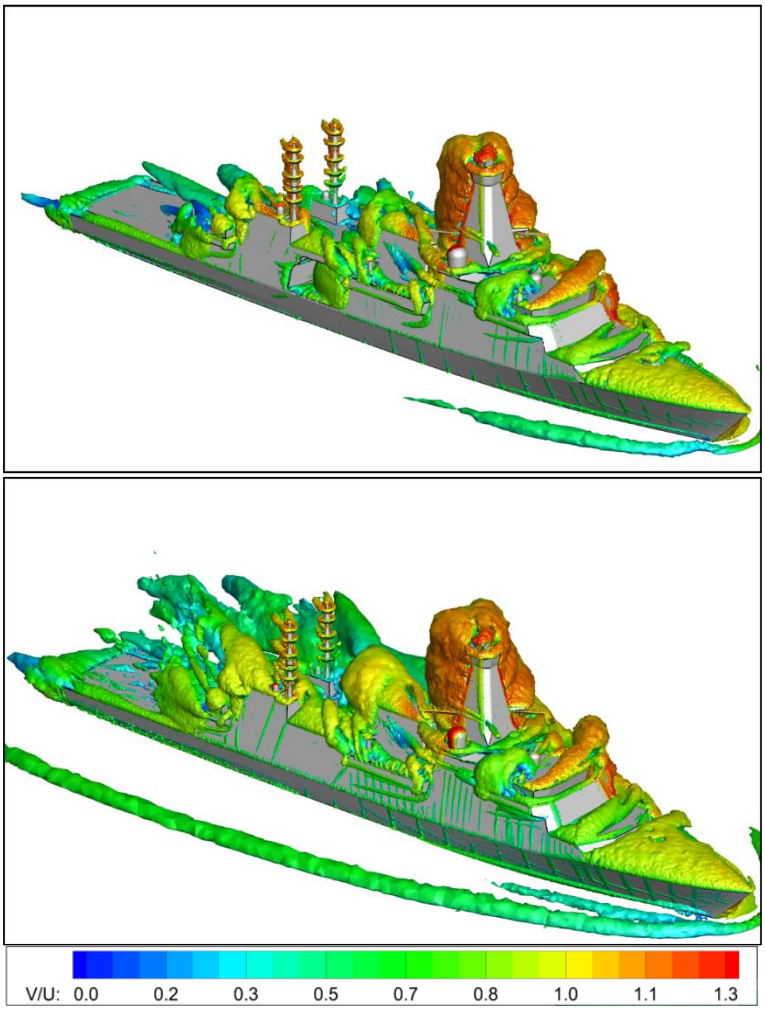

Figure 3.19: Isosurfaces of Q criterion coloured by normalised velocity magnitude for GCS with Mission Bay doors open (top) and closed (bottom) in a Green 30 WOD condition

3.2.2. Assessing the Impact of the Airwakes on a Helicopter

It has been mentioned earlier that related research projects at UoL have been concerned with integrating the unsteady velocity components of ship airwakes with a flight dynamics model of a helicopter in a full-motion flight simulator [23]. The use of piloted flight simulation has not been part of the research being reported in this thesis; however, another benefit of adopting time-accurate CFD is that the computed airwakes could be used with the simulator in the future if needed. It has been recognised in the past that while piloted flight simulation can be used to evaluate the effect of superstructure changes, and hence of the airwake, on a helicopter's handling qualities [81], it has also been recognised that this can be a lengthy and complex process. Researchers at UoL therefore developed a "desktop" flight simulation tool, called the Virtual AirDyn, to evaluate the unsteady loads on a helicopter immersed in a ship's airwake but without involving a motion simulator and a pilot. The Virtual AirDyn was

based on an experimental technique, also developed at UoL and called the AirDyn [82]. The AirDyn was a scale model of a Merlin helicopter with a 300mm diameter main rotor. The model helicopter was mounted on a 6-axis force block and had a motored rotor. By placing the model helicopter in the airwake of a model ship it was possible to measure the unsteady loads imposed on the helicopter [83]; the model helicopter was therefore an instrument which measured the loads from the airwake, i.e. an Airwake Dynamometer, shortened to AirDyn. It was then recognised that the experiment could be replicated using engineering software; the experimental airwake could be created by CFD and the physical helicopter model could be replaced by a mathematical model of the helicopter flight dynamics. The integration of these two mathematical modelling methods is the Virtual AirDyn, or VAD [84].

The VAD is therefore a software analysis tool which makes use of the flight dynamic modelling software FLIGHTLAB [85], and unsteady CFD. A more detailed description of FLIGHTLAB will be presented in Chapter 6. During piloted real-time simulations, unsteady forces are generated on the aircraft causing it to move away from the trim condition, requiring the pilot to counteract the movement through the aircraft's controls. In the VAD the helicopter is trimmed in the prevailing freestream conditions and is then placed at a selected point in the airwake and is fixed in that position. Because the helicopter is no longer trimmed for the conditions within the airwake, it experiences non-zero forces and moments imposed by the airwake, and it is these values that are recorded by the VAD. Therefore, using the VAD technique, the helicopter flight dynamics model quantifies the unsteady forces and moments imparted by the unsteady airwake.

The helicopter model used is the FLIGHTLAB Generic Rotorcraft. This model is configured to represent a Sikorsky SH-60B Seahawk, shown in Figure 3.20, which is a maritime development of the widely used UH60 Black Hawk. This model was chosen because it has been extensively validated, and for the purpose of the airwake analysis the validity of the model is more important than which aircraft is actually used. The weight of the Seahawk is 69 kN (15,500 lb, i.e. a weight between that of a Lynx and a Merlin).

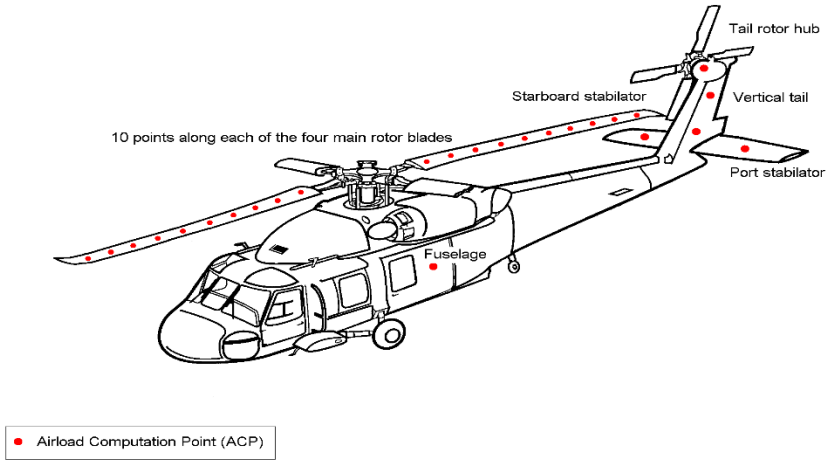

Figure 3.20 The Seahawk UH60 FLIGHTLAB model used in the VAD [84]

The CFD-generated velocity components of the airwake are imposed onto the helicopter model via a number of Airload Computation Points (ACPs) which are located at various points along each rotor blade, fuselage, tail rotor and empennage, shown as red dots in Figure 3.20. The helicopter is held stationary in the ship's airwake and the time histories of the unsteady moments and forces at the helicopter's centre of gravity are recorded over the thirty seconds of airwake data. As described previously, the thirty seconds of unsteady CFD data were generated on an unstructured mesh; for the VAD analysis the unsteady velocity components are interpolated onto a structured mesh with a grid spacing of 1 metre, covering only the region of interest around the flight deck of the ship, as shown in Figure 3.21.

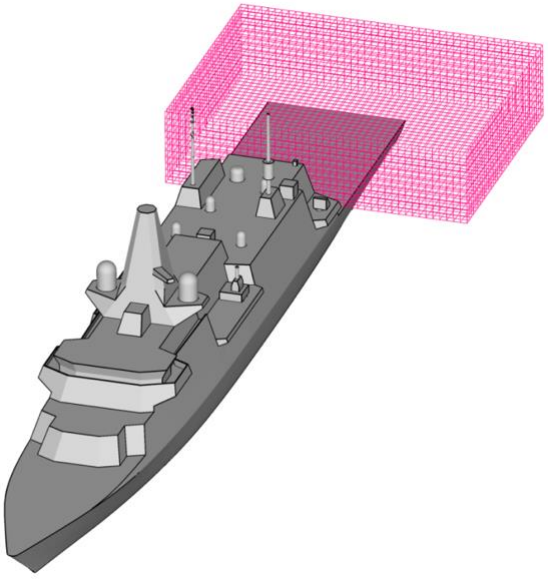

Figure 3.21: The VAD CFD interpolation grid

The VAD was therefore used in this study to compare the helicopter loads imposed by the airwakes of the Type 23 and GCS; the opportunity was also taken to evaluate the effect, if any, on the helicopter of having the Mission Bay doors open. The VAD method involves placing the helicopter at several positions along the lateral translation of the landing flight path which begins off the port side of the ship and passes through the landing spot, which is approximately half way along the landing deck (illustrated earlier in Figure 1.13). Figure 3.22 shows the line over each ship with the seven points where the helicopter is held while the unsteady loads imposed by the unsteady CFD-generated velocity components are obtained. The line is the locus of the centre of gravity of the helicopter, which is at a similar height to the pilot's eye.

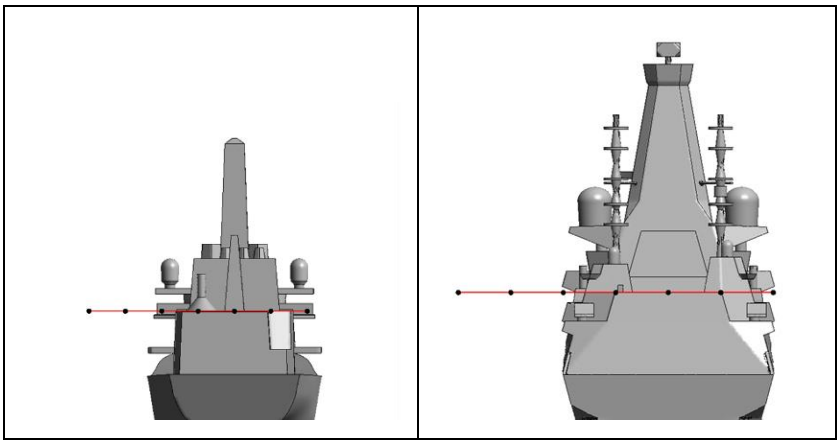

Figure 3.22: Locations where model helicopter is held during VAD analysis

Figure 3.23 shows a typical time-varying output of the thrust load, for three different positions along the line. A measure of the unsteady forces and moments is produced using a method outlined by Lee and Zan [65], whereby Power Spectral Density (PSD) plots are generated from the time histories given by the VAD, and the square root of the integral between the limits 0.2 to 2Hz is used to represent the Root Mean Square (RMS) loadings on the helicopter, Figure 3.24. This analysis technique, which is described in more detail in [84] takes account of the fact that although the unsteady loads are imposed over a very wide frequency range, the higher-frequency loads (>2 Hz) are less important because the inertia of the aircraft means it does not respond significantly, while the lower frequency loads (<0.2Hz) can be counteracted by the pilot through the helicopter's controls. Loads in the frequency range 0.2 to 2 Hz are said to be in the closed-loop pilot response frequency range and have the greatest influence on pilot workload. Higher RMS loads imply higher pilot workload.

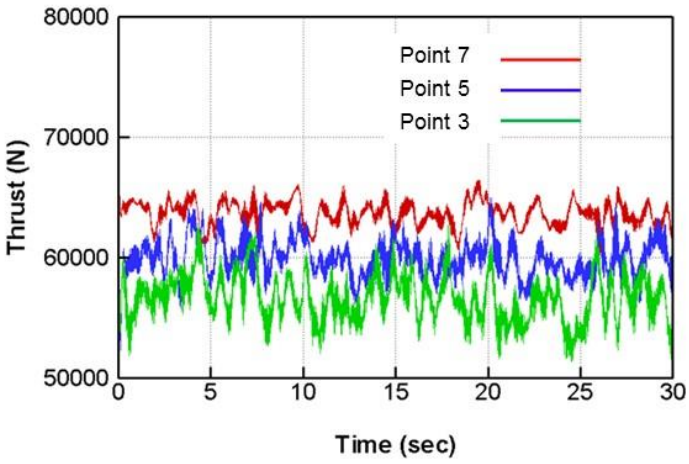

Figure 3.23: Typical time history of thrust load measured by VAD

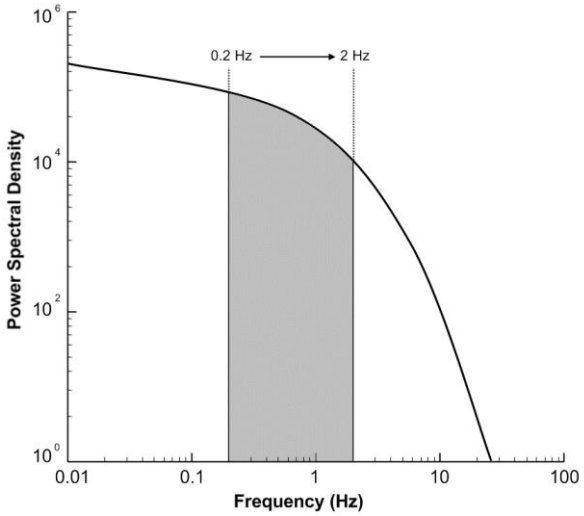

Figure 3.24: Closed-loop pilot response frequency bandwidth used to define RMS loads [82]

Figure 3.25 shows the RMS forces and moments calculated by the VAD technique for the GCS with and without the Mission Bay doors open, and for the Type 23, for a 40 knots headwind. The RMS values are plotted for the positions along the line shown in Figure 3.22; y/b = 0 is at the landing spot, y/b = ±0.5 is over the starboard and port deck edges, and y/b = -1 is one beam width off the port side, i.e. approximately where the lateral translation begins. The greatest contribution to the helicopter loads comes from the main rotor. When the helicopter (VAD) is at y/b = -1 the main rotor is outside of the headwind airwake and so all the RMS loads are the same for the three ships. At y/b =-0.5 approximately half the main rotor is in clean air and half is in the airwake. At y/b = +0.5 approximately half of the main rotor is again in the airwake. At y/b = 0 the whole helicopter is immersed in the airwake. In

the headwind it can be seen that the unsteady loads on the helicopter when over the GCS are actually higher over the port-side half of the deck (0.5>y/b>0) when the Mission Bay doors are open, which is consistent with the CFD in Figure 3.16 which showed higher turbulence on the port side deck edge when the doors are open. At the other positions the RMS loads are similar whether the doors are open or closed. Generally the unsteady loads over the Type 23 are lower and this, as explained by Forrest and Owen [45], is because it is a smaller ship. It can also be seen in Figure 3.25 that although the airwake over the two versions of the GCS are relatively symmetrical about y/b = 0, the RMS loads (e.g. at y/b = ±0.5) are not; this is because the helicopter is not "symmetrical" in that the rotating main rotor blades will be sweeping forward on the starboard side and sweeping backward on the port side so although the air velocities may be similar either side of the ship centreline, they will interact differently with the helicopter rotor blades.

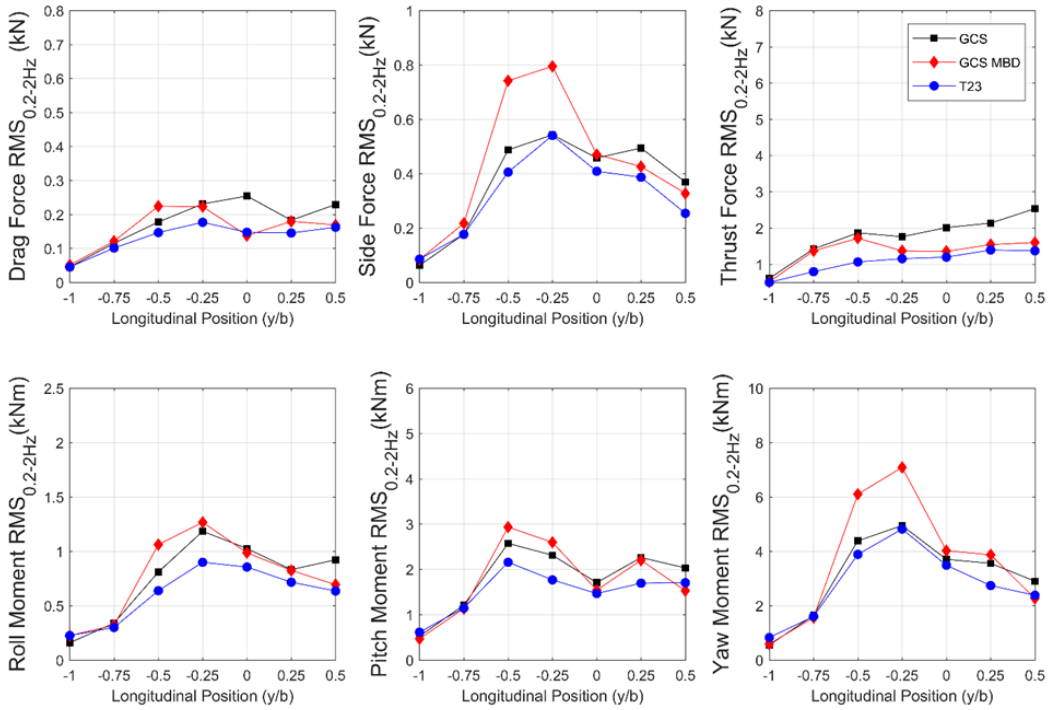

Figure 3.25 RMS Forces and moments measured by VAD over GCS with Mission Bay doors open (MBD) and closed, and over Type 23 in a 40 knots headwind.

Figure 3.26 shows the RMS forces and moments measured by the VAD in the 40 knots Green 30 WOD. In this case the helicopter at y/b = -1 is immersed in the turbulent airwake, as seen earlier in, for example, Figure 3.18. It can be seen that having the Mission Bay doors open does have an effect on the helicopter loads, particularly off the port side, although whether it is better or worse varies across the different axes. In this wind the unsteady loads over the smaller Type 23 are noticeably lower because of the smaller and higher frequency

disturbances in the airwake. Overall it can be concluded that while having the Mission Bay doors open will affect the airwake over and around the flight deck, the effect on the helicopter is less predictable and would have to be taken through to piloted trials in the flight simulator for the pilot to assess the workload required to land the helicopter to the different ships.

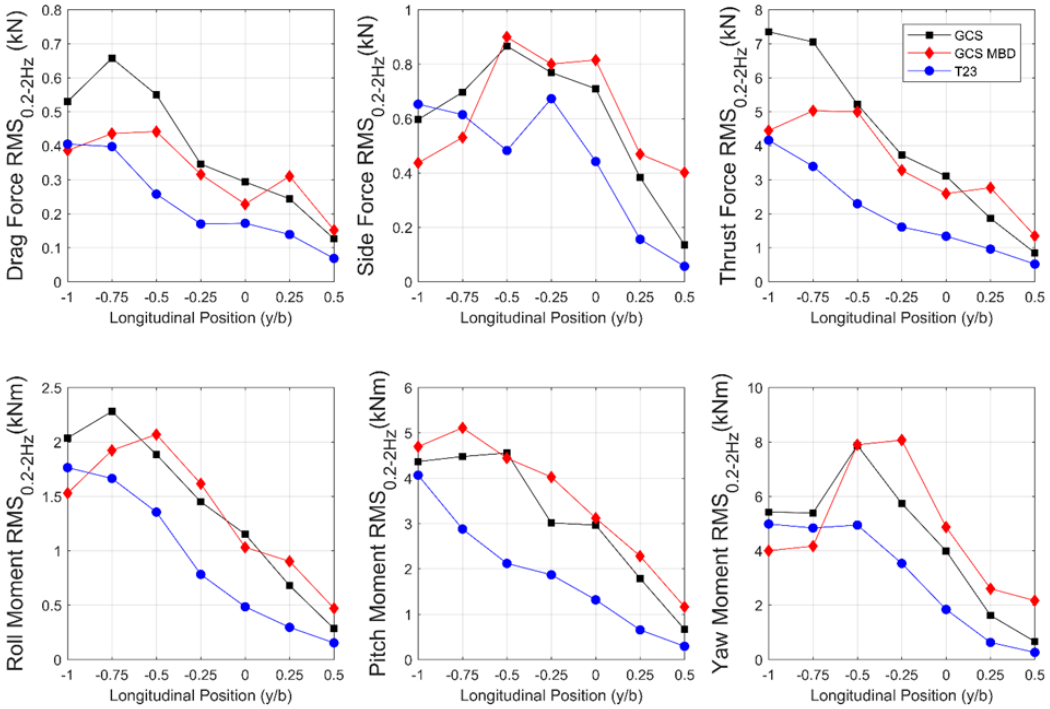

Figure 3.26 RMS Forces and moments measured by VAD over GCS with Mission Bay doors open (MBD) and closed, and over Type 23 in a 40 knots Green 30 WOD.

3.3. Airflow Distortion at Anemometer Locations of Type 23 and GCS

In Chapter 1 it was described how the superstructure aerodynamics can affect the accuracy of the ship's anemometers, and how this, in turn, can affect helicopter operations. Chapter 4 will give a detailed CFD analysis of the GCS anemometers; the purpose of this section is to compare the air flow at the locations of the anemometers that are supported off the masts of the Type 23 and the GCS. As shown in Chapter 1, Figure 1.12, the safe operational envelope for the helicopter is defined by the SHOL. The boundaries of the SHOL are determined by at-sea flight trials where test pilots fly repeated deck landings at different wind angles and wind speeds to find the limiting conditions at which it is safe for a fleet pilot to launch and recover the helicopter. While the wind speed and direction during the trials are usually measured by dedicated temporary anemometers mounted on tall masts at the bow of the ship, in an attempt to avoid the ship's airwake, the readings have to be correlated with the ship's own

anemometers, and for every sortie afterwards it will be the ship's anemometers which measure the wind speed and direction. If the ship's anemometers are incorrect or unreliable, then the SHOL will not be correctly specified in the first instance, and neither will the wind condition be reliably measured for every sortie conducted thereafter. Accurate readings from the ship's anemometers are therefore essential for a reliable SHOL.

The operational parameters for the anemometers are prescribed by Defence Standard 00-133 [86] which, amongst other criteria that will be discussed in Chapter 4, state that the anemometers should be mounted off the ship's mast and be:

(i) positioned in clear air above the edge of the boundary layer created by the ship's superstructure

(ii) located as high as possible on separate port and starboard yard arms

(iii) in a space uncluttered by adjacent equipment, facing forward with at least 3.0m radius free air space around each anemometer

Addressing point (i) first, as has been demonstrated earlier in this chapter, it will be very difficult to mount the ship's anemometers anywhere on the superstructure, including the masts, where they will be in clear air outside of the influence of the airwake. It will also be demonstrated below how meeting requirements (ii) and (iii) are adversely affected by the GCS superstructure.

Figure 3.27 shows head-on views of the Type 23 and GCS ships, with their anemometer locations identified by red squares. The perspective views of the two ships are different and in practice the two sets of anemometers are approximately the same height above sea level, as can be seen in Figure 3.28 which shows the CAD used for the CFD analyses with the ships in proportion. It can immediately be seen that the Type 23 anemometers can be expected to be in less distorted air flow because of the more slender mast and longer forward-facing yardarms on which they are mounted. The larger mast of the GCS, however, as well as the bigger deck house and the additional equipment ahead of and in the vicinity of the anemometers, can be expected to have a greater influence on the air flow. As was described in Chapter 2, when the CAD for the CFD analysis was extracted from the detailed digital engineering drawings of the ships, features smaller than 30 cm were mostly removed. Looking closely at the anemometers identified in Figure 3.26 it can be seen that they are mounted on slender yardarms; these were not included in the CFD analyses as it was deemed that they would not affect the air flow at the anemometer sensors. The yardarms that are

shown on the Type 23 CAD in Figure 3.28 have been added to the image to demonstrate how the apparently isolated anemometers are supported; the yardarms were not included in the CFD analysis.

Figure 3.27: Head-on view of Type 23 [87] *(left) and GCS* [79] *(right) showing locations of main anemometers*

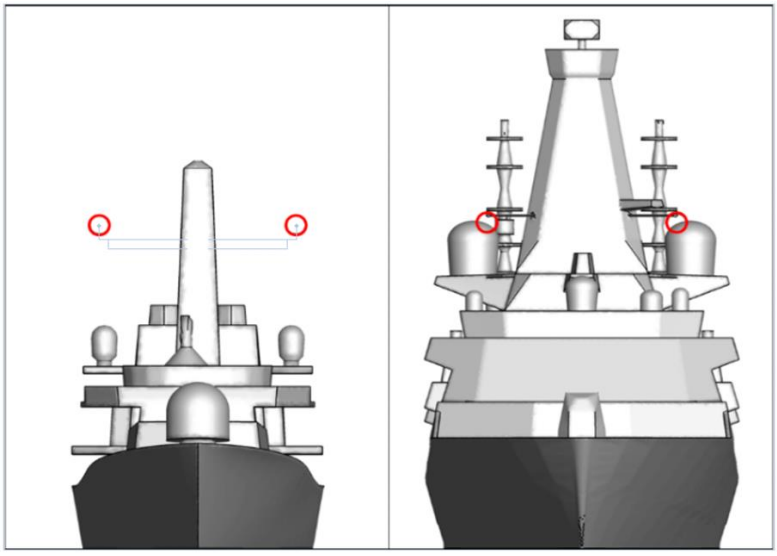

Figure 3.28: Head-on view of Type 23 (left) and GCS (right) CAD for CFD analyses showing positions of main anemometers

How the air flow will be affected by the ships' masts and the local flow distortion at the anemometer locations can be extracted from the CFD-generated airwakes. Figures 3.29 and 3.30 show mean path lines arranged on vertical and horizontal planes to pass through the anemometer locations on the Type 23 and GCS, respectively, for a headwind. It can be seen that the air flows relatively undisturbed through the anemometer locations on the Type 23,

and the wake generated by the mast is quite small. However, for the GCS in Figure 3.30, the air flow at the anemometer locations ahead of the mast is noticeably more disturbed and the wake behind the mast is much bigger and more turbulent.

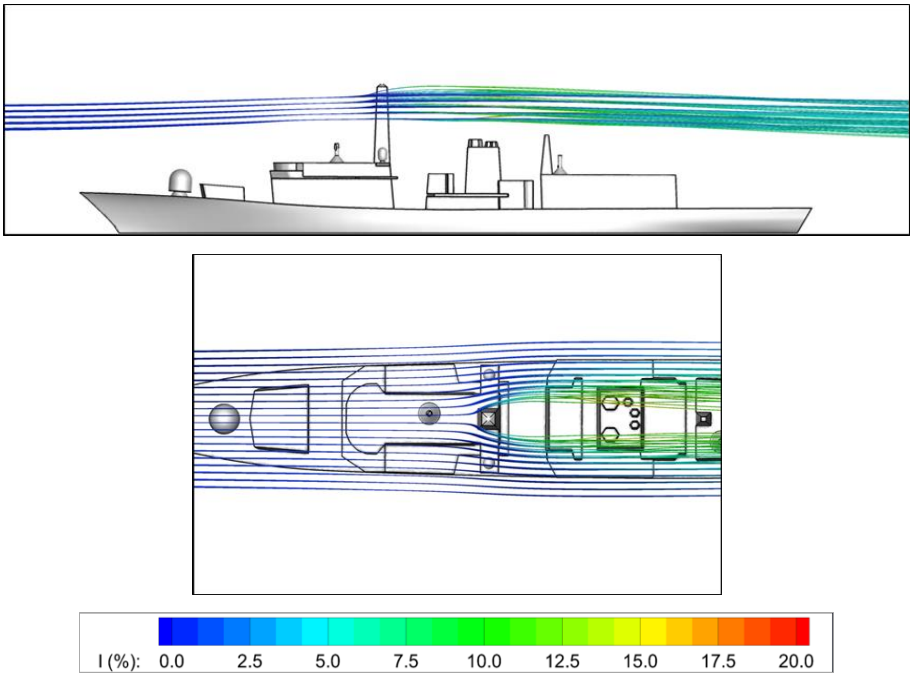

Figure 3.29: Pathlines illustrating headwind flow through anemometer locations of Type 23

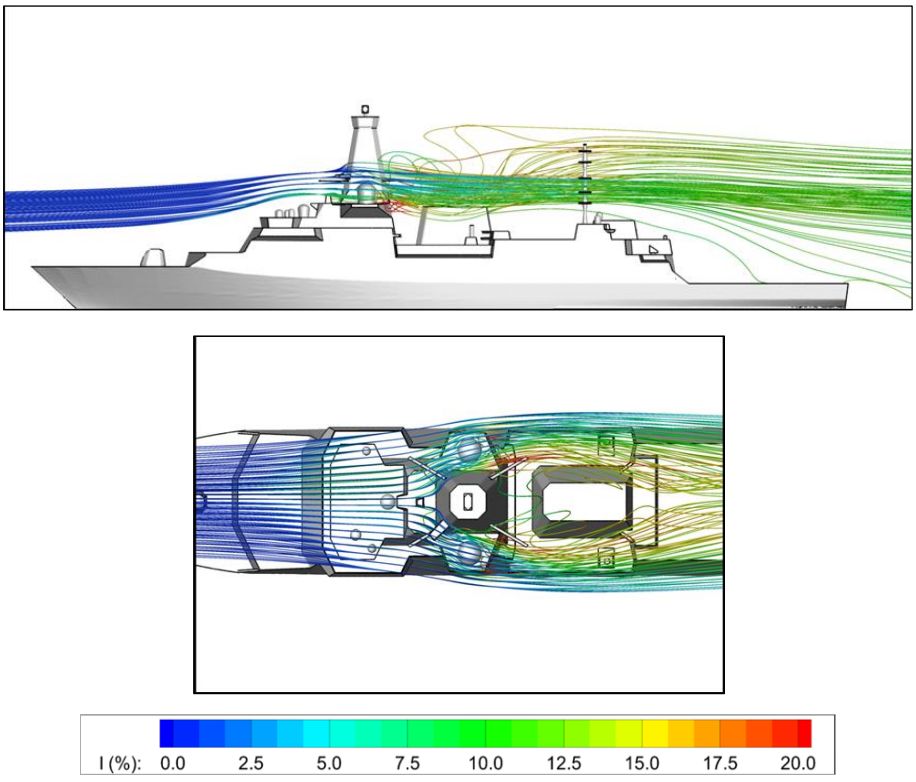

Figure 3.30: Pathlines illustrating headwind flow through anemometer locations of GCS

Figure 3.31 provides further detail of the headwind wake behind the masts in horizontal planes at the height of the anemometers. The two images show the instantaneous flow field in terms of non-dimensionalised vorticity magnitude, ω^*. A characteristic length, L, in this case the length of the ship (150m) and a characteristic velocity, U, taken as the freestream velocity (20.57 m/s), were used to non-dimensionalise vorticity, ω, according to Eqn. 3.2.

$$\omega^* = \omega \frac{L}{U} \tag{3.2}$$

The Type 23 mast on the left has created a conventional vortex street due to the flow shedding alternatively from either side of the mast. The wake behind the GCS mast is very different, not only is it larger due to the larger cross section of the mast, but there is no evidence of periodic vortex shedding, probably due to the highly disturbed air in front of and around the mast due to the elevated superstructure ahead of the mast and the equipment either side of it.

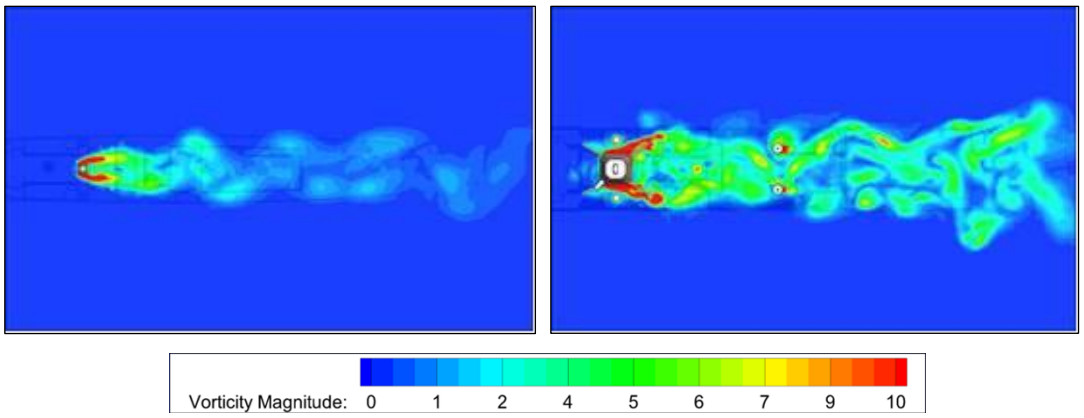

Figure 3.31: Instantaneous CFD image of unsteady wake behind Type 23 mast (left) and GCS mast (right) illustrated by contours of vorticity.

Figure 3.32 shows the time-averaged air flow in a horizontal plane that passes through the anemometer locations, for winds from ahead and Green 30. The contours show the averaged airwake velocity normalised by the free stream value at anemometer height. The bigger wake in the lee of the bulkier GCS mast, and its influence on the flow ahead of the mast, can be clearly seen especially when compared with the more slender mast of the Type 23. The headwind wakes are essentially the time-averaged versions of the wakes illustrated in Figure 3.30.

Figure 3.33 also illustrates the air flow around the masts on the same horizontal plane but this time as turbulence intensity. In both the headwind and the Green 30 winds the air flow around the mast of the Type 23 can be seen to have a turbulent wake, but there is no turbulence ahead of the mast at the anemometer locations. For the larger mast of the GCS it can be seen that there is a turbulent region in front of the mast, particularly in the headwind and this is due to the upwards air flow that is coming off the superstructure in front of the mast.

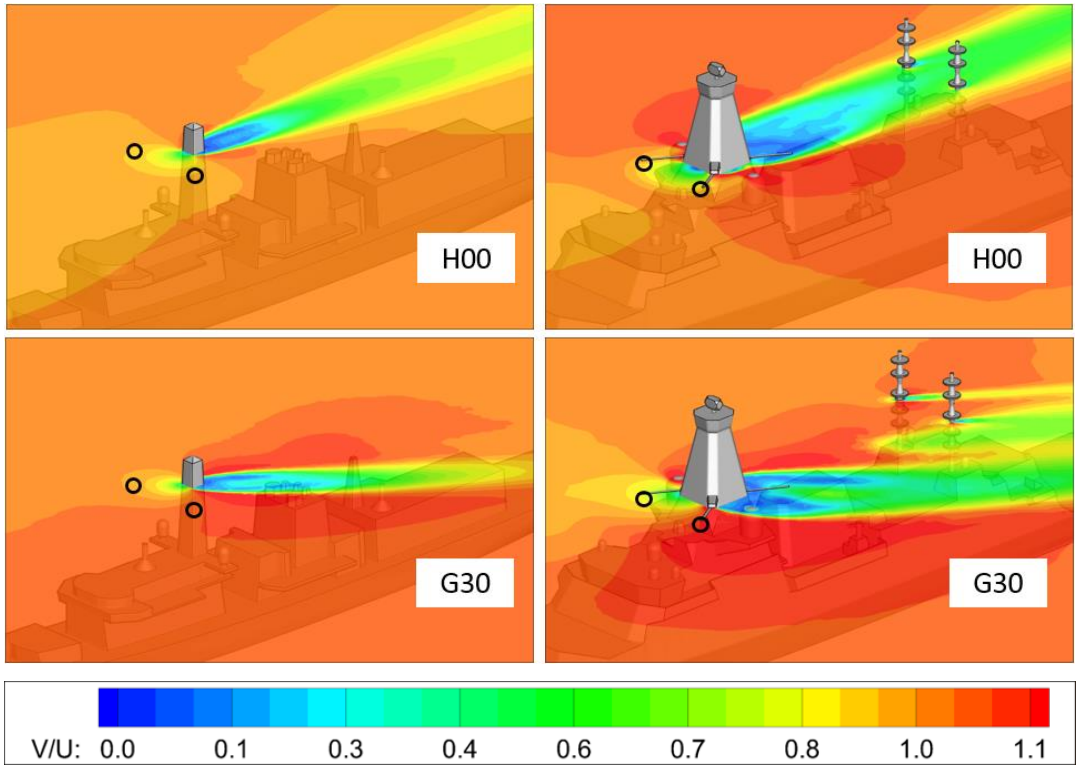

Figure 3.32: Air flow at anemometer positions illustrated by contours of normalised mean velocities for headwind and Green 30 WOD conditions, for Type 23 (left) and GCS (right). Anemometer positions indicated by black circles

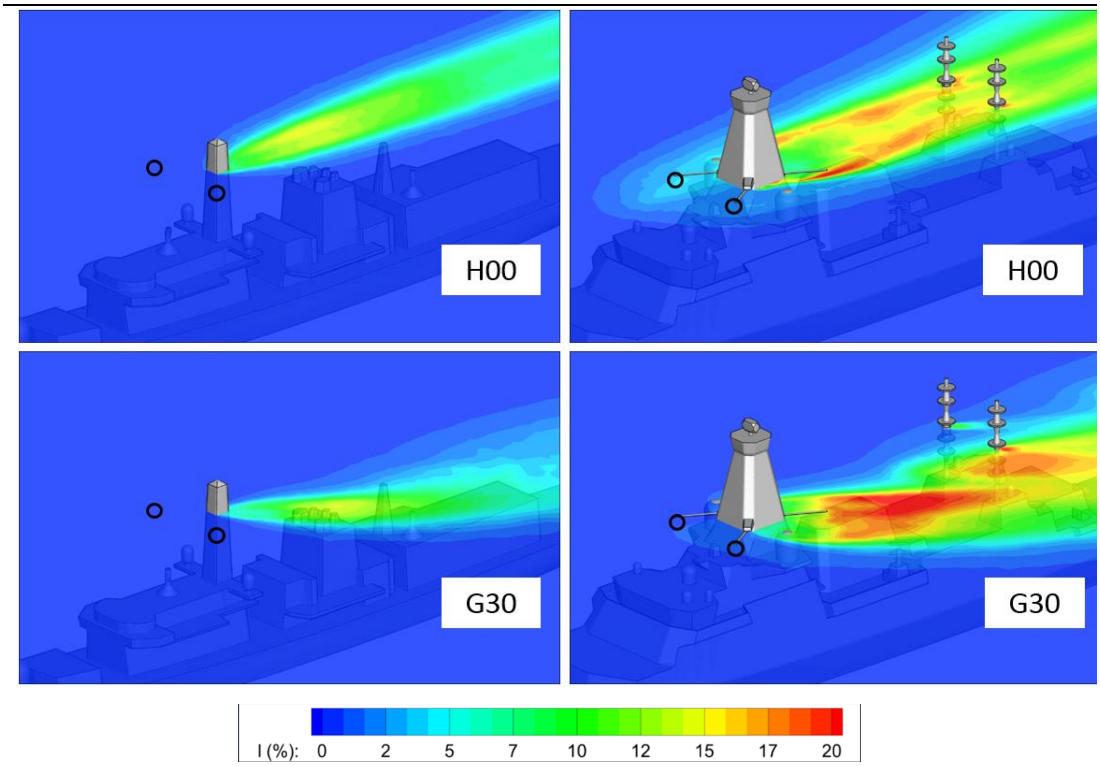

Figure 3.33: Air flow at anemometer positions illustrated by contours of turbulence intensity for headwind and Green 30 WOD conditions, for Type 23 (left) and GCS (right). Anemometer positions indicated by black circles

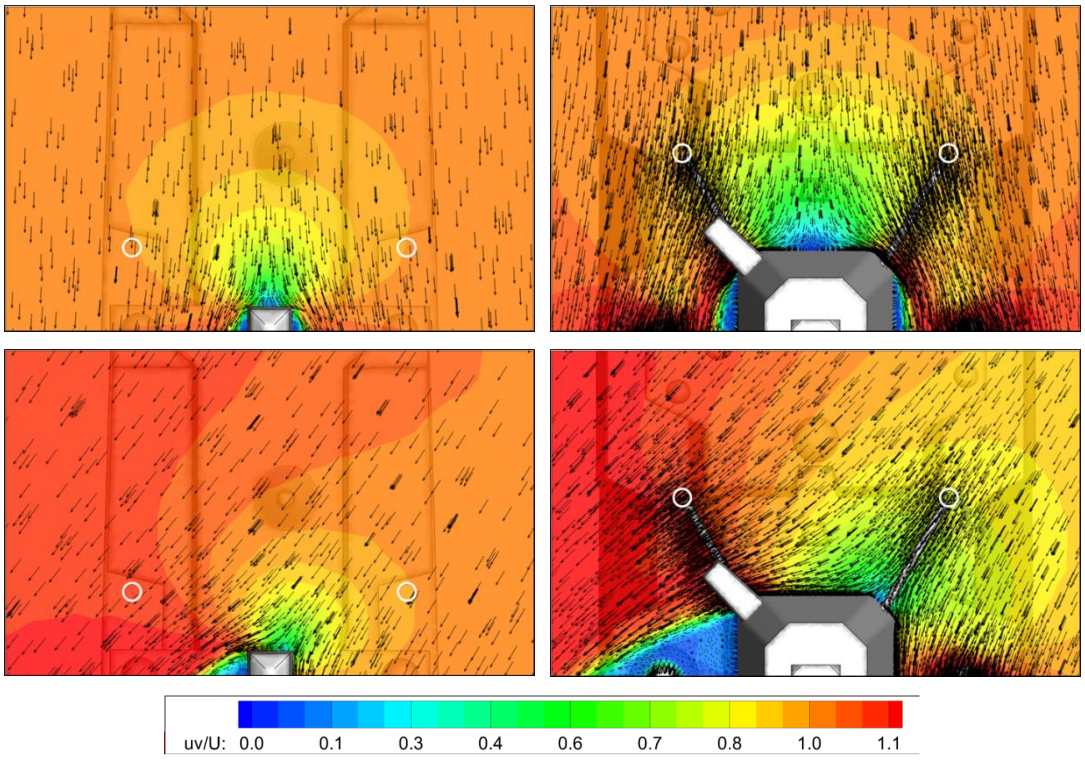

Figure 3.34: Velocity field in horizontal plane through anemometer locations illustrated by vectors and contours of horizontal velocity magnitude for Type 23 (left) and GCS (right) in headwind (top) and Green 30 WOD (bottom)

Looking more closely at the flow distortion at the anemometer locations, Figure 3.34 shows a plan view of the mean flow field ahead of the main mast in the plane of the anemometers for a headwind; the anemometer positions are identified by the white circles. The contours show average velocity magnitude in the horizontal plane (i.e. vector sums of u and v) normalised by freestream velocity, while the vectors represent the average velocity direction and magnitude in the horizontal plane. Conventionally, a ship's anemometer measures wind velocity in the horizontal plane, hence the use of the horizontal velocity components. The clustering of the vectors around the features on the mast is due to the more dense CFD mesh in those regions. Even in the headwind, it can be seen in Table 3.1 that the flow has deviated at the anemometer locations. For the Type 23 the average wind speed in the horizontal plane is about 3% different to the undisturbed free stream velocity at both anemometer locations, and the angular deviation is 4.5°. For the GCS the corresponding differences in the average horizontal velocity magnitude and angular deviation are about 19% and 11°, respectively. In the Green 30 wind the ship would normally use the starboard anemometer as it is facing into the oncoming flow (i.e. the right hand anemometers in the two lower images). For the Type 23 the deviation of the local flow in magnitude and direction is about 4% and 1.5°, respectively, while the corresponding values for the GCS are 19% and 6°. It is clear therefore that the larger mast of the GCS is significantly disturbing the flow at the anemometer locations. Chapter 4 will present a more detailed analysis of the flow at the anemometer locations on the GCS.

Table 3.1: Deviations in wind speed and direction in horizontal plane at anemometer locations

	Type 23		**GCS**	
	Headwind	**Green 30**	**Headwind**	**Green 30**
Deviation in wind speed	3%	4%	19%	19%
Deviation in wind angle	4.5°	1.5°	11°	6°

3.4. Ship Engine Exhaust Dispersion of Type 23 and GCS

Both ships have a combined Diesel-electric and gas turbine propulsion system. The GCS will be powered by a single Rolls Royce MT30 gas turbine with a maximum output of 40MW, while the Type 23 is powered by two 19.5MW Rolls Royce Marine Spey engines; the maximum propulsion power is therefore similar for the two ships. Both ships also operate with four Diesel generators. The volume of hot gases being exhausted, particularly from the gas turbine, can be very high and although the hot gases will mix with the ship's airwake and

be cooled, there can still be elevated air temperatures in areas around the flight deck which can affect the helicopter performance.

Chapter 5 will give a detailed analysis of the GCS exhaust gas dispersion for a range of conditions. In this section the exhaust gas dispersion from the engines of the two ships will be compared for 20 knots winds from Ahead and Green 30. The CFD analysis was carried out with each ship having just two of its Diesel Generators (DGs) running and with the GTs running at maximum power; i.e. both GTs were running on the Type 23. The engine characteristics for the Type 23 were unavailable, but to provide a reasonable comparison between the two ships it was assumed that the total exhaust mass flow from the two Type 23 GTs were the same as the mass flow from the GCS GT, and that they had the same temperatures. This is a reasonable assumption given that the maximum power output of the two propulsion systems are similar.

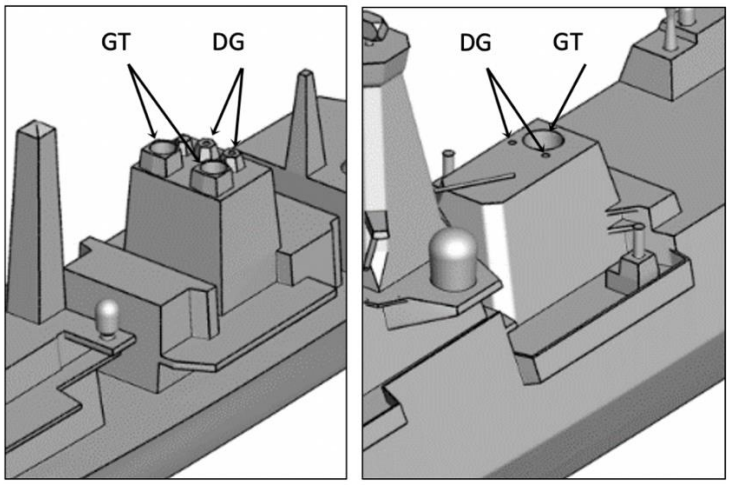

Figure 3.35: Gas Turbine and Diesel Generator exhaust outlets Type 23 (left) and GCS (right)

Table 3.2 lists the exhaust gas and ambient conditions, as provided by BAE for the GCS, and as assumed for the Type 23. The ambient temperature was 38°C (311K); this rather high value was used because, at the time in the project when this analysis was carried out, the requirement from BAE was to investigate how the GCS exhaust gas would disperse in air temperatures such as those found in the Arabian Gulf; the 20 knots relative wind was also a BAE requirement. It can be seen from Table 3.2 that all the DG exhaust ducts have a diameter of 0.5m, while the GT exhaust of the GCS has a diameter of 2.8m and the Type 23 GT exhausts have a diameter of 1.86m. The CFD meshes for the two ships were constructed as described

in Chapter 2, with density boxes used to encompass the trajectory of the exhaust plumes to restrict the cell growth. For each exhaust outlet the duct was extended into the internal geometry of the ship by 5 duct diameters; at the entry to the duct the exhaust flow was introduced as a uniform velocity so that the flow emerging from the exhaust outlet had a representative velocity profile. It can be seen in Table 3.2 that the exhaust exit velocities are similar for the single GCS GT and the two Type 23 GTs.

Table 3.2: Exhaust parameters for GCS and Type 23

	GCS		T23	
	DG	**GT**	**DG**	**GT (x2)**
Mass Flow Rate (kg/s)	5.6	73.5	5.6	36.75
Exhaust Temperature (K)	703.15	689.15	703.15	689.15
Density (kg/m^3)	0.502	0.512	0.502	0.512
Diameter (m)	0.5	2.8	0.5	1.86
Exit Velocity (m/s)	56.8	23.3	56.8	26.05
Ambient Temperature (K)	311		311	

Figure 3.36 shows the dispersion of the hot exhaust plume for both ships in both wind directions. The plumes are illustrated by surface contours of constant average temperature (2, 5 and 10°C above ambient) and it can be seen that, despite the very hot initial temperatures and the very high mass flow rates from the GTs, the temperatures reduce quickly due to the turbulent mixing with the ship airwake. The top two images show that in the headwind the exhaust plume passes high above the landing deck and for normal helicopter operations should not affect the aircraft provided it does not fly high above the deck . It can also be seen that for the GCS the exhaust gases are drawn into the wake of the main mast and may therefore heat the metal surface and increase the ship's IR signature. A similar situation occurs on the Type 45 destroyer and the aft surface on the mast is painted with an IR-reducing paint. In these images the two exhaust plumes from the Type 23 appear to have merged and the core of the plume remains hotter for a longer distance. In the Green 30 wind the exhaust plume is directed over the port side of each ship and into the area where the helicopter will hold position alongside the landing deck before translating sideways to the landing spot; in this case, therefore, the helicopter may be affected.

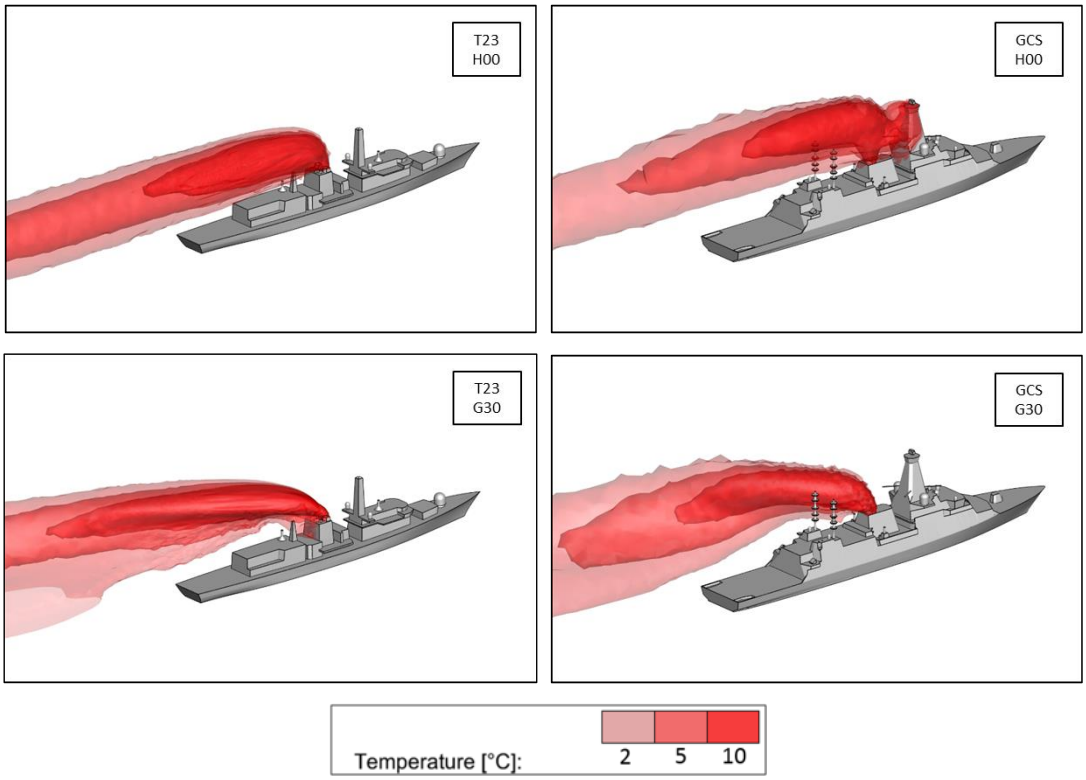

Figure 3.36: Isosurfaces of constant average plume temperatures above ambient for Type 23 (left) and GCS (right) in headwind (top) and Green 30 wind (bottom)

The following three sets of figures show orthographic views of the exhaust gas plumes as contours of temperature above ambient; a logarithmic temperature scale has been used because of the large difference in temperatures between the initial exhaust values of about 700K and the ambient of 311K. Figure 3.37 shows the side view of the two ships and, as indicated in Table 3.1, the GTs have by far the highest mass flow rate, and therefore their exhaust plumes dominate the images compared with the DG exhausts. The two Type 23 GT exhaust outlets lie either side of the ship's centreline and have their centres about 4.5m apart; therefore the side-on image of the Type 23 in the headwind only shows the edges of the hot exhaust jets as they emerge from the two GT exhaust outlets, unlike the GCS jet whose centreline coincides with the plane of the image. It can again be seen how, in the headwind, the GT exhaust efflux of the GCS is entrained into the recirculating flow in the wake of the mast. The situation on the Type 23 is very different where the more slender mast with its smaller recirculation zone does not interact with the exhaust efflux. The heated plume is higher above the deck of the GCS compared with the Type 23. The side view of the two ships in the Green 30 WOD does not reveal much about the exhaust gas dispersion as the plume quickly moves out of the vertical plane on the ships' centrelines.

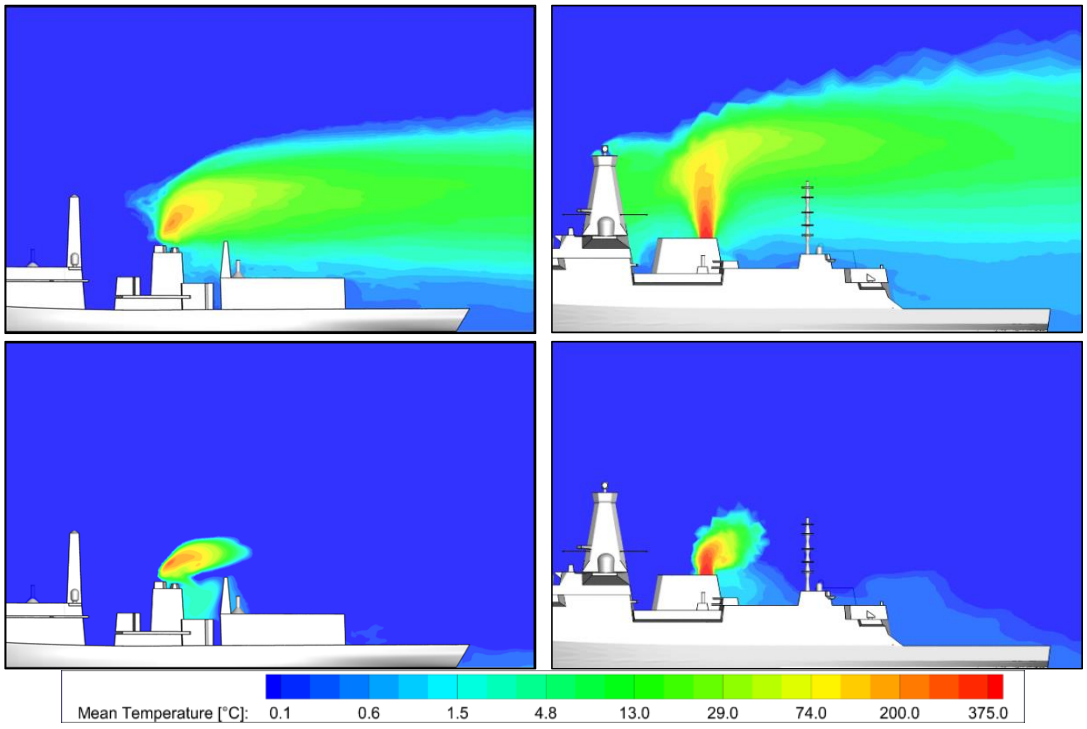

Figure 3.37: Contours of average temperature above ambient on an exponential scale along the ship centreline of Type 23 (left) and GCS (right) in a headwind (Top) and Green 30 (Bottom)

In Figure 3.38 the contours of average temperature above ambient are shown on a horizontal plane that is at the height of the ships' hangars, i.e. 6m and 8m above the landing deck for the Type 23 and GCS respectively. In the headwind there is very little increase in the local air temperature at these heights, about 1.5°C, as the core of the plume passes higher above the deck. In the Green 30 WOD, Figure 3.37 shows how the plume is entrained by the ship airwakes into the area where the helicopter will begin its landing manoeuvre. It can be seen that the average air temperature rise due to the Type 23 exhaust reaches about 6°C above ambient, while for the GCS the maximum temperature is about 10°C above ambient. As will be discussed in Chapter 5, local fluctuating temperatures of this magnitude can affect the helicopter performance. The air temperatures above the deck are very close to ambient, because the plume is deflected away from the deck by the oblique wind.

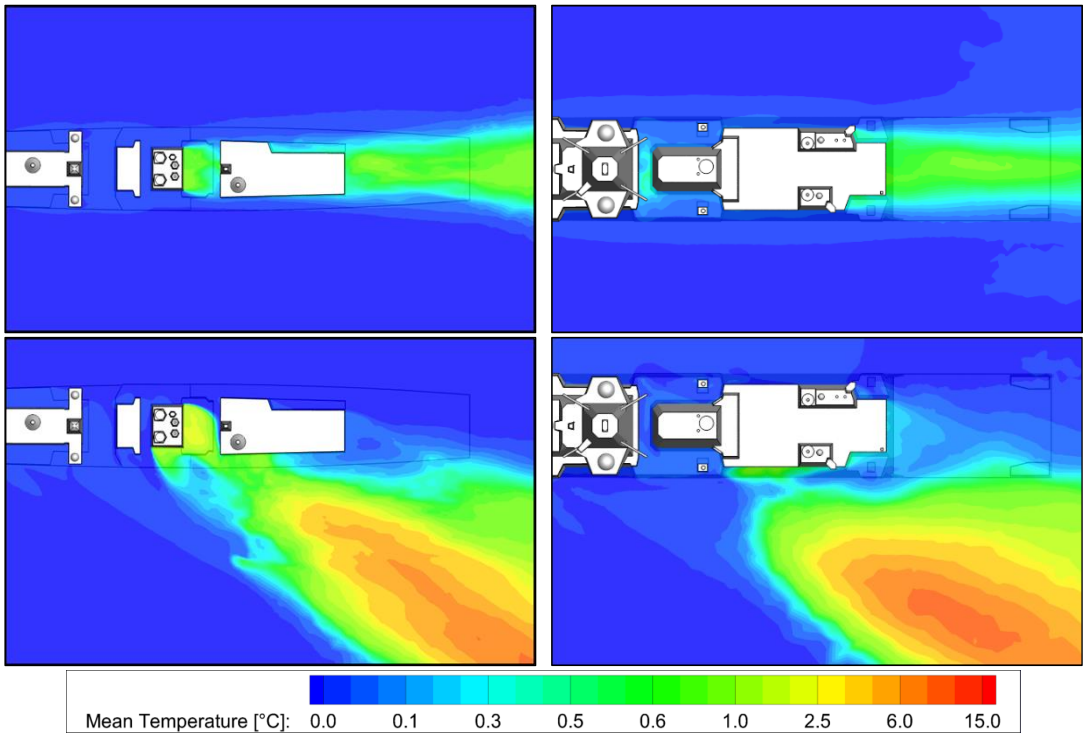

Figure 3.38: Contours of average temperature above ambient on an exponential scale taken at hangar height on Type 23 (left) and GCS (right) in a headwind (Top) and Green 30 (Bottom)

Figure 3.39 shows the exhaust plumes as contours of average temperature above ambient on a vertical plane that passes through the landing spots, i.e. about half way along each of the ships' landing decks. In the headwind, the core of the plume can be seen above the flight deck. For the Type 23 there is still some evidence of the two GT exhaust flows, but they have largely merged. The core plume temperature on this plane is about 15°C above ambient and is not so high above the flight deck. The core of the GCS plume has a slightly lower temperature of about 12°C and is higher above the deck. Both plumes have cooled significantly from the initial exhaust temperature of 416°C, but they are still predicted to have temperature elevations that would adversely affect the helicopter should it fly in these areas. The plume from the Type 23 is therefore a greater threat to the helicopter (although it should be noted that no issues have been reported due to elevated air temperatures for helicopter operating to the Type 23).

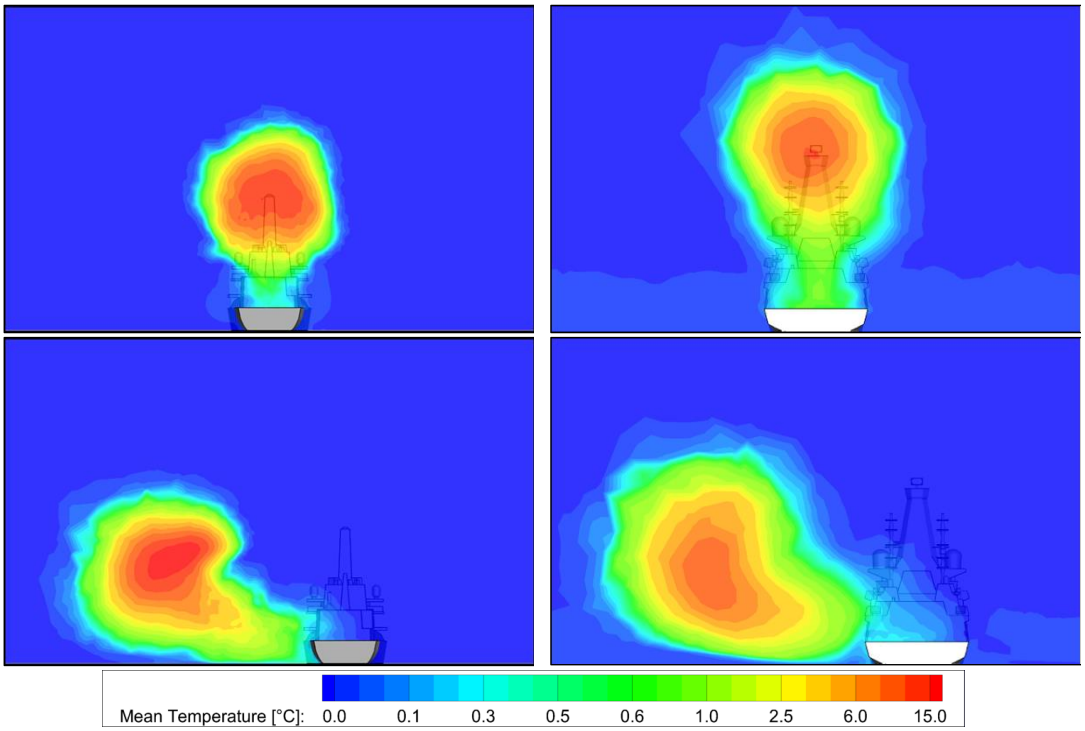

Figure 3.39: Contours of temperature above ambient on an exponential scale taken on a vertical plane across the landing spot on Type 23 (left) and GCS (right) in a headwind (Top) and Green 30 (Bottom)

The lower images in Figure 3.39 illustrate how the exhaust plumes in the Green 30 WOD have not only been deflected to the port side of the ships, but they have also been entrained to a lower height due to the downward deflection of the airwake in the lee of each of the two ships. The bulkier geometry of the GCS causes a greater downwash so that even though the exhaust plume is initially taken higher, as seen in the headwind images, the core of the plume in the Green 30 WOD is now at a similar height to the Type 23. The core of the Type 23 plume is more than 15°C above ambient and is hotter than that of the GCS, possibly because the more turbulent airwake of the larger GCS has cooled the exhaust efflux more. Looking at the two ships from astern, when the helicopter is off the port side of each ship to begin its landing manoeuvre, the main rotor will be just above the hangar height and will be typically one ship's beam width away from the port side; i.e. the rotor will be drawing in the hotter air flow from the plume and the performance may well be affected.

3.5. Chapter Summary

This chapter has shown how the superstructure design characteristics of the modern RCS-compliant warship can be expected to affect the air flow over the ship and, in turn, how this could affect the operation of the ship's helicopter. The air flow over the GCS has been

compared with that of its predecessor, the Type 23 frigate. The GCS is noticeably different from the Type 23 in a number of aspects: the GCS is a larger ship, it has a flat less-fragmented superstructure, and it has a larger, bulkier main mast. The evolution of RCS-compliant ships has paid little attention to superstructure aerodynamics and how they might affect the ship and its helicopter. This chapter has assessed the air flow for two wind angles, Ahead and Green 30. Winds can approach a ship from all angles but, because the ship moves forward, the majority of the winds come from the fore. Oblique winds from the starboard, i.e. Green winds, are particularly challenging for the helicopter because when implementing the port-side landing approach (illustrated in Chapter 1), an oblique wind from starboard creates turbulent air on the port side of the landing deck and a steep unsteady shear layer across the flight deck.

Using unsteady CFD analysis, it has been shown that the air flow over and around the flight deck of the GCS is more challenging for the helicopter, compared with the Type 23, and this is due to both the size of the ship and the way its flat, continuous sides do not break up or slow down the air flow before it reaches the flight deck. A supplementary study was also undertaken in which it was shown how the air flow over and around the GCS flight deck would be affected by having the ship's Mission Bay doors open. The VAD was introduced as a simulation technique to investigate the effect of the CFD-generated unsteady air flow on a flight dynamics model of a helicopter; the Type 23 was shown to have a less aggressive airwake than the GCS. The VAD also showed that having the GCS Mission Bay doors open would affect the helicopter, particularly in an oblique wind, but whether or not that would lead to higher pilot workload was inconclusive and would require piloted simulations.

It has been shown that the larger main mast of the GCS is detrimental to the ship's anemometers and the situation is made worse by placing the anemometers low down on the mast so they are in highly disturbed air. The air flow at the anemometer locations on the Type 23, with its more slender mast and more effective yardarms, is much less disturbed. Chapter 4 will present a more detailed study into the air flow at the GCS anemometer locations.

A CFD study of the dispersion of the hot exhaust efflux from the engines of the two ships has shown that the hot gases cool quickly due to turbulent mixing with the ships' airwakes. A comparison of the exhaust gas dispersion from the two ships has shown that the Green 30 wind presents more difficulty for the helicopter because the exhaust plume is entrained into the area off the port side of the ship where the helicopter will begin its landing manoeuvre.

It was also shown that the exhaust plume from the Type 23 cools less quickly than that of the GCS, possibly because the bulkier superstructure of the GCS, including the mast, creates a larger and more turbulent wake. In a headwind, the larger wake behind the GCS mast entrains the GT exhaust gases and could lead to surface heating of the mast, thereby increasing the ship's IR signature. A more detailed study of the exhaust gas dispersion from the GCS will be presented in Chapter 5.

Chapter 4. Mast Structure Effects on Anemometer Readings

In Chapter 3, the main mast structures of the GCS and its predecessor, the Type 23, were compared and the local flow in the region of the mast structures was viewed with respect to the performance of each ship's wind measurement system. Chapter 4 begins with a review of the design evolution of the ship's mast, from the ships of the line in the mid-19th century to the modern warships of today's naval forces. A more detailed discussion and CFD study of the air flow at the anemometer locations on the GCS will be presented and interpreted in the light of the required anemometer performance as specified by the relevant defence standards.

4.1. The Ship Mast

Historically, early ships of war had pole masts that were used primarily as a means to attach sails to harness wind power for propulsion, commonly referred to as sail masts. As seen earlier in Figure 1.1, several sail masts were required in various arrangements to affix the large fabric sails, with each mast traditionally being made from tall trunks of conifer wood. The aerodynamics of the mast was not important, unlike its structural purpose in holding the sails high above the ship's decks, as well as providing a lookout point by means of a crow's nest. The Royal Navy built sail-frigates up until the mid-19th century and, even as methods of propulsion turned to engine power in the late 19th century, continued to use sails to supplement steam power as late as the 1880s when the last of the sail-rigged corvettes, HMS Calliope, was launched in 1884, Figure 4.1. As ship design evolved beyond the use of sails, the role of the ship's masts began to change. Although no longer necessary for the rigging of sails, tall structures were still required to provide a lookout point to aid navigation, as well as to inform fall of shot for calculating gunfire trajectories, and, as time progressed, to mount radio antennae; therefore, the pole mast endured.

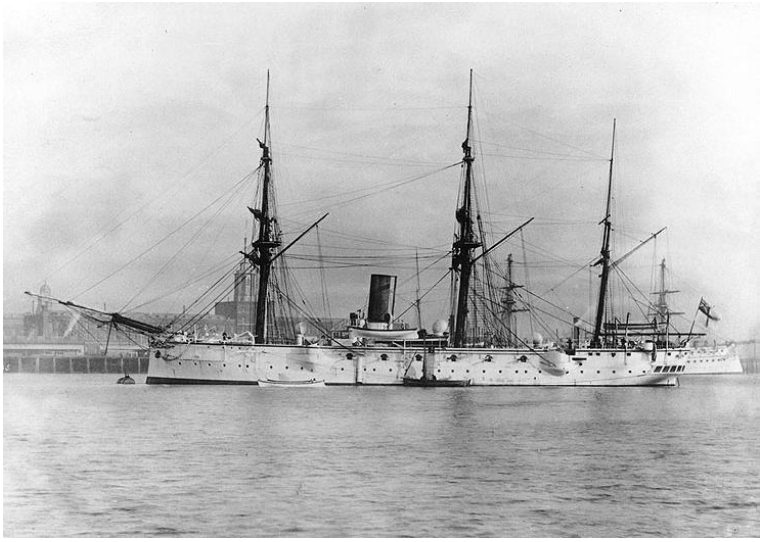

Figure 4.1: HMS Calliope (1884) with three pole masts [88]

At the beginning of the 20th century, the Royal Navy built the first dreadnought, an iconic battleship that became a symbol of military power; so much so, that any ship before its time became referred to as 'pre-dreadnought'. Powered solely by steam engines and equipped with a heavy duty gun battery, the 'all-big-gun' dreadnought was a catalyst for naval architectural advancement around the world as nations rushed to acquire such power in what was the arms race of its day. As a result of the heavy duty battery, the main mast of the dreadnought had to cope with the shock of weapon fire and remain sturdy at the crow's nest for the crew on lookout and calculating fall of shot. A tripod mast was used as the main foremast on HMS Dreadnought, Figure 4.2., the first of its class, in place of a pole mast to ensure rigidity and stability.

Figure 4.2: HMS Dreadnought (1906) [89]

Following the launch of HMS Dreadnought, in the subsequent race for naval power the ship designers for the US Navy rejected the traditional pole mast structure in favour of lattice mast structures, often referred to as caged masts, Figure 4.3. Their design was known as a hyperboloid structure and was revolutionary at the time. Due to their hollow, caged construction, the mast's structure was regarded as weight-saving compared with earlier large ship masts and they were also seen as less susceptible to damage from enemy fire and structural vibrations from heavy weapon machinery. The significance of the lightweight mast was not just on the weight (displacement) of the ship, but also its stability and movement in roll because a heavy tall mast raises the centre of gravity of the ship. However, after an incident on the USS Michigan in 1918, when a lattice mast collapsed during a severe weather storm, issues regarding their structural integrity began to arise. Excessive stresses as a result of heavy storms, along with the weight of the equipment being attached to the mast, resulted in the failure of the structure at its narrowest point. Additional issues that contributed to the mast's failure included poorly repaired damage due to a gun explosion and poorly joined sections due to structural lengthening. Another ship of the class, USS Connecticut, was also found to have a lattice mast structure showing signs of buckling. Lattice mast structural issues continued into the 1920s and 30s, many of which were found to be as a result of structural corrosion from the ship's exhaust gases [90]. As a result, the US Navy began altering some ships in service, replacing lattice mast structures with pole masts and, later on, introducing the tripod mast, as used successfully by the Royal Navy, an example of which can be seen in Figure 4.4. of the modified USS New York with a tripod main mast structure.

Figure 4.3: USS South Carolina with lattice mast structures [91]

Figure 4.4: USS New York modified with tripod mast and with first shipboard XAF radar system installed [92]

The USS New York was also chosen for the installation of the first shipboard radar in 1939, the XAF, which marked the start of what was to become a new era in stealth combat. The XAF experimental radar can be seen in Figure 4.4., installed just in front of the main tripod mast structure. As World War II continued, so too did the acceleration in technological advancements of warfare systems, so much so, that by the end of 1943 most combatant vessels were fitted with surface search radar systems [93]. Furthermore, following the first successful landing of a helicopter to a frigate by Alan Bristow in 1946 [4], the performance of the ship's wind measurement system was now much more important. Ships now needed to use anemometers to measure the wind speed as accurately as possible, not just for navigation and manoeuvring purposes, but also to inform the pilots of the over-deck wind conditions when launching and recovering to the ship's flight deck. Another role of the main mast structure was therefore siting the ship's wind measurements systems high above the superstructure and flight deck to obtain the best possible reading of the freestream wind-over-deck (WOD) condition.

In the decades that followed, as radar systems became more advanced, the advantages of designing a warship to disguise itself under radar observation became ever more apparent. Mast design had changed to accommodate the increasing number of electronic systems required as warfare technology developed. The result of such rapid technological advancement was visible in the increased equipment and instrumentation on the superstructure and the main mast of the warships of the late 20th Century. An example of such a ship is the US Navy Arleigh-Burke Class with its tripod mast structure which carries equipment such as the anemometer, antennae, sensors and navigation lights, Figure 4.5.

Figure 4.5: USS Arleigh Burke with tripod mast structure carrying numerous attachments [94]

Since coming into service in 1991, the Arleigh-Burke class has undergone a number of design evolutions and still forms the backbone of the US Navy's destroyer fleet. The close proximity of the various electronic devices on the ship can cause many issues, particularly when designing the operational layout of the ship's mast, in order to prevent electronic interference. In addition, because of the continued development and improvement of radar technology, the design of the warship became geared towards reducing its radar cross section (RCS – a measure of the amount of incoming radar energy that is reflected back to the source). Noticeable changes in superstructure design began to emerge as ship stealth from radar detection became a primary concern, and therefore prominent changes to the shape and size of the main mast structure were seen. Curvature in any form increases RCS by scattering the radar energy in many directions, and therefore the traditional cylindrical pole mast structure is becoming all but obsolete on the modern warship. Masts have

gradually become further integrated with the ship's main superstructure with electronic instruments and radar systems being housed inside large bulky mast structures in a bid to reduce surface clutter that can increase RCS. Known as an enclosed mast, this type of configuration is now popular with the newest warships, helping to not only significantly reduce a ship's overall RCS, but also to decrease structural weight through the use of composite materials, and to improve issues with electronic interference by designing the structure as one all-inclusive unit.

The UK Royal Navy first employed an enclosed mast on HMS Ark Royal, an Invincible class aircraft carrier. The mast, known as the Advanced Technology Mast (ATM), made use of fibre reinforced plastic material to ensure that electromagnetic radiation can pass through, allowing sensors to be housed inside the mast structure and therefore protecting them from the environment [95]. The octogonal tapered cross section of the mast, seen on HMS Invincible in Figure 4.6, gives the structure a large physical footprint, necessary to accommodate all of the systems housed within.

Figure 4.6: HMS Ark Royal with ATM Mast [96]

Similarly, in 1997, the US Navy installed an Advanced Enclosed Mast (AEM) on USS Radford, Figure 4.7, which enables the radar systems housed within it to emit and receive signals through frequency selective material (FSS). More recently, the enclosed mast unit has been designed and built as a stand-alone unit from specialist companies, bought as a standard design and fitted to the ship, an example of which is the integrated mast (I-Mast) as seen on the Holland Class Ocean Going Patrol Vessel in Figure 4.8. The much bulkier, larger footprint

of this type of mast is apparent, even in comparison to the earlier enclosed mast designs of the ATM and AEM/S. Such imposing main mast structures are now commonplace on more recent frigates and destroyers, e.g. the Royal Navy's Type 45 Daring Class destroyer, which will be discussed in more detail below. However, the most recent and most striking change in mast design came in 2016 with the commission of the US Navy Zumwalt Class Destroyer, Figure 4.9, and shown earlier in Chapter1, Figure 1.8. The Zumwalt class was designed with stealth in mind, with no pronounced mast structure and instead opting for a fully integrated deck house with incorporated radar/sensors and equipment. The absence of a mast structure altogether, along with its clean top surfaces and wave-piercing tumblehome design, has resulted in a 190m long warship with an RCS that is so low it resembles that of a small fishing boat.

Figure 4.7: USS Radford – Spruance Class – Upgraded with AEM/S [97]

Figure 4.8: Holland Class Ocean Going Patrol Vessel of Royal Netherlands Navy with I-Mast [98]

Figure 4.9: USS Zumwalt with fully integrated deckhouse structure [99]

Although such innovations in ship mast design are proving very successful in the reduction of a ship's RCS, they are simultaneously creating issues for the safe operation of aircraft in the vicinity of the ship's flight deck. Such large bulky mast structures produce regions of local flow distortion that are so significant, they are having both a direct and indirect effect on aircraft operations. As illustrated in Chapter 3, the mast structures themselves directly

increase turbulence levels in the ship's airwake as the freestream air is pushed around the structure, shedding off its sharp edges, producing a large wake and therefore increasing turbulence levels across the flight deck; they also create a distorted and unsteady air flow, in which the anemometers are likely to be located, producing erroneous readings of the freestream flow at the ship's anemometers. Engineering a solution to achieve an optimal location for the ship's wind measurement systems is, at present, a challenge of increasing difficulty and importance.

4.2. Ship's Anemometers

A ship's wind measurement system is important not only for navigational and meteorological purposes, but it is also critical for determining whether or not the prevailing wind conditions will permit the safe launch and recovery of the ship's helicopter as specified by the SHOL, as discussed earlier in Chapter 1. The anemometer is important for establishing the SHOL in the first place through flight trials, and for every launch and recovery operation thereafter when the WOD conditions need to be measured. As described in Chapter 1, the modern warship utilises ultrasonic anemometers to obtain real-time readings of the prevailing WOD condition, which the personnel in the Flying Control (FlyCo) room on board the ship use to determine whether the wind speed and direction is within the safe limits provided by the SHOL. The traditional placement of anemometers on warship has been on yardarms that come off the main mast and are angled forward. To obtain an accurate reading of the freestream flow condition, the anemometer must be sited in clear airflow that has not been disturbed by nearby structures. If the anemometer is placed in a disturbed air flow, then it is still possible that it can be calibrated in-situ, and a correction made to the displayed reading. However, calibration becomes impractical if the air flow is so turbulent that reliable mean measurements cannot be taken.

4.2.1. Regulations for Combat Ship Wind Measurement Systems

The UK Ministry of Defence (MoD) uses numerous defence standards to inform the design of warships to ensure that each piece of equipment fitted onto the ship is working to the performance levels that are required. For a ship's wind measurement systems, the defence standard DEFSTAN 00-133 Part 2 [86] is used to provide a set of criteria for the ship designers to adhere to for aviation equipment integration, amongst which is the siting and performance of the anemometers. Each defence standard is reviewed regularly, with the current, DEFSTAN 00-133 Part 2, superseding DEFSTAN 08-133 Part 2 [100]. The latter

document was released in 2008 and was reviewed and modified to produce the 2014 edition. A further review is likely to take place within the next few years.

The differences between the 2008 and 2014 documents are subtle, but there is an importance in this comparative discussion as the wording shows a clear change in view by the MoD with regard to the importance of anemometer siting and performance criteria for the modern warship entering into service. Table 4.1 displays the relevant standards defined in each document with the key changes in wording underlined. Key comparative standards has been numbered from 1 – 7 in Table 4.1 to allow for ease of discussion. A shift has been made from clearly defined standards that are to be adhered to, to rather loosely binding standards with a phrasing of, "…should be…". The significance in the use of this terminology is the definition of standards that are now less strict in the sense that they are much closer to a recommendation – they do not 'have to be' adhered to, they now only 'should be'. Given the RCS-driven superstructure designs that are now commonplace for modern warships, the differences between the standards will be made by comparing key statements; the discussion will be in relation to a current warship, the UK's Type 45 Daring Class Destroyer, as well as the GCS.

Table 4.1: Comparison of the two most recent defence standards for ship anemometer placement

Statement No.	**Defence Standard 08 -133 (2008)**	**Defence Standard 00 -133 (2014)**
1	**7.2.10 a)** Anemometers are to be positioned in clear air above the edge of the boundary layer created by the ship's superstructure. The height of the boundary layer is to be determined by model tests, the results of which are to be forwarded to DMSD-INT	**7.4.2.2.1.** Anemometers **should** be positioned in clear air above the edge of the boundary layer created by the ship's superstructure. The height of the boundary layer **should** be determined by model tests.
2	**7.2.10 b)** Anemometers are to be located as high as possible port and starboard, and have a switching facility to enable selection according to wind speed and direction. Consideration should be given to additional anemometer installations as appropriate for larger ships.	**7.4.2.2.2.** Anemometers **should** be located as high as possible on separate port and starboard yardarms, and have a switching facility to enable selection according to wind speed and direction. Consideration **should** be given to additional anemometer installations as appropriate for larger ships.

3	**7.2.10 c)** Anemometers sited on masts are to be in free air in space uncluttered by adjacent equipment, preferably on separate port and starboard yardarms, facing forward with at least 3.0 m radius free air space around each anemometer.	**7.4.2.2.3**. Anemometers sited on masts **should** be in a space uncluttered by adjacent equipment, facing forward with at least 3.0m radius free air space around each anemometer.
4	**7.2.10 d)** Anemometers are to be positioned so that they do not produce unwanted radar reflections and consideration given to the employment of solid state systems	**7.4.2.2.5** Anemometers **should** be positioned so that they do not produce unwanted radar reflections and consideration given to the employment of solid state systems.
5	**7.2.11.2.** Accuracy of Indicators should be as follows: Wind Speed ± 10% error Wind Direction ± 5 degrees error	**7.4.2.2.7** Accuracy of Indicators **should** be as follows: **a)** Wind Speed ± 5% error **b)** Wind Direction ± 5 degrees error
6	**7.2.11.3** Wind flow trials must be carried out in conditions where it is possible, with the use of the ship's engines, to achieve speeds of 45 knots over the bow and 15 knots over the stern.	**7.4.2.2.8** Wind flow trials should be carried out in conditions where it is possible, with the use of the ship's engines, to achieve speeds of 45 knots over the bow and 15 knots over the stern.
7	**7.2.11.4** It is recommended that the vertical component of wind speed is also measured.	**7.4.2.2.9** It is recommended that the vertical component of wind speed is also measured.

Statement 1 refers to an ideal placement of a warship's anemometers above the height of the ship's boundary layer. The ship's boundary layer is referred to in this thesis, and more widely, as the ship's airwake. It is not practical to mount the anemometer on the ship and for it to be outside of the airwake. The bulky non-aerodynamic geometry of the RCS-driven superstructure and main mast increases the height of the ship's airwake to at least that of the height of the mast (as seen earlier, e.g. Figure 3.6). Statement 1, therefore, is unrealistic, although the most recent wording of the statement that the anemometers "should be" placed above the airwake offers some leeway. Statement 1 also refers to model tests that should be conducted to determine the extent of the ship's airwake. Traditionally this has been done by wind tunnel tests (as was the Type 45). The GCS is the first UK destroyer/frigate that has been modelled using CFD; an undertaking which the research reported in this thesis was part of.

Statement 2 requires that there should be two anemometers, one on either side of the ship, and that they should be as high as possible; this latter requirement, as will be shown below, is not currently being fulfilled. Statement 2 also raises the option of additional anemometers; the GCS is the first UK warship that will have an anemometer towards the stern of the ship to measure winds coming from astern, the supporting analysis for this anemometer was also part of the research being reported in this thesis.

Statement 3 requires that each anemometer should be mounted on yardarms off the main mast and should be at least 3m away from surrounding equipment. When this statement was first written it referred to individual pieces of equipment (e.g. sensors, navigation lights) that would be mounted on a more slender mast, such as that on Type 23; it wasn't written to account for the large enclosed mast. At this point it is worth considering the first three statements in relation to the Type 45 destroyer shown in Figure 4.10 The head-on view of the Type 45 shows the proportions of the main mast and, indicated by red squares, the locations of the ship's anemometers. It can be seen that the anemometers are not outside the airwake, or as high as possible, or away from adjacent equipment. The measurement accuracy of the anemometers has been compromised to avoid increasing the ship's RCS and to therefore comply with statement 4.

Figure 4.10: Type 45 Daring Class Destroyer with anemometer locations highlighted [101]

Given the relaxing of the standards for the siting of the ship's anemometers, it is therefore surprising that the release of the 2014 DEFSTAN tightened the required accuracy of the anemometers through statement 5. In the 2008 edition of the standard the required accuracy of the wind measurement system was ±10% in speed, and ±5° in heading (angle). In the 2014 version the required accuracy has been altered to ±5% in speed, and ±5° in heading. As will be seen later, it is difficult enough to meet the 10% desired accuracy on a ship with an enclosed mast, let alone the 5% criterion. At the outset of the wider research programme into the aerodynamics of the GCS, to which the contents of this thesis are contributing, the 2008 standard was current and so, where relevant, the results that are to be presented will be compared with the ±10% and ±5° for wind speed and heading. These criteria have also been retained because the informed judgement of the author is that the more stringent 2014 requirement will have to be reviewed.

The accuracy of the ultrasonic anemometers themselves are very good (±2% in speed, and ±0.5° in heading is claimed by the manufacturers [102]. The measurement inaccuracy comes about from the air flow distortion at the anemometer position. Before a warship enters

service, the efforts to comply with DEFSTAN 00-133 Part 2 are tested through the Air Flow Air Pattern (AFAP) trials that are referred to in statement 6, and specified in detail in an associated defence standard, DEFSTAN 00-133 Part 4 [103]. The ship is taken to sea for a period of time, during which the ship's wind measurement systems are tested relative to reference anemometers that are temporarily placed on slender vertical pole masts, usually at the ship's bow, to obtain a close-to freestream WOD reading. For the modern warship with a large, bulky, enclosed mast structure, the disagreement between the ship's anemometers that are sited within the local flow distortion caused by the mast, and that of the reference anemometer that is in relatively clean airflow, can be significant. As a result of erroneous wind velocity readings caused through local flow distortion, some modern warships currently in service have experienced issues in successfully determining the true WOD condition, as acknowledged in a confidential report on the AFAP trials of the Type 45 [104]. The inability to achieve acceptably accurate readings across the full azimuth can result in a restricted SHOL – an issue which has anecdotally arisen with the Type 45. Effectively, the operational envelope of the helicopter is limited to fewer than necessary WOD conditions, not because the pilot is finding it too difficult to launch and recover, but because the WOD condition cannot be determined with certainty.

From the above discussion it is clear that the pursuit of stealthy warship designs with a reduced RCS has compromised the current method of measuring the ship's relative wind speed and direction, and this can have significant consequences for the ship's helicopter. Anemometer readings are being affected more than ever by the topside aerodynamic disturbances produced from large, bulky, RCS-compliant masts and superstructures. The defence standards written to aid their successful installation for satisfactory performance have not kept up with the design of the modern warship.

4.2.2. An Aerodynamic Assessment of the GCS Anemometer Locations

The wind measurement system on the GCS consists of two main anemometers sited in a traditional configuration on the main mast, supplemented by an additional aft anemometer located on a more slender mast on the roof of the hangar.

Figure 4.11 shows a head-on view of the proposed locations of the port and starboard anemometers positioned on yardarms at the fore of the main mast structure. Figure 4.12 shows in a plan view how the 6m long yardarms are angled at 30 degrees from the centreline of the ship. As can be seen, each yardarm is located relatively low on the mast and in close proximity to large pieces of equipment that are positioned above the bridge deck and on the

port and starboard sponsons (e.g. the large white radomes either side of the mast in Figure 4.11). The similarities in the main mast design shown in Figure 4.11 and that of the Type 45 shown in Figure 4.10 are clear to see.

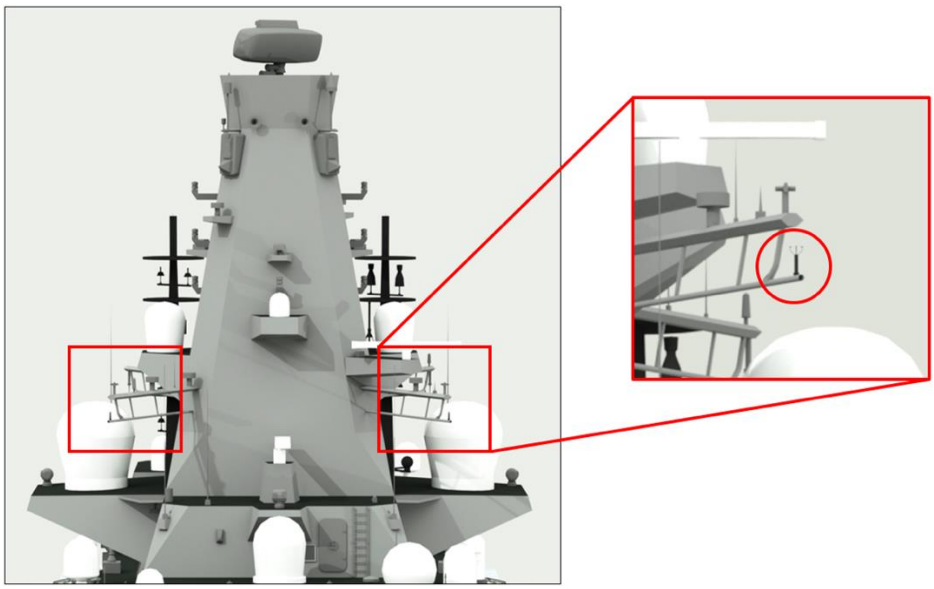

Figure 4.11: GCS main anemometer locations with close-up of anemometer supporting structure [79]

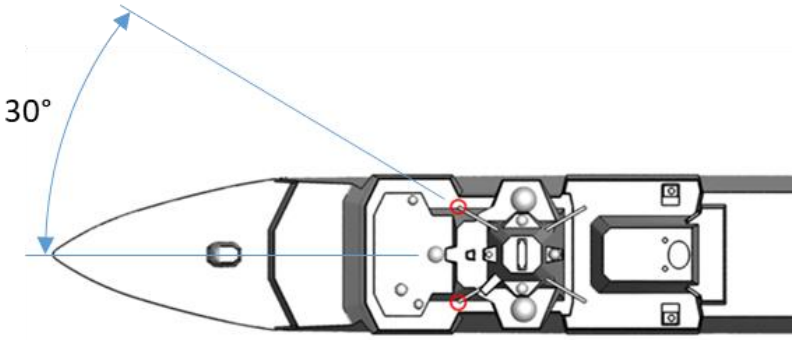

Figure 4.12: Plan view of CGS showing anemometer locations on angled yardarms

There are two anemometers on the main mast, one on each of the port and starboard sides, because when the winds come from, say, the beam (90°), the leeward anemometer will be more affected by the wake of the mast and so it will be expected to give an erroneous reading of wind speed and direction, hence statement 2 in Table 4.1. Also mentioned in statement 2 and discussed above is the aft anemometer; because winds coming from astern will not have passed over the superstructure of the ship, the aft anemometer should be able to be located in a less disturbed air flow. However, as can be seen in Figure 4.13, the proposed location of

the aft anemometer is toward the bottom of a pole mast on a small yardarm, outboard, slightly aft and to port of the pole mast's central axis. The pole mast is mounted on an equipment housing that is on the port side of the hangar roof.

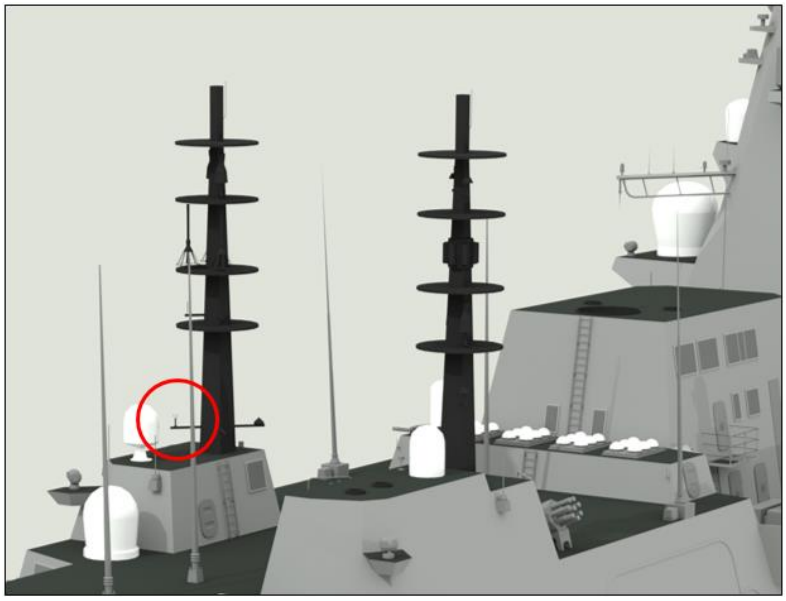

Figure 4.13: GCS rear anemometer location on rear port pole mast [79]

As specified by statement 1 in Table 4.1, the MoD requires that model testing be carried out to analyse the ship's airwake. The research reported in this thesis forms a major part of that analysis and is the first time the UK has conducted a CFD analysis in place of the traditional wind tunnel tests. A comprehensive study has been undertaken to evaluate the local flow behaviour at the proposed anemometer locations on the GCS, as well as possible alternative locations. The unsteady airwake of the GCS has been computed using the time-accurate CFD methodology described in Chapter 2. A total of 31 airwakes have been computed to create a 360° data set in 15° increments, producing a complete assessment of the full azimuth. The first 24 WOD conditions were computed to assess the two main anemometers on the ship's main mast structure, as well as an aft anemometer that was attached to a rear port pole mast of cylindrical cross-section. The initial GCS design incorporated cylindrical section rear pole masts but these were subsequently altered to be RCS-compliant square section pole masts so therefore a further 7 WOD conditions were computed to re-assess the rear anemometer location. All 31 airwake simulations were computed for a nominal relative wind speed of 40 knots.

4.2.2.1. CFD Study of the GCS Main Mast Anemometer Locations

The air velocity approaching the ship changes with height due to the imposed Atmospheric Boundary Layer (ABL); therefore, when considering the wind speed at a particular

anemometer location, the height of that location, and hence the wind speed at that height, should be allowed for. The wind speeds for which the CFD analysis was conducted was 40kts (20.57m/s) which corresponds to a height of 35.94m above sea level (31.31m above the flight deck). As seen in Figure 4.11, the main anemometers are on the forward yardarms that can be seen towards the bottom of the main mast. Preliminary work, partly reported in Chapter 3, revealed that the proposed anemometer locations will be in highly disturbed air flow, so provision was therefore made in the CFD analysis to sample the unsteady velocities at an alternative location higher up the mast to find a height at which the anemometers could be placed above the worst of the air flow whilst still complying with traditional placement standards referred to in Table 4.1. The higher new locations were therefore decided upon by determining the 3D location of the anemometers due to moving the yardarms of fixed length up the tapered mast by 5 metres. The two anemometer locations are therefore not directly vertically above each other, as a result of the mast's tapered structure. The red points in Figure 4.14 show the anemometer positions corresponding to the initial location, whilst the blue points illustrate a location that is 5m higher.

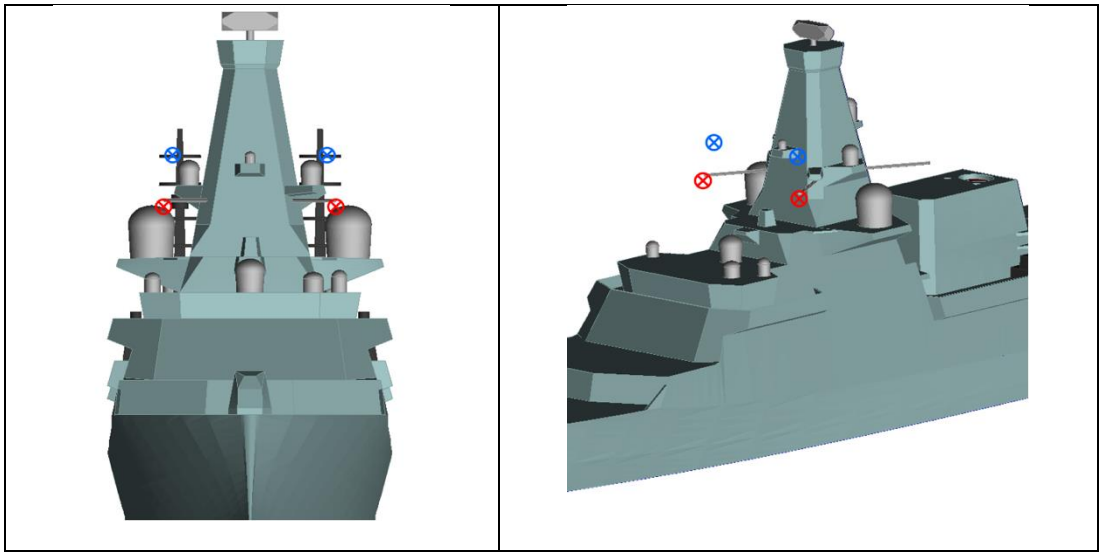

Figure 4.14: Main Anemometer sampling locations on GCS; initial location (red) and +5m location (blue)

To investigate the unsteady three-dimensional flow characteristics around the main mast, sampling points were set within the CFD solution at the port and starboard anemometer positions, at the initial and the higher (+5m) locations. The sampling points, shown in Figure 4.14, were set to capture three-dimensional velocity data over the 30 second sampling period at a frequency of 100 Hz; the mean and RMS values were then calculated for each velocity component. Traditionally, ships' anemometers have not measured the vertical (w)

component of velocity; specified wind speed and direction are conventionally considered in the horizontal plane only, which can be calculated from the streamwise (u) and lateral (v) components, see Figure 4.15. Tables 4.2 to 4.5 show the CFD-derived mean and RMS velocity components at the initial and +5m locations for selected wind angles.

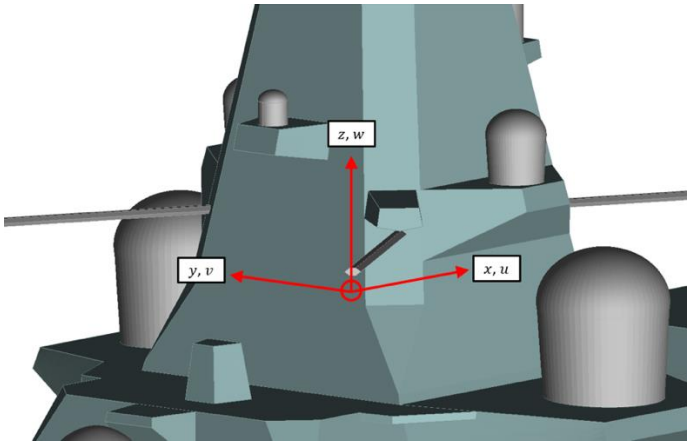

Figure 4.15: Velocity components at initial starboard anemometer location

Table 4.2: Mean velocity components and RMS values (m/s) at initial anemometer position and at +5.0m for a nominal 40kts headwind WOD condition

Headwind				
	Port		Starboard	
Initial Pos.	Mean	RMS	Mean	RMS
Streamwise	17.7	0.6	17.5	1.0
Lateral	-3.5	0.2	3.3	0.5
Vertical	-0.2	0.6	-0.2	0.6
	Port		Starboard	
Initial Pos. + 5m	Mean	RMS	Mean	RMS
Streamwise	17.4	0.1	17.5	0.2
Lateral	-3.1	0.1	3.1	0.1
Vertical	1.4	0.1	1.3	0.2

Looking more closely at the headwind data in Table 4.2 for the port anemometer at the original position, combining the streamwise and lateral velocity components shows that the resultant air velocity in the horizontal plane has a magnitude of 18m/s $\left(\sqrt{17.7^2 + 3.5^2}\right)$ and an angle of 11° $(\tan^{-1}(3.5/17.7))$, this compares with a "true" wind speed at that height of

19.4 m/s and a direction of 0°. For this anemometer in the headwind therefore, the reading can be expected to be in error by −7.4% in magnitude and 11° in heading. The equivalent deviations at the starboard anemometer position are −8.3% and −10.7°. The headwind case is one in which the mast interferes least with the incoming flow, so it can be expected (and will be shown) that the deviations can be worse for other WOD conditions. It can also be seen in Table 4.2 that the vertical velocity components, which would be zero in the freestream, are quite small; but nevertheless the flow is deflected vertically. Comparing the mean velocity components in Table 4.2 for the initial position with the +5m it can be seen that the deviations in the flow are similar at the higher height; however, the turbulence levels are much lower at the higher position. At the +5m positions the resultant velocities in the horizontal plane at the port and starboard anemometer locations are 17.7 m/s and 17.8 m/s respectively, with corresponding headings of 10.2° and −9.9°. At this anemometer height the "true" wind speed is 19.8 m/s so the port anemometer can be expected to be in error by −10.6% in speed and 10.2° in heading, while the starboard anemometer can be expected to have corresponding errors of −10.4% and −9.9°. Considering these data for the two anemometer heights it is evident that the higher position does not present a less distorted flow to the anemometers, although at this WOD the turbulence levels at the higher position are significantly lower, an observation that will be discussed later.

Table 4.3: Mean velocity components and RMS values (m/s) at initial anemometer position and at +5.0m for a nominal 40kts Green and Red 30 WOD condition

	Green 30				**Red 30**			
	Port		Starboard		Port		Starboard	
Initial Pos.	Mean	RMS	Mean	RMS	Mean	RMS	Mean	RMS
Streamwise u	13.3	0.3	12.8	0.1	12.5	0.1	13.5	0.2
Lateral v	-17.0	0.2	-9.4	0.1	9.4	0.1	16.8	0.2
Vertical w	-0.7	0.2	3.1	0.1	3.1	0.1	-0.6	0.3
	Port		Starboard		Port		Starboard	
Initial Pos. + 5m	Mean	RMS	Mean	RMS	Mean	RMS	Mean	RMS
Streamwise u	13.6	0.1	13.5	0.1	13.4	0.1	13.9	0.1
Lateral v	-15.7	0.1	-9.3	0.1	9.4	0.1	15.4	0.1
Vertical w	1.2	0.1	3.3	0.0	3.3	0.0	0.8	0.1

Table 4.4: Mean velocity components and RMS values (m/s) at initial anemometer position and at +5.0m for a nominal 40kts Green and Red 90 WOD condition

	Green 90				Red 90			
	Port		Starboard		Port		Starboard	
Initial Pos.	Mean	RMS	Mean	RMS	Mean	RMS	Mean	RMS
Streamwise u	-0.9	2.8	-5.4	0.1	5.5	0.2	-1.3	3.5
Lateral v	0.7	4.5	-16.6	0.3	17.1	0.6	1.5	5.9
Vertical w	2.1	3.2	7.0	0.4	6.7	0.6	2.4	3.4
	Port		Starboard		Port		Starboard	
Initial Pos. + 5m	Mean	RMS	Mean	RMS	Mean	RMS	Mean	RMS
Streamwise u	-1.3	1.4	-4.1	0.1	-4.1	0.1	-0.7	1.9
Lateral v	-19.8	2.8	18.0	0.2	18.4	0.3	20.3	2.6
Vertical w	4.9	2.0	5.7	0.3	5.5	0.4	4.5	2.2

Table 4.5: Mean velocity components and RMS values (m/s) at initial anemometer position and at +5.0m for a nominal 40kts tailwind WOD condition

Tailwind				
	Port		Starboard	
Current Pos.	Mean	RMS	Mean	RMS
Streamwise u	-12.8	5.5	-9.9	5.5
Lateral v	0.2	2.8	-0.2	2.8
Vertical w	-1.9	3.1	-1.6	3.3
	Port		Starboard	
Current Pos. + 5m	Mean	RMS	Mean	RMS
Streamwise u	-11.5	4.5	-13.4	4.6
Lateral v	-1.9	1.9	1.4	1.9
Vertical w	-2.5	2.1	-2.3	2.4

The data in Tables 4.3 to 4.5 are for Green and Red 30, Green and Red 90 and a tailwind. Calculations and observation such as those discussed above for a headwind can also be made for these wind angles, but the overall situation becomes clearer when looking at the deviations in wind speed and heading for the two anemometer heights around the azimuth in graphical form.

Figure 4.16, and the equivalent (industry standard) polar plot in Figure 4.17, show the expected deviation in wind speed at each initial location of the port and starboard anemometers for the 360° azimuth, 0° representing a headwind. The most significant deviations (approx. 80% to 100%) that can be seen for each anemometer are when the anemometer is in the wake of the main mast; when one of the anemometers is in the mast's wake, the other anemometer will tend not to be, hence the symmetrical graphs for the two anemometers. For some of the wind angles, and for when the anemometer position is not in the mast wake, the computed horizontal velocity component lies within the ±10% limits of the 2008 DEFSTAN; however, there are significant ranges of wind angles where the air speed at neither anemometer is within limits (30°-60°, 165°-195°, 300°-330°). The associated wind angle at each WOD condition are shown in Figure 4.18 and equivalent polar plot, Figure 4.19; this time the DEFSTAN limits are ±5° of horizontal wind angle and, as can be seen, the angular deviations are significant, up to 130° for those wind angles that place one or other of the anemometers in the wake of the mast. The range of wind angles for which both anemometers are outside the DEFSTAN heading limits is even greater than for the wind speeds.

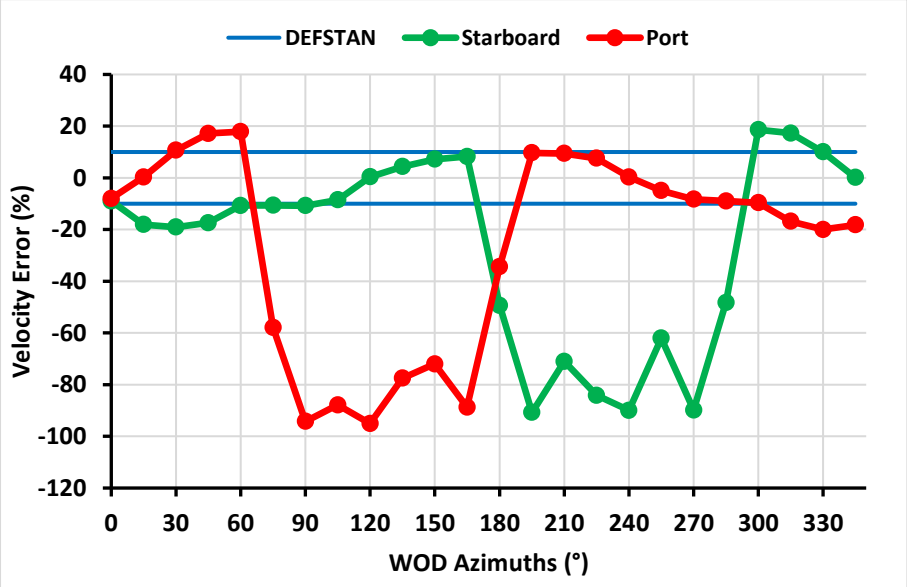

Figure 4.16: Predicted mean horizontal velocity magnitude deviation at initial anemometer height

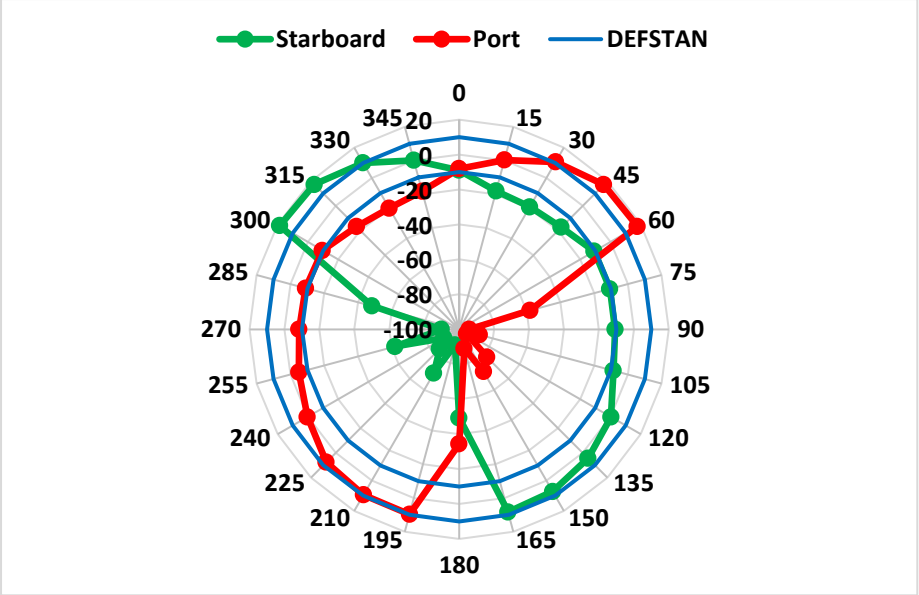

Figure 4.17: Polar plot of the predicted mean horizontal velocity magnitude deviation at initial anemometer height

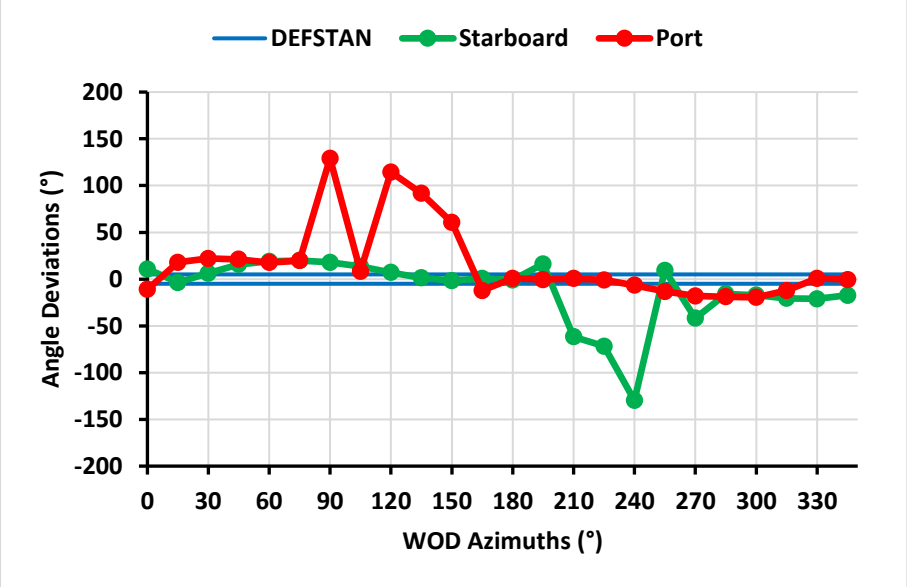

Figure 4.18: Predicted horizontal angular deviations from the mean horizontal angle at initial anemometer height

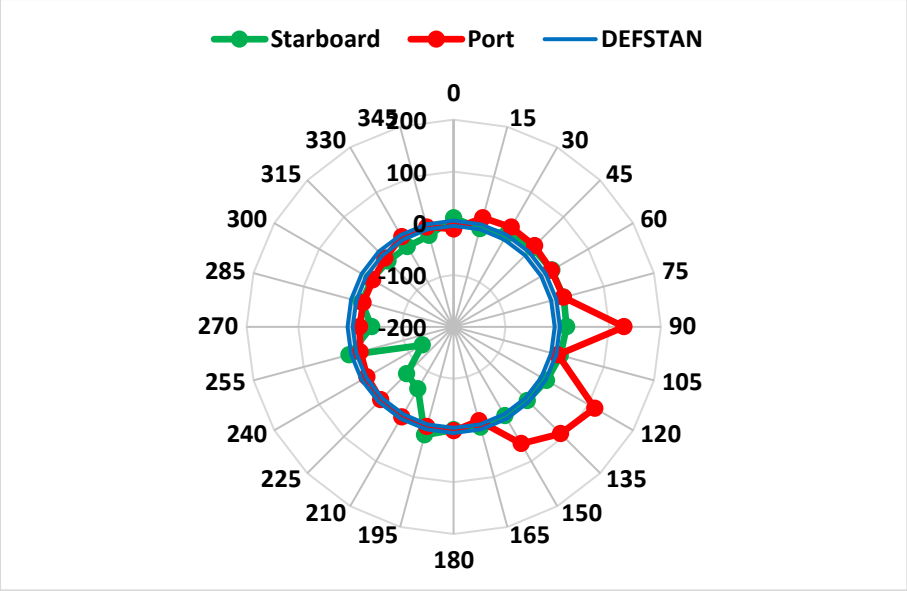

Figure 4.19: Polar plot of the predicted horizontal angular deviations from the mean horizontal angle at initial anemometer height

When the anemometer yardarms are raised by 5 metres the velocity magnitude deviations are as shown in Figure 4.20 and the equivalent polar plot, Figure 4.21; the angular deviations are shown in Figure 4.22 and the equivalent polar plot, Figure 4.23. As can be seen, the angular ranges where the anemometer readings are very significantly in error are considerably reduced; this is because at the +5m height there are fewer objects on the superstructure to disturb the flow and the mast section is narrower, as seen earlier in Figure 4.14. Nevertheless, there are significant angular ranges for which both anemometers will experience deviations that exceed the DEFSTAN limits, particularly in heading.

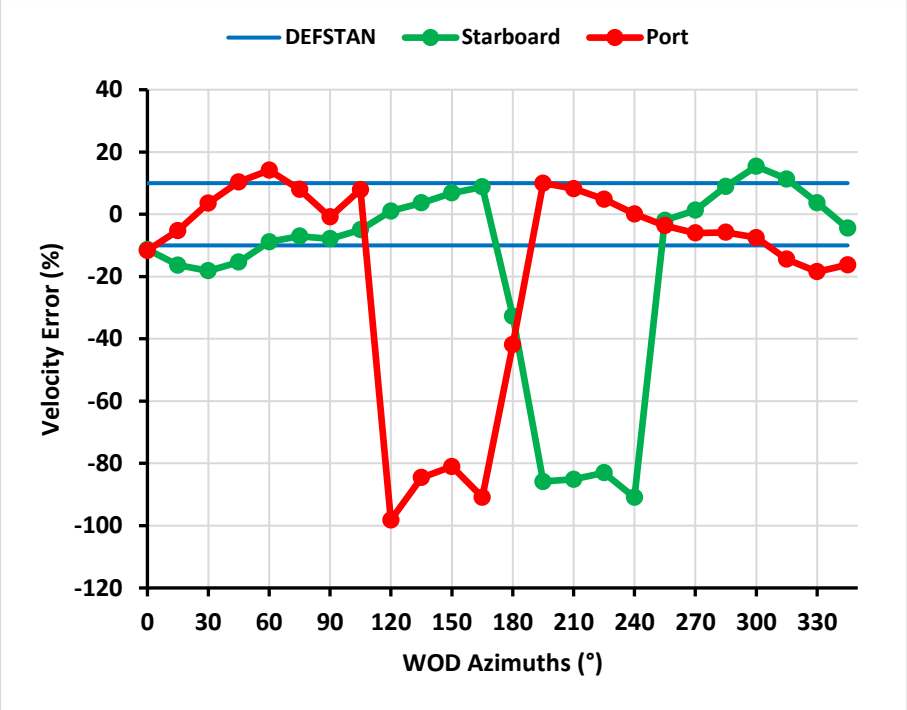

Figure 4.20: Predicted mean horizontal velocity magnitude deviation at +5m height

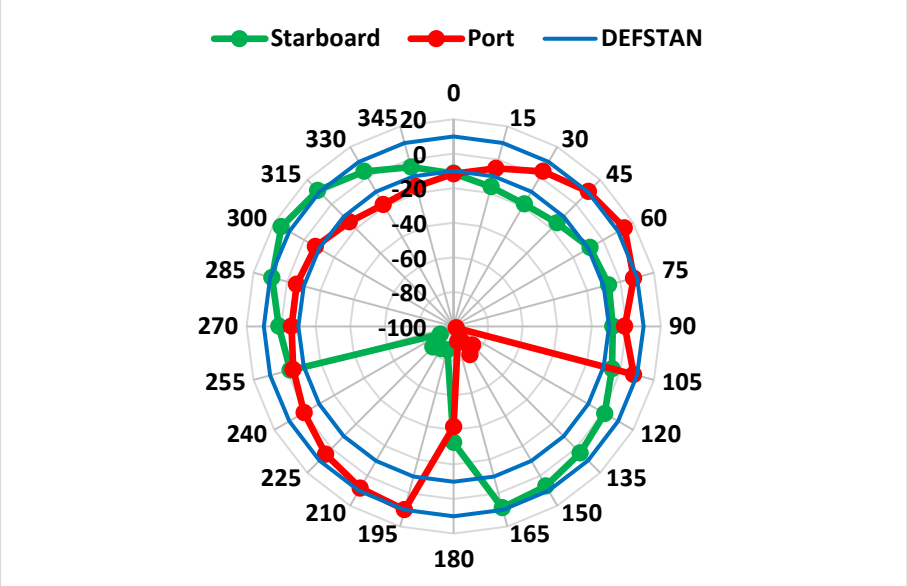

Figure 4.21: Polar plot of the predicted mean horizontal velocity magnitude deviation at +5 metres height

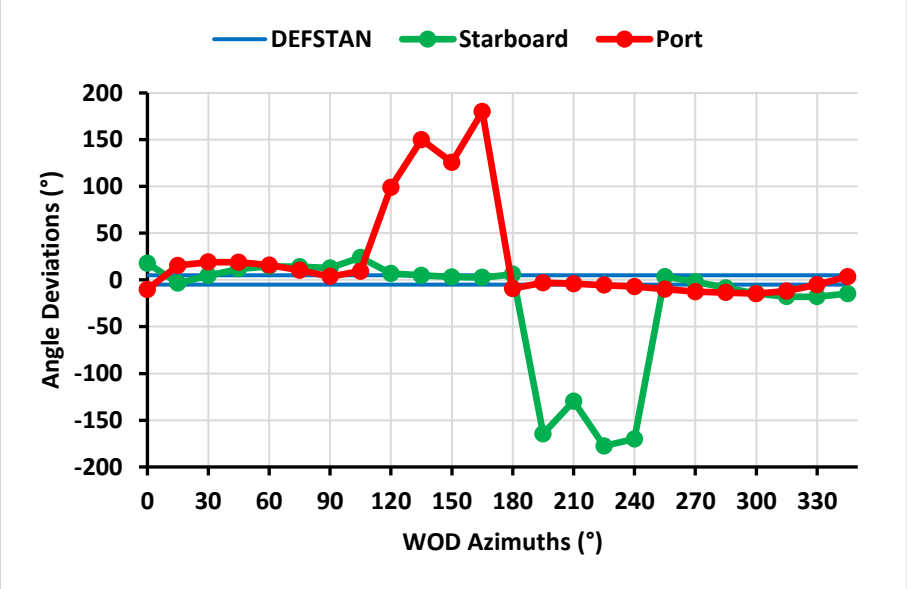

Figure 4.22: Predicted angular deviations from the mean angle at +5 metres height

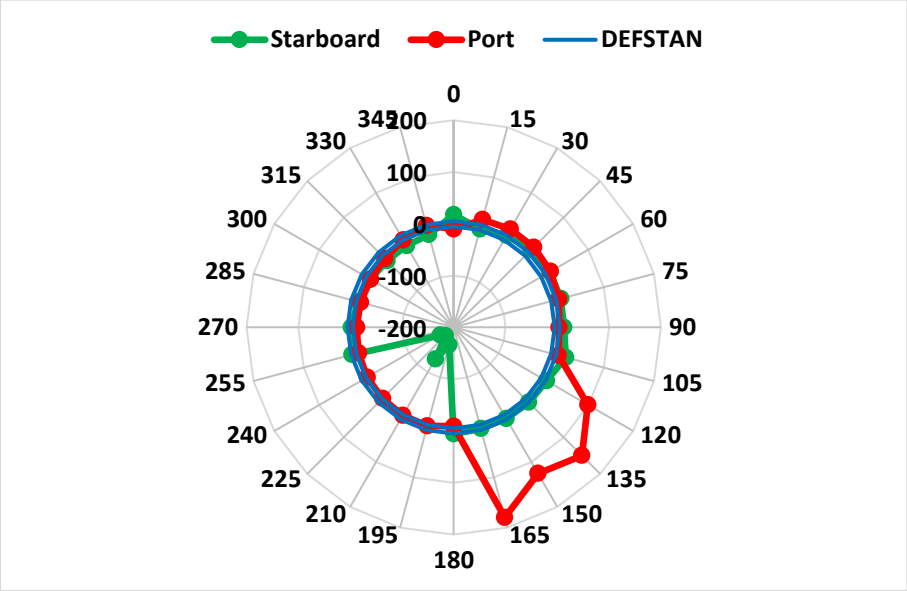

Figure 4.23: Predicted angular deviations from the mean angle at +5 metres height

Additional information from the CFD which can be used to compare the anemometer locations at the initial and +5m heights are the vertical velocity components. Figure 4.24 shows the vertical velocity component at the initial anemometer locations, and Figure 4.25 shows the vertical component at the +5m locations. Apart from the tailwind condition, there is a significant upward vertical velocity component at all four locations because the air flow over the ship is deflected upwards over the superstructure.

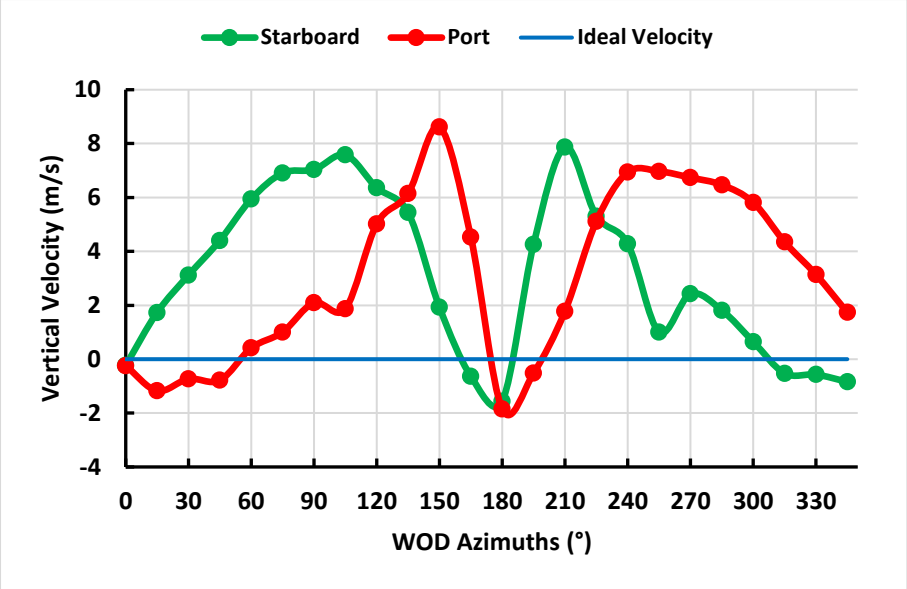

Figure 4.24: Predicted vertical velocity component at initial anemometer locations

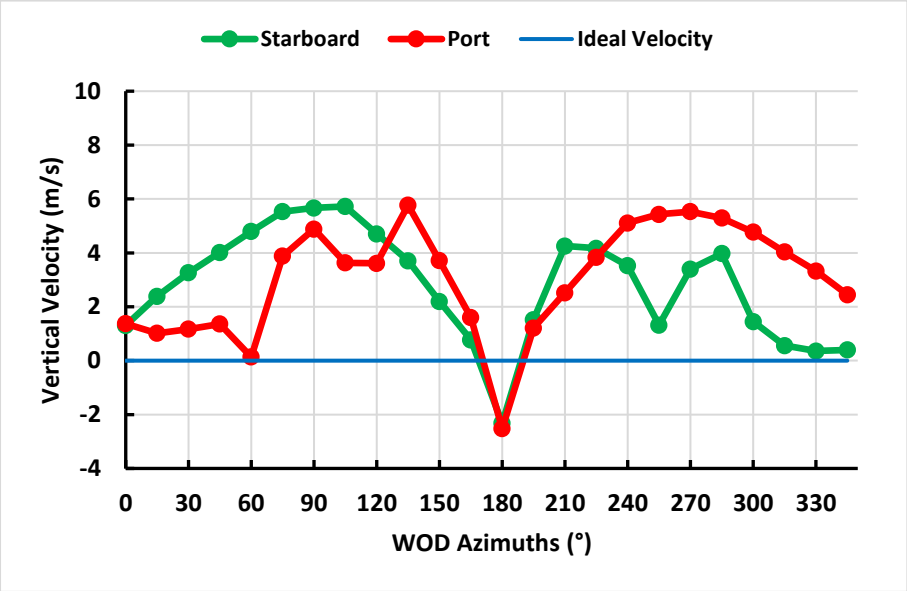

Figure 4.25: Predicted vertical velocity component at +5m height

As well as the deviations in the mean values of wind speed and angle, there is also the unsteadiness in the flow to consider. A repeatable mean reading that differs from the true mean may be corrected through calibration during at-sea AFAP trials. Tables 4.2 to 4.5 show the RMS values for the specified wind angles and, in general, the RMS, or turbulence, is reduced at the higher positions due to there being less disturbance from the superstructure and local equipment. This is demonstrated more clearly in Figures 4.26 and 4.27; the figures show the computed RMS values in the three velocity components at the port and starboard

anemometer location, at the two heights. Also shown is the total turbulence intensity, i.e. the combined RMS values, normalised by the nominal freestream velocity of 40kts (20.576m/s). Comparing first the profiles of the port and starboard locations it can be seen, across the board, that the port anemometer is in more turbulent flow from 60° to 180°, and the starboard anemometer is in turbulent flow from 180° to 300°, again reflecting how when one anemometer is affected by the unsteady flow being shed from the mast, the other one is in less disturbed air flow. The other observation to be made is that the overall turbulence intensity at the higher locations is lower than at the original locations, for the reasons discussed above. At the initial locations the turbulence intensity is up to 30%, while values of 15% are more typical at the higher locations. As was seen earlier in Figures 4.16 to 4.23, the deviations in the air flow at the anemometer locations do not comply with the DEFSTAN, however, due to the steady nature of the air flow at the higher position it may be possible to correct the anemometers through in-situ calibration.

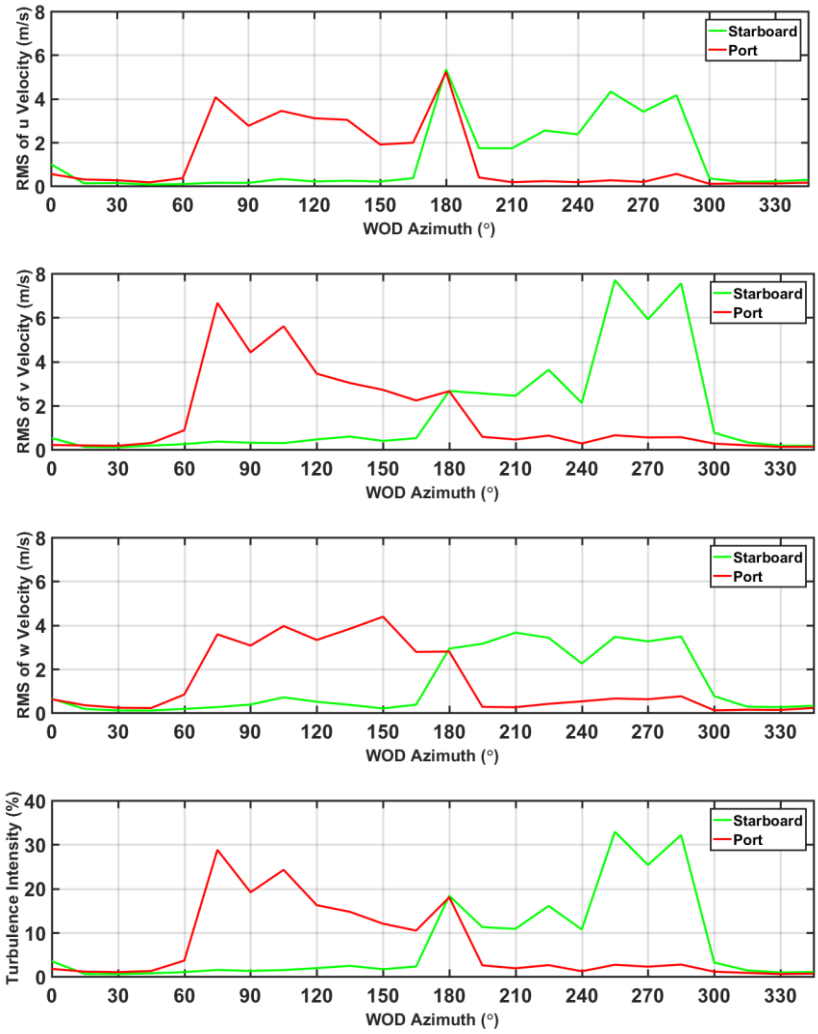

Figure 4.26: RMS velocities and total turbulence intensity at the initial main anemometer locations on GCS around azimuth

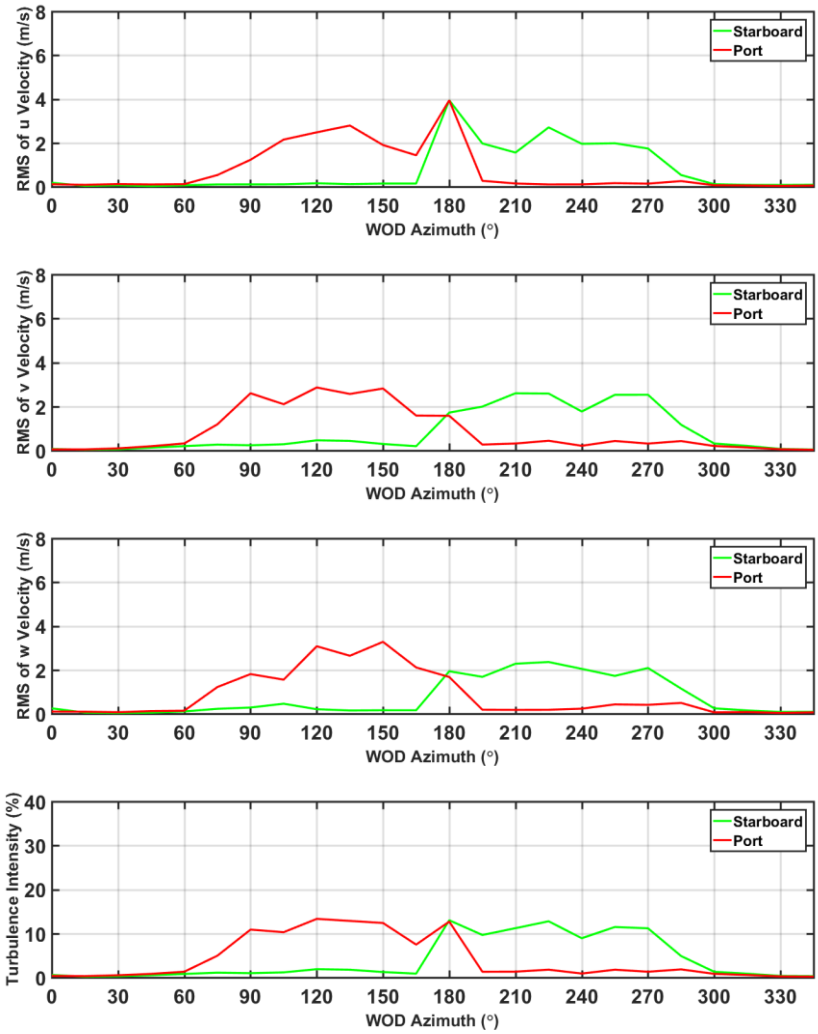

Figure 4.27: RMS velocities and total turbulence intensity at the +5 metre main anemometer locations on GCS around azimuth

More information of the air flow at the anemometer locations can be obtained from the detailed CFD analyses. Figures 4.28 to 4.32 illustrate the air flow field at the main anemometer locations as vectors of velocity and contours of total turbulence intensity for a headwind, Green 30, 90 and 135 and a tailwind. Considering first Figure 4.28 for a headwind, the top figure shows the flow field in the horizontal plane through the initial anemometer locations, the middle figure shows the same but in a plane through the higher +5m height and the bottom figure shows the flow field in a transverse vertical plane through the original anemometer locations and with the higher anemometer locations also shown (which will be in a slightly different plane due to the tapered mast). The bottom image is the view from the front of the ship so that the mast can be included in the image; this means that for the top two images the port and starboard anemometer locations are on the left and right side while on the bottom image they are on the right and left respectively. It should be pointed out that

the black clusters of velocity vectors in the top figure are because the plane is close to the yardarms and the port and starboard radomes where the near-surface CFD mesh is finer and therefore the velocity vectors are more dense; i.e. the black areas are due to the computational mesh, not the flow field. In fact, in the headwind the flow field at the two heights is not that different, as was seen earlier in Table 4.2 and can also be seen in the bottom image. The top two images show how the air flow at the anemometer locations has a low level of turbulence and has been diverted laterally to flow around the mast (typically ±10° as discussed earlier). The bottom figure shows that the turbulence created by the ship superstructure ahead of the anemometer locations does not impact on the anemometers although, as shown earlier in Figures 4.24 and 4.25, the flow has been deflected upwards. The velocity vectors in the bottom figure are in the vertical plane, i.e. they are a combination of v and w, which in a headwind are low, hence the short vectors.

Figure 4.29 shows the velocity field for a Green 30 WOD. Looking at the top image it can be seen that the flow has deviated significantly from the incoming 30° and, referring back to Fig. 4.18 it can be seen that at this angle the flow at the initial port anemometer location has deviated by about 25° in heading. Figure 4.18 also shows that the starboard anemometer has deviated by about 5° and, although not discernible on Figure 4.29, the flow direction at the starboard anemometer can be seen to be closer to the incoming flow angle. Looking at the middle image, it can be seen that the situation is similar at the higher +5m locations, although from the bottom image it can be seen that the flow at the starboard anemometers has a significant upward velocity component, while the flow in that plane is essentially horizontal at the port anemometers (on the right in bottom image), consistent with Figures 4.24 and 4.25. It can also be seen in Figure 4.29 that the flow at the anemometer locations has low turbulence, consistent with Figures 4.26 and 4.27.

Figure 4.30 shows the flow field for a Green 90 (beam) wind. It can be seen in the top image that the local superstructure geometry has created a significantly turbulent region in the proximity of the port anemometer at its initial height; looking back at Figures 4.16 and 4.18 it can be seen that flow is significantly disturbed in both speed and direction. Figure 4.26 also showed that the port anemometer is in highly turbulent flow while the starboard anemometer is in relatively steady flow. The middle image in Figure 4.30 shows that the while the port anemometer is still in turbulent flow at the +5m location it is not as bad as at the initial location and the vectors show the flow direction is closer to the incoming heading. The bottom image shows how the port (right in image) anemometers are in the turbulent shear layer formed by the flow separating from the leeward edge of the superstructure.

Figure 4.31 shows the flow field for a Green 135 wind, i.e. at an angle of 45° from the stern. It can again be seen that the starboard anemometer is in a relative steady air flow, while the port anemometer is in the turbulent wake of the mast. Looking at the bottom image it can be seen that the port anemometers (right on image) are completely immersed in the mast's wake and the flow is significantly distorted in the vertical and horizontal planes. It is this flow that is responsible for the deviations of 100% seen in the flow speed and 100° in the flow angle seen earlier in Figures 4.16 and 4.18 respectively.

Finally, for this discussion of the CFD flow field at the anemometer locations, Figure 4.32 shows the results for a tailwind. It is clearly seen that the two anemometers are in the turbulent shear layers formed by the wind separating from the mast and the highly disturbed flow is the reason why the main anemometers are ineffective in a tail wind and why an aft anemometer is also being considered for winds from astern.

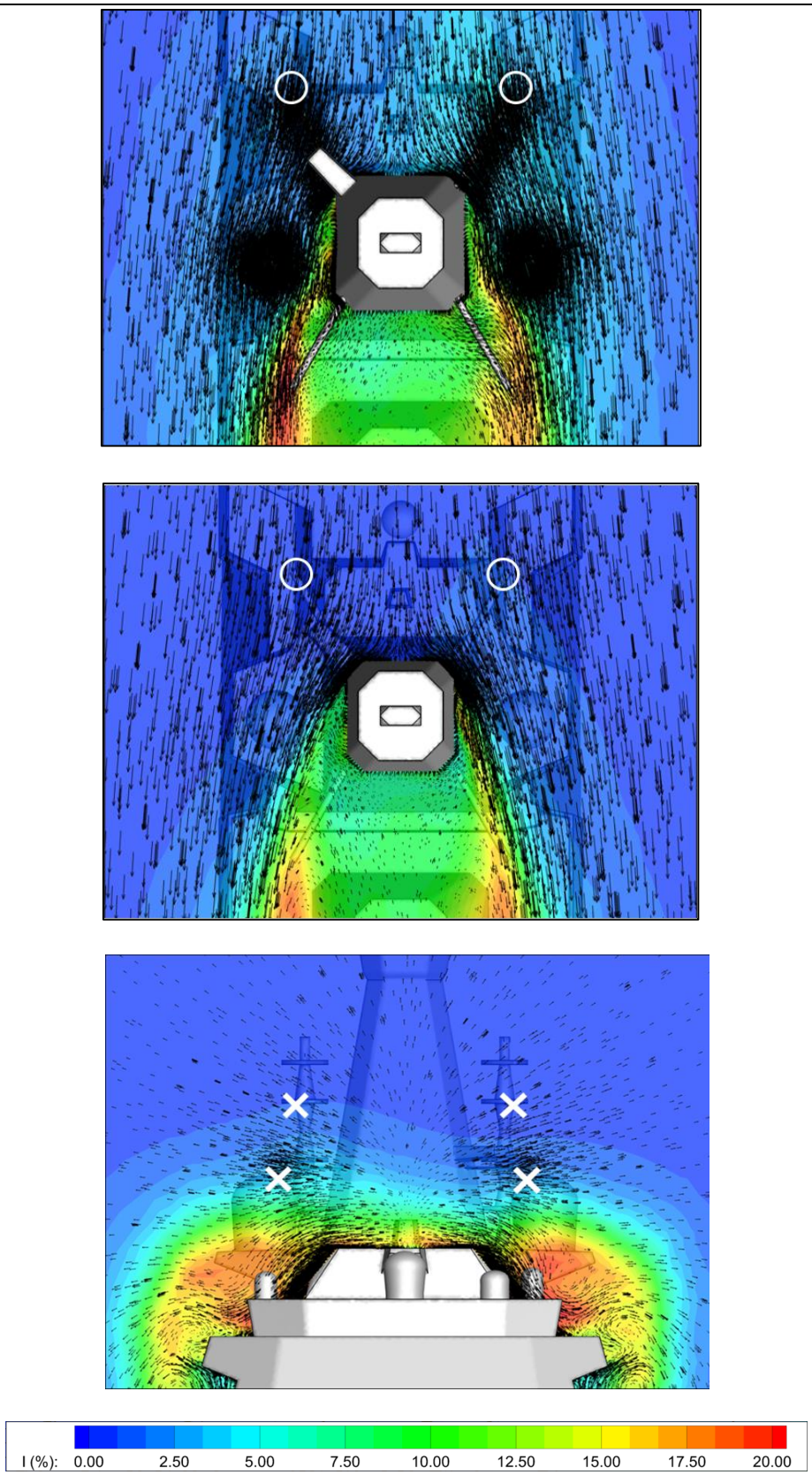

Figure 4.28: Contours of turbulence intensity with vectors of velocity magnitude in a nominal 40 knot headwind WOD condition at initial anemometer height (top), anemometer height +5m (middle) and in vertical plane (bottom)

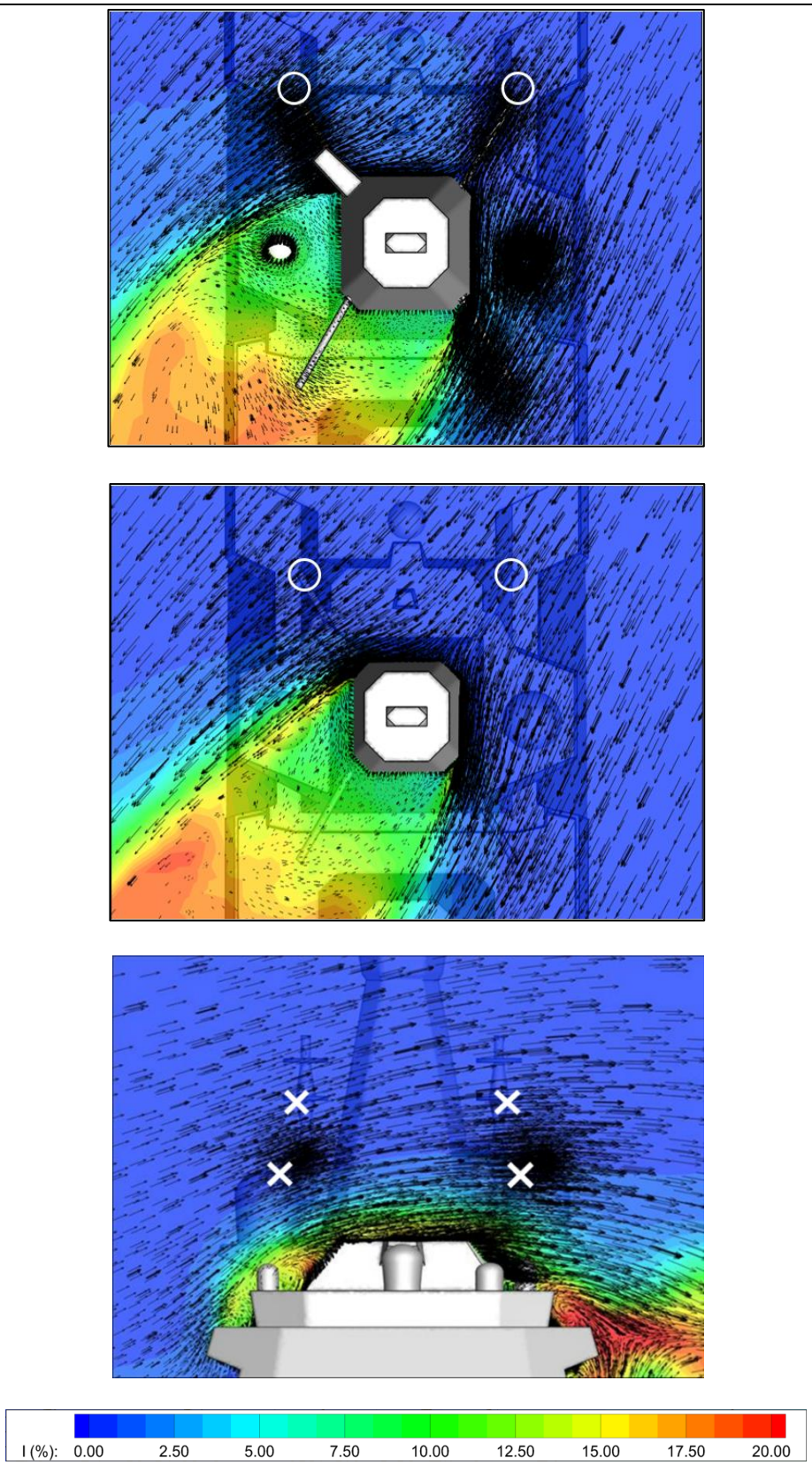

Figure 4.29: Contours of turbulence intensity with vectors of velocity magnitude in a nominal 40 knot Green 30 WOD condition at initial anemometer height (top), anemometer height +5m (middle) and in vertical plane (bottom)

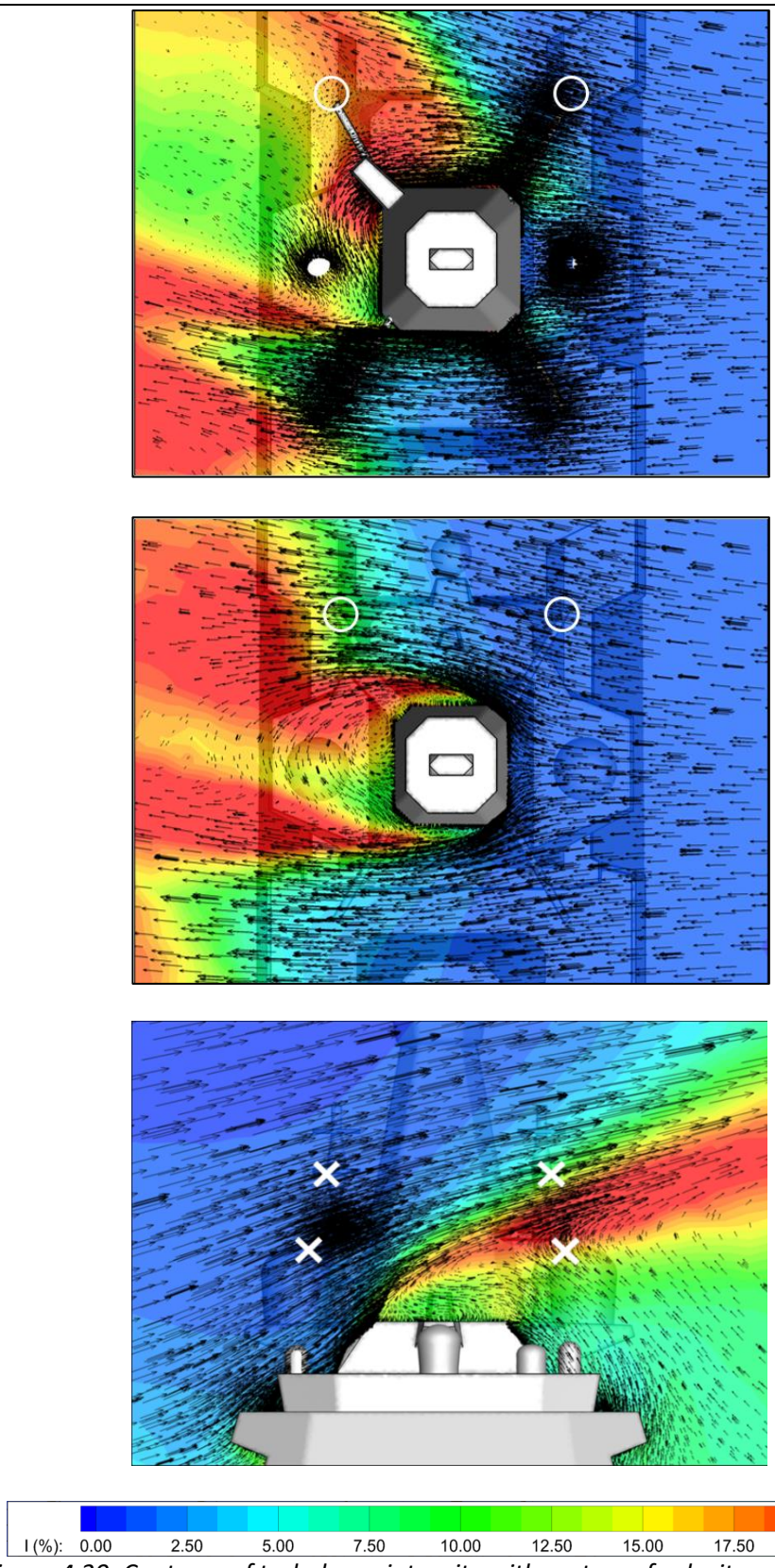

Figure 4.30: Contours of turbulence intensity with vectors of velocity magnitude in a nominal 40 knot Green 90 WOD condition at initial anemometer height (top), anemometer height +5m (middle) and in vertical plane (bottom)

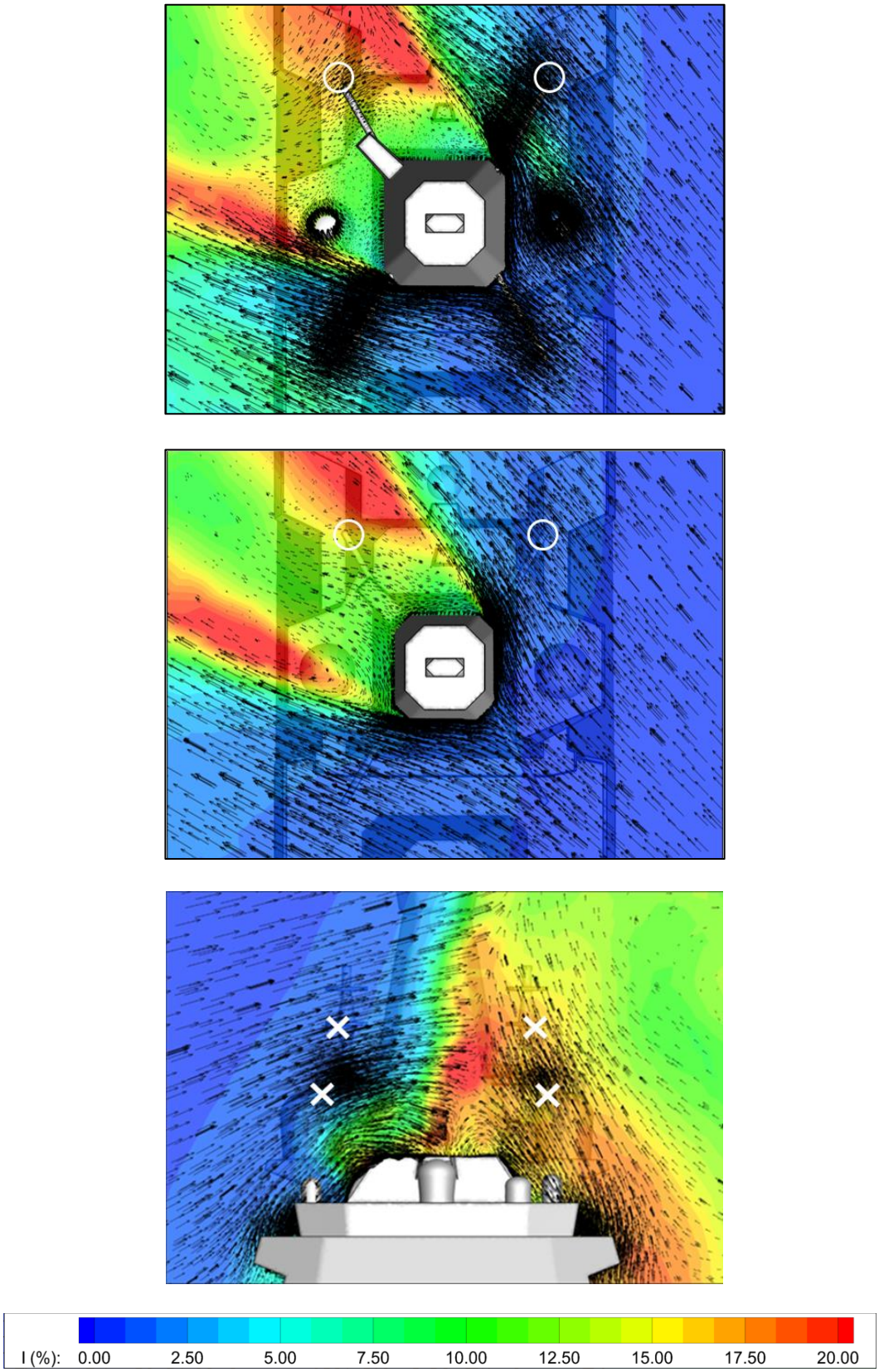

Figure 4.31: Contours of turbulence intensity with vectors of velocity magnitude in a nominal 40 knot Green 135 WOD condition at initial anemometer height (top), anemometer height +5m (middle) and in vertical plane (bottom)

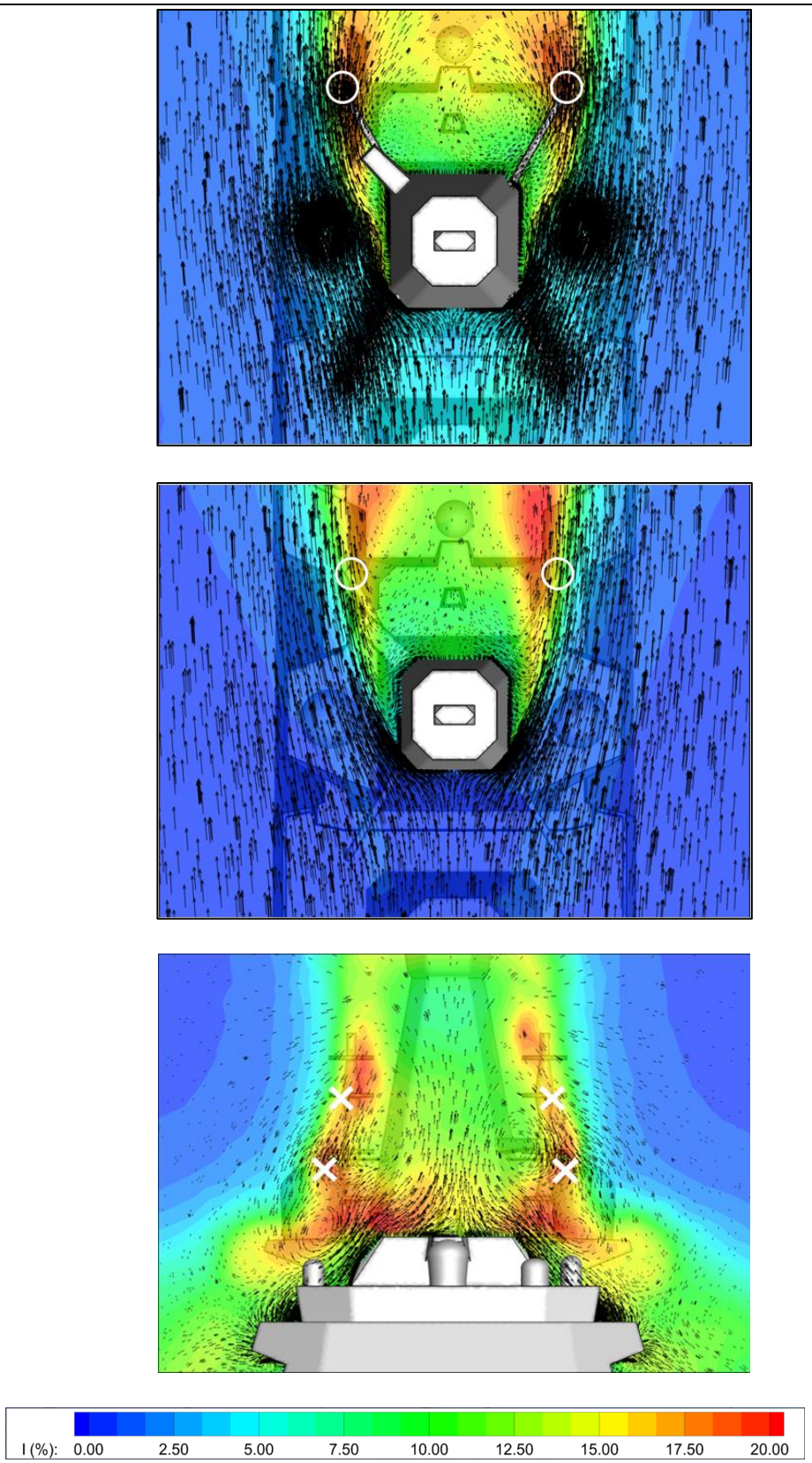

Figure 4.32: Contours of turbulence intensity with vectors of velocity magnitude in a nominal 40 knot tailwind 180° WOD condition at initial anemometer height (top), anemometer height +5m (middle) and in vertical plane (bottom)

A ship's mast is a bluff body, i.e. it presents a significant obstacle to the flow and, as seen in the CFD images discussed above, it creates a significant wake, unlike a streamlined body such as an aerofoil. One characteristic of a regular bluff body, for example a cylinder in cross flow, is that the flow separating from the sides of the body does so periodically creating an effect known as the von-Kármán vortex street whereby the eddies shed from the cylinder do so at a regular frequency for a given speed of the incident flow (see Figure 3.30). At higher Reynolds numbers the frequency of vortex shedding is described by a constant Strouhal number St:

$$St = \frac{f\ D}{V} \tag{4.1}$$

Where f is the shedding frequency, D is the characteristic diameter, and V is the incident velocity.

The main mast on the GCS is not a regular bluff body; it is a tapered structure that has a square cross section with chamfered corners. It has a width at its base of 9m, a height of 14.8m and a width at the top of 3.2m; the surface slope is 11°. While there is a lot of published information on the flow past bluff bodies, the geometry of the mast makes it a very non-standard shape. Furthermore, the flow approaching the mast is already complex due to the ship superstructure and the ABL. Nevertheless, it was noted that in winds from astern, such as the Red 135 and the tailwind shown in Figures 4.31 and 4.32, one of the anemometers is immersed in the wake and therefore the velocity at this point could be sampled at a frequency of 100Hz for the 30 seconds of computed unsteady airwake. The opportunity was taken, therefore, to investigate the frequency of the flow shedding from the mast and to compare it with what related information could be found in the literature.

For a square cylinder the values of St at high Reynolds number is 0.13 [105]. However the mast does not have a constant or a square cross section. Tamura & Miyagi [106] showed that the Strouhal number (St) can increase to about 0.17 for a square cylinder with chamfered corners, and that for incident angles between 0 and 30° the value of St reduced to 0.14. The effect of the mast taper will also alter the vortex shedding frequency because, as it narrows, Eqn. 4.1 shows that the frequency can be expected to increase. This fact is sometimes used to reduce the wind loading on tall buildings since in a tapered building the change in the natural frequency of shedding up the height of the building prevents coherent vortex shedding and reduces the likelihood of resonant unsteady wind loads. Kim & Kanda [107] have shown that for a tall building with a taper on the side of about 3° the value of St

decreases from 0.13 to 0.09 at increased height up the structure, and that the spectrum of the unsteady loads on the building become weaker and broader.

Figure 4.33 shows how the computed lateral, v, velocity component varies with time at the starboard anemometer in a Red 150 WOD. Although it can be seen that there could be some periodicity in the fluctuating velocity, the FFT of the data in Figure 4.34 shows that there is no single dominant vortex shedding frequency. However, returning to the previous discussion about the range of shedding frequencies that can be expected from a modified square cylinder, if the ideal St value of 0.13 is adopted then at the anemometer height on the mast a shedding frequency of 0.43 Hz is obtained, which is in the middle of the spread of dominant frequencies shown in Figure 4.34, indicating that the vortex shedding is highly irregular, but within a range that can be expected for a mast of this size and shape.

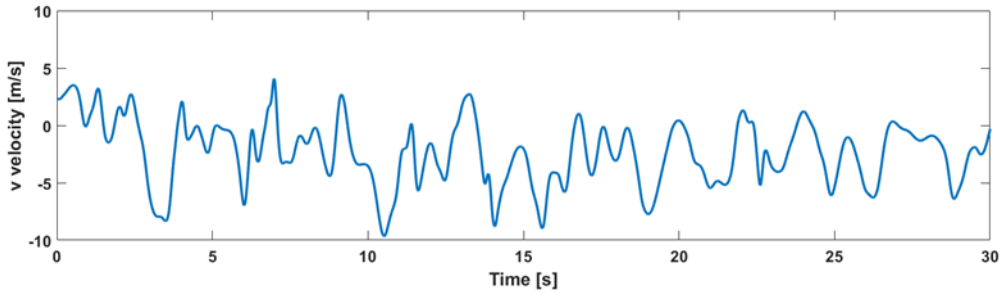

Figure 4.33: Time history of lateral velocity component at starboard anemometer location

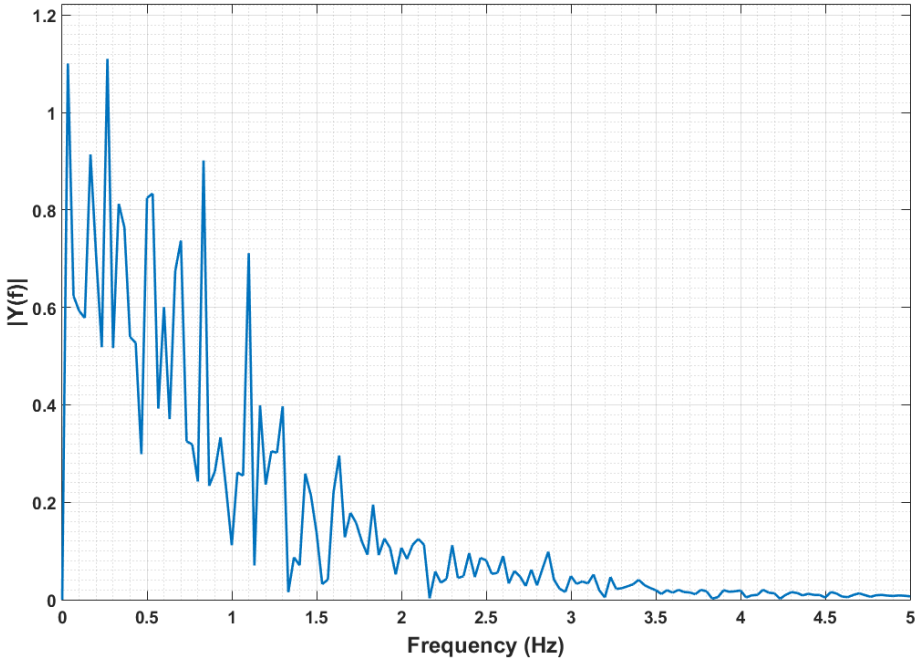

Figure 4.34: FFT of lateral velocity component at starboard anemometer location

4.2.2.2. CFD Study of the GCS Aft Anemometer Locations

It is clear from the previous section that winds from astern are particularly problematic for the GCS's main anemometers as they are effectively in the lee of the large main mast. As already indicated, the DEFSTAN makes provision for additional anemometers to be installed and so the GCS will be the first UK frigate/destroyer to be fitted with an aft anemometer. Figure 4.13, discussed earlier, shows one of the proposed locations of the aft anemometer. The two pole masts in the image are located on equipment housings on the roof of the hangar, just forward of the landing deck. It can be seen that the location, low on the mast and close to other equipment, is far from ideal.

At the time the analysis of the air flow at the aft anemometer began, the GCS design incorporated circular section pole masts, with the anemometer located as shown by the red circle in Fig. 4.35, which is a view of the ship from astern. The anemometer is located on a short yardarm and is positioned alongside the pole mast on its inboard side. Using the methodology described above for the main anemometers, the unsteady velocity components were computed for the anemometer location to determine the flow conditions at that point for winds coming from astern (tailwind ±45°). However, there was then a design change such that the masts were now a tapered, square cross-section pole mast for reduced RCS; there were also changes to the local superstructure. A decision was also made to locate the aft anemometer at one of the two locations shown in Fig. 4.36. The CFD study for the aft anemometer therefore considered these three locations, i.e. one for the cylindrical mast and two for the square section mast. The anemometer on the square pole mast is supported by a short yardarm angled 45° aftwards (as seen earlier in Fig. 4.13). Studying the air flow for two pole masts gave an opportunity to assess the consequences, if any, of the different masts.

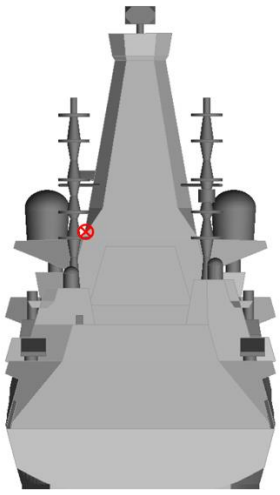

Figure 4.35: Aft anemometer sampling location on cylindrical pole mast (red)

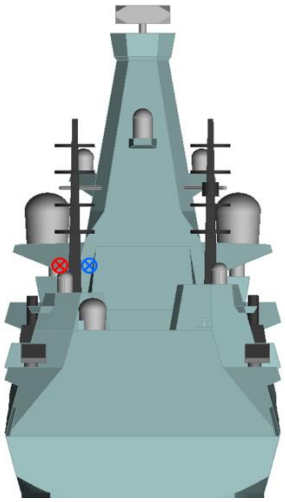

Figure 4.36: Aft anemometer outboard (red) and inboard sampling locations (blue)

The aft anemometer is located on a more slender mast and, with careful positioning, it could be located in relatively undisturbed air flow approaching the ship from astern. Figure 4.37 shows the ship airwake, illustrated by the normalised streamwise velocity component, for a 180 degree wind (tailwind); as can be seen, the flow over the stern of the ship and in the vicinity of the rear pole mast above the hangar is relatively undisturbed as it rises above the superstructure. At the top of the pole mast the contours indicate the wind speed is close to the nominal freestream 40kts; however, as indicated in Figures 4.35 and 4.36 the proposed locations of the aft anemometer are not at the top of the mast.

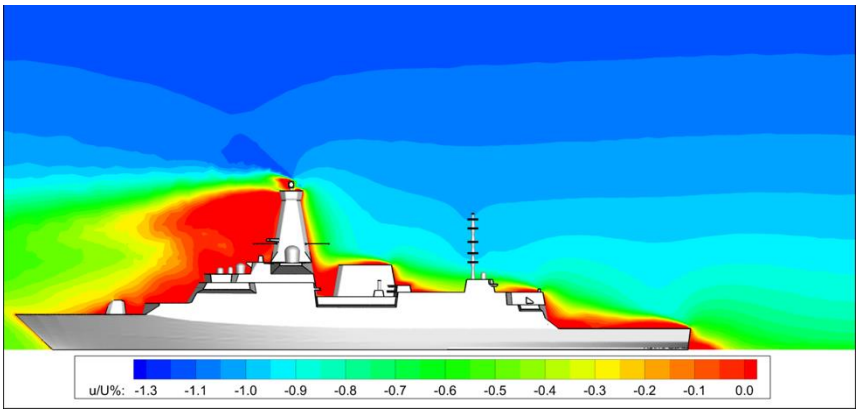

Figure 4.37: Contours of normalised longitudinal velocity in a tailwind at 40 knots

Figure 4.38 shows the percentage difference between the air velocity magnitudes in the horizontal plane and that in the undisturbed flow for “true” wind directions 135° to 225° (Green 135 to Red 135). The purple line shows the percentage difference at the anemometer position on the cylindrical pole mast while the green and red lines line correspond to the

inboard and outboard anemometer locations on the square pole mast. The error bars on the data points show the standard deviation in the data due to the unsteadiness in the flow (i.e. turbulence). The blue band shows the maximum tolerance according to DEFSTAN 00-133 Part 2, of ±10%. Figure 4.39 shows the angular deviation from the "true" wind direction for the three anemometer locations, including the DEFSTAN limits of ±5°.

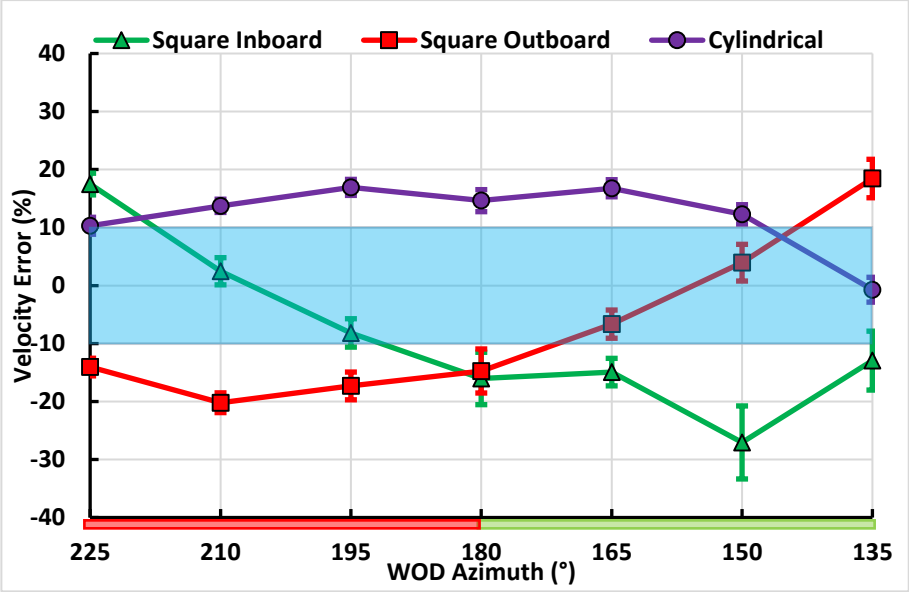

Figure 4.38: Comparison of the predicted deviations in mean horizontal velocity magnitude at aft anemometer locations for cylindrical and square mast cross-section

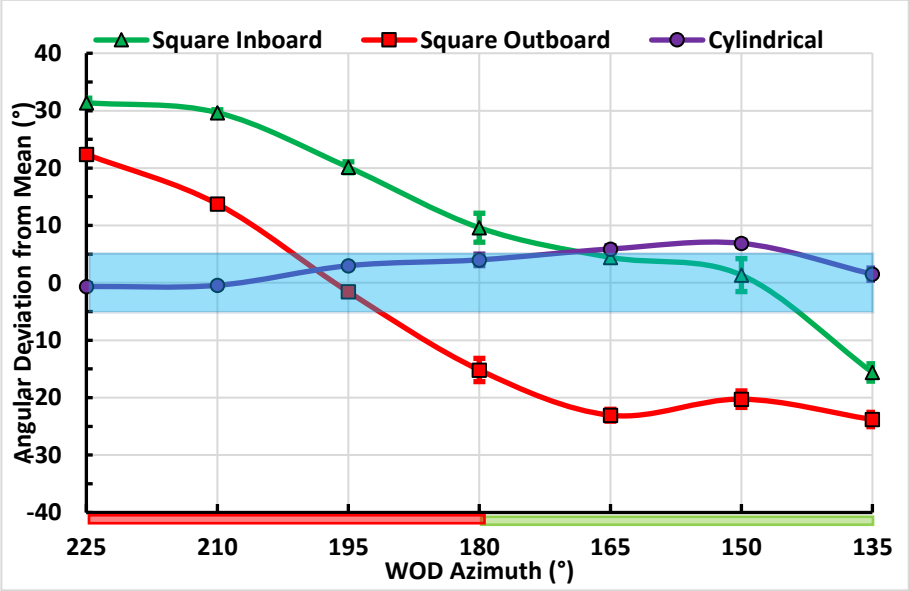

Figure 4.39: Comparison of the predicted deviations in mean horizontal wind angle at aft anemometer locations for cylindrical and square mast cross-section

It can be seen in both Fig. 4.38 and 4.39 that the flow at the anemometer location on the cylindrical pole mast is much closer to the DEFSTAN requirements; it also has a low turbulence as indicated by the error bars. In contrast, deviations in both the velocity magnitude and direction for air flow at the two anemometer locations on the square mast are significantly outside of the required limits; the flow is also more unsteady. The reasons for these observations can be seen in the CFD flow field, which will be discussed using data for Green 135, Tailwind (180°), and Red 135.

Figure 4.40 shows the velocity field in a horizontal plane through the anemometer locations for the GCS with cylindrical and square pole masts for a Green 135 WOD; the ship bow is to the left and the stern to the right. Comparing Fig. 4.35 and 4.36, the height of the sampled anemometer position for the cylindrical mast is higher than that of the square mast, therefore in Fig. 4.40 the plane of the cylindrical mast CFD image is higher than that of the square mast. The arrows illustrate the magnitude and direction of the flow, and the coloured contours refer to the velocity magnitude in the horizontal plane. The anemometer positions are indicated as white circles; for the square pole mast the two positions represent the inboard and outboard locations, and it can be seen that they are angled at 45°. The velocity magnitude is normalised by the “true” wind speed at main anemometer height; therefore, contours greater or less than 1.0 represent wind speeds that are higher or lower than the freestream value, respectively. Looking at the inboard anemometer for the square pole mast it can be seen that in this wind the normalised air speed at the inboard anemometer location is less than 1.0, and at the outboard location it is greater than 1.0, which corresponds with the velocity error at this angle on Figure 4.38. It can also be seen in Figure 4.40 that the square mast creates a wider wake than does the circular one, and the lower position of the anemometer places it in more disturbed flow. Figure 4.41 shows the same flow field in vertical planes through the anemometer positions, viewed from astern; in this case the contours represent turbulence intensity. It can be seen that the lower anemometer locations on the square mast are in more turbulent air flow, and this is reflected in the wider error bars in Figures 4.38 and 4.39.

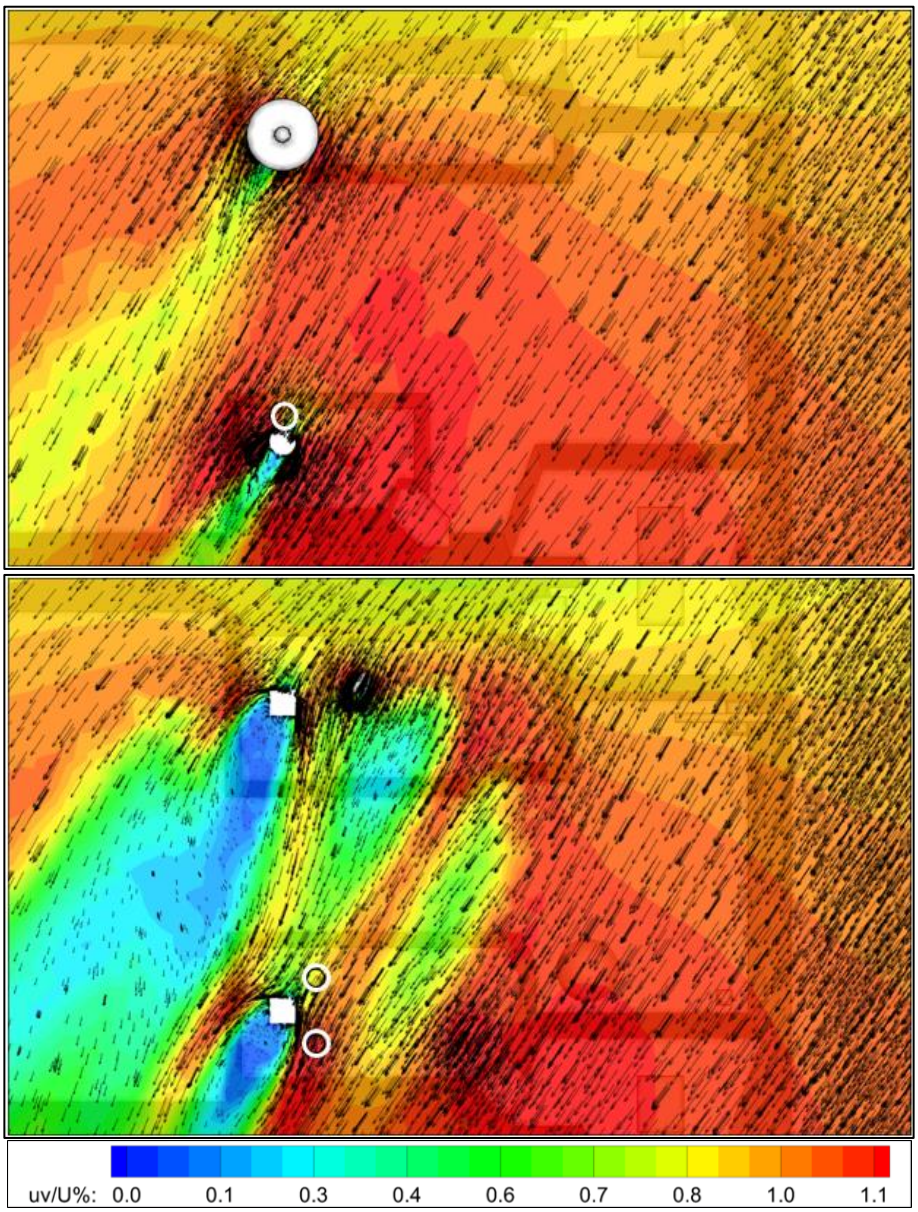

Figure 4.40: Plan view of contours of velocity in the horizontal plane with vectors of mean velocity magnitude in a Green 135 WOD condition for the GCS cylindrical pole mast (top) and square pole mast (bottom)

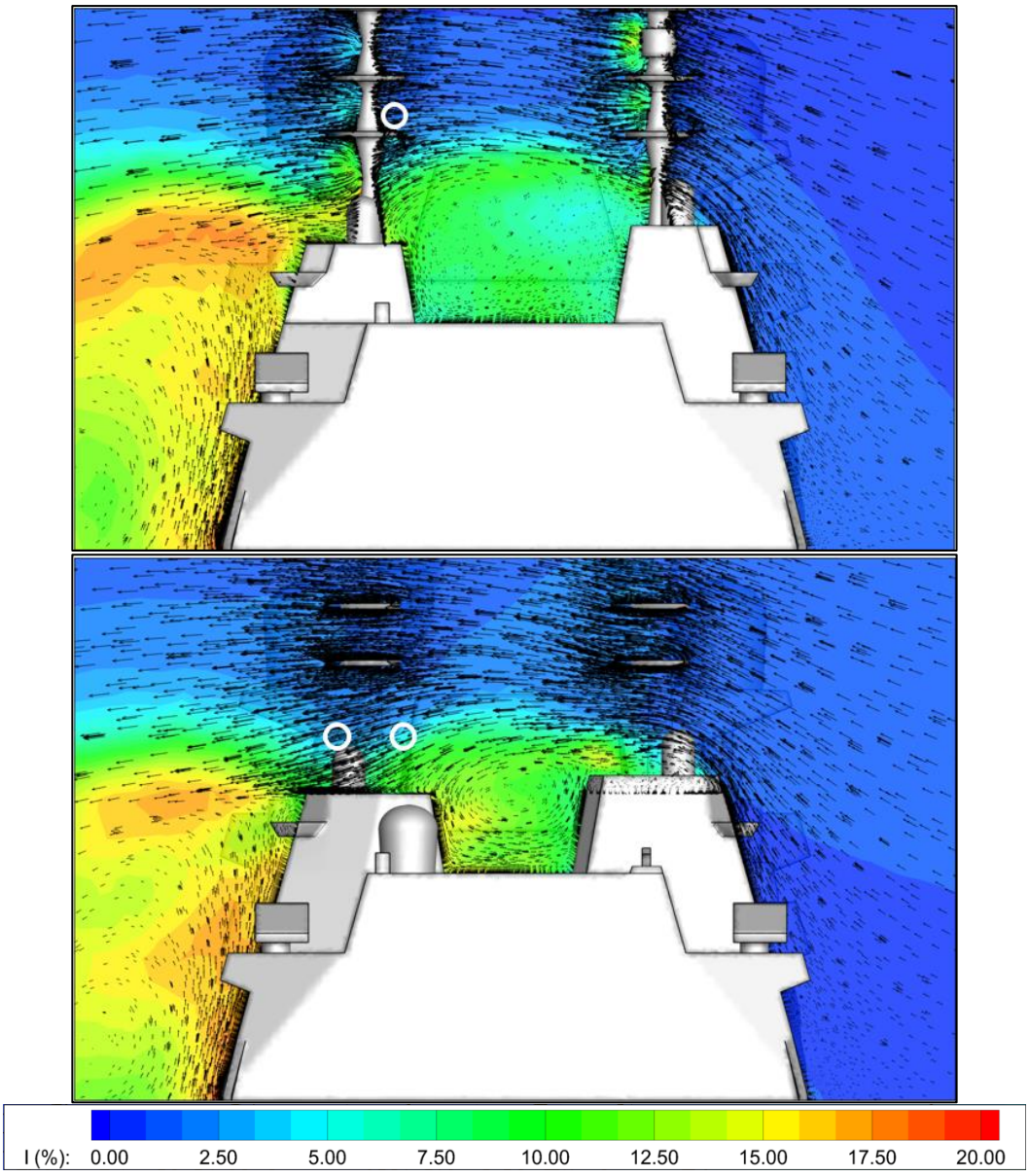

Figure 4.41: Stern view of contours of turbulence intensity in the vertical plane with vectors of mean velocity magnitude in a Green 135 WOD condition for GCS with cylindrical pole mast (top) and square pole mast (bottom) anemometer locations

Figure 4.42 shows the air flow field for the tailwind condition. Relating this to Figure 4.38 it can be seen that the cylindrical pole mast anemometer would be expected to read high, this is because the anemometer is to the side of the mast where the local flow accelerates. The larger wake of the square pole mast is again evident, and the two locations produce velocity deviations in Figure 4.38 that are low. The angular deviation at this wind angle in Figure 4.39 is not symmetrical because the flow approaching the anemometers is disturbed by the

equipment nearby on the superstructure. The view of the flow field from astern in Figure 4.43 shows, once again, how the lower anemometer location on the square pole mast is on the edge of the turbulent flow.

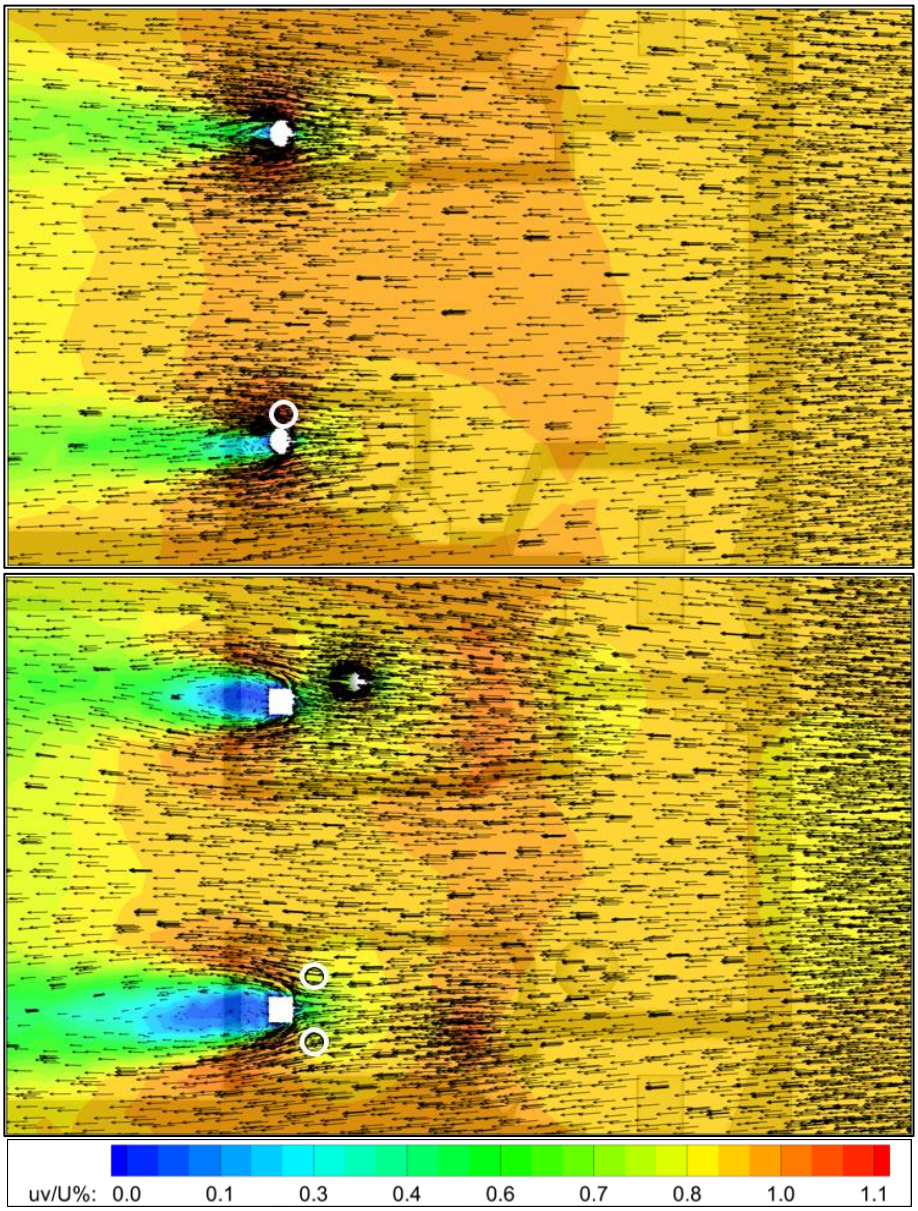

Figure 4.42: Plan view of contours of velocity in the horizontal plane with vectors of mean velocity magnitude in a Tailwind WOD condition for the GCS cylindrical pole mast (top) and square pole mast (bottom)

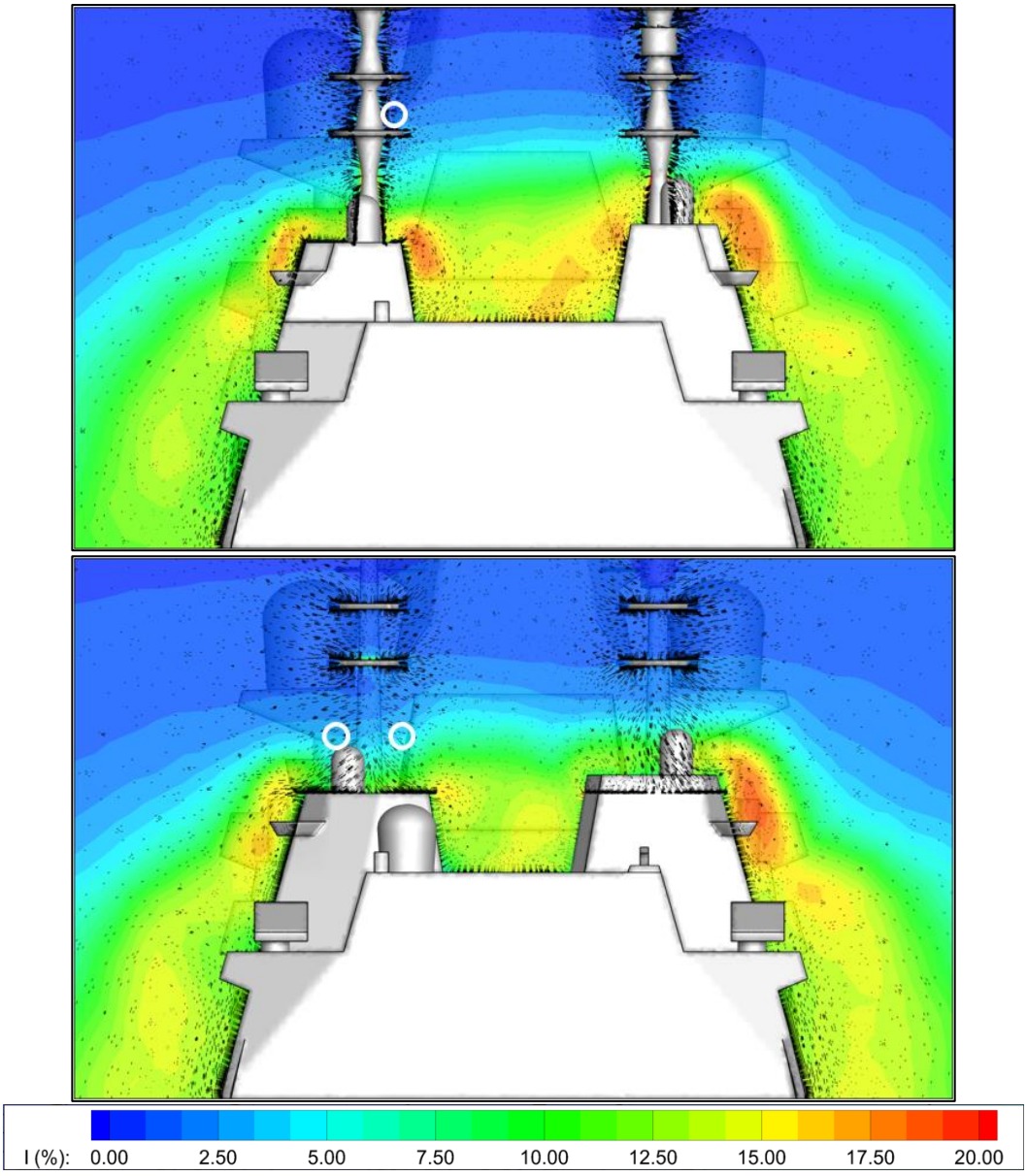

Figure 4.43: Stern view of contours of turbulence intensity in the vertical plane with vectors of mean velocity magnitude in a Tailwind WOD condition for GCS with cylindrical pole mast (top) and square pole mast (bottom) anemometer locations

The air flow field for Red 135 is relatively symmetrical with Green 135, except that the shorter port side equipment housing on the GCS with cylindrical pole mast affects the flow in that area. Figure 4.44 shows the velocity field in the horizontal plane through the anemometer positions, the distortion in the flow at the anemometer positions is a reflection of that in Figure 4.40 for the Green 135 wind, and this is consistent with Figure 4.38 where the error in the inboard and outboard anemometer locations in the Red wind are the opposite of those in the Green wind. The effect of the shorter equipment housing on the air flow is more evident in Figure 4.45 where the cylindrical pole mast flow field in the vertical plane for Red

135 WOD is different to that in Green 135 in Figure 4.41, specifically the recirculating flow between the port and starboard equipment housings. The Red and Green 135 velocity fields for the GCS with square pole masts are more comparable, except for the effect of the slightly higher starboard equipment housing. Again, the lower anemometer of the square pole mast is on the edge of the turbulent flow, unlike the higher anemometer location of the cylindrical pole mast.

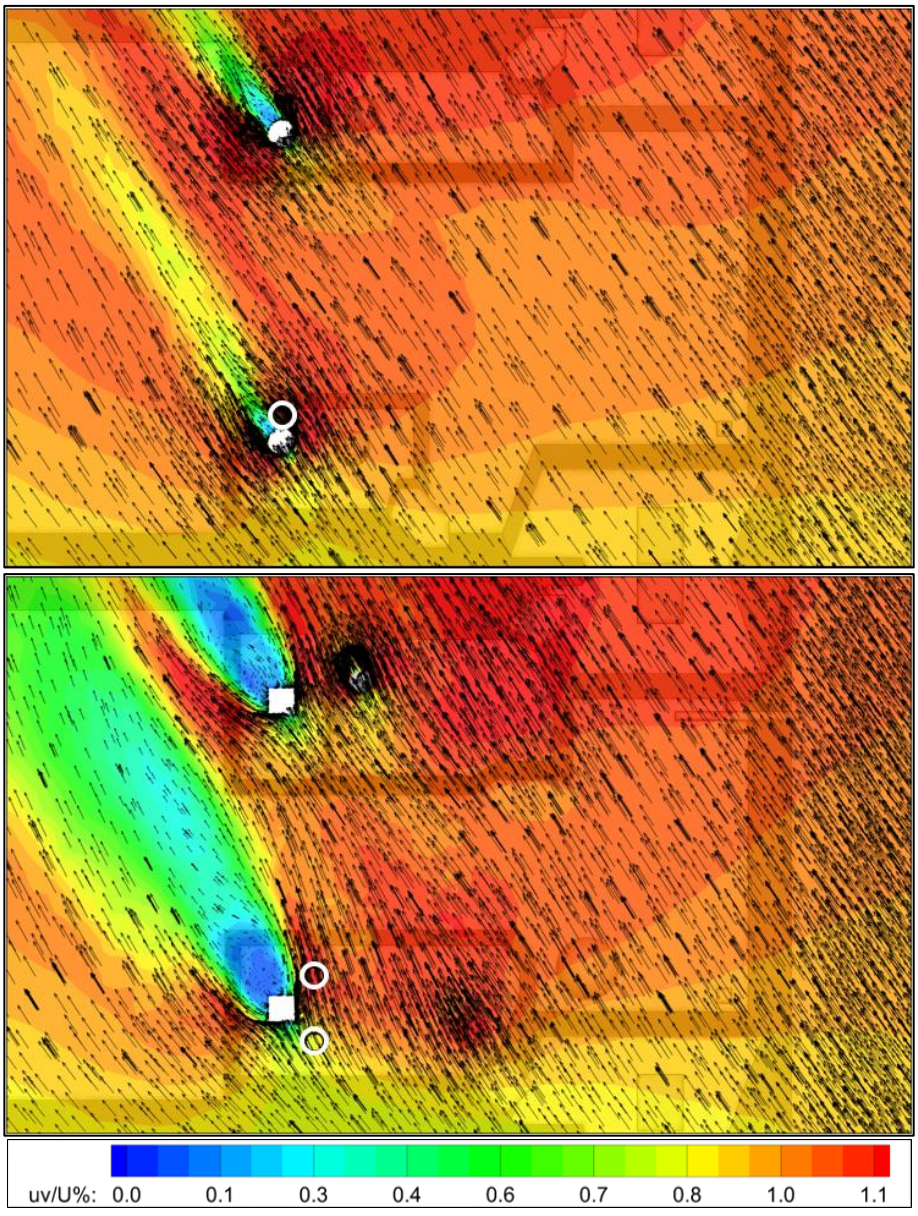

Figure 4.44: Plan view of contours of velocity in the horizontal plane with vectors of mean velocity magnitude in a Red 135 WOD condition for the GCS cylindrical pole mast (top) and square pole mast (bottom)

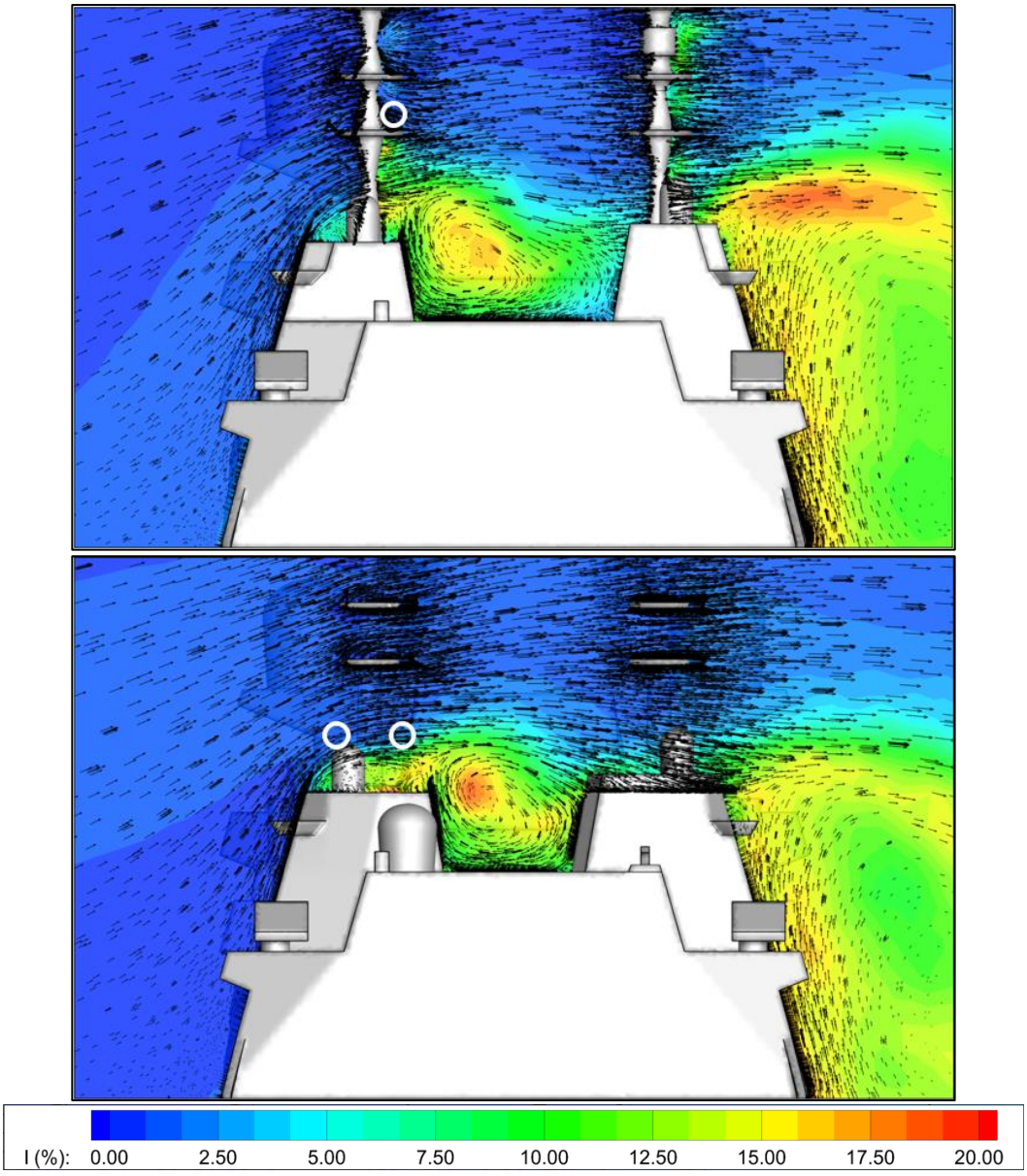

Figure 4.45: Stern view of contours of turbulence intensity in the vertical plane with vectors of mean velocity magnitude in a Red 135 WOD condition for GCS with cylindrical pole mast (top) and square pole mast (bottom) anemometer locations

The main observation from this comparative study of the aft anemometer location is that the anemometer could be effective if it is appropriately located and that the square mast increases the size of the local wake at the anemometer positions compared with the circular mast. For both masts the anemometer would benefit from being located immediately aft of the mast to face into the oncoming tailwind. The anemometer on the cylindrical pole mast is 2m higher than that on the square pole mast and the analysis shows that higher up the mast the approaching air flow becomes disturbed by the presence of the mast within a

distance of three mast widths. The anemometer should therefore be placed aft of the mast at a distance of three (local) mast widths from the mast centreline and as high as possible

4.2.2.3. Predicted performance of the GCS Wind Measurement System

As currently designed, and as a result of the analysis presented in this chapter, the GCS will have the anemometers on the main mast raised from its initial height (although not as high as the 5m for structural reasons), and the aft anemometer will be placed on the square pole mast at the outboard location. Figures 4.46 and 4.47 show the combined graphs of deviation in wind speed for the initial fore and aft anemometers. It can be seen that the aft anemometer will only improve the situation for the tailwind. The corresponding data for the angular deviation is shown in Figures 4.48 and 4.49 where it can be seen that the aft anemometer does not particularly improve the expected accuracy of the wind angle measurement, because it is so low on the aft pole mast.

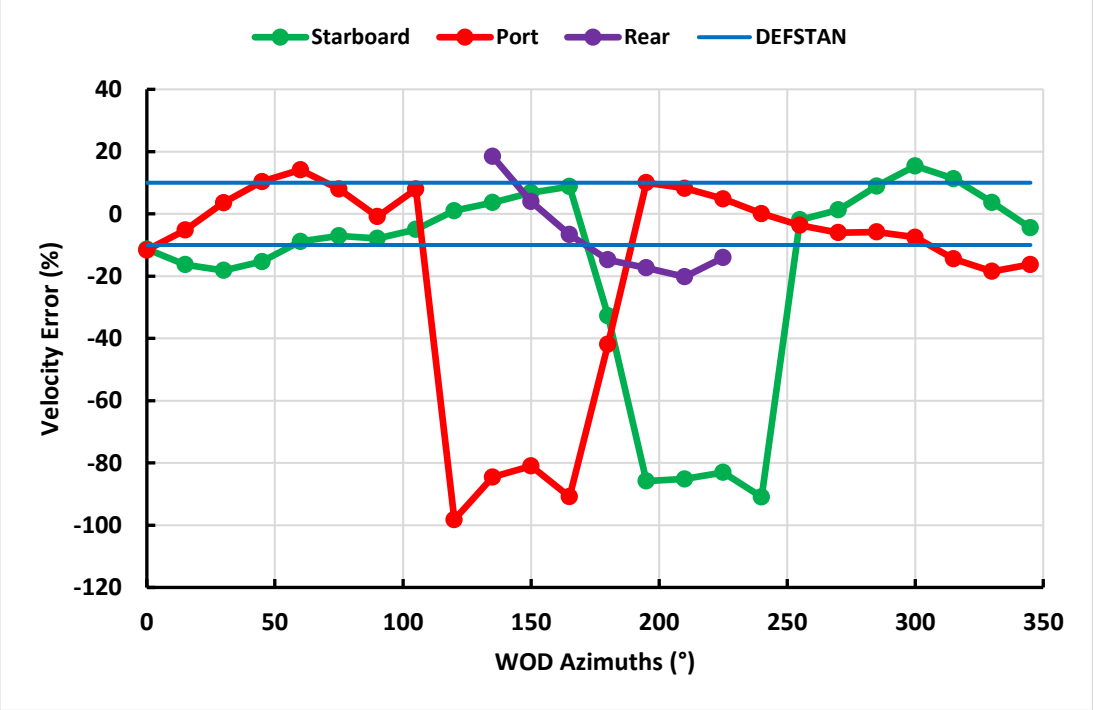

Figure 4.46: Predicted ship wind measurement system performance in mean horizontal velocity magnitude percentage error at +5m main anemometer height and outboard square mast aft anemometer location

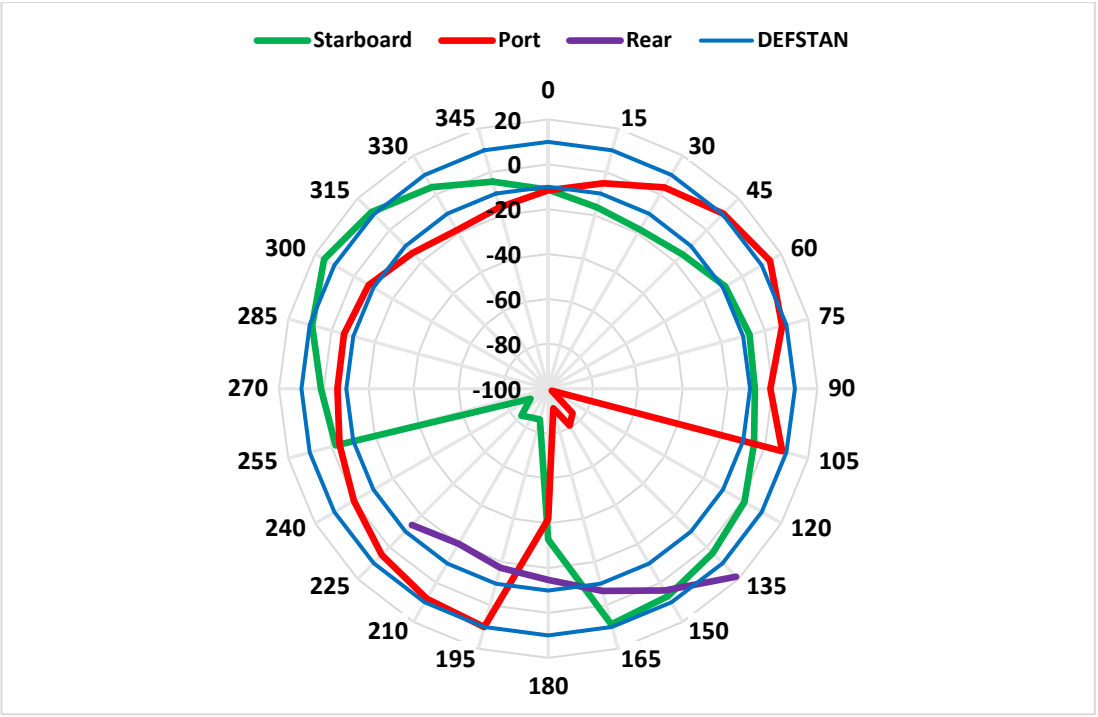

Figure 4.47: Polar plot of predicted ship wind measurement system performance in mean horizontal velocity magnitude percentage error at +5m main anemometer height and outboard square mast aft anemometer location

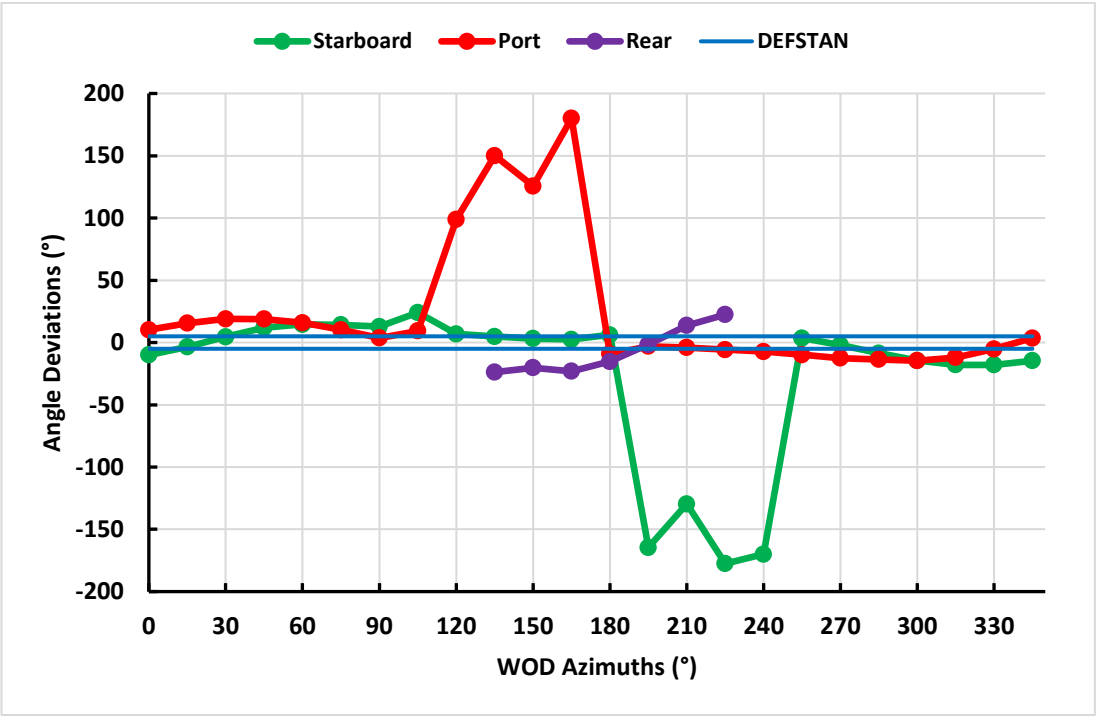

Figure 4.48: Predicted ship wind measurement system performance in mean angle deviation at +5m anemometer height and outboard square mast aft anemometer location

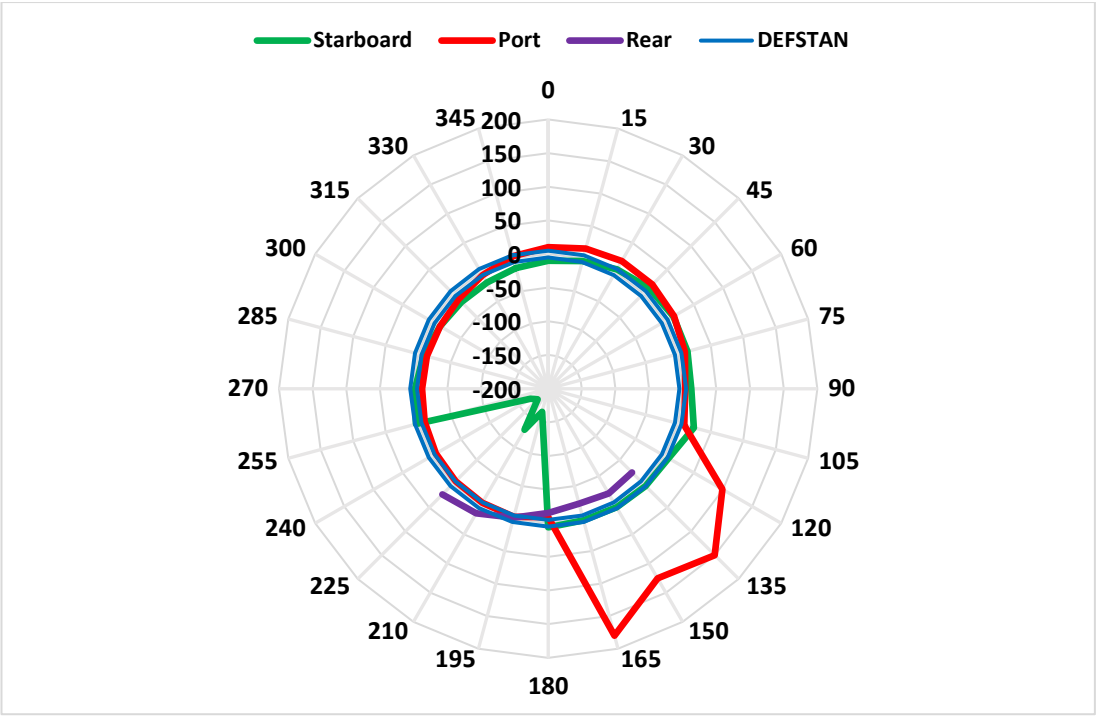

Figure 4.49: Polar plot of predicted ship wind measurement system performance in mean angle deviation at +5m anemometer height and outboard square mast aft anemometer location

4.3. Chapter Summary

This chapter had demonstrated how the CFD methodology developed as part of the research being reported in this thesis can be used to evaluate the expected accuracy of the ship's wind measurement system. An accurate measurement of the wind speed and direction is critical for the safe deployment of the ship's helicopter; both in establishing the original SHOL, and for every launch and recovery operation thereafter. Ship's anemometers are still being installed using the guidance provided by DEFSTAN 00-133 Part 2; however, the standard does not account for the bulky enclosed masts that are being used on modern warships. Ship design is driven by many imperatives such as speed, stability, resilience, weaponry and, increasingly, stealth. The aerodynamics of the ship does not appear to be high on the list of priorities, despite its importance for one of the ship's most potent systems: its helicopter. There also appears to be an ignorance of the importance of the anemometers and their positioning on the ship. Referring back to Figure 4.13, it is difficult to understand how this can be considered as a good location for a sensitive and accurate wind measuring instrument.

Nevertheless, this study has shown that it is possible to identify and examine suitable locations for the ship's anemometers using CFD. Even if, as has been shown to be the case,

the ship superstructure inevitably distorts the local air flow, provided this distortion is predictable and repeatable then CFD could be used to calibrate the ship's anemometers or, at the least, inform the AFAP trials. Furthermore, the unsteady analysis is able to quantify the turbulence levels in the flow at the location and to indicate whether calibration is practical.

It is clear from the study conducted that if the anemometer locations are to be on the main mast, as is the convention, then they should be as high as possible on yardarms that are angled forward and away from any other equipment. As far as the GCS is concerned, it has been recommended that the anemometers be raised at least 5m above their initial height where, even though the anemometers will be in distorted flow, the air will be less turbulent and more amenable to calibration.

The main anemometers are particularly ineffective for winds from astern so it has been recommended that an aft anemometer be installed on the GCS. While this suggestion has been adopted, the CFD analysis clearly shows that for the aft anemometer to be effective it needs to be located as high as possible on the rear pole mast and facing directly aftward. While adopting a square pole mast does introduce additional flow disturbance and turbulence, the RCS compliant design can still be adopted if the anemometer is placed appropriately.

Chapter 5. Effect of Ship Superstructure Aerodynamics on Exhaust Gas Dispersion

The propulsion systems of today's warships employ various combinations of gas turbines, Diesel engines and electric motors to provide the necessary power to both move the ship and to generate electricity for its on-board systems. The gas turbine and Diesel engines discharge exhaust gases at very high temperatures into the ship's airwake. In particular, the gas turbine can emit a significant mass flow rate of exhaust efflux, most commonly from midships. As was seen in Chapter 3, the interaction of the exhaust gases with the ship's airwake shapes the trajectory of the exhaust plume and affects the dispersion of the exhaust efflux, including the raising of air temperatures in regions around the flight deck.

While Chapter 3 showed how the exhaust gas dispersion over the GCS compared with that of the Type 23 frigate, in this chapter the study is focussed on the GCS and includes more wind-over-deck (WOD) condition and different engine power settings. A further enhancement has been to conduct an analysis of the exhaust gas dispersion when there is an exhaust gas cooling system installed in the GCS. Furthermore, an experiment has been designed in which hot air is injected as a jet from the top surface of a rectangular body into the air flow in a wind tunnel to provide experimental data to compare with CFD computations; preliminary results from that study are presented. The chapter will begin with a review of the evolution of the design of ship exhaust stacks.

5.1. Exhaust Gas Dispersion

In the same way that the design and purpose of the warship's mast evolved, so too did the ship's funnel. Referring back to Figures 4.1 to 4.3, the ships' funnels can be clearly seen sitting amidships and standing tall. HMS Dreadnought, Figure 4.2, was fuelled by coal sprayed with heavy fuel oil and, as can be seen in the figure, the funnels discharged dirty soot-laden exhaust gases. In those early days of steam-powered warships the function of the funnel was simply to discharge the boiler exhaust gases high enough so they were clear of the ship. How dirty the funnel efflux could be is seen in Figure 5.1 which shows an unusual aerial view, while Figure 5.2 shows a similar class of ship with the exhaust efflux passing relatively low over the aft sections of the ship. Post World War 1, new ship designs used fuel oil to power

their steam turbines, which, although not totally removing the dirty, highly visible, exhaust plume, the problem was significantly reduced, as shown in the image of a Royal Navy WWII destroyer in Figure 5.3.

Figure 5.1: USS Wyoming, ca. 1915 [108]

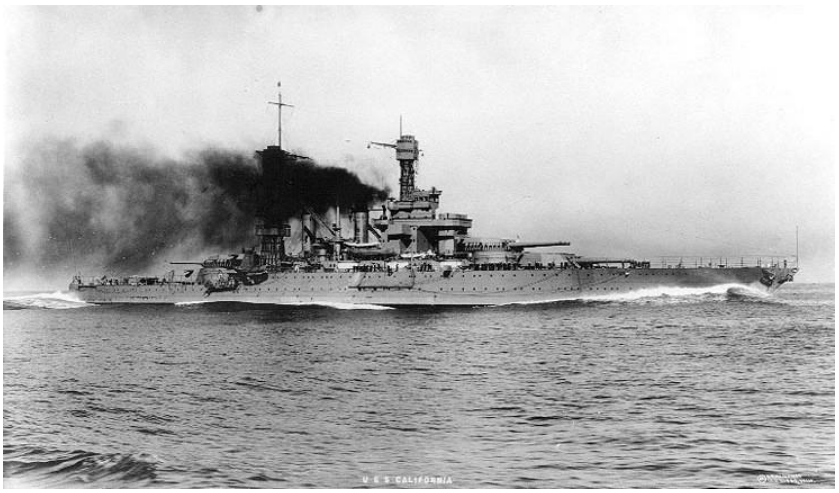

Figure 5.2: USS California ca. 1921 [109]

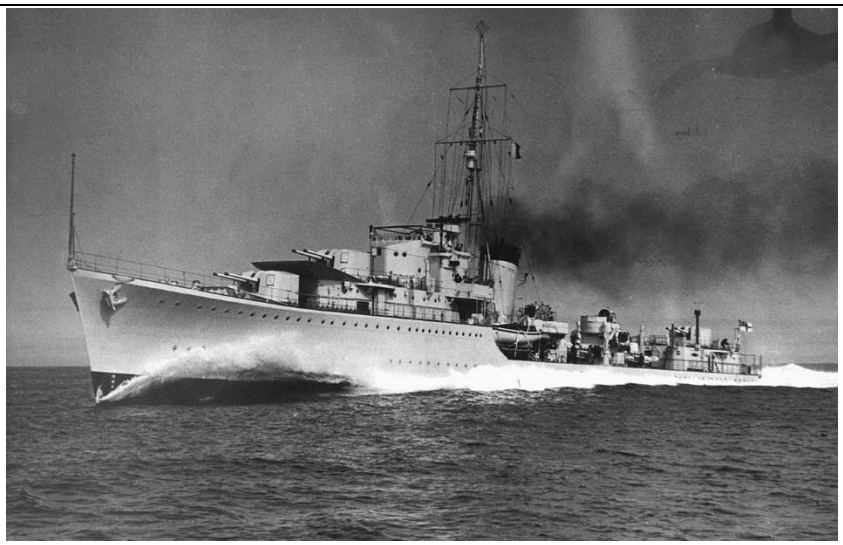

Figure 5.3: HMS Kelly ca. 1940 [110]

By the 1950s, funnel design was well advanced, whether for the comfort of passengers on luxury liners, or for the comfort of the crew and the effectiveness of operations on cargo or combat ships. In each case the issue was the same: the downwash of the exhaust gases through entrainment into the wake behind the funnel and its mixing with the ship airwake. On the passenger liners, smoke dispersion was essential for on-deck passenger comfort and to avoid the exhaust being ingested into the below-deck ventilation system. Similarly, on combat ships, personnel comfort above and below decks was an issue, as was the need for the ship to have low visibility at sea. As steam propulsion gave way to Diesel and gas turbine engines, the issue of funnel exhaust gas ingestion into the engine air intakes was added to the list of concerns.

While early ship designs had tall funnels that lifted the exhaust gases clear of the ship airwake, the negative effects on ship weight, stability and visibility became an issue. Similarly, as radar detection became more important, tall exhaust stacks and funnel casings were undesirable. The increasing requirement for effective but smaller funnels created the need for research and design guidance to better inform the design of warships. In 1952 Acker [111] published a study on the effect of funnel design on exhaust gas dispersion, in which a wind tunnel and smoke flow visualisation was used to investigate how different funnel geometries and damper configurations affected the exhaust gas entrainment and downwash. In 1959 Ower & Third [112] published a comprehensive study in which the common features of a ship's superstructure were presented in graphical form with recommendations for suitable dimensions and geometric ratios. An example design chart extracted from [112] is shown in Figure 5.4.

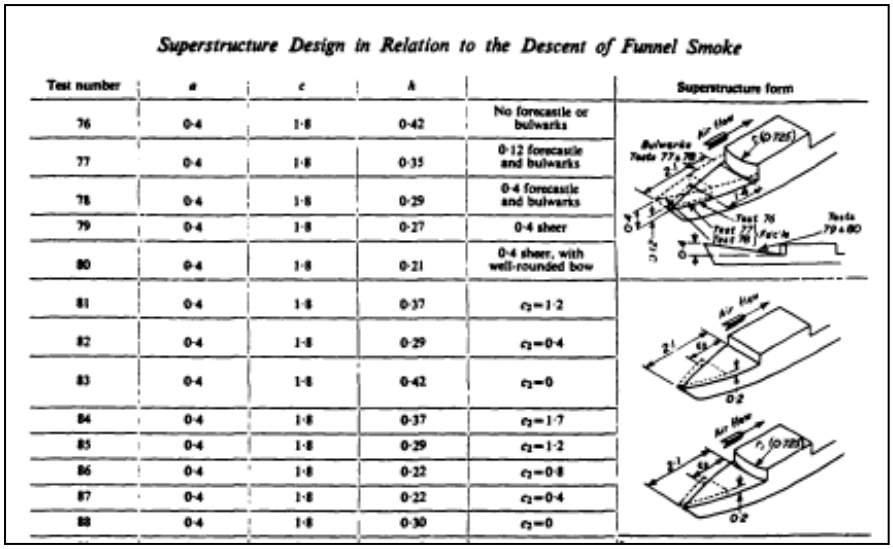

Superstructure Design in Relation to the Descent of Funnel Smoke

Test number	a	c	h		Superstructure form
76	0·4	1·8	0·42	No forecastle or bulwarks	
77	0·4	1·8	0·35	0·12 forecastle and bulwarks	
78	0·4	1·8	0·29	0·4 forecastle and bulwarks	
79	0·4	1·8	0·27	0·4 sheer	
80	0·4	1·8	0·21	0·4 sheer, with well-rounded bow	
81	0·4	1·8	0·37	$c_2=1·2$	
82	0·4	1·8	0·29	$c_2=0·4$	
83	0·4	1·8	0·42	$c_2=0$	
84	0·4	1·8	0·37	$c_2=1·7$	
85	0·4	1·8	0·29	$c_2=1·2$	
86	0·4	1·8	0·22	$c_2=0·8$	
87	0·4	1·8	0·22	$c_2=0·4$	
88	0·4	1·8	0·30	$c_2=0$	

Figure 5.4: Superstructure design chart to alleviate funnel smoke problems [112]

In 1977 Baham & McCullum [113] published an updated study on ship geometry and funnel design in a period when exhaust gas interference with ship instrumentation and electronics was becoming an issue, and gas turbines engines had begun to appear. Elements of these studies were drawn together in a practical funnel design manual published by the Naval Ship Engineering Center at Hyattsvile, USA, in 1976 [114]. Figure 5.5 shows a diagram extracted from [114] in which the gas turbine exhaust is fed to an eductor where it is mixed with cooling air and can be sprayed with water to reduce the exhaust gas temperature.

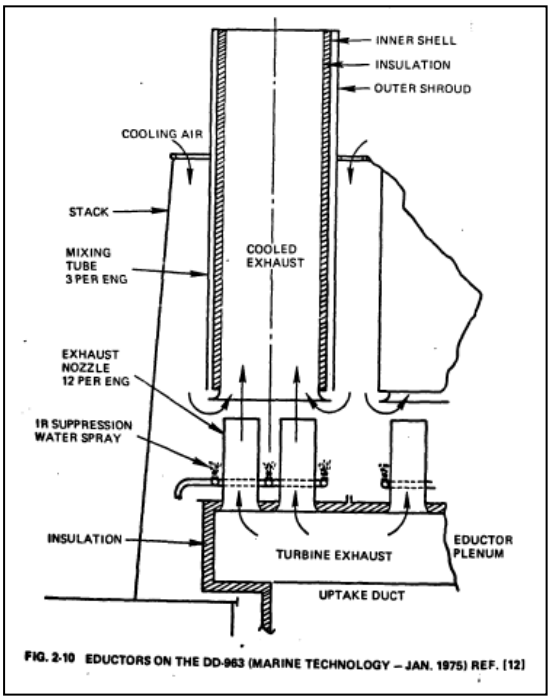

Figure 5.5: Eductor for exhaust gas cooling [114]

Although heavy smoke particulates are no longer an issue for ships powered by gas turbine and Diesel engines, the effective dispersion of the exhaust efflux is still a concern as the exhaust gases can be at very high temperatures, and can cause an array of issues [115]–[118]. The superstructure of the modern warship hosts a myriad of complex external electronic systems and sensors, infrared (IR) guided missiles, engine air intakes, and a helicopter flight deck, all of which can be affected by hot engine exhaust. Ineffective dispersion of the ship's high temperature exhaust efflux therefore gives rise to numerous potential operational hazards which need to be investigated and quantified, before the ship enters service, to determine the degree of risk posed.

As stealth is a primary driver for modern warship design, in addition to ensuring the minimisation of RCS, the ship's IR signature is an important factor to be considered. The heat energy in the ship's exhaust gases, as well as the many mechanical systems that are operational on board, can create a prominent IR signature that can result in unwanted detection by enemy forces, perhaps most alarmingly from IR guided anti-ship missiles [14]. The successful use of infrared signature suppression (IRSS) to help reduce IR signature is therefore an important aspect of warship design to mitigate these risks. The very high temperature of the gas turbine exhaust can significantly increase the IR signature of the ship, and warship designs usually incorporate cooling methods to reduce the temperature of the exhaust gases by the time they reach the exit plane of the uptakes [119]. Further discussion on ship exhaust gas cooling and how it has been investigated in this study will be presented in the following section.

It has been standard design practice for many years to enclose the exhaust ducts in funnel casings, or fairings, and originally these were round, sometimes with an aerodynamic shaping. In more recent years the funnel casing has become more rectangular with sloping sides to conform to RCS reduction; furthermore the casings also shield the hot exhaust uptakes, preventing IR emissions. An example of how the design of the funnel casing has evolved in recent years can be seen in Figure 5.6 which shows an early version of the US Arleigh-Burke class of destroyer which entered service in 1991, and a later version that entered service in 2000. There are two funnel casings behind the main mast and it can be seen in the left hand image that the exhaust uptakes are exposed, while in the later design the uptakes are flush with the top of the casing.

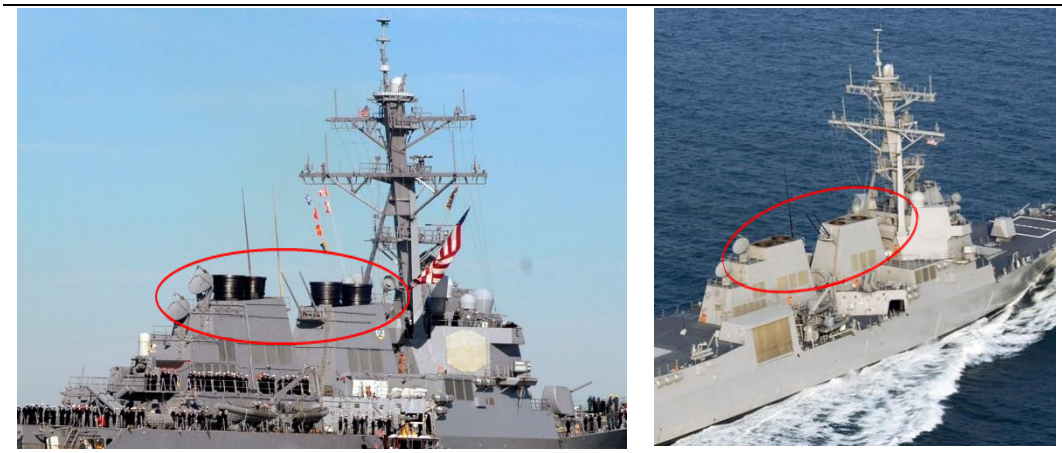

Figure 5.6: US Arleigh Burke Destroyers with exposed funnel uptakes on left [120] *and flush uptakes on right* [121]

Measures to reduce the temperature of the ship's exhaust gases can also have a positive effect on the safe operation of helicopters over and around of the ship's flight deck. The hot exhaust gases that are commonly ejected at midships interact with the ship's airwake and are dispersed downstream on a trajectory that often leads to the plume passing directly over the flight deck, or into other areas where the helicopter may operate, as shown in Chapter 3. Depending upon the initial temperature of the exhaust gases, by the time they have mixed and dispersed with the airwake and reached the flight deck the air temperature there can still be well above ambient and the reduced air density can affect both the lift of the helicopter's main rotor as well as its engine performance. The potential effect of ship exhaust gases on naval maritime helicopter operations has been reported by Scott et al. [122].

A common daily use of the helicopter in civil aviation, which has some parallels with the naval operation, is the transport of workers to offshore oil and gas platforms. Gas turbines are used on offshore platforms for power generation and the exhaust gases are usually discharged vertically upwards, and temperatures in excess of 400°C are normal. The scenario is therefore similar to that on a ship, except the rig exhaust ducts are generally higher above the deck, and the wind over deck is that due to the prevailing wind alone. The Civil Aviation Authority (CAA) publication 'CAP 437: Standards for Offshore Helicopter Operations' [123], makes the following statement that should be applied to the volume of airspace above the helideck up to 30ft plus wheels to rotor height plus rotor diameter above the flight deck (typically 30 m for a medium-weight helicopter):

> "*Unless there are no significant heat sources on the installation or vessel, offshore duty holders should commission a survey of ambient temperature rise based on a Gaussian dispersion model and supported by wind tunnel tests or CFD studies for*

> *new-build helidecks, for significant modifications to existing topside arrangements, or for helidecks where operational experience has highlighted potential thermal problems. When the results of such modelling and/or testing indicate that there may be a rise of air temperature of more than 2°C (averaged over a three-second time interval), the helicopter operator should be consulted at the earliest opportunity so that appropriate operational restrictions may be applied."*

The 3-second period is representative of the response time of a helicopter engine to a sudden temperature change. The origin of the 2°C criterion is not clear but it is believed to relate to the loss of lift equivalent to one passenger; it may also relate to the resolution of the Weight Altitude and Temperature (WAT) charts used by pilots to determine the payload for a given set of environmental factors. The ambient air conditions over a ship's landing deck have similarities to those on the oil platforms that are regulated by the CAA; however; there are no comparable naval regulations. Although there appears to have been no recorded incidents related to naval operations, there have been helicopter accidents in civil aviation that have resulted in a rapid descent and crash landing, attributed to the sudden ingestion by the helicopter of hot exhaust gases [124], [125].

Reference [126], which was used to inform CAP 437, provides some simple analysis of the adverse effects on a helicopter of temperature increments due to hot plumes. If the air temperature passing through the rotor increases then lift is reduced. Therefore to support the weight of the helicopter the power to the main rotor needs to be increased, which means that the margin of thrust control left to the pilot is reduced. The 2°C threshold in CAP 437 requires an increase in power of 0.24% which equates to a loss of thrust margin of 0.17%. The corresponding figures for a 10°C rise in air temperature are 1.22% and 0.86%.

Reference [126] also discusses the effect of transient air temperature changes on helicopter engine performance and shows that a 10°C rise in temperature is estimated to result in a transient loss of power of 1.65%, and a loss of control margin of 1.1%. Graphs of simulated engine response are shown in Figure 5.7 where it can be seen how a 10°C step change in turbine inlet temperature sustained for 3 seconds affects the engine rotational speed and power output. The combined loss (rotor plus engine) of control margin due to a 10°C air temperature rise is therefore nearly 2%, which in itself is not a large value, but it should be compared with the minimum thrust margin that the pilot can accept, which is 10%. Furthermore, from the perspective of the naval helicopter pilot, when the aircraft is at the

limits of its controllability over the small and moving landing deck, that is not the time to experience an additional loss of lift.

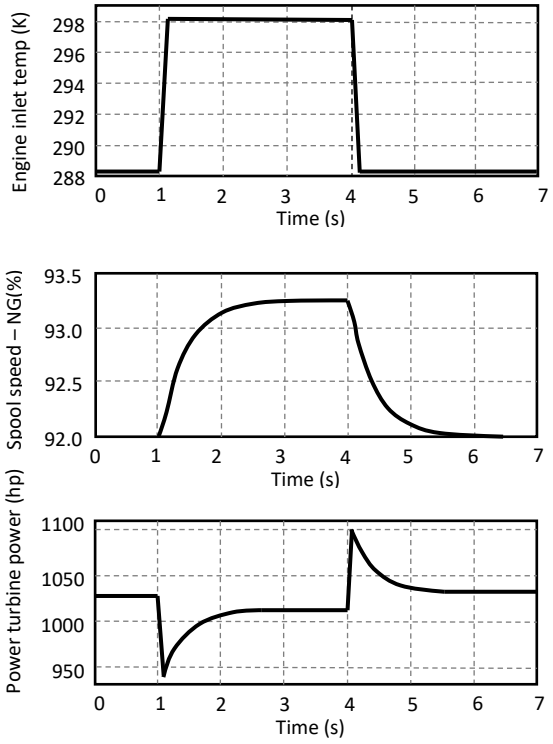

Figure 5.7: Simulated response of a typical helicopter engine to a 10°C change in bulk inlet temperature, held for 3 seconds [126]

Another concern of rapid temperature rise highlighted in [126] is that of engine surge which can occur if the ambient air temperature increases at a rate towards 1000°C/s. The situation can be further complicated if the air temperature is different across the face of the engine, which it could well be due to the discrete turbulent structures that form within the ship's exhaust plume.

Clearly, from the discussion above, an understanding of the unsteady air temperatures in the region around the landing deck is important for the safety of the helicopter, while hot exhaust gases also have implications for the ship's IR signature and stealth.

5.2. CFD Analysis of the GCS Engine Exhaust Gas Dispersion

Wind tunnel tests have been the traditional method of investigating exhaust gas dispersion and were used when the previous generation combat ship, the Type 45 destroyer, was being developed. However for the GCS, CFD analysis has been employed, and formed part of the research being reported in this chapter.

5.2.1. GCS Propulsion and Exhaust System

The GCS is powered by a CODLOG (combined Diesel electric or gas) propulsion system that consists of a Rolls Royce marine gas turbine engine (GT), the MT 30, and four MTU Diesel generators (DGs) which power electric motors, as shown in Figure 5.8. The CODLOG system is designed to operate each drive source independently; a quiet drive forward and astern is provided when operating with its electric motors, powered by four high-speed DGs with the GT being used only when high speeds are required [127]. The ability to provide a sudden increase in power through the GT allows for quick manoeuvrability, beneficial to a warship's operational requirements.

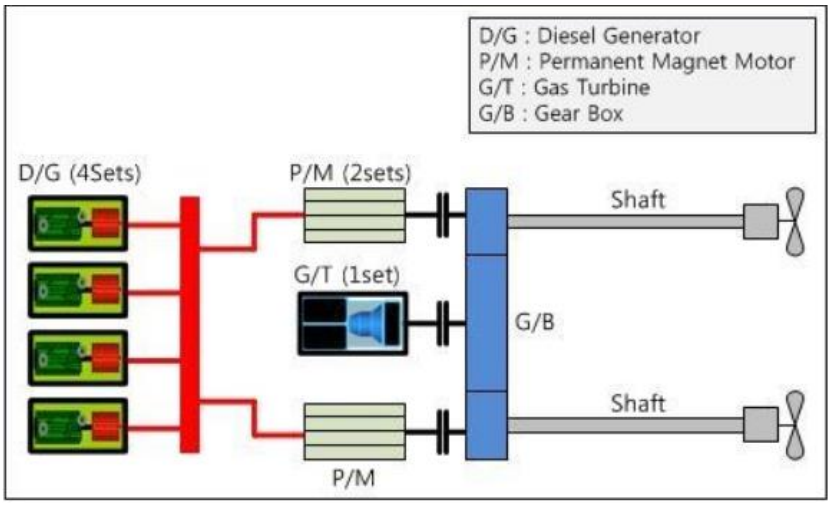

Figure 5.8: Schematic of a Combined Diesel Electric or Gas (CODLOG) propulsion system [128]

The GT produces exhaust gas at a high mass flow rate and temperature. The DGs also produce high temperature exhaust gases, albeit at much lower mass flow rates. In service these very high temperature exhaust emissions can make the ship vulnerable to enemy fire from IR missiles, they can affect the operation of the ship's own IR missiles, interfere with sensitive electronic equipment installed on the superstructure, and potentially create a hazardous operational environment for helicopters attempting to launch and recover to the ship. In an attempt to reduce the risks associated with the ship's high temperature exhaust plume and consequently increased IR signature, efforts can be made to entrain cool air into the exhaust uptakes, through the use of an eductor/diffuser, as shown in Figure 5.9 [119].

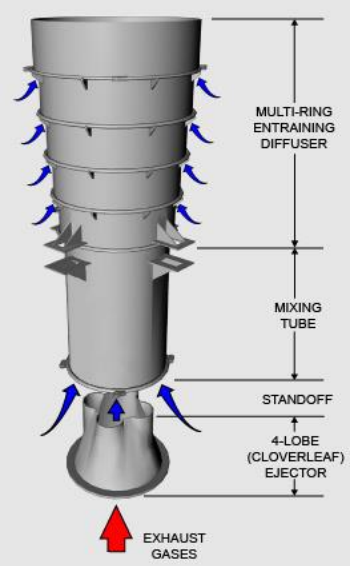

Figure 5.9: Diagram of an exhaust eductor/diffuser system [119]

The basic principle of the eductor is to use the venturi effect by initially increasing the velocity of the GT exhaust gases through a convergent section, thereby simultaneously reducing the pressure of the fluid. The exhaust gases are released into a slightly larger diameter mixing tube where the pressure difference between the higher pressure stagnant air outside of the mixing tube and the lower pressure exhaust gases draws the comparatively cooler air inside the exhaust uptake. Operating in this mode the eductor is classed as being passive. However, to increase the amount of cooling air, additional fans are used to force supplementary air into the exhaust closure (as could be seen earlier in Figure 5.5); the fans also act as ventilation fans for the adjacent below-decks compartments. This additional air is also forced into the diffusing section of the eductor as shown in Figure 5.9 and thereby creates a cooled air film around the hot gas which serves to reduce the heating of the exhaust ducting as a further measure to reduce IR emissions.

The cooling of the exhaust gases are important from two perspectives: one is the reduction of the potential of the hot gases to heat the surfaces of the ship, including the exhaust uptake, and second the cooling of the gas itself, which, although it has a low emissivity, will still emit IR radiation of certain wavelengths. Figure 5.10, extracted from [129] shows the calculated lock-on range for a heat-seeking missile around the azimuth of a ship for different exhaust plume temperatures. It should be pointed out that in action the ship's commander will have a number of tactical options, including spraying water into the eductor to increase the cooling, and throttling back or shutting down the gas turbine.

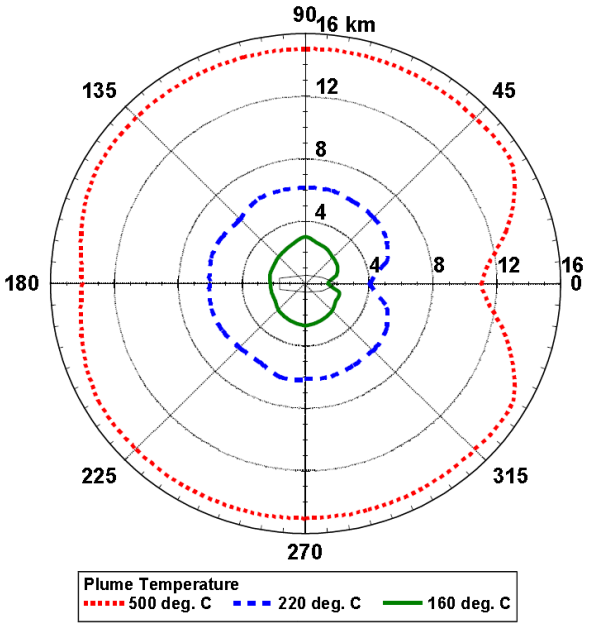

Figure 5.10: Effect of plume temperature on missile lock-on range [129]

The CFD exhaust gas study was conducted in two stages. In the first there was no information available on the eductor cooling system and the analysis was conducted for the engine exhaust gases alone using given exhaust temperatures and mass flows, as well as the exhaust duct diameters (consistent with the analysis presented in Chapter 3). The analysis assumed that the gases could be represented by air, which is reasonable considering the large amount of excess combustion air that is provided, particularly to the GT. In this initial analysis, the hot air flow was introduced as a uniform velocity profile into a duct of 5 diameters in length to allow a representative velocity profile to develop before the flow was discharged from the funnel into the airwake. This stage allowed the analysis to proceed, the CFD technique to be developed, and for preliminary data to be provided to BAE and other stakeholders.

In the second stage, additional information was provided from the eductor manufacturer who had used their own analytical tool and steady-state CFD to predict the velocity and temperature profiles at the exit of the eductor's diffuser. The combined mass flow rates of the GT exhaust and cooling air were significantly higher than the values used in the first stage analysis and the temperatures were lower; also the duct outlet geometry was non-circular.

Figure 5.11 shows a plan view of the funnel casing for the two cases, which have been called GCS-Ex1 and GCS-Ex2. The left hand image shows the initial circular exhaust while the right hand image shows the flattened circular geometry of the eductor outlet. Also shown in the image are the uptakes for the forward port and starboard DGs. There are two more (aft) DG

exhausts on the starboard equipment housing on the roof of the hangar. It can also be seen in Figure 5.11 that the slope of the funnel casing was reduced between the design changes from GCS-Ex1 to GCS-Ex2; the newer angle is still effective for radar reflection and allows more space within the funnel casing, which also functions as storage space.

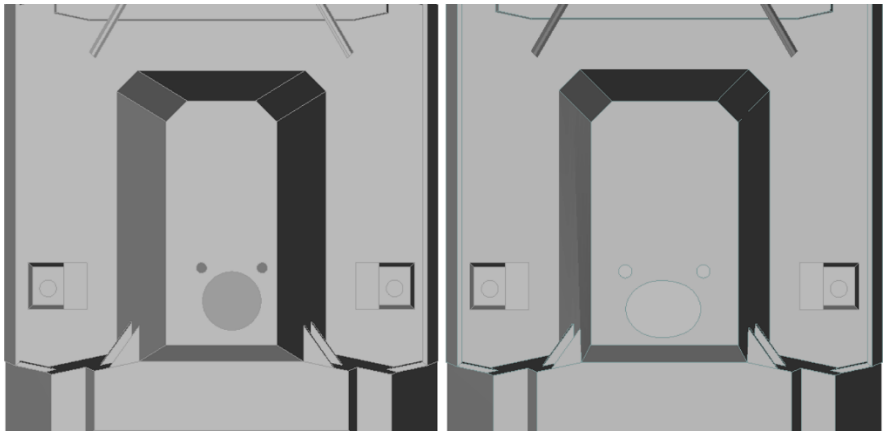

Figure 5.11: Plan view of the GCS exhaust geometry for a standard exhaust pipe system, GCS-Ex1 (left) and exhaust system with eductor/diffuser, GCS-Ex2 (right)

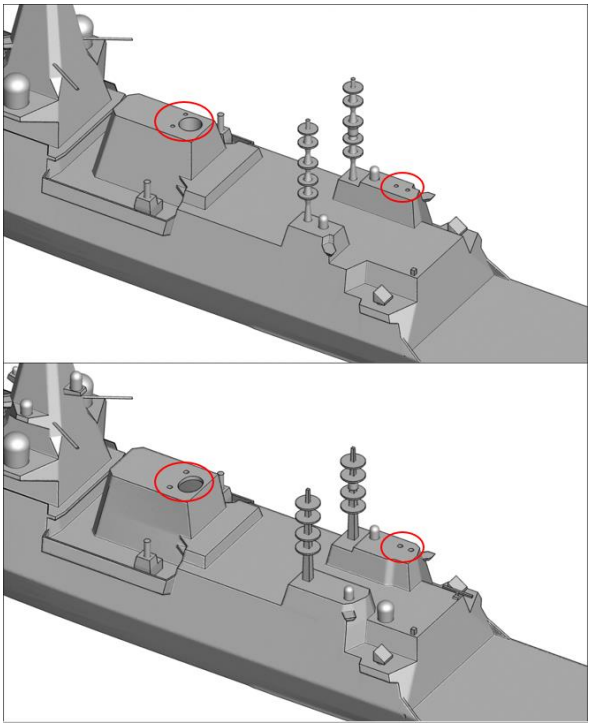

Figure 5.12: Wider isometric view of GCS exhaust geometry for a standard exhaust pipe system, GCS-Ex1 (top) and exhaust system with eductor/diffuser, GCS-Ex2 (bottom)

Figure 5.12 shows a wider view of the two GCS geometries, indicating the locations of the main GT and the two forward DG exhausts as well as the two aft DG exhaust uptakes on the starboard equipment housing just forward of the flight deck. It can also be seen in Figure

5.12 that some additional geometric changes were made to the two pole masts and the port equipment housing. These changes will not significantly affect exhaust gas dispersion in the airwake, and simply had to be accepted as an imposed design change.

During the course of the project a significant number of different wind conditions were investigated with the simpler circular uptake geometry; also, different GT/DG combinations were considered because different engine combinations are used for different ship speeds and therefore, indirectly, different relative wind speeds. To simulate overseas missions, a number of different ambient temperatures were also considered. However, only two wind conditions are presented below to compare the CFD results for the two exhaust configurations, a 25 knots headwind and a 25 knots Green 30 WOD, both with ambient temperatures of 30°C. It was assumed that the GT would be operating with one forward DG and one aft DG. Following this comparative analysis, four additional conditions using just the GCS-Ex2 configuration were analysed for relative wind speeds of 12 and 18 knots from Ahead and Green 30; for the slower 12kts WOD the GT was not in use and only the port-side forward and one aft DG were operating. The headwind case is considered because the exhaust plume will travel along the ship and over the flight deck, while the Green 30 WOD is considered because it represents an oblique wind coming from the starboard side that will deflect the exhaust plume into the area off the port side of the landing deck as discussed in Chapter 3.

5.2.2. Comparative CFD Analysis of GCS Exhaust Gas Dispersion with and without Infrared Signature Suppression

The results for the two different exhaust configurations are presented and discussed first, before going on to consider the additional cases for just the GCS-Ex2 with the IRSS eductor system.

5.2.2.1. Boundary Conditions for Exhaust Inlets

As described above, the GCS-Ex1 and GCS-Ex2 configurations have different exhaust geometries (Figure 5.11). Furthermore, because of the additional cooling air introduced through the eductor, the mass flow and temperatures of the two systems are very different. Table 5.1. shows that for the circular GT duct (GCS-Ex1) the mass flow is that of the exhaust efflux from the turbine, 132 kg/s, while for the eductor system with the additional cooling air the mass flow has increased to 158.9 kg/s; the average GT exhaust gas temperatures have also decreased from 833.15 K to 609.8K, respectively. It can also be seen in Table 5.1 that the DG flow rates, which are much lower than those from the GT, have also changed between

GCS-Ex1 and GCS-Ex 2; because the DG flow rates are so low these imposed differences are not significant, but should nevertheless be borne in mind when comparing the two analyses.

Table 5.1: CFD boundary condition parameters for GCS-Ex1 and comparative values for GCS-Ex2

	GCS-Ex1			GCS-Ex2		
	GT	**Fwd Port DG**	**Aft DG**	**GT**	**Fwd Port DG**	**Aft DG**
Exhaust Mass Flow (kg/s)	132	5.18	5.18	158.9	4.38	4.38
Exhaust Temp. (K)	833.15	753.15	753.15	609.8	590.2	590.2
Exhaust Av. Exit Velocity (m/s)	23.3	56.8	56.8	39.3	28.3	28.3
Freestream Velocity (m/s)	12.86 (25knots)			12.86 (25 knots)		
Ambient Temp. (°C)	30°C			30°C		

As mentioned above, for the initial analysis the GT and DG exhaust ducts were assumed to be circular, with diameters of 2.8m and 0.5m respectively, and were given a length of 5 diameters to allow a representative exit velocity profile to develop. The flow was introduced at the inlet to the ducts with uniform profiles of velocity and temperature and, as the walls of the duct were adiabatic, the temperature profiles remained uniform up to the exit plane. When the eductor information became available, data was obtained for the velocity and temperature profiles at the exhaust plane. Figure 5.13 shows the temperature and vertical velocity (w) distribution at the non-circular GT exhaust plane, while Figure 5.14 shows the corresponding distributions for the smaller DG uptakes. For both uptakes it can be seen that the core of the exhaust flow has a reasonably uniform temperature distribution, but with significantly lower wall temperatures due to the IRSS cooling systems. The velocity profiles, however, are not uniform, particularly for the GT. The reason for this will lie in the entry conditions at the eductor where the engine exhaust gases, which exit the engine horizontally, are turned to flow vertically upwards; the detailed information was not made available.

The data shown in Figures 5.13 and 5.14 was provided as ASCII files with temperature and u, v, w velocity components specified for different x, y, coordinates and was used as the inlet conditions for the unsteady CFD calculations. A Matlab code was therefore written to plot the velocity and temperature profiles and to assign interpolated values onto the CFD mesh that had been generated for the GCS.

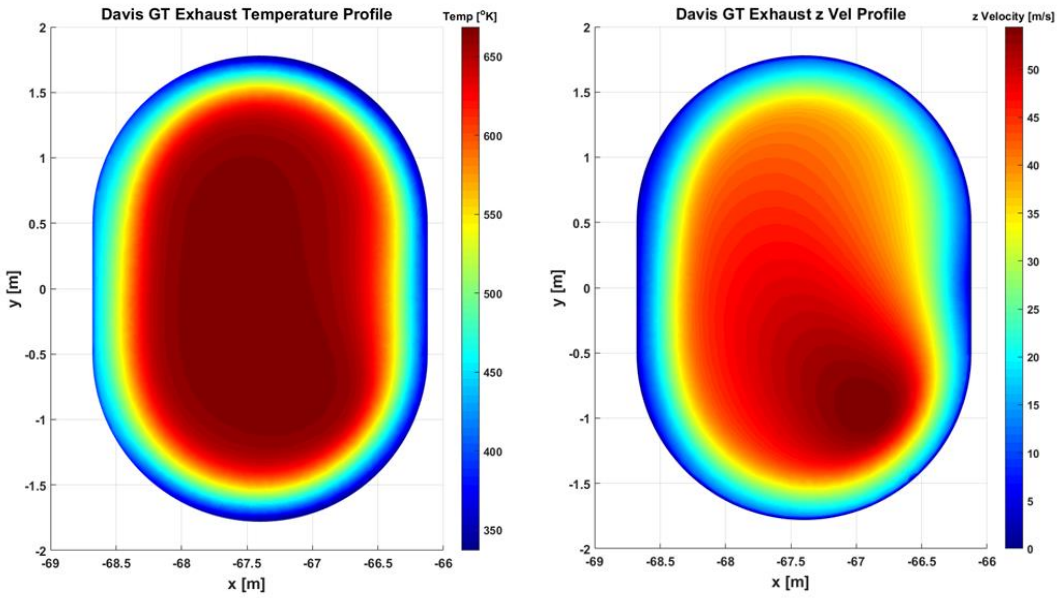

Figure 5.13: Non-uniform temperature and velocity profiles at GCS-Ex2 GT exhaust

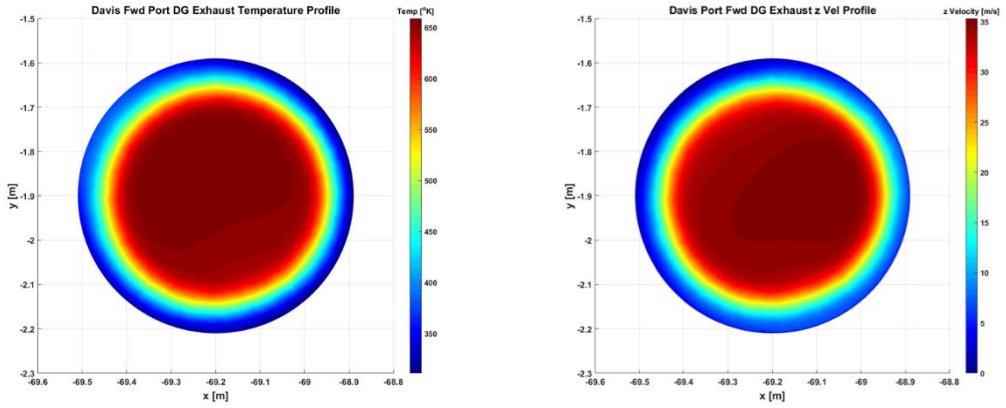

Figure 5.14: Non-uniform temperature and velocity profiles at GCS-Ex2 DG exhaust

5.2.2.2. Comparison of Exhaust Gas Dispersion for GCS-Ex1 and GCS-Ex2

As described earlier in Chapter 2 the CFD mesh for calculating the unsteady mixing of the engine exhaust with the ship airwake used density boxes to ensure the cell size of the computational mesh in the regions of interest did not grow too coarse. There was a measure of trial and error in this as an initial plume trajectory had to be calculated first to determine where the density boxes were needed.

To give an overview of the exhaust plume, Figure 5.15 shows an isometric view of the ship with the exhaust plumes illustrated by isosurfaces of constant average temperature (2, 5 and 10°C) above ambient. The top two figures are for GCS-Ex1 and GCS-Ex2 in a headwind and the bottom two figures are for a Green 30 wind. It can be seen that the dominant exhaust flow is from the GT; the aft DG exhaust plumes are clearly seen but the forward DG exhaust, which is close to the GT outlet, is obscured.

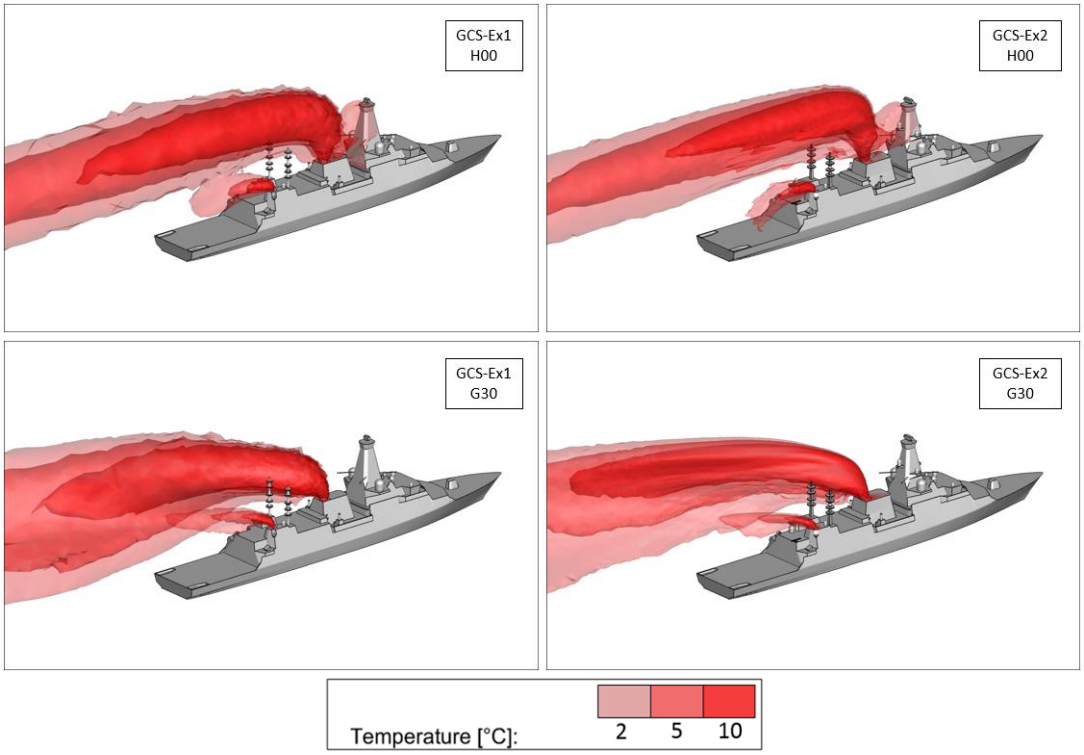

Figure 5.15: Isosurfaces of constant average plume temperatures above ambient for GCS-Ex1 (left) and GCS-Ex2 (right) in headwind (top) and Green 30 wind (bottom)

The following three sets of figures are orthographic views of the ship with the exhaust plumes illustrated by contours of average temperature above ambient; the colour scale is exponential because of the large temperature range. Considering Figure 5.16 for a headwind, the first observation to make is that the temperatures of the very hot exhaust gases from the GT, 560°C and 337°C for GCS-Ex1 and GCS-Ex2 respectively, have reduced to less than 10°C above ambient by the time they reach the flight deck, due to the very energetic mixing with the turbulent airwake. It can be seen that the hot GT exhaust jet rises vertically before it is deflected horizontally by the 25 knots WOD. The core of the jet from the eductor of CGS-Ex2 rises higher before deflecting, due to its higher momentum flux. As observed in Chapter 3, the exhaust gases are drawn into the wake of the main

mast and may therefore heat the metal surface and increase the ship's IR signature. The vertical plane on which the temperature contours are presented is through the centre of the ship (and through the centre of the GT exhaust uptake), therefore in the oblique Green 30 wind the exhaust plume is deflected out of the plane and away from the flight deck region; however, the exhaust from the aft starboard DG is drawn down onto the deck and raises the temperatures by a small amount, typically 1°C.

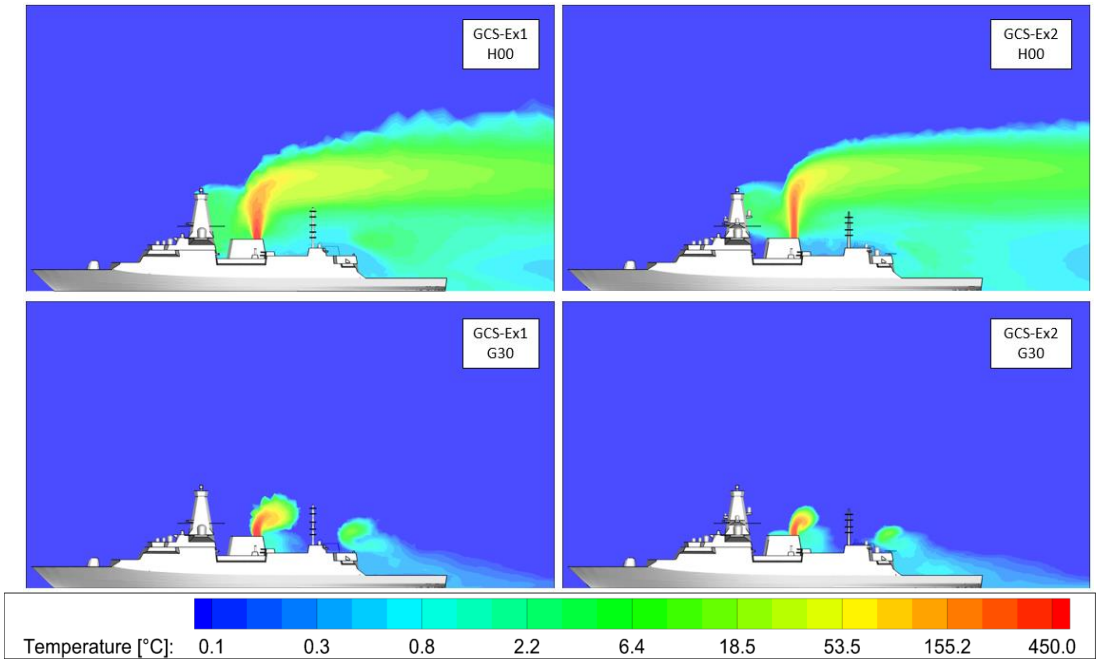

Figure 5.16: Contours of mean temperature above ambient on a vertical plane through the ship centreline for the GCS-Ex1 (left) and GCS-Ex2 (right) in headwind (Top) and Green 30 (Bottom) WOD conditions at 25 knots

Figure 5.17 shows a plan view of the ship where the direction of the exhaust plume in the headwind and the oblique 30° wind can be seen. The horizontal plane on which the temperature contours are presented is at the height of the ship's hangar (8m above the deck), which is approximately the height of the helicopter's main rotor during the majority of the landing manoeuvre. In the headwind the plume covers the width of the landing deck for both exhaust configurations and there is a small area of elevated temperature, about 3-4°C, which is due to the DG exhaust. In the Green wind there is little temperature rise above the two flight decks and what there is, 1-2°C, is again due to the aft DG. The GT plume in the Green 30 wind is clearly visible off the port side of the ship and the effectiveness of the eductor in cooling the exhaust gas is again evident in the right hand image.

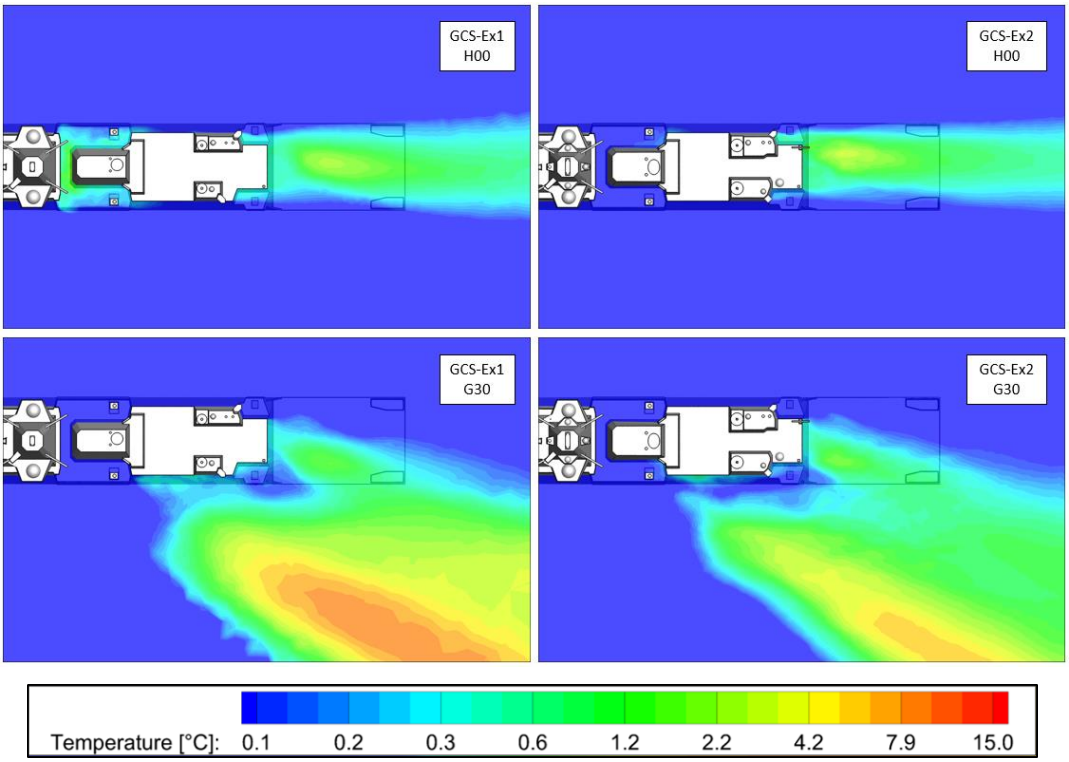

Figure 5.17: Contours of mean temperature rise above ambient on an exponential scale at hangar height on the GCS-Ex1 (left) and GCS-Ex2 (right), in headwind (top) and Green 30 (bottom) WOD conditions at 25 knots

The third orthogonal view of the ship and the exhaust plumes is from astern, Figure 5.18; this time the vertical plane is through the landing spot which is about half way along the landing deck. In the headwind the initial GCS-Ex1 analysis shows that the maximum average temperature above ambient is about 25°C and is in the core of the jet about 35m above the landing deck. The effect of the eductor in cooling the plume is clearly seen in the right hand image where the core of the plume is now only about 15°C. For both cases, the temperature rise above the deck, up to hangar height, is only 1-2°C and is due mainly to the exhaust from the aft DG. Figure 5.18 shows clearly how the Green 30 WOD deflects the exhaust plume to the port side of the ship. Furthermore, the oblique wind is deflected downwards in the lee of the ship so the airwake draws the exhaust plume down into the area occupied by the helicopter when hovering off the port side (the rotor hub will be about one ship-width off the edge of the deck). In both cases, therefore, the outer section of the rotor disc will experience average temperatures 5-6°C above ambient. Consistent with the observation in Chapter 3, the greater threat to the helicopter from the GT plume is not in the headwind case, because the height of the plume core is significantly above the height where the ship's helicopter will operate, unlike in the oblique wind where the airwake will entrain the hot exhaust gases downwards into a region where the helicopter can be expected to operate.

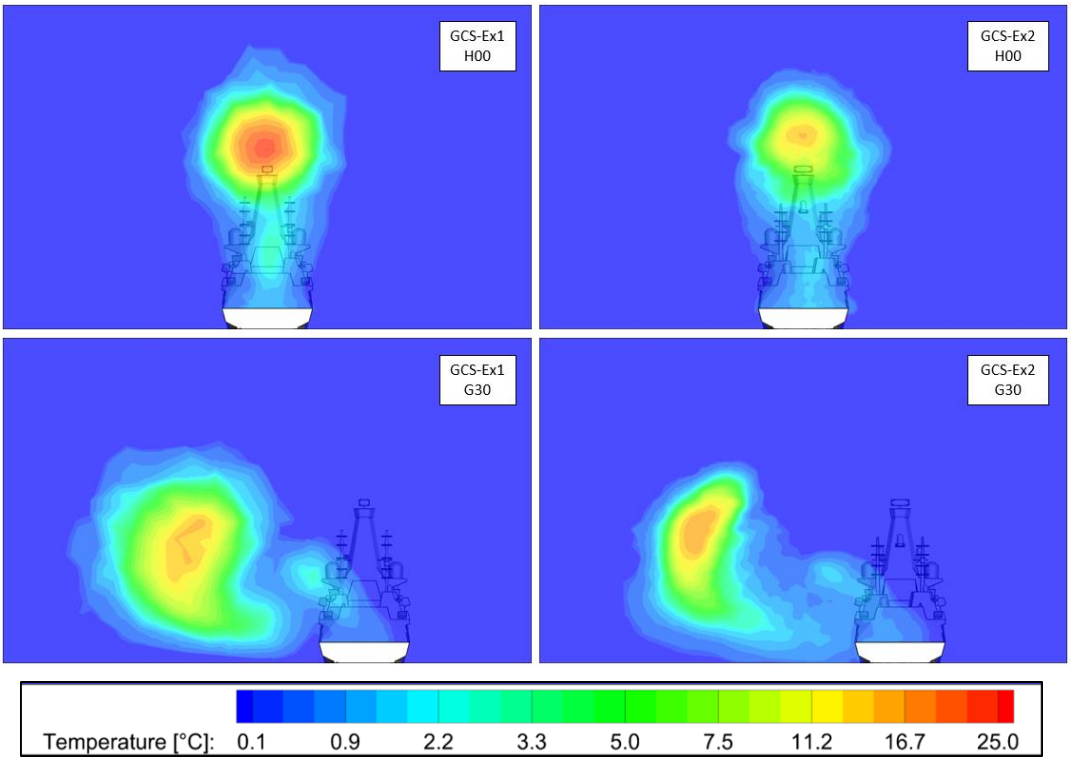

Figure 5.18: Contours of mean temperature rise above ambient on an exponential scale across the landing spot on the GCS-Ex1 (left) and GCS-Ex2 (right), in headwind (top) and Green 30 (bottom) WOD conditions at 25 knots

From the discussion above it can be seen that the addition of the eductor has affected both the cooling of the engine exhaust gases and their trajectory; nevertheless, the initial analysis without the eductor was still valuable during the period of development of the GCS as the issues raised were still pertinent when the eductor was included. In the following section, further analysis of the exhaust gas dispersion was undertaken for the eductor system of GCS-Ex2 with different operating conditions.

5.2.2.3. Exhaust Gas Dispersion for GCS-Ex2 with Different Engine Settings

In this section the conditions were varied such that different engine power settings were used and, because this will affect the ship's speed, different wind speeds were applied. Furthermore, the ambient temperatures were changed. The conditions tested were specified by BAE Systems to cover a range of potential operational scenarios.

Table 5.2 lists the parameters used in the CFD analysis. There are three wind speeds; the 25 knots already considered and two new wind speeds of 18 and 12 knots. For the slower 12 knots the GT is not operating and power comes from one forward and one aft DG; for this case the ambient temperature was taken as 10°C – a representative average operational condition. For the 18 knots case the GT is operating, along with the two DGs and the ambient temperature is 20°C. For the 25 knots case, as in the previous section, the GT and two DGs

are operating and the ambient temperature is 30°C – a condition only likely to be encountered when operational in areas such as the Gulf, but one most likely to cause concern for helicopter operations. The CFD analysis was again carried out for winds from Ahead and Green 30 and for this part of the study more information is given in the results on the unsteady nature of the temperatures to provide greater detail for the helicopter operators.

Table 5.2: Exhaust configurations for a comparative assessment of plume trajectory and dispersion of the GCS-Ex2 for three operating conditions

	12 knot			18 knot			25 knot		
	GT	**Fwd Port DG**	**Aft DG**	**GT**	**Fwd Port DG**	**Aft DG**	**GT**	**Fwd Port DG**	**Aft DG**
Exhaust mass flow (kg/s)	N/A	4.38	4.38	158.9	4.38	4.38	158.9	4.38	4.38
Exhaust Temp. (K)	N/A	590.2	590.2	609.8	590.2	590.2	609.8	590.2	590.2
Exhaust Average Exit Velocity (m/s)	N/A	28.3	28.3	39.3	28.3	28.3	39.3	28.3	28.3
Freestream Velocity (m/s)	6.17			9.26			12.86		
Ambient Temp. (°C)	10			20			30		

As in the previous section, the CFD output for the exhaust gas dispersion is presented in three orthogonal planes. Figure 5.19 presents a side view of the average temperature contours in the exhaust plume for the GCS-Ex2 (i.e. with the enhanced cooling due to the eductor) for the three different wind speeds and engine power outputs, and for the winds coming from ahead and from Green 30. Considering the headwind cases first, i.e. the left hand images, the top image is for the 12 knots wind speed with just one forward and one aft DG operating. The average air temperature above the flight deck is 1-2°C above ambient, due mainly to the gases from the aft exhaust being entrained into the lee of the hangar. Some of the exhaust gas from the forward DG is entrained into the wake of the main mast so surface heating in this area is a possibility. When the GT is operating and the wind speed is 18 knots it can be seen that the GT exhaust dominates, although the high temperature plume passes high above the flight deck and the temperatures over the flight deck are mainly due to the aft DG, as in the 12 knots case. There is again hot gas entrainment into the wake of the mast so surface heating is an issue. In the 25 knots case the GT and DG exhaust mass flows and

temperatures are the same as in the 18 knots case, so the temperature contours are similar except that the plume does not rise so high due to the stronger headwind.

In the three Green 30 cases it is only the aft DG exhaust gases that pass over the landing deck, although for progressively stronger winds. As a consequence, the core of the plume gets progressively cooler and passes lower over the deck as the wind speed increases, but the differences are not great.

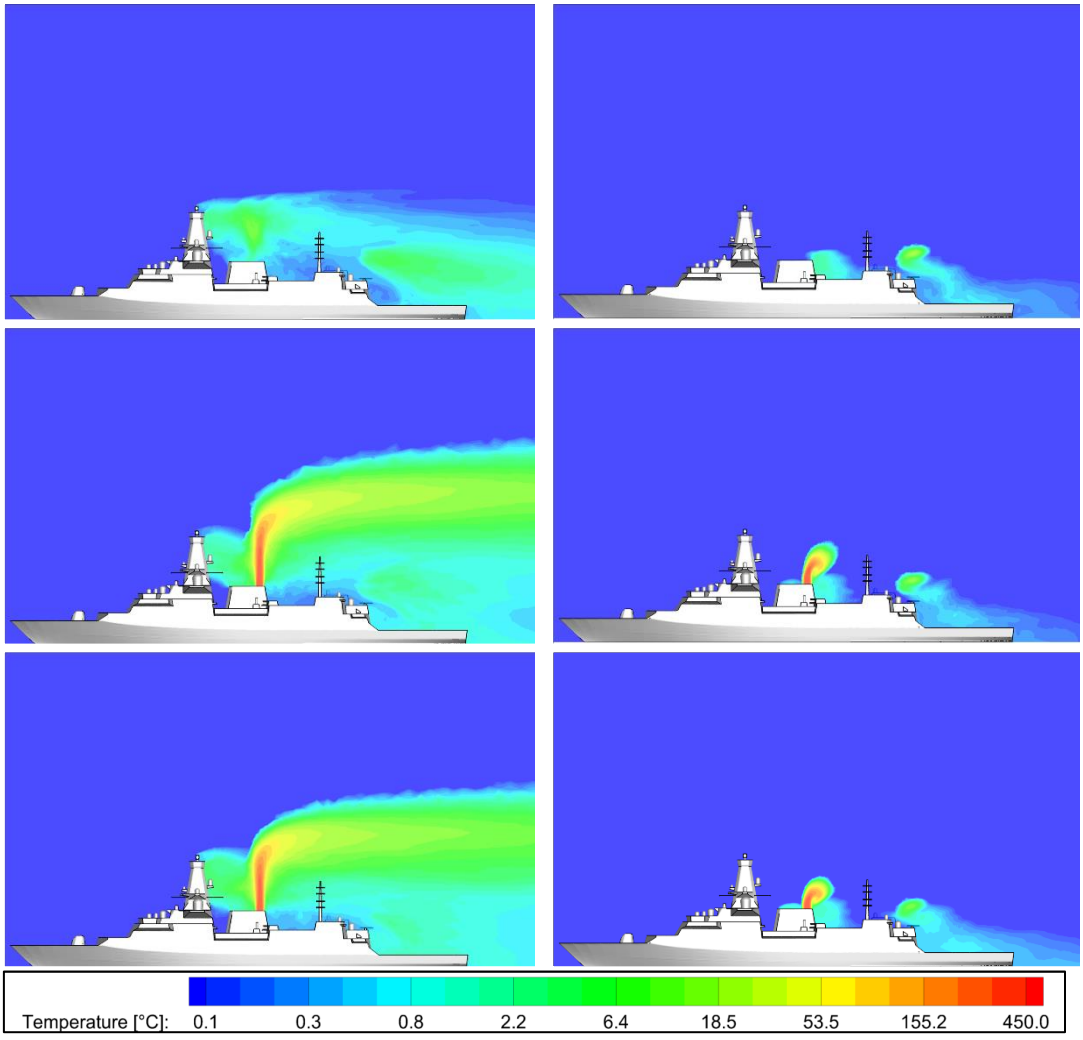

Figure 5.19: Contours of mean temperature above ambient on an exponential scale along the ship centreline in a 12 knots (Top), 18 knots (Middle) and 25 knots (Bottom) condition for a headwind (Left) and Green 30 (Right) WOD

Figure 5.20 shows a plan view of the exhaust plume where, again, the plane is at the height of the hangar. In the headwind it can be seen that the plume at that height is relatively narrow for the 12 knots wind speed when just the DGs are operating, and it gets wider when the GT is operating, probably due to some of the exhaust gases at the bottom edge of the GT exhaust plume being entrained down towards the deck. The slightly higher average

temperature from the core of the DG plume can be seen over the centre of the deck in each case.

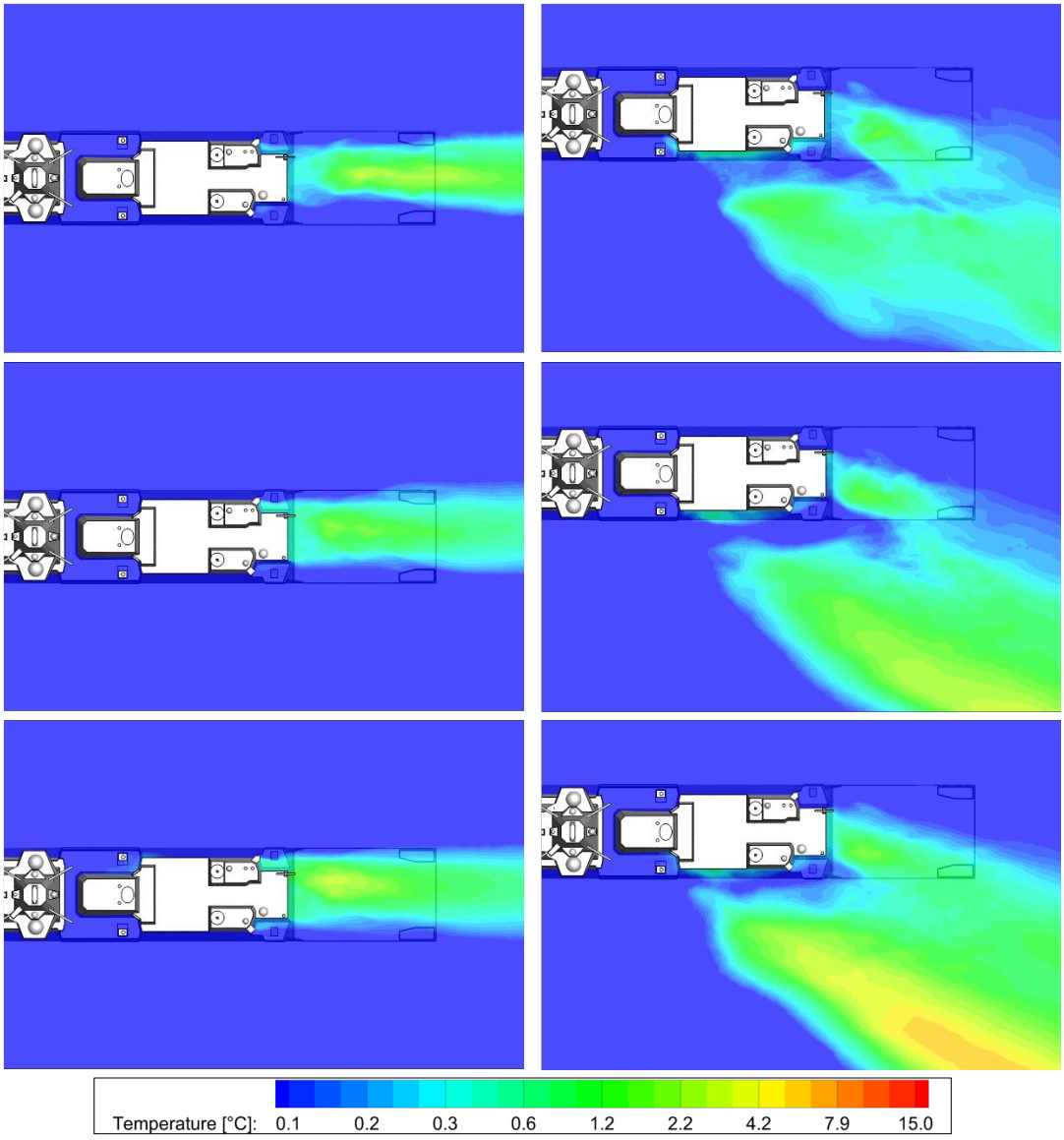

Figure 5.20: Contours of mean temperature above ambient on an exponential scale at hangar height in a 12 knots (Top), 18 knots (Middle) and 25 knots (Bottom) condition for a headwind (Left) and Green 30 (Right) WOD

In the Green 30 wind the aft DG exhaust plume can be seen passing across the flight deck in all three cases, while the plume from the forward DG and the GT passes across the area where the helicopter will hover alongside before translating to land on the deck. When only the DGs are operating, and the wind speed is 12 knots, it can be seen that the forward DG plume extends quite far off the port side, but the average temperature rise is less than 1°C. When the GT is operating in the 18 knots wind the core of the plume can be seen off the port side of the ship, with a maximum average temperature rise of about 3°C, and when the wind

speed increases to 25 knots the average temperature in the same area rises to about 6°C, due to the stronger wind deflecting the GT plume downwards more in the lee of the ship.

Figure 5.21 shows the increase in average air temperature above ambient in the vertical plane through the landing spot, viewed from astern, in a headwind. As previously, the average temperature above ambient is presented as coloured contours. Also included in these figures are plots of the average increase in temperature along a lateral line across the deck at hangar height, i.e. the red line, and the bars superimposed on the red line are plus/minus one standard deviation in the fluctuating temperatures. The plots were produced from interpolated mean data, taken at points spaced at 1m intervals across a 40m traverse line - represented by the position of the x axis on the image. In the 12 knots wind with just the DGs operating the small, low temperature plume can be seen; the slightly hotter zone over the flight deck is due to the aft DG, while the higher cooler plume is due to the forward DG. The red line shows that the maximum average temperature increase at the centre of the deck at hangar height is 2°C and that the fluctuation is quite large with a standard deviation of ±2°C, showing that the plume is unsteady with hot pockets of air passing through.

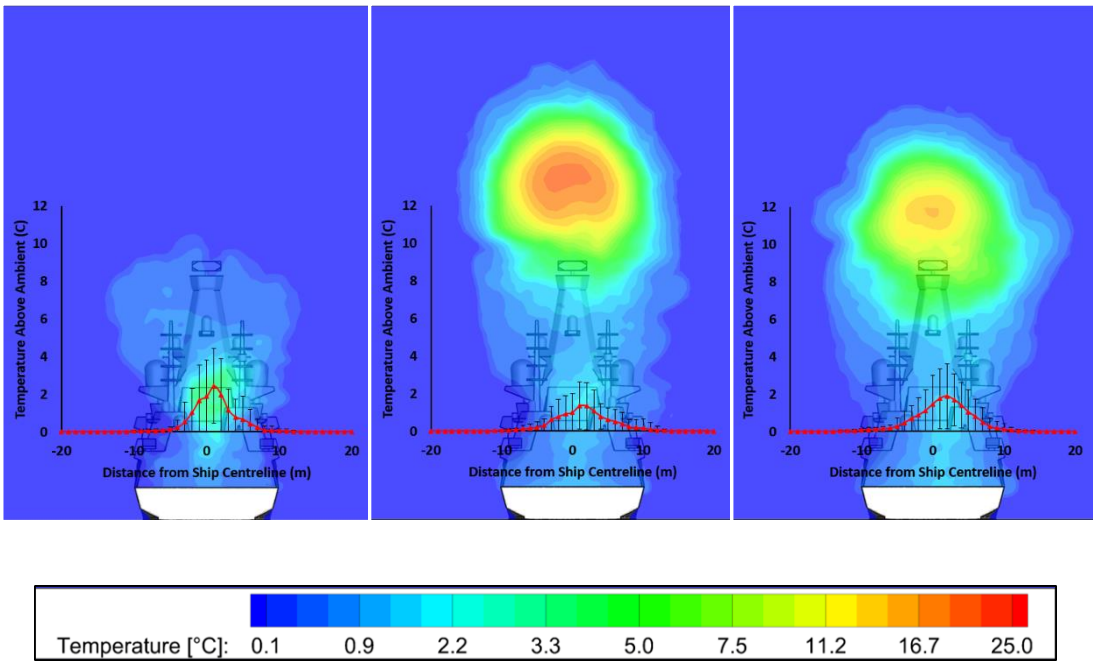

Figure 5.21: Contours of mean temperature rise above ambient on an exponential scale on a vertical plane across the landing spot for a 12 knots (Left), 18 knots (Middle) and 25 knots (Right) Headwind WOD condition with graphs of mean temperature rises along a lateral line at hangar height with the associated local standard deviations

In the 18 knots wind the GT plume is high above the deck with the core being at about 44m with an average temperature of about 25°C above ambient. At hangar height above the deck the red graph shows that the peak temperature is about 1°C above ambient, and will be due

to the aft DG exhaust which will now be cooled more in the 18 knot wind than in the 12 knot wind, and the fluctuations are lower. In the 25 knots case the average temperature at the core of the plume is about 15°C above ambient and at hangar height over the deck is slightly higher than the 18 knots case, probably due to some of the heated air in the lower portion of the GT plume being convected towards the deck, which is consistent with the higher values in the standard deviation.

To provide more detail of the unsteady air temperatures, Figure 5.22 shows the computed temperatures above the landing spot at hangar height (denoted on figure legend as HH), for the three different headwind speeds. The highest peak in the temperature is for the 12 knot case and is due to the aft DG whose exhaust outlet is just ahead of the flight deck and will therefore not have cooled so much. Temperature fluctuations such as these, if the air is ingested into the helicopter's engine, can cause problems for the engine's control system which monitors air inlet temperature.

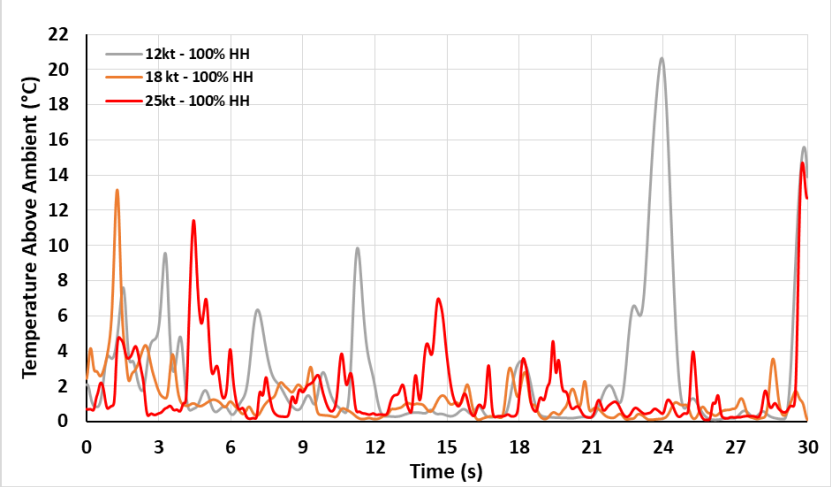

Figure 5.22: Unsteady temperature increases above the landing spot on the flight deck at hangar height, in a 12, 18 and 25 knot Headwind WOD condition

Another way of looking at the same data is to consider the 3-second average, as shown in Figure 5.23, which CAP 437 specifies should not exceed 2°C above ambient. It can be seen that for most of the time the predicted increase in the averaged air temperature is 2-3°C above ambient. The obvious exception is the peak in the 12 knots case; as mentioned above this will be due to the aft DG exhaust, which although it is relatively hot, it will not be a large mass of air and by the time it is ingested into the helicopter engine it would probably be cooled further. Nevertheless, the fluctuating air temperatures need to be taken into account by the helicopter operator.

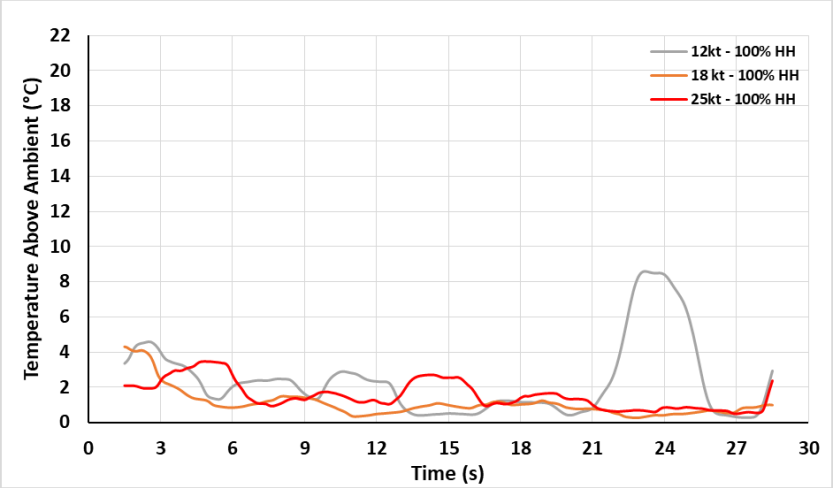

Figure 5.23: 3 second moving average of the unsteady temperature increase above the landing spot on the flight deck at hangar height, in a 12, 18 and 25 knot Headwind WOD condition

Figure 5.24 shows both the unsteady temperature and the 3-second average for the 18 knots case in the core of the plume, high above the landing spot (see Figure 5.21). At this height, 44m (550% HH), the plume is above the area where the helicopter will operate but, nevertheless it can be seen that the unsteady elevated temperatures present a threat to the helicopter should it fly through this part of the plume.

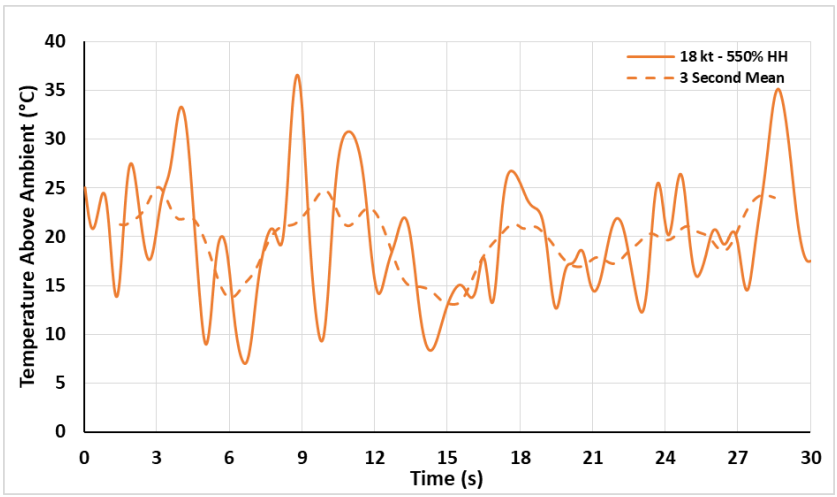

Figure 5.24: Unsteady temperature and moving 3-second average at 44m (550% hangar height) above the landing spot, at the approximate core of the plume for the 18 knot headwind

Considering the plume temperatures for the Green 30 winds at 12, 18 and 25 knots, Figure 5.25 shows contours of average air temperature above ambient in the vertical plane through the landing spot, including the area off the port side of the ship where the helicopter will begin its landing manoeuvre. Also included in the images are the average temperature along a line at hangar height and the bars indicating plus/minus one standard deviation.

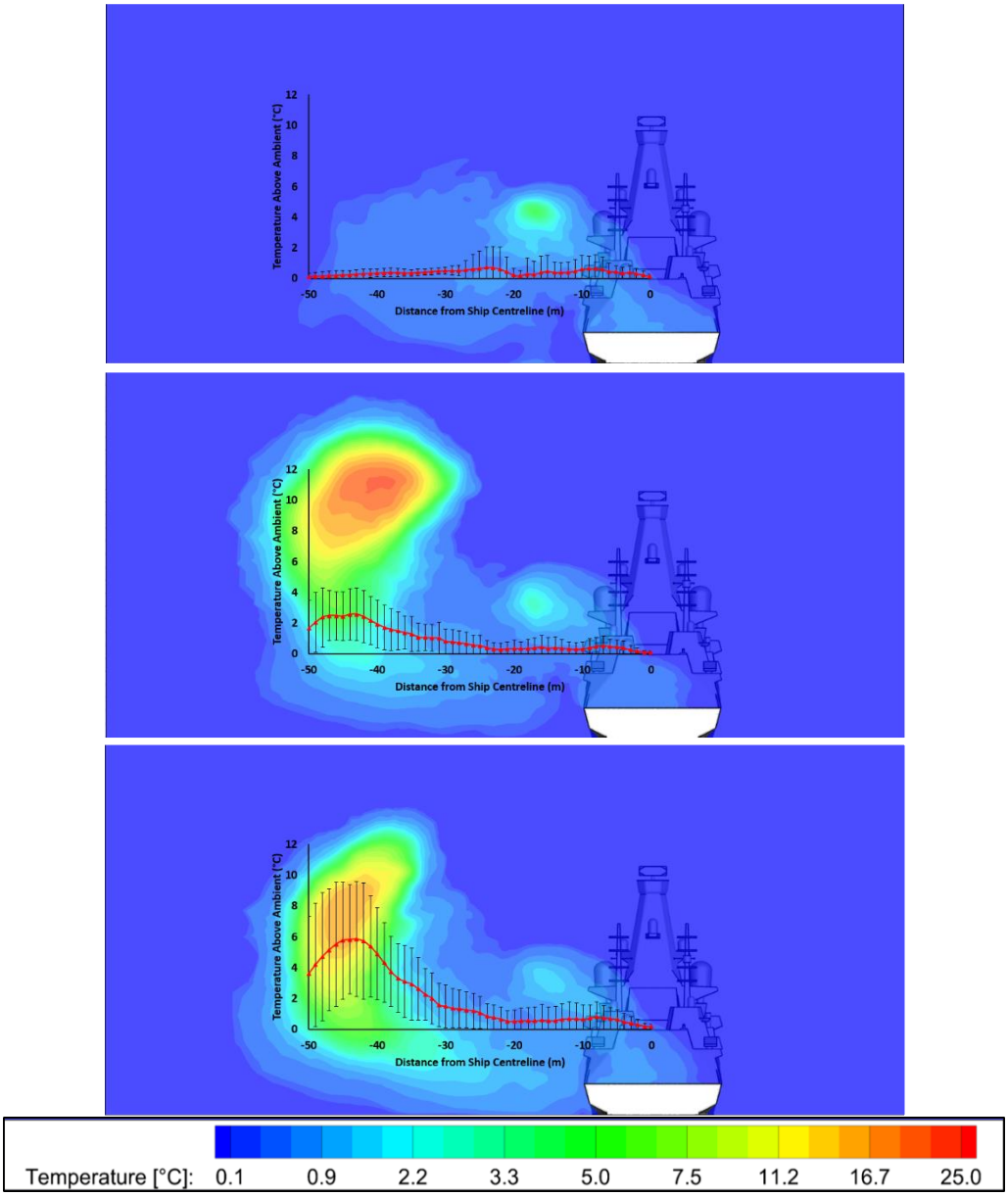

Figure 5.25: Contours of mean temperature rise above ambient on an exponential scale on a vertical plane across the landing spot for a 12 knot (Top), 18 knot (Middle) and 25 knot (Bottom) Green 30 WOD condition with graphs of mean temperatures along a lateral line at hangar height with the associated local standard deviations

In the 12 knots case the exhaust plume from the forward DG exhaust can be seen in Figure 5.25 but the average increase in temperature is less than 1°C, although there are fluctuations as indicated by the standard deviations. The more significant data are for the 18 and 25 knots cases where, comparing them, it can be seen that although the 18 knots case has the higher plume temperature, because the lower wind speed creates less energetic mixing and less of a downdraft, the core of the plume is higher than that for the 25 knots case. The greater threat to the helicopter, therefore, is in the 25 knots wind due not only to the higher local

temperature off the port side of the ship, but also the greater fluctuations. Having said that, the higher temperature plume in the 18 knots case does present a significant threat for the helicopter should it fly in that area.

Figure 5.26 shows the computed unsteady air temperatures at a point 30m (1.5 beam widths) off the port side of the ship, at hangar height, in line with the landing spot for the three wind speeds. Consistent with the discussion above, the highest temperature elevations and the highest fluctuations are for the 25 knots case. Looking at the 3-second averages in Figure 5.27 it can be seen that the values are above the 2°C recommended by CAP 437 so this condition should be considered as threat by the helicopter operator.

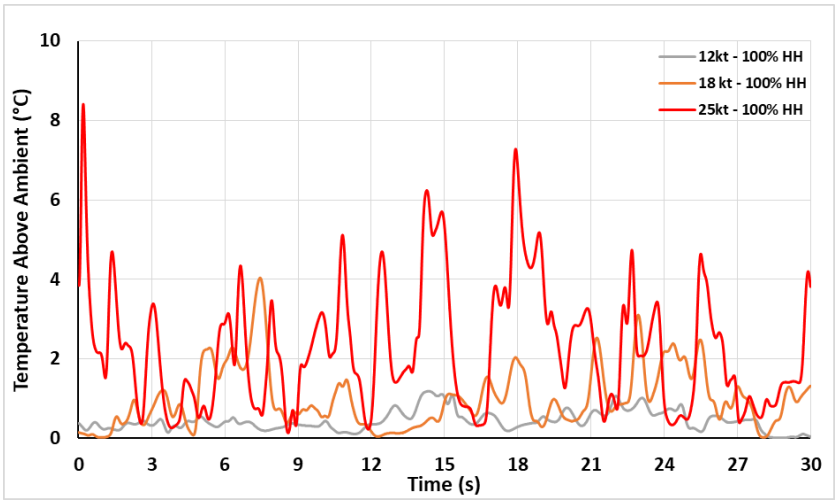

Figure 5.26: Unsteady air temperature increase at 1.5 beam widths to port of the landing spot at hangar height, in a 12, 18 and 25 knot Green 30 WOD condition

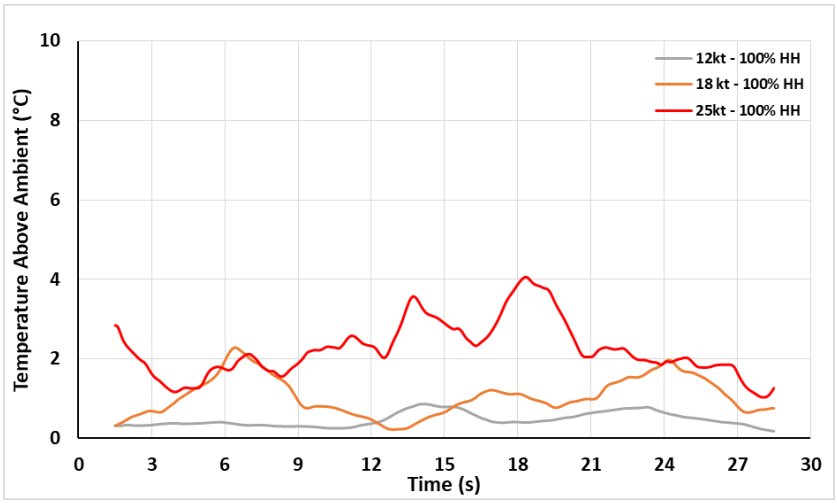

Figure 5.27: 3-second moving average of the unsteady temperature increase at 1.5 beam widths to port of the landing spot at hangar height, in a 12, 18 and 25 knot Green 30 WOD condition

The visualisation of the plume as contours of average temperatures above ambient that has been used in the discussion to this point gives the impression that the plumes are “solid” volumes of heated air, albeit with a temperature variation within them. The unsteady nature of the plume is as important as the average values of temperature rise, which is why the more demanding time-accurate CFD analysis has been undertaken. The final set of figures in this discussion of the engine exhaust gas dispersion contains three sets of ten images that show instantaneous temperature contours of the plume in three orthographic views, in the 18 knots headwind, Figure 5.28, 5.29 and 5.30. The images are recorded at 3 second intervals and so the 10 images represent the 30 seconds of computed flow. The plume is highly chaotic and has voids within it which are reflective of the unsteady data presented above. The combined data set will be used to establish protocols and procedures for how the ship’s helicopter should be operated, in particular when the GT is in operation. The study that has been presented is the first time that the exhaust plume from a Royal Navy ship has been evaluated using CFD, rather than wind tunnel testing; it is also believed that this is the first time it has been done for any naval ship in the world.

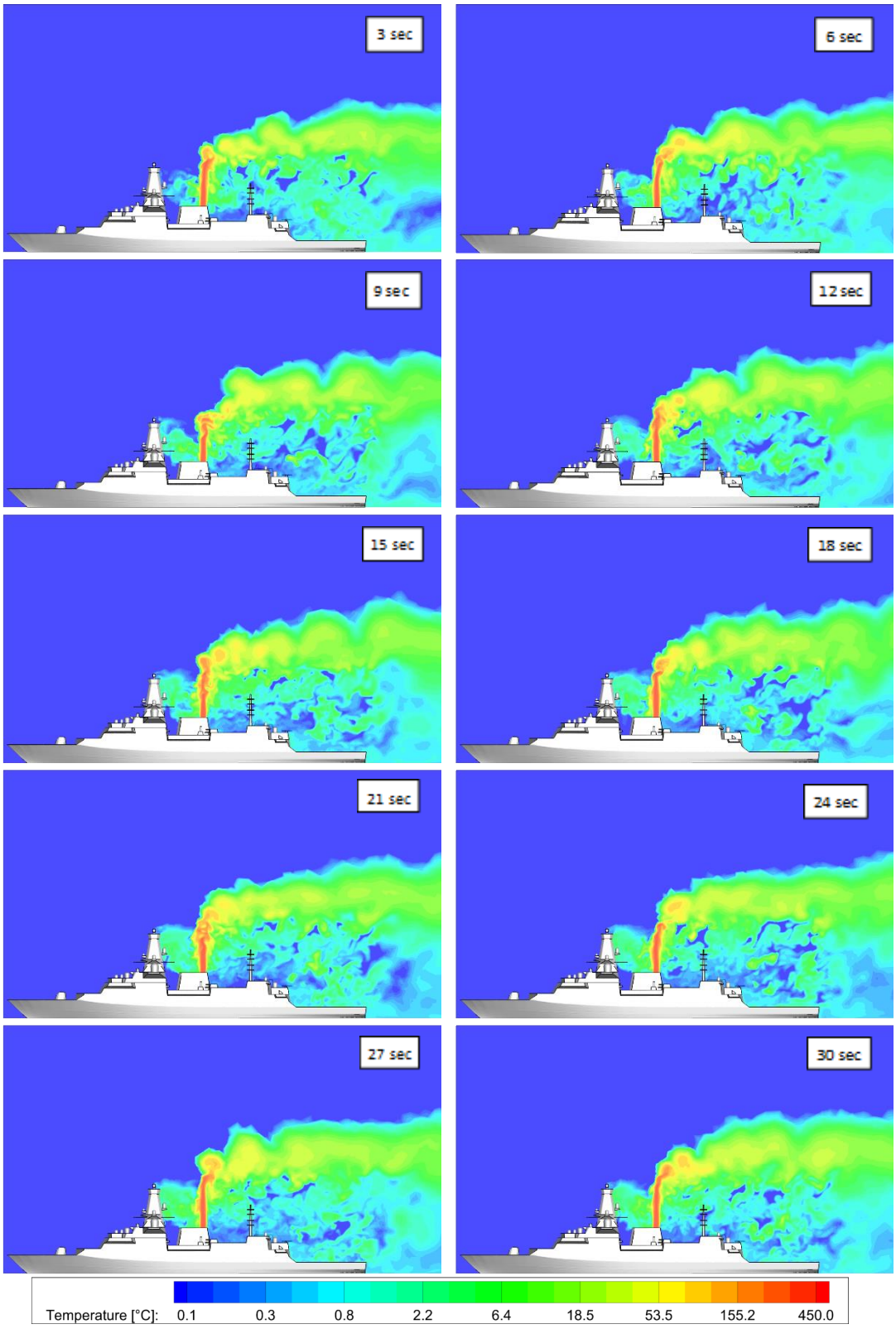

Figure 5.28: Side view of instantaneous contours of temperature above ambient with GCS-Ex2 in a headwind condition at 18 knots taken at 3 second increments from a 30 second data set

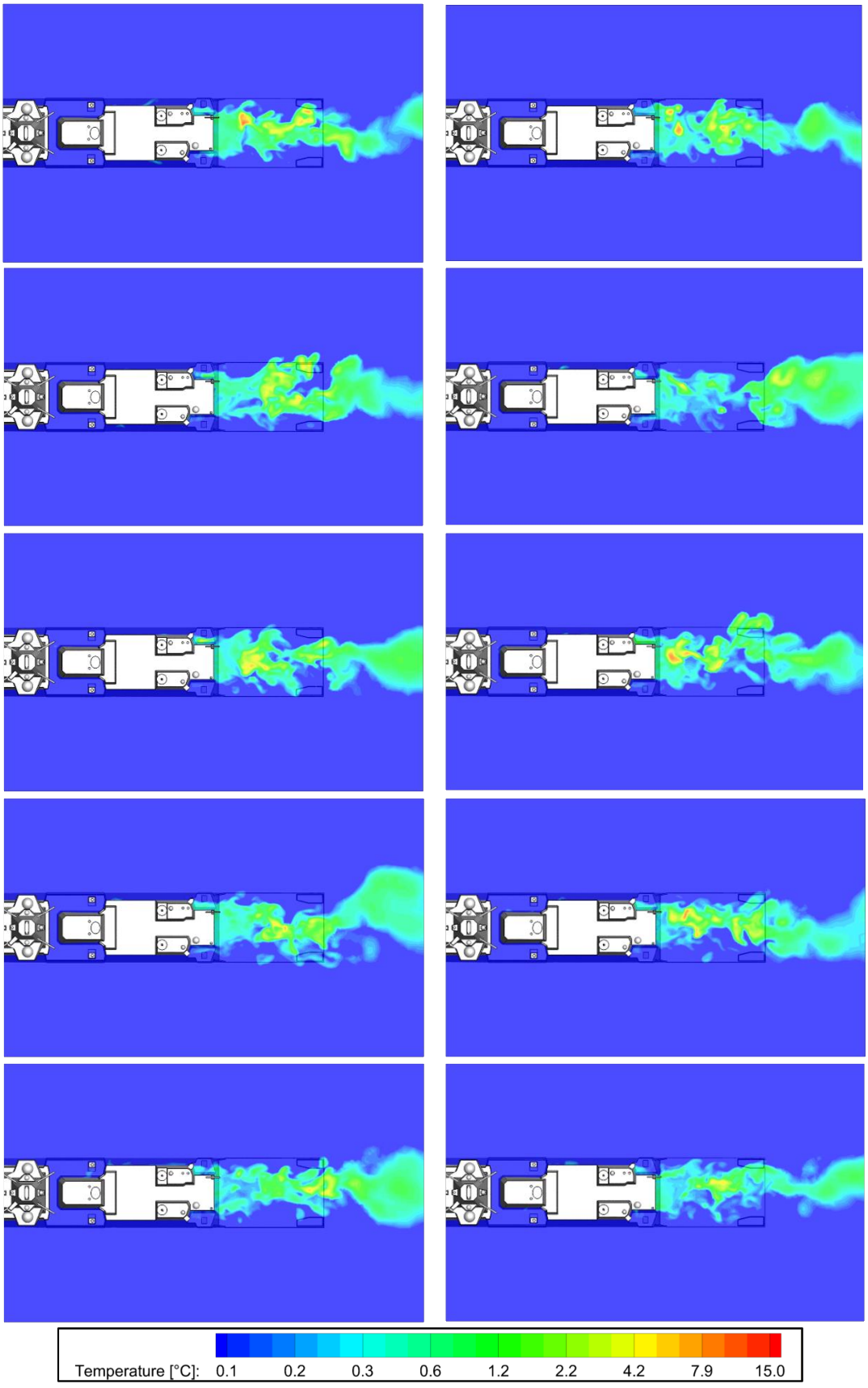

Figure 5.29: Plan view of instantaneous contours of temperature above ambient, shown at hangar height of the GCS-Ex2 in a headwind condition at 18 knots taken at 3 second increments from a 30 second data set

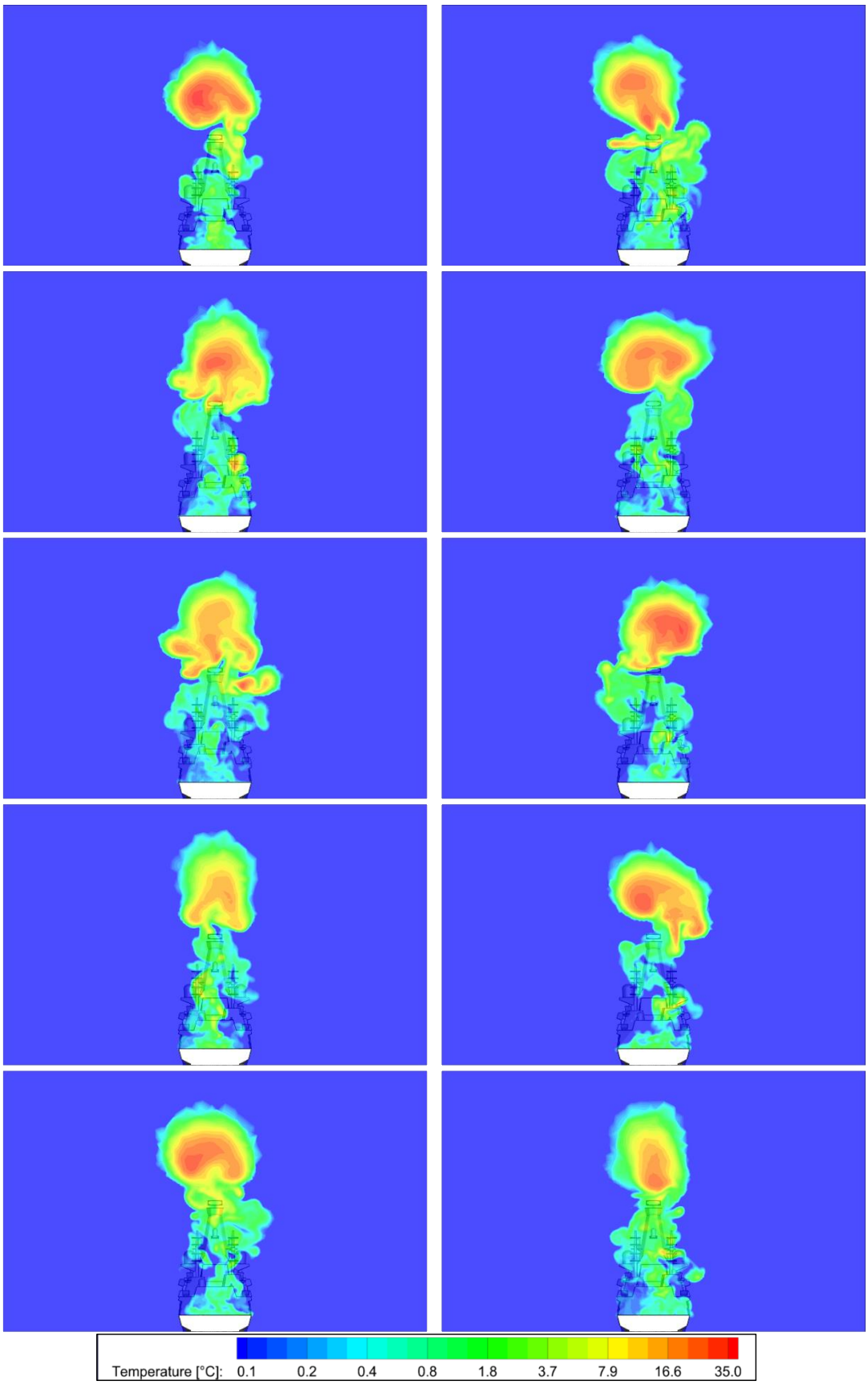

Figure 5.30: Stern view of instantaneous contours of temperature above ambient across the landing spot of the GCS-Ex2 in a headwind condition at 18 knots taken at 3 second increments from a 30 second data set

5.3. An experimental Study of a Hot Air Jet in Turbulent Cross-Flow

As seen in the previous sections, the mixing of the hot engine exhaust gases with the turbulent cross-flow of the ship's airwake creates a highly complex flow field. While there are experimental data to provide some validation of the isothermal ship's airwake, there is no comparable data for the mixing of the hot air jet with the airwake. Although not in the original scope of work, it was decided towards the end of the project that an experiment should be conducted using a simple geometry to provide data to compare with a CFD solution. A rectangular box was placed on the floor of a wind tunnel, to represent the bluff body of the ship's superstructure, and a jet was discharged into the turbulent cross flow through a convergent nozzle that was flush with the top surface of the box. Unsteady three-component velocity measurements were taken downstream of the box for an unheated jet with a 4-hole Cobra Probe, while unsteady temperature measurements were taken for a heated jet using an ultra-fine wire Type K thermocouple. The wind tunnel experiment was then replicated using the same unsteady CFD methodology employed for the full-scale ship airwake simulations and the results compared.

5.3.1. Heated Jet in Cross-Flow

While there are published data for wind tunnel tests on ships with exhaust gas [115], [117], [130], these mostly involve smoke flow visualisation and there is no data available for unsteady temperature measurements suitable for unsteady CFD validation. In its most fundamental form the funnel exhaust flow is a jet in cross-flow, which has been extensively studied. Figure 5.30, derived from Fric & Roshko [131], shows a jet emerging from an orifice that is flush with the surface. The momentum of the cross-flow causes the jet to deflect while the shear-stress on the jet surface causes the formation of a counter-rotating vortex pair. This double vortex structure is known to enhance the mixing between the jet and the cross flow. In the context of a jet discharging into the airwake of a ship, the additional turbulence caused by the flow being shed from the ship superstructure should cause the jet to mix even more effectively. For typical flow velocities and temperatures found in the discharge of engine exhausts over a ship, the flow is momentum-dominated, and buoyancy forces are secondary [132], [133]. This observation was supported in a study by Johnson et al [134] of the heated airflow from a raised circular stack. Also, reviewing the literature, there is some difference of opinion on whether the jet trajectory is characterised by the ratio of the jet to cross-flow velocities, or by the ratio of the corresponding momentum fluxes.

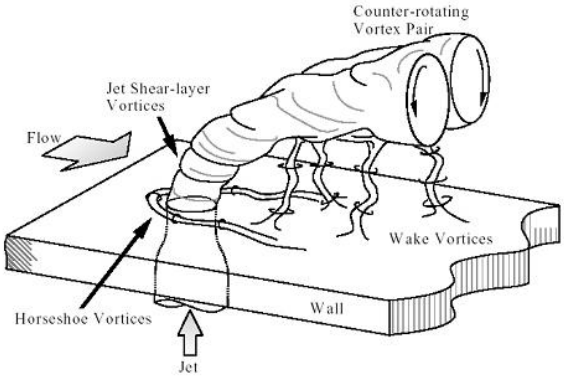

Figure 5.30: Common vortical structures of a jet in crossflow [131]

A simplified dimensional analysis of the flow over a cuboid, Figure 5.31, was used to determine the important dimensionless relationships that characterise the plume trajectory and mixing. The plume trajectory can be characterised by a displacement, s, which will be a function of many variables. Discounting the thermal properties of the fluid (i.e. conductivity and specific heat), s is a function of the velocities of the jet and cross-flow, as well as their densities and viscosities. The effect of buoyancy is recognised in the dimensional analysis by including g, the gravitational acceleration, while the length scale is recognised through the height of the box, L. Therefore, s is a function of:

$$s = f\left(U_c, U_e, \rho_c, \rho_e, \mu_c, \mu_e, g, L\right) \tag{5.1}$$

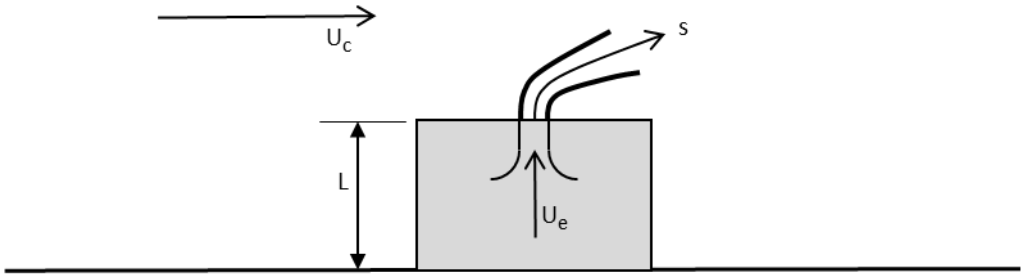

Figure 5.31: Dimensional analysis of flow over cuboid with jet

The dimensionless groups can be constructed in many ways; here they are collected according to the convention that has emerged from the extensive research into jets in cross-flow and chimney exhaust plumes.

$$\left\{\frac{s}{L}\right\} = f\left\{\frac{\rho_c U_c L}{\mu_c}, \frac{\rho_e U_e L}{\mu_e}, \frac{\rho_e U_e^2}{\rho_c U_c^2}, \frac{\rho_e}{\rho_c}, \frac{g L}{U_c^2}\frac{\left(\rho_c - \rho_e\right)}{\rho_c}\right\} = f\left\{Re_c, Re_e, J, \frac{\rho_e}{\rho_c}, Ri\right\} \tag{5.2}$$

Where Re is the Reynolds number, J is the momentum flux ratio, and Ri is the Richardson number.

As is often the case, it is not possible to simultaneously match all the dimensionless numbers when scaling between model and full scale experiments, but experience shows that the flows, particularly over bluff bodies with sharp edges, are independent of Reynolds number, and the scaling is well represented by:

$$\left\{\frac{S}{D}\right\} = f\left\{J, Ri\right\} \tag{5.3}$$

Matching the momentum flux ratio, J, between the model-scale [m] and the full-scale [f]:

$$\left[\frac{\rho_e U_e^2}{\rho_c U_c^2}\right]_m = \left[\frac{\rho_e U_e^2}{\rho_c U_c^2}\right]_f \tag{5.4}$$

or, if the cross-flow is ambient air for both the model and full-scale, then

$$\left[\frac{U_e}{U_c}\right]_m = \sqrt{\frac{\left[\rho_e\right]_f}{\left[\rho_e\right]_m}}\left[\frac{U_e}{U_c}\right]_f \tag{5.5}$$

Matching the Richardson number gives:

$$\left[\frac{D}{U_c^2}\frac{\left(\rho_c - \rho_e\right)}{\rho_c}\right]_m = \left[\frac{D}{U_c^2}\frac{\left(\rho_c - \rho_e\right)}{\rho_c}\right]_f \tag{5.6}$$

And if the cross-flow is ambient air in both cases, then:

$$\left[\frac{D\left(\rho_c - \rho_e\right)}{U_c^2}\right]_m = \left[\frac{D\left(\rho_c - \rho_e\right)}{U_c^2}\right]_f \tag{5.7}$$

In the case of the heated jet, for the two scaling parameters in Eqns. 5.5 and 5.7 the density ratio can be replaced by the ratio of the absolute temperatures (Ideal Gas Law), so that:

$$\left[\frac{U_e}{U_c}\right]_m = \sqrt{\frac{[T_e]_m}{[T_e]_f}}\left[\frac{U_e}{U_c}\right]_f \tag{5.8}$$

and:

$$\left[\frac{U_c}{\sqrt{D\left(1-\frac{T_c}{T_e}\right)}}\right]_m = \left[\frac{U_c}{\sqrt{D\left(1-\frac{T_c}{T_e}\right)}}\right]_f \quad (5.9)$$

And temperatures between the model and full-scale are represented by:

$$\left[\frac{T-T_c}{T_e-T_c}\right]_m = \left[\frac{T-T_c}{T_e-T_c}\right]_f \quad (5.10)$$

As mentioned above, there is some difference of opinion in the literature on whether the ratio of jet to cross-flow velocity or momentum flux are the appropriate scaling parameters. As can be seen from Eqn. 5.4, the momentum flux ratio is the correct parameter but if the two flows have the same density then the velocity ratio can be used. Also, referring to the literature, the statement is often made that in the case where the flow mixing is highly turbulent the process will be momentum dominated and the weaker buoyancy force will not be significant [132], [133]. Unfortunately there doesn't appear to be a recommended distinction between momentum dominated flows and buoyancy dominated ones. Returning to the current experiment (and the ship exhaust dispersion) both the cross flow and the jet have significant velocities and for the highly turbulent flow in the region close to the cuboid (and ship) it is reasonable to assume that momentum will dominate, while further downstream away from the area of interest buoyancy may become more significant. If this proposition is accepted, then the hot jet trajectory and the temperature field can be scaled using only the momentum flux ratio; this was tested in the experiment by choosing different jet temperatures and velocities that maintained a constant momentum flux ratio between the jet and the cross flow.

5.3.2. Experimental Investigation

The experiment was conducted in an open-section blower wind tunnel. Figure 5.32 shows a schematic of the experimental apparatus. The blower tunnel test section is immediately preceded by a settling section and a contraction that creates an air flow with a uniform inlet velocity profile in the 4ft x 2ft working cross-section; the air flow is controllable up to a maximum speed of 20 m/s. A 20 x 40 x 20 cm (width x length x height) rectangular box was used as a bluff body (simple representation of a ship superstructure) with a 25mm internal diameter exhaust outlet positioned centrally and flush to the top surface. The box was manufactured from rectangular panels of 25mm thick ceramic insulation board. The heated air for the jet was injected from the heating system into the bottom of the rectangular box

onto an internal flat plate to force the flow to spread radially and promote mixing/settling inside the box before being accelerated through a convergent section into a 25mm diameter × 25mm long pipe to ensure a uniform velocity profile at the jet exit plane.

The jet air heating system consisted of a centrifugal blower attached to a pipe with a mass flow rate meter, feeding into a heater made of two hot wire thermal elements taken from De Walt DW340K heat guns. A closed-loop feedback control system was devised that adjusted the heating power to maintain a constant temperature measured by a Type K thermocouple placed inside the box close to the inlet of the exhaust nozzle. The electronic control system therefore allowed the jet mass flow rate and temperature to be controlled through a combination of the power supplied to the centrifugal blower and to the heater elements. At maximum power to the centrifugal blower motor and heating elements (4kW), 52kg/hr of air flow could be produced at a temperature of 265°C; higher jet temperatures could be reached by reducing the air mass flow rate.

A manually operated 3-D traverse system was designed, incorporating a sting arm to probe into the open test section and locate the measurement instrument to a positional accuracy of about 1mm in all directions. The sting arm was designed with two interchangeable mounting tips to hold either the ultra-fine wire Type K thermocouple or the Cobra Probe.

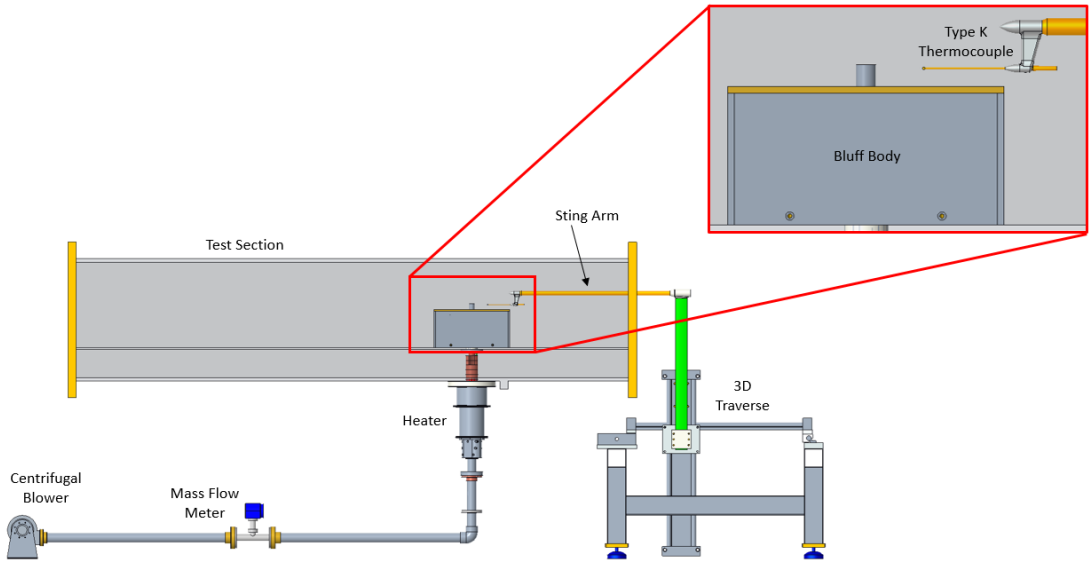

Figure 5.32: Schematic of Wind Tunnel Experiment

A Medtherm Corporation ultra-fine wire Type K thermocouple (Nickel-Chromium / Nickel-Alumel) was chosen as the instrument for temperature measurement due to its ability to capture high frequency transient gas temperatures and its common use in internal

combustion engine research to measure temperature fluctuations. The specific model used for this experiment consisted of a 0.0005" (0.0127 mm) diameter fine wire. A diagram of the probe is shown in Figure 5.33 where it can be seen that the very fine wire forms a small junction, which is exposed directly to the fluid being measured.

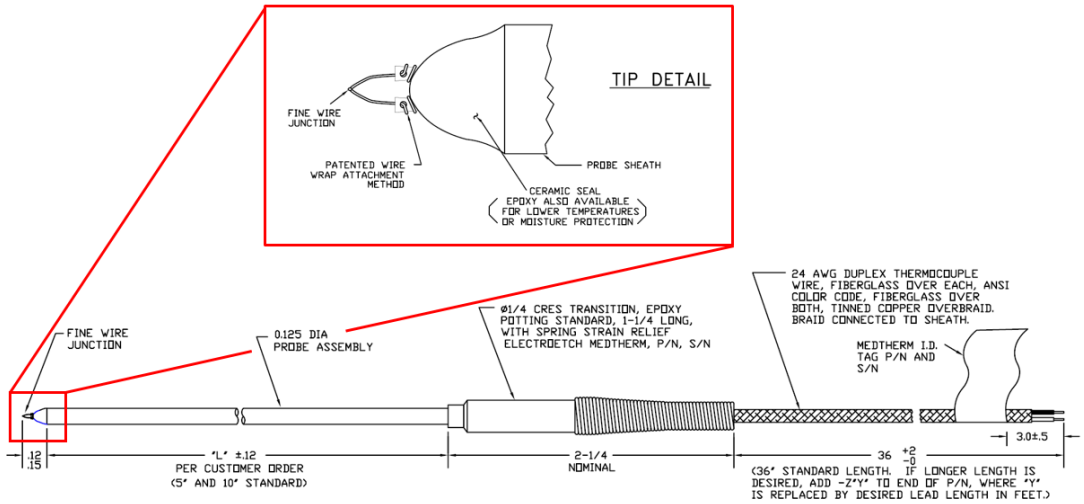

Figure 5.33: Ultra-fine wire Type K rapid response thermocouple [Medtherm™]

The frequency response of a thermocouple is determined by the size (mass) and specific heat capacity of the thermocouple junction, and the convective heat transfer between the fluid being measured and the junction. Carbon et al., [135] provide an equation, derived from a heat balance, of the temperature change of the thermocouple junction with time.

$$(T_i - T) = (T_i - T_a)\left(1 - e^{-\tau/\beta}\right) \tag{5.11}$$

Where,

$$\beta = \frac{\rho D c}{4h} \tag{5.12}$$

T_i= initial temperature as indicated by thermocouple before temperature change occurs

T= temperature indicated by thermocouple τ seconds after change occurs

T_a = temperature of air stream after temperature change occurs

ρ = density of thermocouple material

c = specific heat of thermocouple material

h = coefficient of heat transfer

D = diameter of thermocouple wire

τ = time elapsed after temperature change occurs.

The heat transfer coefficient, h, is calculated from the convection correlation recommended by [135].

$$Nu = 0.32 + 0.43(Re)^{0.52} \tag{5.13}$$

Where, Re, is the Reynolds number of the air flowing past the thermocouple junction defined by:

$$Re = \frac{\rho V D}{\mu}\Big]_a \tag{5.14}$$

To provide an indication of the expected response time for the thermocouple, Equations 5.11 to 5.13 were used to calculate the value of τ for different values of $(T_i - T)/(T_i - T_a)$ by taking typical values for properties of air and of nickel, which is the principal material in the thermocouple. From the experiment it was found that a typical temperature of the heated plume was 50°C so the following values were used for an average air temperature of 35°C:

Air
ρ=1.13 kg/m^3
k = 0.027 W/m.K
μ = 1.95×10^{-5} kg/m.s
V = 10 m/s

Nickel
ρ = 8900 kg/m^3
c = 440 J/kg.K
D = 12.7×10^{-6} m

The resultant graph of $(T_i - T)/(T_i - T_a)$ vs response time in milliseconds is shown in Figure 5.34; so, for example, when there is an instantaneous change in air temperature, the thermocouple will read 99% of the true value in 17ms.

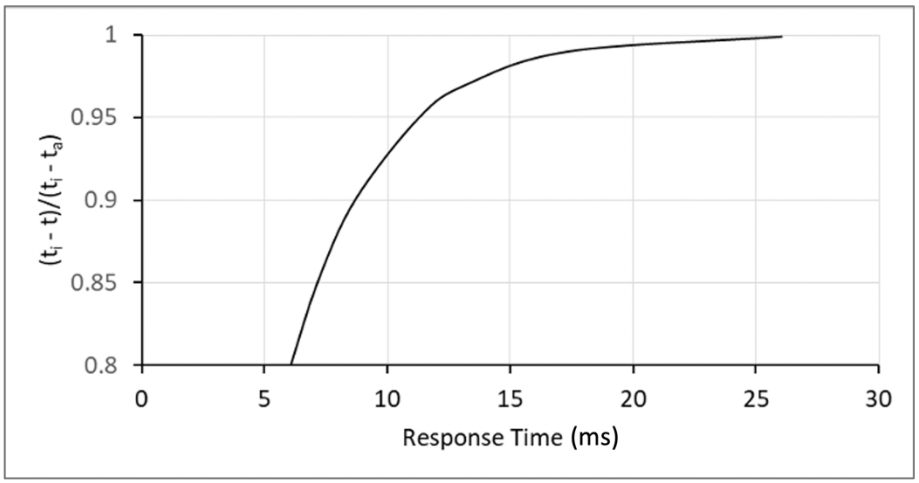

Figure 5.34: Thermocouple response

Figure 5.35 shows a typical output from the thermocouple when placed in the middle of the plume over a 10 second period; inserted into the figure is an expansion of the plot over 1 second, showing the major fluctuations appear to have a frequency of typically 40Hz, suggesting the thermocouple is sufficiently responsive to measure the unsteady temperature fluctuations in the experiment.

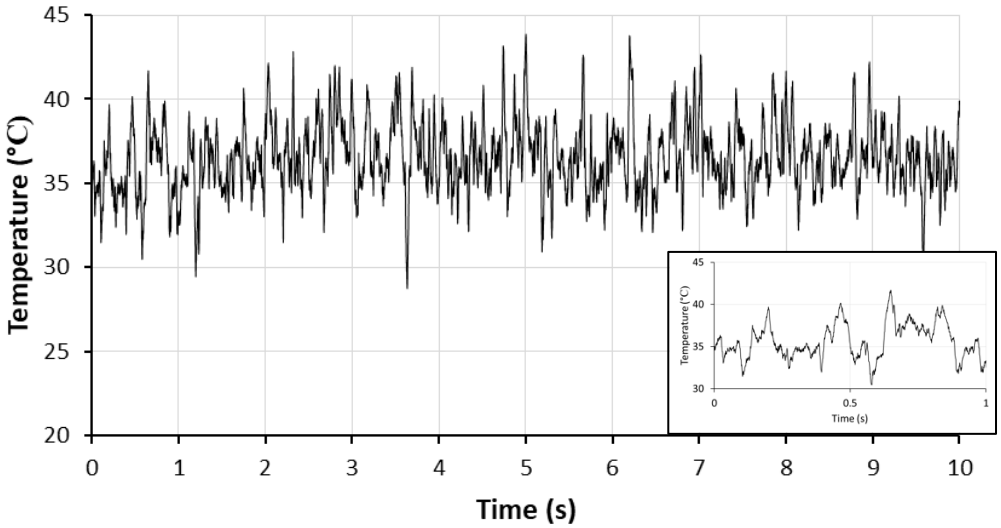

Figure 5.35: Typical unsteady output from fine-wire thermocouple

Air velocities were measured by a Cobra Probe™ which is a four-hole pressure probe and which, therefore, could not be used when temperatures were changing. The velocity measurement experiment was therefore conducted with ambient air temperatures and for different jet and wind tunnel air speeds that gave a constant momentum flux ratio. The Cobra Probe, Figure 5.36, is manufactured by Turbulent Flow Instrumentation, who claim it is capable of capturing 3-component velocity data and pressure measurements across a wide frequency range from 0 Hz to upwards of 2000 Hz. The probe can take measurements of flow from angles within a 45° acceptance cone, Figure 5.37. There have been a number of independent studies into the use of the Cobra probe in various flow scenarios, for example [136], [137], who confirm the performance of the instrument.

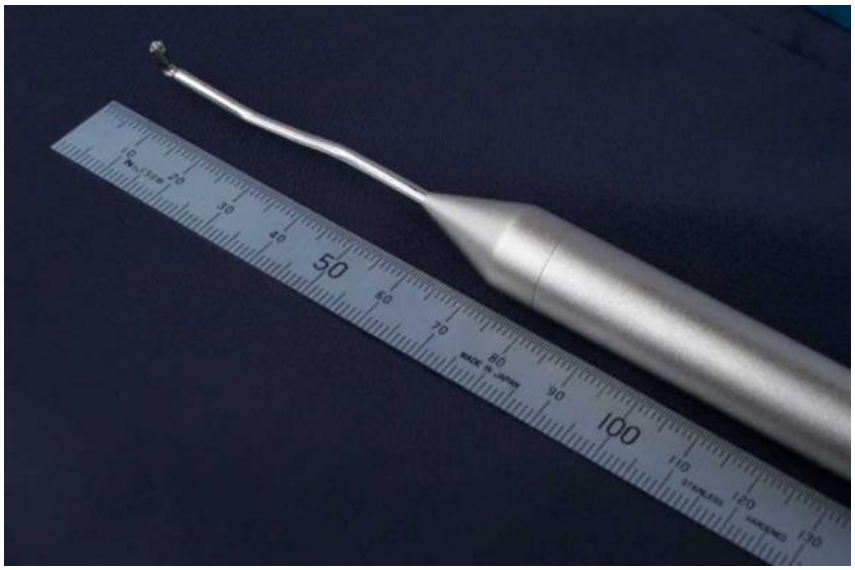

Figure 5.36: The Cobra Probe™ [138]

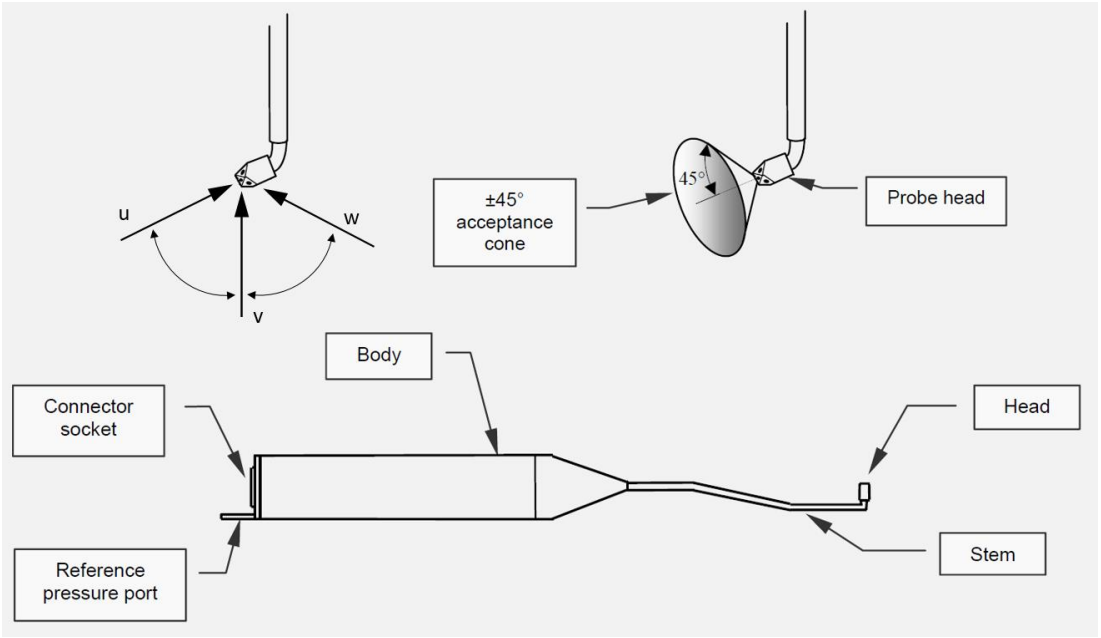

Figure 5.37: Cobra Probe (Turbulent Flow Instrumentation) [138]

5.3.2.1. Flow Visualisation

It was important that the jet emerging from the top of the box created a plume that did not interfere with the roof of the wind tunnel; it was also important to find a combination of jet and wind tunnel speeds and jet temperatures that produced a constant ratio of jet to cross-flow momentum flux. The first experiment undertaken used smoke flow visualisation to observe the jet trajectory while adjusting the flow speeds and temperature to obtain suitable and constant momentum flux ratios. Table 5.3 shows three settings of the experiment that produced both a suitable plume that did not get too close to the wind tunnel roof, and gave a constant momentum flux ratio of 5.82. For the earlier case of the GT exhaust of GCS-Ex2 with a 25 knots wind, the momentum flux ratio was 4.65, so 5.82 is also a realistic value. It can be seen from Table 5.3 that the range of jet temperatures was 168 to 253°C, while the jet and wind tunnel air velocities ranged from 12.49 to 21.54m/s and 3.87 to 6.06m/s, respectively. The range of conditions was therefore significant and provided a good test for the momentum flux ratio as a scaling parameter. Figure 5.38 shows three images of the plume, one for each setting in Table 5.3, which was visualised by introducing smoke at the jet outlet. Despite the unsteady nature of the flow and the variability of introducing the smoke, the images show that, at least qualitatively, the plume trajectories are the same.

Table 5.3: Wind Tunnel Experiment Parameters for Heated Jet

	Setting 1	**Setting 2**	**Setting 3**
Jet Exhaust Temp (°C)	168	364	253
Jet Exhaust Density (kg/m^3)	0.8	0.55	0.67
Jet Mass Flow Rate (kg/s)	0.00605	0.00605	0.00425
Jet Velocity (m/s)	14.92	21.54	12.49
Crossflow Velocity (m/s)	5.04	6.06	3.87
Momentum Flux Ratio	5.82	5.81	5.81

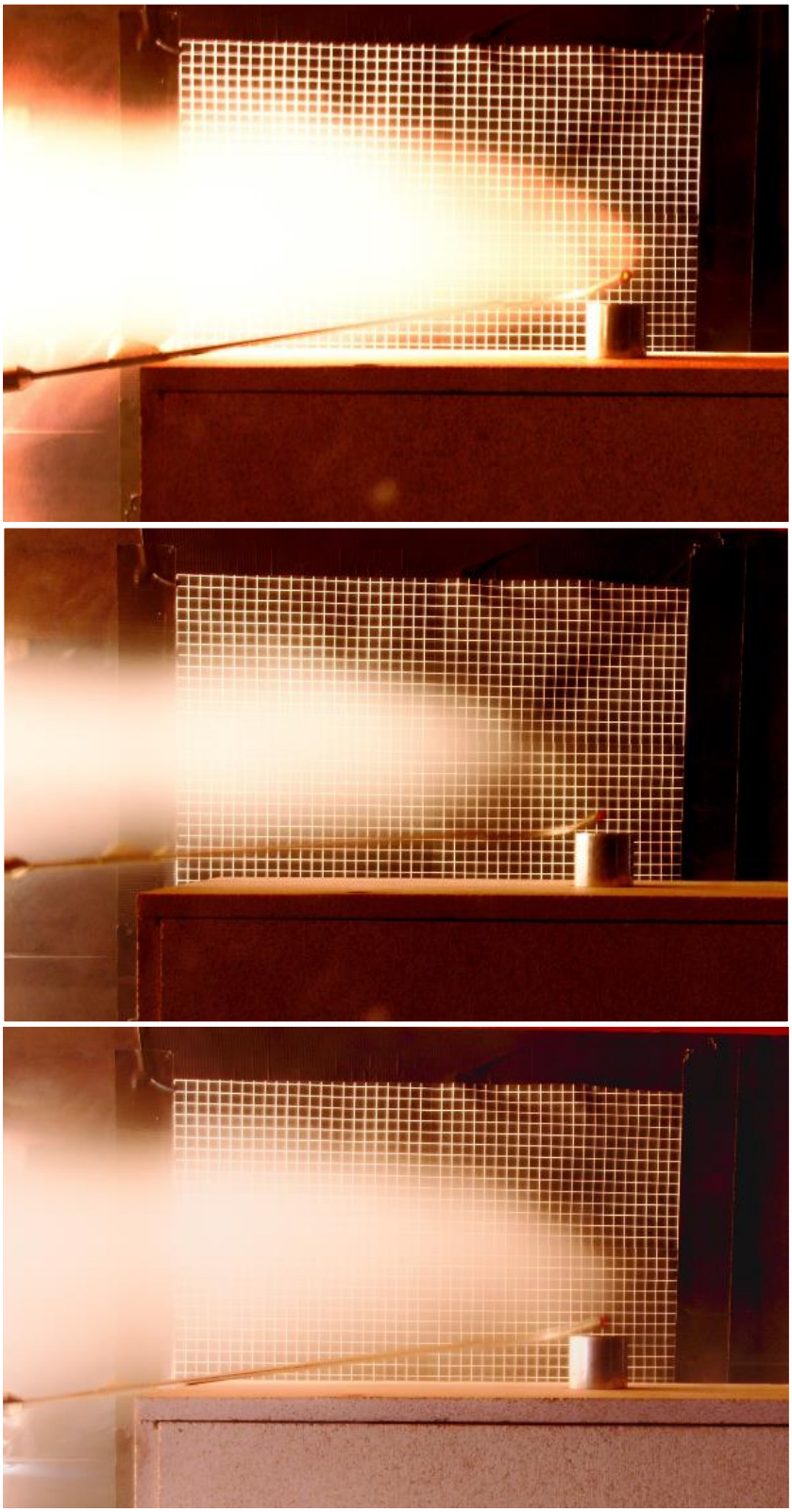

Figure 5.38: Flow visualisation of the heated jet trajectory for momentum ratio 5.8 with Setting 1 (Top), Setting 2 (Middle) and Setting 3 (Bottom), cross-flow wind direction from right to left of image.

5.3.2.2. Velocity Measurements

The next exploratory experiment was to measure the velocity profile of the jet as it was swept downstream and to do this it was necessary to use an unheated jet, which therefore limited the range of parameters that could be varied. Table 5.4 shows two settings that were used (labelled 4 and 5), and the momentum flux ratio was kept much the same as before.

Table 5.4: Wind Tunnel Experiment Parameters for Isothermal Jet

	Setting 4	**Setting 5**
Ambient Temp (°C)	20	20
Air Density (kg/m^3)	1.2	1.2
Jet Mass Flow Rate (kg/s)	0.0013	0.0134
Jet Velocity (m/s)	18.51	21.95
Crossflow Velocity (m/s)	7.68	9.09
Momentum Flux Ratio	5.8	5.8

Velocity measurements were taken with the Cobra probe to produce a series of vertical profiles of streamwise velocity. The profiles were measured to a distance of 18 cm above the top of the box, and at distances of 8, 12, 16 and 20 cm downstream of the rear edge of the box. The results are shown in Figure 5.39; the top row of figures show the actual measured values in m/s, while the bottom row shows the same data but this time normalised by the cross-flow velocity measured upstream of the box. It can be seen that for the two different settings the velocity profiles collapse quite well when normalised. The influence of the jet in the lower region of the velocity profile, particularly around 6 cm, is to slow the cross-flow, this is because the emerging jet actually causes a blockage to the cross-flow. In the higher region of the profile, above 14 cm, the velocity is higher than the upstream flow and this is because of the blockage caused by the box in the wind tunnel combined with the additional flow of the deflected jet. As discussed earlier, and illustrated in Figure 5.30, the jet in cross-flow creates a complex three-dimensional flow field; however, time was pressing on the project and so the experiment moved on to investigate the temperature field in the jet plume.

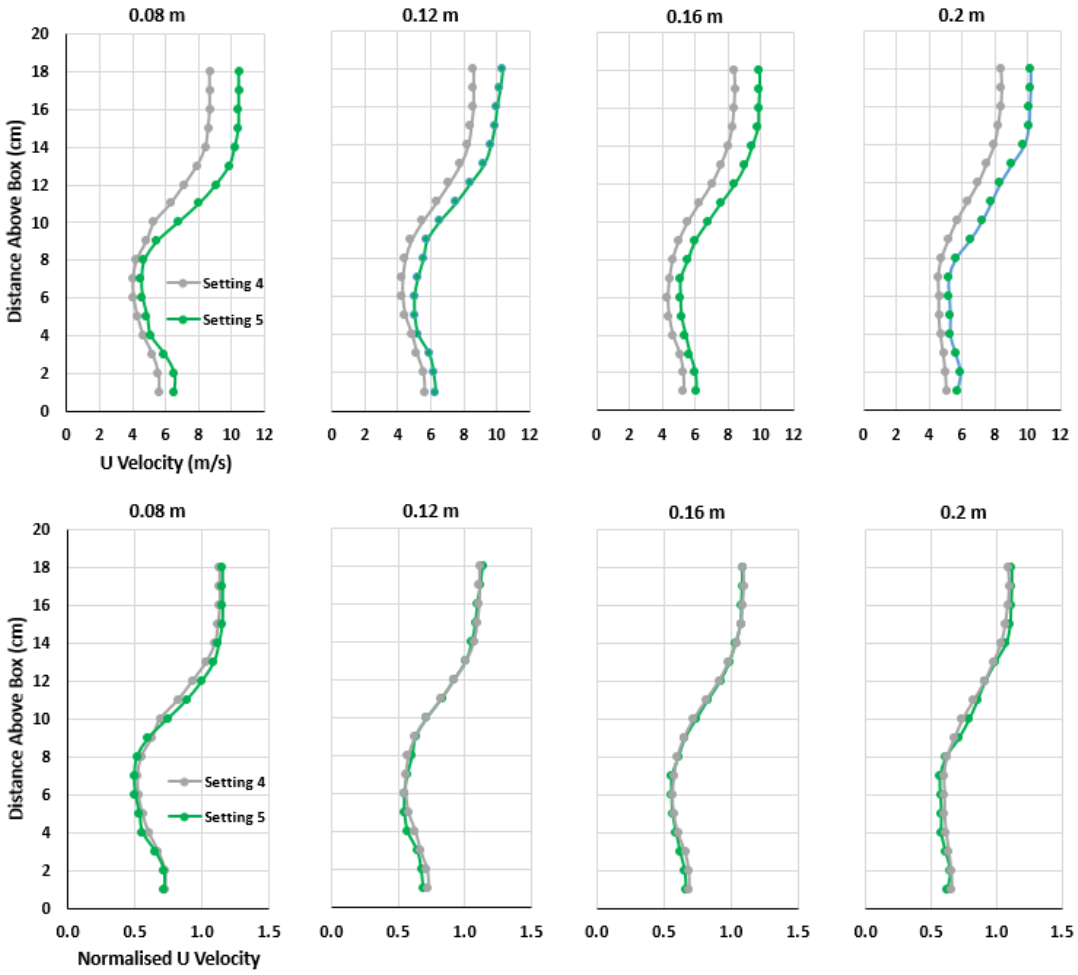

Figure 5.39: Vertical profiles of streamwise velocity downstream of box

5.3.2.3. Temperature Measurements

In this case vertical temperature profiles were measured, again to a height of 18 cm above the top surface of the box, but this time at distances of 0, 4, 8, 12, 16 and 20 cm downstream of the back edge of the box. The flow conditions were those used in the flow visualisation experiment, i.e. Settings 1, 2 and 3 in Table 5.3. The results are presented in Figure 5.40 as vertical profiles of mean temperature; in the top row the actual measured values for the three settings are shown, while in the bottom row the temperatures are normalised according to Equation 5.10 (i.e. $(t_i - t)/(t_i - t_a)$). It can be seen that the normalised temperature profiles for Settings 1 and 3 collapse together nicely, while the data for Setting 2 is not so good. Time for further experimentation was not available and the wind tunnel was taken out of service for laboratory refurbishment so this anomaly had to be left unresolved at the time; although as will be discussed later, it was revisited briefly.

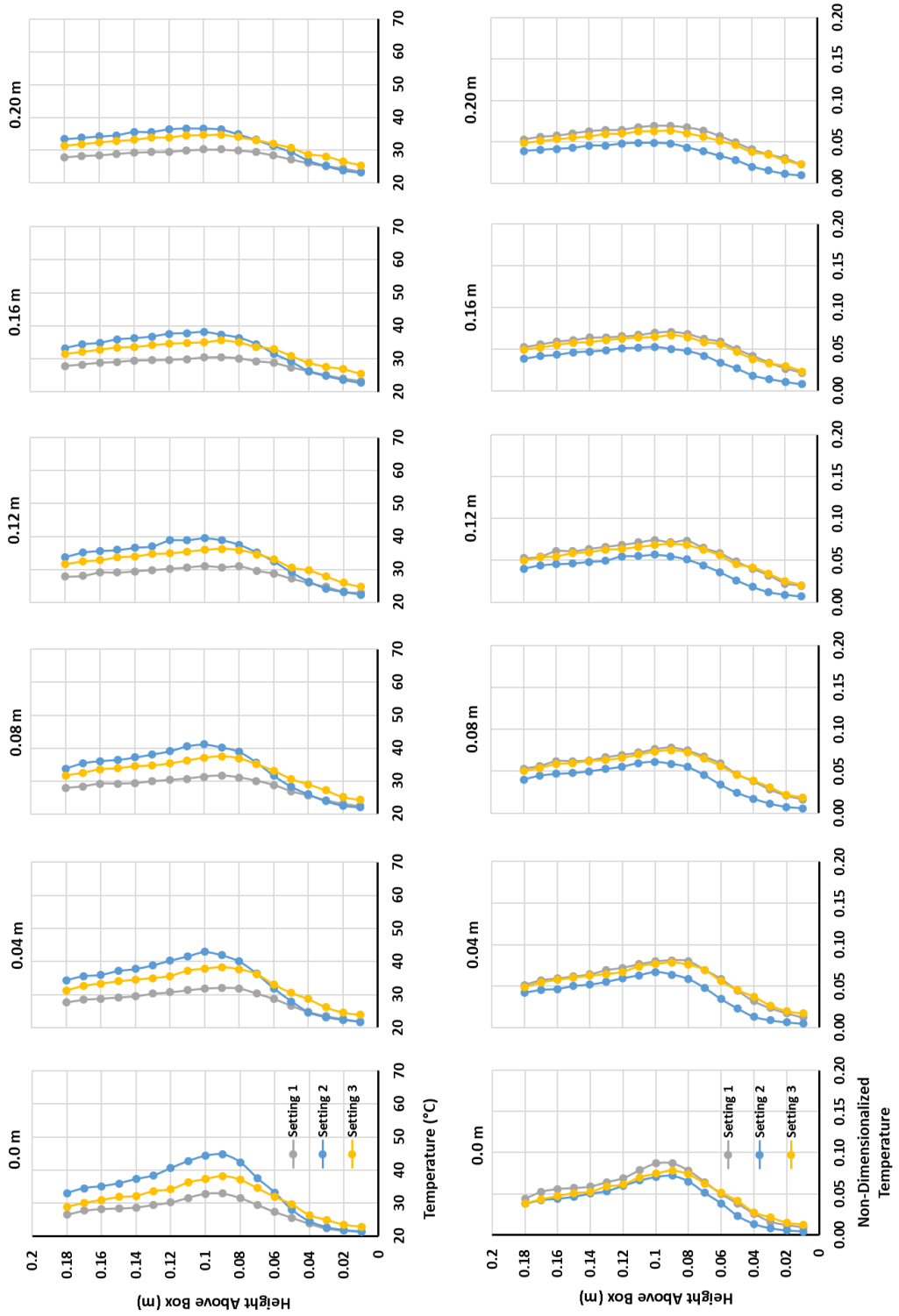

Figure 5.40: Vertical profiles of average temperature (top) and normalised temperature (bottom) downstream of the box

5.3.3. CFD Study of Heated Jet Ejected from a Bluff Body in Cross-Flow

As stated earlier, the purpose of the experiment described above was to provide data to compare with CFD. Therefore, the CFD methodology applied to the ship exhaust, and described in Chapter 2, was applied to the wind tunnel experiment

5.3.3.1. Computational Approach

To begin, a CAD model was produced in ANSYS ICEM which represented the wind tunnel working section as a long rectangle, containing a box with a jet outlet, as seen in Figure 5.41. To prevent inlet effects on the solution, the green portion in Figure 5.41 was added and the walls were given a slip boundary condition so the boundary layer would not begin to develop until it reached the working section, as it would in the real wind tunnel. Similarly, the domain downstream of the wind tunnel section was extended to prevent exit effects influencing the solution near the box.

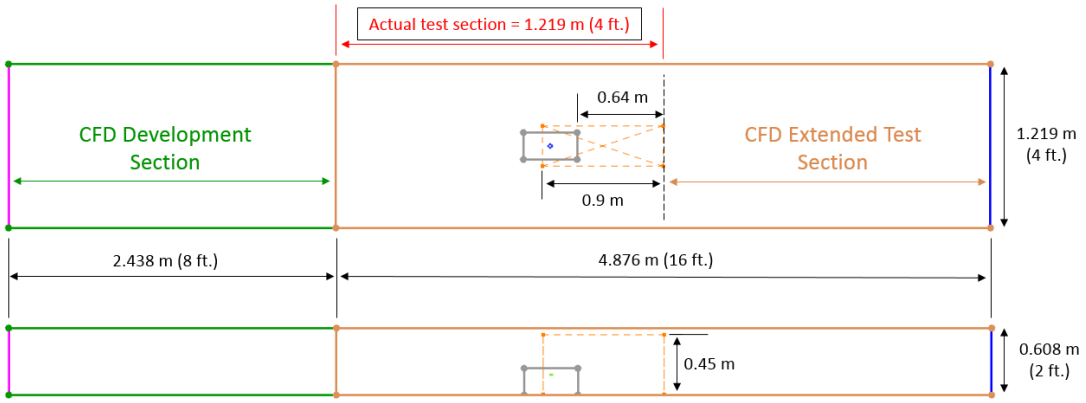

Figure 5.41: Wind Tunnel CFD Geometry

The geometry was meshed in a similar way to that used for the full scale ship, but at a much smaller scale, including the use of a density box in the area of jet mixing. The resulting mesh size was approximately 16 million cells and therefore similar to the 18 million cell mesh produced for the full-scale ship exhaust computations. The size of the surface cell used on the ship was 300mm; therefore, using the relative heights of the ship hangar and the box as a scaling factor, the surface cell size for the experiment was 7.5mm; this was also the maximum size of the cell in the density box, shown in Figure 5.42. Similarly, the mesh for the short 25mm diameter pipe for introducing the jet was considered in the same way by scaling the 200mm mesh used in the 2.8m exhaust uptake (GCS-Ex1) and this indicated a cell size of 1.8mm for the experimental exhaust pipe. The difference in cell size between the main flow domain and the exhaust pipe was greater for the experiment than the full-scale ship. A

similar mismatch between full-scale and experiment was found in the resultant values of the Courant number $C = U\Delta t/\Delta x$ (Equation 1.7, Chapter1) which ideally should be less than 1. The Courant number essentially determines the time step for solving the governing equations and depends on the local velocity and the cell size. The Courant number in the great majority of the domain is less than 1, but in the small volume of flow inside and emerging from the jet it was higher (1.6). However, Fluent is sufficiently robust to deal with this anomaly and the great majority of mixing (momentum and energy transfer) between the jet and the cross flow takes place away from the jet exit.

The CFD was set up to model the conditions of Setting 3 as it had the lowest velocities and hence the least issue for the Courant number. The solution procedure was the same as for the full scale, i.e. a steady solution was first obtained before implementing the unsteady solver, and then a settling period was allowed before 30-seconds of flow was sampled.

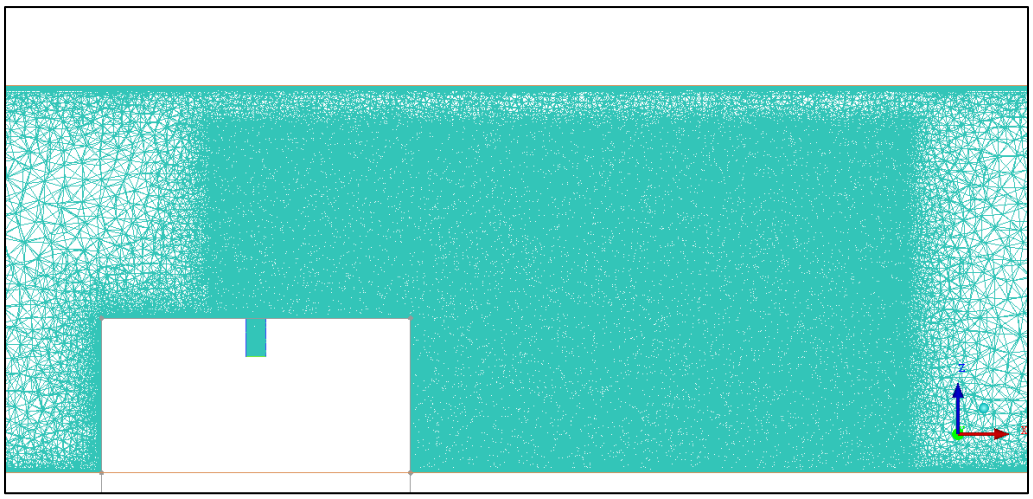

Figure 5.42: Cross-plane through the centre of tetrahedral mesh for wind tunnel experiment CFD including density region

5.3.3.2. Results

Considering first the velocity field of the heated jet mixing with the cross flow, Figure 5.43 shows a series of vertical planes along the top of the box, starting at the rear edge and finishing at the front edge, spaced at 5cm intervals. The flow is represented by streamlines of mean flow in the plane and contours of turbulence intensity. Looking closely at the images, the top surface of the box is at the bottom of each and the sequence of images shows how the flow develops as it progresses down the box. The centre of the box, and of the jet, is at 20 cm so before then the images are showing the flow separating from the front of the box. From 20 cm forward the influence of the jet can be seen, particularly the development of the counter-rotating vortex pair, as illustrated earlier in Figure 5.30.

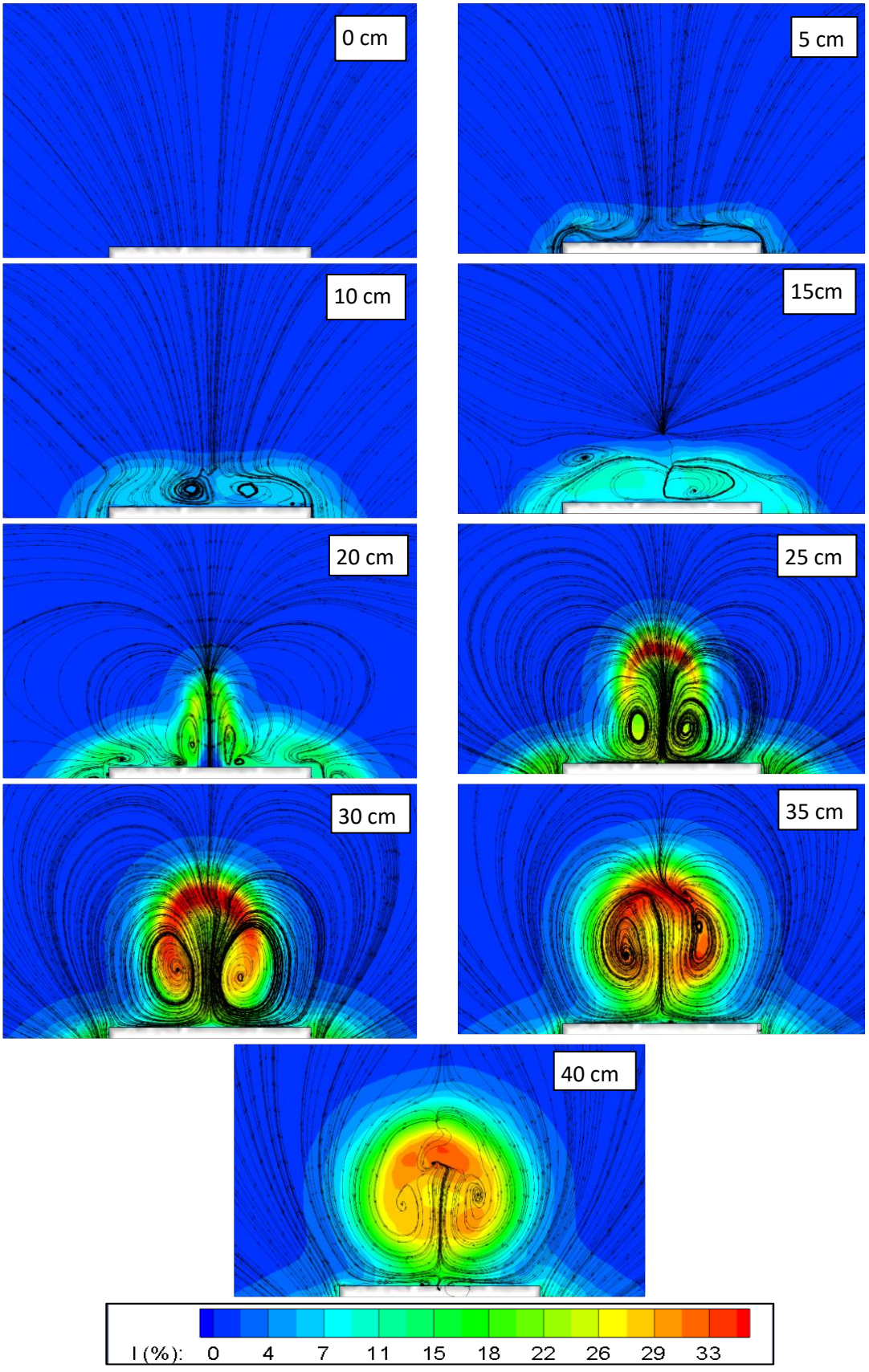
0 cm
5 cm
10 cm
15cm
20 cm
25 cm
30 cm
35 cm
40 cm
I (%): 0 4 7 11 15 18 22 26 29 33

Figure 5.43: Vertical transverse planes spaced at 5cm intervals showing streamlines and contours of turbulence

Figure 5.44 shows the contours of average temperatures in a plane through the centreline of the box/plume. The deflection of the plume is clearly seen and the initial core temperature of 253°C is predicted to fall quickly to about 40°C at about 20 cm downstream of the box. Figure 5.45 shows a series of cross-sections of average temperature contours which also show how the hot core of the jet quickly disappears.

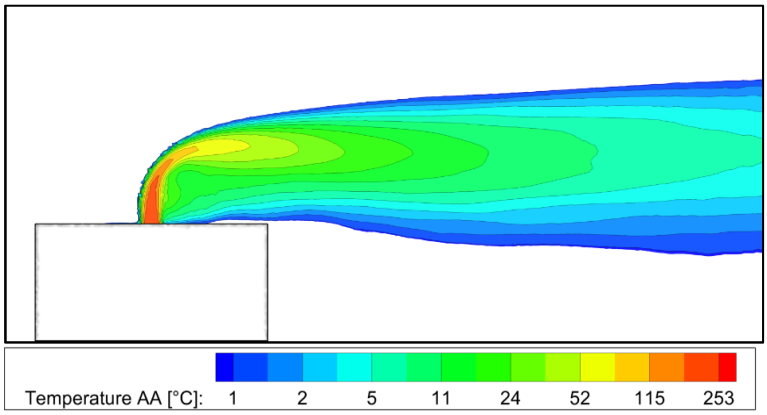

Figure 5.44: Heated jet trajectory visualised in contours of mean temperature above ambient

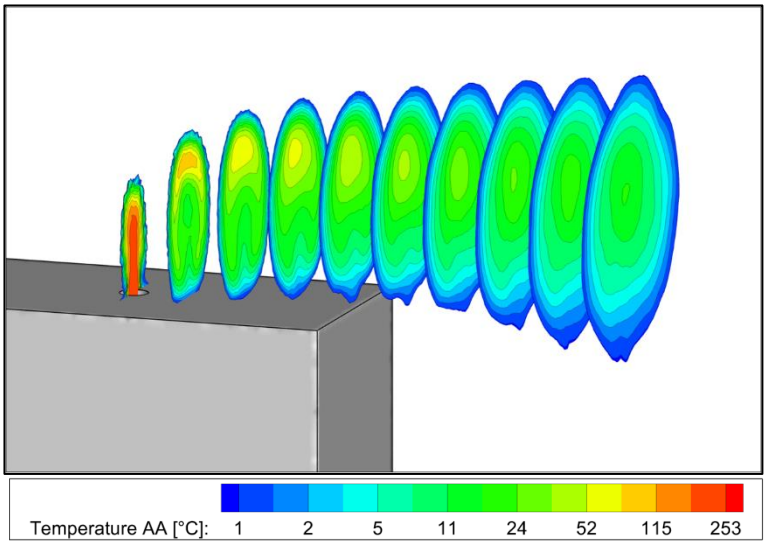

Figure 5.45: Cross-sections of the dispersing heated jet visualised in contours of mean temperature above ambient

5.3.4. Comparison of Wind Tunnel Experimental and CFD Data

While the CFD data presented in the previous section looks reasonable, when it is compared with the experimental data it is seen that there are significant differences, Figure 5.46. At this stage it was debated whether these results should be included in the thesis, but it was decided that for any future study it is important that these differences are acknowledged and then further investigated.

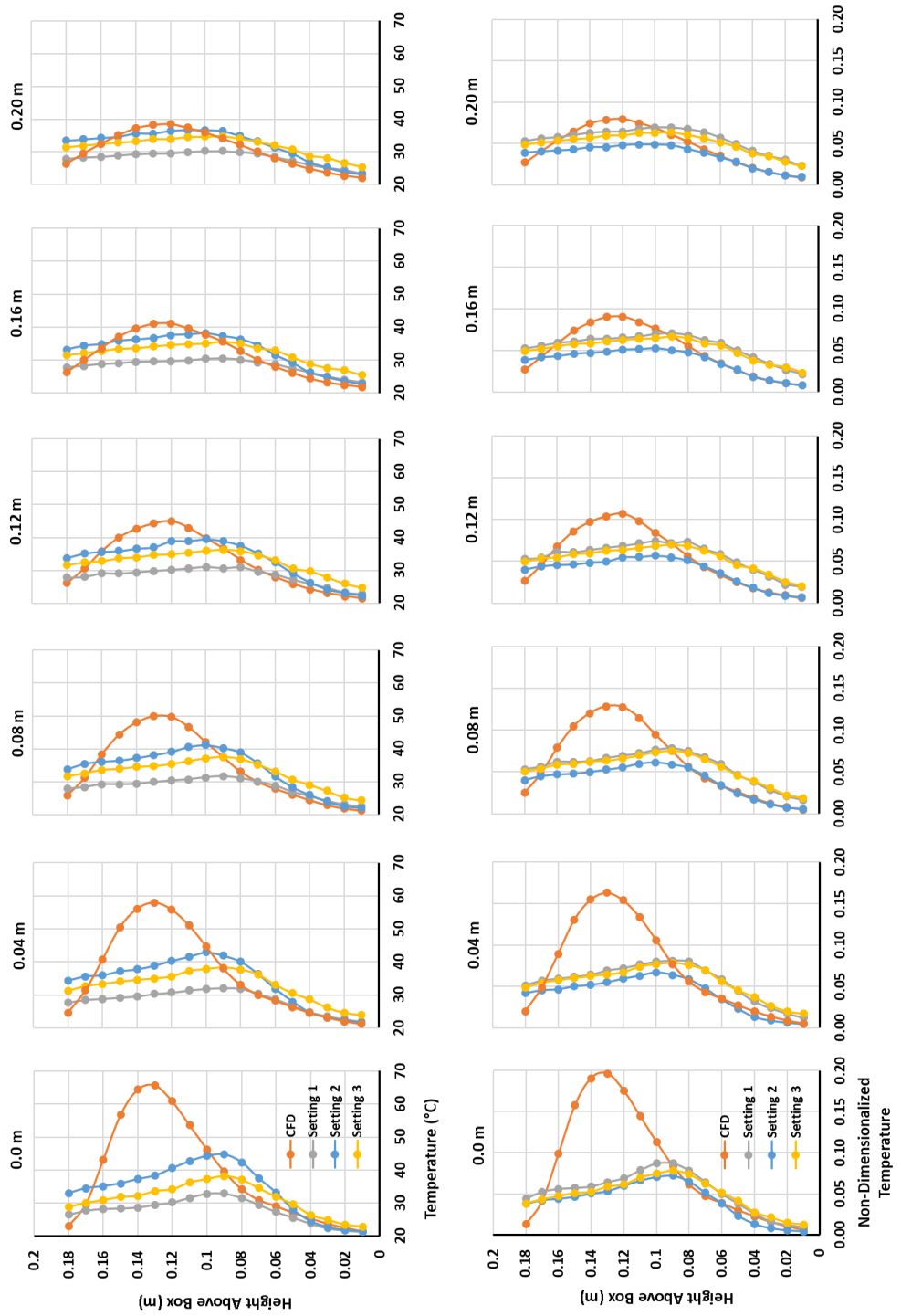

Figure 5.46 Comparison of experimental and CFD contours of average temperature profiles

The temperature profiles, as before, are presented as actual values in the top row, and then normalised in the bottom row. In both cases it can be seen that the computed jet temperatures are significantly higher than those measured. Perhaps what is surprising is that the very significant rate of cooling predicted by the CFD is still less than the cooling in the experiment. In the limited time available, both the design of the experiment and the CFD were reviewed.

As alluded to earlier, the experiment was conducted in some haste, due to the time remaining on the project and to the loss of access to the facilities while laboratory refurbishment took place. Nevertheless the experiment was revisited and some issues were found. The first was that there was some leakage of hot air from within the box at the joints between the slabs of insulating material from which it was manufactured; these leaks were not present at the onset of the experiment and were due to the ceramic cement failing. Second, the outer surface of the ceramic box was not, as assumed in the CFD, at ambient temperature, it was typically 40°C. Finally, a thermocouple was placed in the exit plane of the exhaust jet and the air temperature was found to be about 30°C lower than that recorded by the control system thermocouple within the box. The reason for the discrepancy could not be found in time, but the difference is significant and alone could account for much of the discrepancy between the experiment and CFD.

The CFD was also reviewed and, as well as the meshing and Courant number issues, an area that is worthy of further investigation is the use of the value of 0.85 for the Turbulent Prandtl number, Pr_t (Equation 2.5, Chapter 2). The default value for Pr_t in Fluent is 0.85; clearly if the Reynolds analogy was strictly correct Pr_t would be unity. In a review of Pr_t in 1994 Kays [62] demonstrated the widely acceptable value of 0.85, but also pointed out that it is not uniform across a boundary layer. In fact, the value of Pr_t is often evaluated for boundary layers because of its importance in calculating heat transfer. However, Kays reported that in wake regions Pr_t can tend towards a value of 0.5 to 0.6. In a study using a heated square jet, Chua et al. [139] point out that Pr_t is not constant across or along a jet, while Craske et al. [140] derived an analytical value of Pr_t of 3/5, a value that they showed to be consistent with experiments. What is unclear from this discussion is how sensitive the jet dispersion CFD modelling is to Pr_t and, had time been available, it would have been investigated. However, this, and the design of the experiment, is something to be explored in another project in the future, drawing on the groundwork laid out above.

5.4. Chapter Summary

The review of ship funnel design presented in this chapter has shown how, after the Second World War, significant knowledge was built up, and applied, to the aerodynamic design of ship exhaust stacks. The current designs of ships' funnels do not seem to draw upon that body of information and, in the quest to reduce RCS, there appears to be little consideration given to the aerodynamics of the exhaust funnel. Modern warships are powered by a combination of DGs and GTs; for normal cruising the DGs are the prime mover of choice, but when additional power is required the GT is engaged. It is the GT that provides the greatest threat to IR emissions and to the ship's helicopter. An unsteady CFD analysis has shown how, when operating with the GT, there are areas around the ship where the local air temperatures can be both elevated and unsteady. According to the regulations adopted for helicopter operations to offshore platforms the levels of temperature increases around the ship's flight deck would be a cause for concern. The caution in the offshore industry is based on a small number of accidents that have occurred and, probably more importantly, the risk if a helicopter was to crash onto a highly combustible gas/oil platform.

The CFD analysis has provided valuable information on the potential risks from the hot engine exhaust gases, particularly for the ship's helicopter. The initial analysis conducted without the eductor provided important interim data by identifying the areas of concern. The issues were also present when the eductor was accounted for in the CFD, but the additional cooling was seen, as intended, to be beneficial. Unsteady inlet air temperatures can cause problems for helicopter engine control systems and the study has predicted what these fluctuations could be. Therefore, important information has been provided for the helicopter manufacturer and operator to consider. The overall GCS project, of which this study is a part, is the first time that ship exhaust gas dispersion has been investigated using CFD as opposed to wind tunnel experiments.

The experimental investigation, despite its shortcomings, has pointed the way forward to obtain experimental data for validating the CFD of hot gas mixing in a turbulent cross-flow. The main problem in the experiment was the difference between the temperature measurements of the hot air inside the box and of the jet as it emerged from the nozzle. The experiment should be redesigned and pursued, as should an investigation into the sensitivity of the CFD analysis to the value of turbulent Prandtl number.

Chapter 6. Effect of Ship Superstructure Aerodynamics on UA Deployment

Chapter 3 demonstrated that ship designs can be modified to reduce the effect of a ship's airwake on helicopter operations. A combination of CFD, flight mechanics modelling and the Virtual AirDyn tool, was used to examine the effect of ship design features on a simulated helicopter's response during deck recovery operations. The aim was to use modelling and simulation to better understand, and improve, the helicopter-ship dynamic interface prior to commencing real-world operations. In this Chapter, a new simulation environment has been developed to explore Unmanned Aircraft (UA) shipborne launches to gain insight into operational challenges prior to any real-world deployment.

6.1. Shipborne UA Clearances – the Need for a New Approach

Since 2001 there has been a major expansion in the ability to deploy unmanned systems in theatre to satisfy a range of tactical roles. The US Department of Defense (DoD) currently operates over 11,000 Unmanned Aerial Systems [141] many of which are deployed on ships, e.g. the Northrop Grumman Fire Scout shown in Figure 6.1, which has a rotor diameter of 8.4m.

Figure 6.1: Northrop Gunman MQ-8 (Fire Scout) UAV [142]

Whilst the capability of these systems continues to increase, so does the procurement, training and operational costs associated with them. In order to maximise the benefit afforded by these platforms in future operations, new methodologies are required to ensure their rapid integration and exploitation. This requirement was identified by the United States in the publication of the Unmanned Systems Integrated Roadmap (FY2013-2038) [143]. The report acknowledges that to be able to address emerging and future security requirements, a vision for the next 25 years is needed, outlining "*actions and technologies for DoD, industry, universities, and others to pursue to achieve the sustained, affordable, rapid integration and application of unmanned systems*." One of the methods that can be used to reduce risk and improve integrations times of UA platforms is by using modelling and simulation (M&S). The development of a new toolset to satisfy this requirement is the focus of this Chapter.

In the UK, it was recognised that a dedicated test unit was needed to evaluate emerging technologies with maritime applications. 700 Naval Air Squadron (700 NAS), an experimental test unit within the Royal Navy's Fleet Air Arm, was formed in 1940 to test aircraft catapult equipment for ship launches. The unit has been dis-banded and re-formed several times in its history according to operational needs. Its current version, 700X, was formed in 2014 to "*oversee the development and innovation of cutting-edge remote-piloted flight systems within the Royal Navy*" including the introduction of the Insitu ScanEagle, Figure 6.2, which has a wingspan of 3.1m. The unit focusses on 'traditional' hardware test and evaluation methods and has yet to embrace the benefits M&S tools can afford.

Figure 6.2: Insitu ScanEagle [144]

These benefits were recognised in a study by Cox et al. [145] as part of the NATO/Partnership for Peace (PfP) Interoperability and Re-Use Study (NIREUS), which recognised that "*simulation offers a powerful methodology for developing ship/UAV operating limits in a*

flexible and cost effective manner". More recently AgustaWestland (now Leonardo Helicopters) was awarded the Rotary Wing Unmanned Air System (RWUAS) Capability Concept Demonstrator contract by the Royal Navy [146]. The purpose of this contract was to "*understand whether a multi-role Rotary Wing Unmanned Air System can provide utility in the Mine Counter Measures, Hydrography & Meteorology, Offensive Surface Warfare and general Situational Awareness capability areas*." A M&S approach was central to this activity [147] and the Type 23 airwake data described in Chapter 3 was supplied (by the Author) to Leonardo Helicopters and integrated into their simulation environment.

There are several challenges that affect the launch and recovery phases of maritime UA operations. As described previously, aircraft are influenced by the turbulent airflow over the deck in the lee of the ship's superstructure. For manned aircraft, Ship Helicopter Operating Limits (SHOLs) are developed to indicate the safe boundaries for launch and recovery operations. Whilst there may be a significant overlap between the environmental hazards faced by manned and unmanned aircraft during a deck launch or recovery, the removal of the pilot from the system and the much lighter weight of UAs (causing them to be more susceptible to airwake disturbances), makes subjective assessment of safety limits more difficult to determine. However, examining a UA's response to an airwake encounter provides a valuable insight into the risk of deck launch operations. The accuracy of the launch and recovery in different conditions, proximity to the superstructure and the amount of control authority used during these operations would be candidate measures for determining UA limits. As the UK moves forward with new UA procurement activities, the development of a new simulation environment to examine this challenge is timely.

6.1.1. Review of Maritime Unmanned Aircraft Operations

To frame any discussions on UAs in maritime operations, it is helpful to use the correct terminology and classification method for these aircraft. The UK MoD defines a UA as "*an aircraft that does not carry a human operator, is operated remotely using varying levels of automated functions, is normally recoverable, and can carry a lethal or non-lethal payload*" [148]. This can be incorporated with an Unmanned Aircraft System (UAS) which includes additional equipment, network capability and personnel necessary to control the UA.

In the UK, the Military Aviation Authority, who regulate the use of manned and unmanned vehicles, has adopted the NATO UAS classification framework, as shown in Table 6.1, which

provides a convenient means for developing standards and training appropriate to the role, size and complexity of the aircraft. Examples of each class are shown in Table 6.1 [149].

Table 6.1: NATO UAS Classification Framework

Class	Category	Normal Employment	Normal Operating Altitude	Normal Mission Radius	Example Platform
Class I < 150kg	MICRO < 2kg	Tactical Platoon, Section, Individual (single operator)	Up to 200ft Above Ground Level	5km Line of Sight	Black Widow (R)
	MINI 2-20kg	Tactical Sub-Unit (manual launch)	Up to 3,000ft Above Ground Level	25km Line of Sight	ScanEagle (F), Skylark (F), Raven (F)
	SMALL > 20kg	Tactical Unit (employs launch system)	Up to 5,000ft Above Ground Level	50km Line of Sight	Luna (F), Hermes 90 (F)
Class II 150–600 kg	TACTICAL	Tactical Formation	Up to 10,000ft Above Ground Level	200km Line of Sight	Firescout (R), Sperwer (F), Watchkeeper (F)
Class III > 600kg	Medium Altitude Long Endurance	Operational / Theatre	Up to 45,000ft Above Ground Level	Unlimited Beyond Line of Sight	Reaper (F), Hummingbird (R)
	High Altitude Long Endurance	Strategic / National	Up to 65,000ft Above Ground Level	Unlimited Beyond Line of Sight	Global Hawk (F),

R – denotes rotary wing, F – denotes fixed-wing

Maritime launch and recovery UA operations have an additional complexity compared with manned operations in that there is no pilot onboard to undertake the procedures. The launch of the lighter Class I fixed-wing UAs from ships can be achieved manually or via use of a mechanical launch mechanism, e.g. the ScanEagle launcher shown in Figure 6.3. The heavier Class II and III launches require automatic flight control systems and in the case of fixed-wing UAs also require sufficient runway lengths that inhibit deck launches from frigates. There has been very little published on using M&S to examine UA launch requirements. Crump and Bil [150] examined the use of M&S for fixed-wing Class I fixed-wing launches, using a simplified 6 degree of freedom vehicle model coupled with a tuned Dryden atmospheric disturbance model [151]. Whilst this approach captures the main elements of a vehicle's response to an atmospheric disturbance, an enhancement in the fidelity of the

modelling approaches is warranted to be representative of real-world operations, particularly in the area of ship airwake modelling.

Figure 6.3: UA mechanical launch system [152]

Current literature on maritime UA recovery methods is focused on the equipment used in the approach phase rather than the environment over/around the ship. For the approach navigation to the ship, a variety of methods are being explored including Ship Relative GPS (SRGPS), Millimetre-wave radar [153] and optical methods [154] to guide the UA to the ship. Once near the ship, offboard measurements of the environment using UAs have been undertaken to characterise the ship's airwake and provide CFD validation data [155]. This type of field measurement is challenging to undertake, and the validation process has yet to mature.

The final phase of UA recovery operations for Class I aircraft depends on their configuration. Rotary-wing landings can be conducted in the same manner as manned operations i.e. a hover alongside/astern of the frigate followed by a descent to land on the deck during a quiescent period i.e. when the deck motion is small enough to allow a landing. Visual landing aids e.g. landing period designator or use of a landing signal officer, can aid in judging deck motion limits in manned operations but are not suitable for UA. An alternative approach for UAs is to incorporate ship motion prediction methods into the automatic flight control systems for rotary-wing aircraft. Ferrier et al. [156] as part of the NIREUS study, demonstrated that ship motion data can be incorporated into a simulation environment as part of a rotary-wing autoland capability.

Another limiting factor in the landing phase of a rotary-wing UA is the control authority of the flight control system i.e. the available frequency and amplitude of the control surface actuators than can be used to reject any gusts acting on the vehicle. This topic was the subject of a separate dstl funded research project at UoL [157], [158], which began to determine flight control system requirements for different UA Classes using M&S.

Fixed-wing UA approach and landings are subject the same environmental conditions as their rotary-wing counterparts; however, due to their configuration, the solution to this phase of operation can be simplified. For example, the Skyhook system for Class I UAs (Figure 6.4) employs a net system to catch the UA in flight.

Figure 6.4: Skyhook capture of a Scaneagle UA [159]

As the mass of the UA increases for Class II and III UAs, so does the area required for the landing and a more conventional fixed-wing approach profile is adopted.

The extent to which a new UA that is brought into service will be affected by the ship airwake, including defining its operational limits, is determined during at-sea trials/tests. Adopting the approach suggested in [145], a new flight simulation environment is presented in the next section to enable the effect of ship airwakes on UA launches to be examined.

6.2. Building a UA Simulation Environment

A simulation environment was developed to represent real-world UA-ship operating conditions. The US Coast Guard Standard Operating Procedure for the ScanEagle [160] was used to develop the launch scenarios described later in Section 6.3. In this thesis only the launch phase has been considered as that poses the most significant threat to a UA in a

maritime environment. As shown in Figure 6.5 the environment consists of a flight dynamics model with an integrated airwake coupled with a deck launch system; these components are detailed further in the following sections.

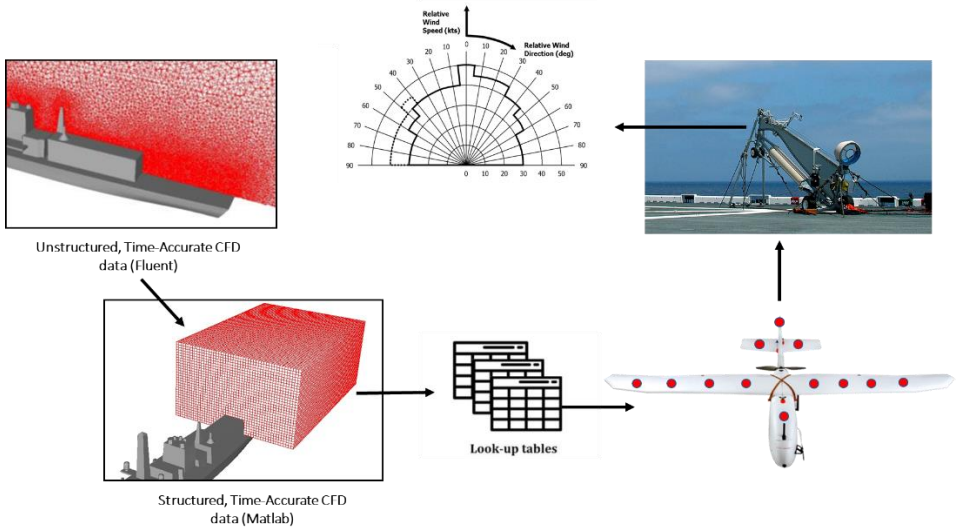

Figure 6.5: UA-Ship dynamic interface environment

6.2.1. FLIGHTLAB Modelling and Simulation Software

FLIGHTLAB, which was referred to briefly in Chapter 3, is a commercially available multi-body dynamics modelling and simulation environment from ART Inc. [161]. The software uses a modular approach to developing flight dynamics models, producing a complete vehicle system from a library of predefined components. In particular, FLIGHTLAB provides a range of tools to assist in the rapid generation of highly complex, non-linear, multi-body models, reducing the effort required for computer coding that are typical of many flight simulation activities. Although FLIGHTLAB was originally developed for rotorcraft simulations using Blade Element Models, it can also be used as a simulation tool for fixed wing aircraft.

The FLIGHTLAB Model Editor (FLME), Xanalysis, Control System Graphical Editor (CSGE) are among the GUIs available for the construction and analysis of flight simulations models from a pre-defined set of subsystem components. The subsystems are integrated into a full flight dynamics simulation by first solving the forces and moments produced by each subsystem before resolving them at the aircraft's centre of gravity. The forces and moments are then used in the 6 degree of freedom rigid body equations of motion.

FLME is a subsystem model editor which allows a user to develop models from higher level primitives such as propellers and airframes. Typically, a user will select and configure the

subsystem of interest by inputting data and references tables, selecting options that determine the level of sophistication thereby providing a selective fidelity modelling capability and maximising computational efficiency. Models are created hierarchically, with a complete vehicle model consisting of lower level subsystem models, which in turn are collections of primitive components; this is the Model Editor Tree, which puts all the predefined vehicle subsystems into a logical “tree'' structure.

Five main categories of components are included in the library:

- Structural (masses, translations, elastic effects etc)
- Aerodynamic (aerofoils, induced flows, interferences etc)
- Control (transfer functions, gains etc)
- Engine & Drivetrain (engine, bearings, shafts etc)
- Solution (tools to facilitate the solution of the non-linear equations of motion)

Figure 6.6 shows how a typical fixed-wing model is constructed from the component library.

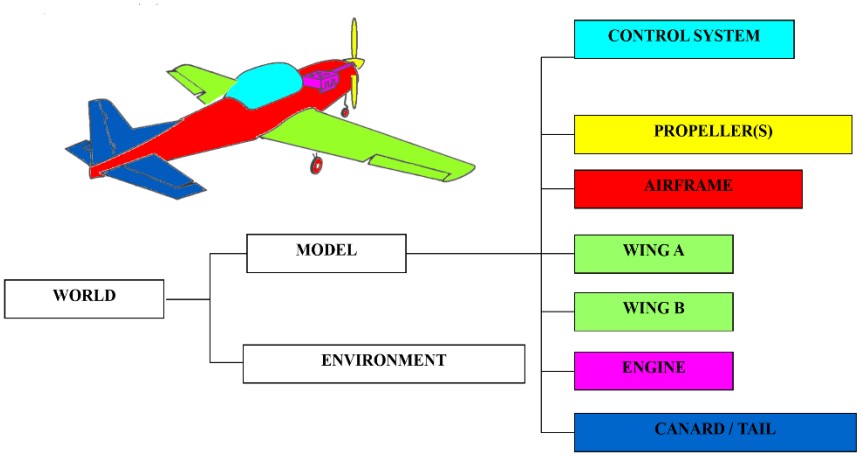

Figure 6.6: FLIGHTLAB model structure

The components are combined into a single model definition file (MODEL) which, along with the definition of the simulated environment, e.g. temperature, pressure, completes the model (WORLD).

The world model can be analysed using Xanalysis. This GUI has a number of tools allowing a user to change model parameters and examine the dynamic response, stability, performance and handling qualities characteristics of design alternatives. Additional tools are available to generate linear models, perform eigen-analysis, time and frequency response analyses and control system design.

CSGE allows the design and implementation of control systems into a vehicle model, including linking the vehicle controls to any aerodynamic surfaces through a flight control system, enabling a user to design and integrate higher level functions such as an autopilot. The user creates the flight control system in a block diagram format which is then connected to variables in the model such as the control surfaces.

6.2.1.1. FLIGHTLAB RTF-ScanEagle Model

An existing model template of a 3D Robotic's Ready-to-Fly (RTF) Aero UAV [162]–[164] (Figure 6.7), was used as the basis for the model developed in this thesis (RTFAeroCFDSEagle). The physical parameters from the original model were adjusted to be representative of a Class I flying wing aircraft, e.g. ScanEagle, to produce a new simulation model. The ScanEagle has a 3.11 m wingspan, a cruise speed of 50-60 knots and has an empty weight of 16 kg and a 3.4 kg payload. The RTFAeroCFDSEagle uses a standard fixed-wing configuration (unlike ScanEagle which is a flying wing configuration); the top-level model is structure is shown in Figure 6.8. and the main model parameters are listed in Table 6.2.

Figure 6.7: 3-D Robotics Aero UA [165]

The standard FLME component library did not contain an electrical motor component which is used need for electrically powered aircraft. A new component was therefore created in [162] and was adjusted to be representative of the vehicle used in this thesis. The aerodynamic data for the lifting surfaces in the model were generated with Xfoil [163].

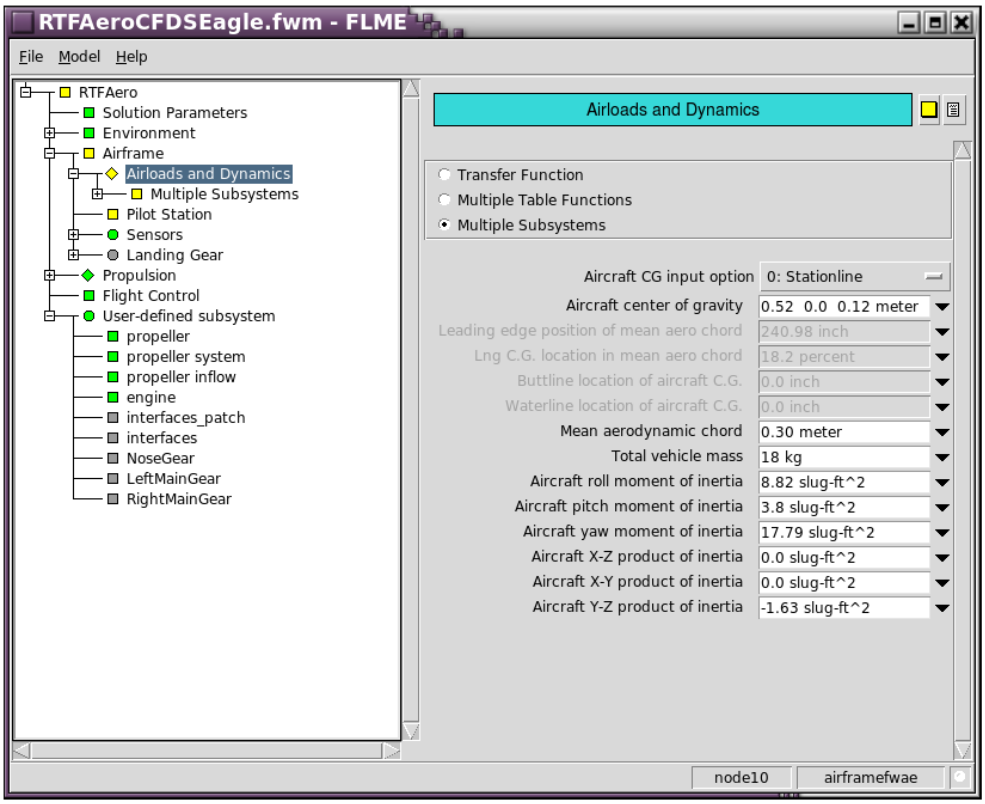

Figure 6.8: RTFAeroCFDSEagle FLME model structure

Table 6.2: RTFAeroCFDSEagle main model parameters

Model Item	Value
Total vehicle mass	18 kg
Payload	3.4 kg
Roll moment of inertia	11.95 kg/m^2
Pitch moment of inertia	5.15 kg/m^2
Yaw moment of inertia	24.10 kg/m^2
Main wing aerofoil section	GOE798
Wingspan	3.11 m
Chord	0.23 m
Stabiliser aerofoil section	NACA0042
Left/right vertical stabilisers	0.39 m
Elevator control range	+/- 12.8°
Roll control range	+/- 16.8°
Yaw control range	+/- 20.5°
Engine power	20 W

6.2.1.2. Automatic Flight Control System

To simulate a mechanical catapult launch, a prototype waypoint navigation system was included in the model. This allows the user to define several waypoints which the Automatic Flight Control System (AFCS) follows in flight, including the initial 12-degree launch angle from the ship's deck. The system works in a similar manner to an aircraft Instrument Landing System in that it provides vertical and horizontal navigation demands to the flight controls.

Figure 6.9 shows top-level ACFS structure in the model. The waypoints are defined in the planner control group (fromplanner) and these commands are fed into the AFCS using pitch (xb) and throttle (xc) for vertical navigation and roll (xa) and yaw (xp) and for horizontal navigation (headingacquire control block).

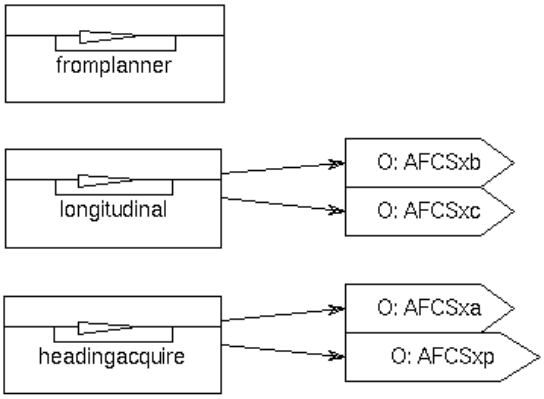

Figure 6.9: Waypoint control architecture

An example of the control subsystems blocksets is shown in Figure 6.10. In order to acquire and maintain the desired flight path (FP), elevator control demands are satisfied by adjusting the pitch control, xb. An autothrottle system (speedholdthrottle) is also included to ensure that sufficient power (xc) is delivered to the propeller to maintain the required airspeed in climbing/descending flight.

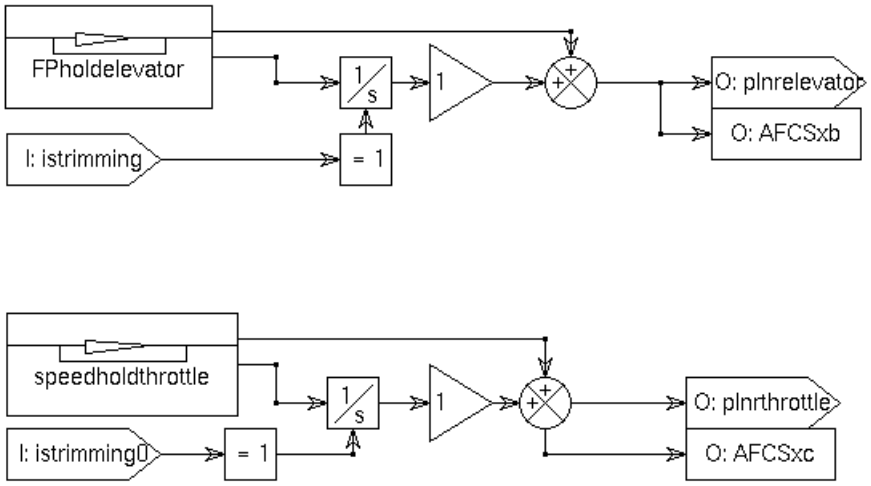

Figure 6.10: Longitudinal control sub-block

6.2.2. GCS Airwake

For the UA-Ship environment, a Green 45 airwake was computed at 40 knots for the GCS using the methodology described in Chapter 2. The airwake was computed to produce 750 .ip files containing 3-component velocity data at each cell centre within the computational domain. The entire CFD domain is unnecessary for the simulation of a UA launch from a ship's flight deck as it will be clear of the airwake and in freestream flow shortly after the launch.

6.2.2.1. CFD Mesh Refinement for UAV Operations

Due to the large file sizes for a full unstructured grid, an interpolated grid is used to reduce the size of the airwake whilst being fine enough to retain the significant flow features that will affect the UA. The process first involves producing a structured grid using Matlab on which to interpolate the computed unstructured airwake data. The structured grid used for this study had a uniform grid mesh sizing of 0.5 metres (sufficient resolution for a Class I UA) and covered an area of 100 x 140 x 16 metres as shown in Figure 6.11. The grid was symmetrical in the port and starboard directions to enable deck launches into headwind and crosswind conditions. The original CFD solution was computed at 100Hz and this was down-sampled to 25Hz to reduce the amount of data stored in the simulation model. Thirty seconds of unsteady data was integrated into the flight simulation model.

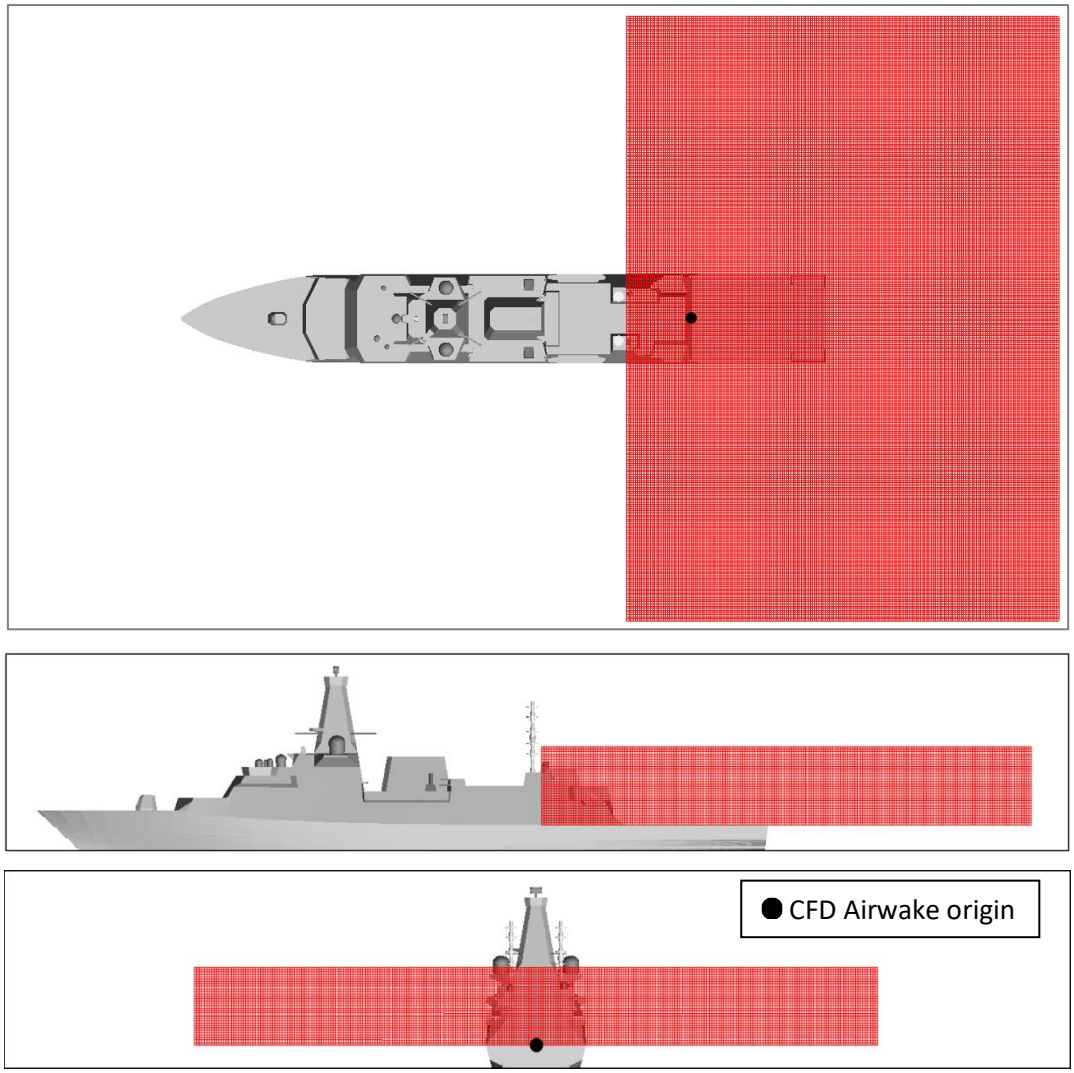

Figure 6.11: Structured grid used for interpolation of unstructured airwake CFD data

6.2.2.2. Integration of an Interpolated Airwake into a FLIGHTLAB Model

Typically, fixed-wing flight dynamics models use look-up tables of air velocity components to generate forces on the aerodynamic surfaces. The angle-of-attack is computed at a single location, the centre of gravity, where the air velocity components at that point are applied [166]. This method neglects any velocity gradients across the lifting surfaces as would be experienced in the ship's airwake. To enhance the model's fidelity these airwake disturbances and velocity gradients can be applied to FLIGHTLAB vehicle models via Airload Computation Points (ACPs), which are discrete aerodynamic locations in the model where the local airflow is altered by the airwake. Using a superposition method, the time-varying u, v, w velocity perturbations calculated using CFD are 'added' to the local inflow velocities at each ACP. This produces a change in the aerodynamic load calculated at those points and

creates the forces and moments imposed onto the aircraft by the unsteady airwake. Figure 6.12 shows the ACP locations used in the model. Eight ACPs are located on the wing, one on each horizonal stabiliser and one each on the fuselage and vertical fin, giving a total of 12 ACPs.

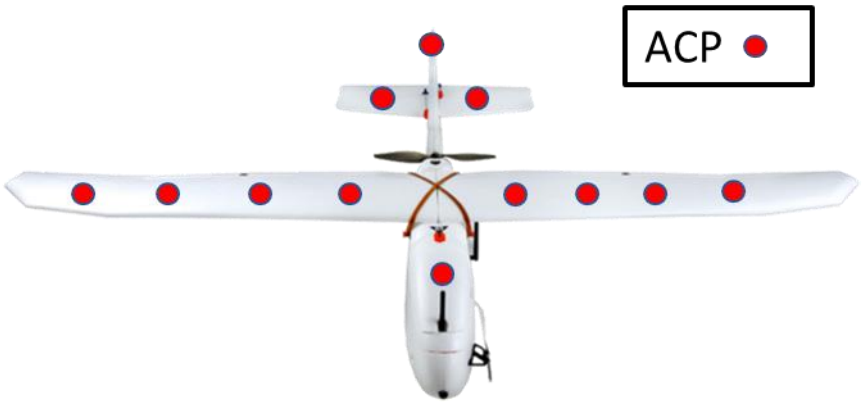

Figure 6.12: ACP locations on the RTFAeroCFDSEagle FLIGHTLAB model

The structured airwake file was integrated into look-up tables containing seven variables: t_a, X_a, Y_a, Z_a, U_a, V_a, W_a [167]. Table 6.4 lists the data format of each of the variables.

Table 6.4: Structured airwake data format

Variable	Description	Array	Array Size	Variable
t_a	Time vector	1-D	1 x 750 (30 secs) @ 25 Hz)	t_a
X_a	Array of	1-D	Length (X_a) x 1	X_a
Y_a	Array of	1-D	Length (Y_a) x 1	Y_a
Z_a	Array of	1-D	Length (Z_a) x 1	Z_a
U_a	Airwake *X*	4-D	Length (X_a.Y_a.Z_a.t_a)	U_a
V_a	Airwake *Y*	4-D	Length (X_a.Y_a.Z_a.t_a)	V_a
W_a	Airwake *Z*	4-D	Length (X_a.Y_a.Z_a.t_a)	W_a

The origin of the interpolation box origin is at the bottom centre of the ship's hangar door, as shown in Figure 6.11.

As the airwake velocities data are stored in look-up tables in the CFD/ship coordinate system, the ACP positions in the simulation coordinate system (X_{sim}, Y_{sim}, Z_{sim}) are converted into

airwake/CFD coordinate system (X_a, Y_a, Z_a) to capture the airwake velocity data (U_a, V_a, W_a), using the Eqns. 6.1-6.3.

$$X_a = -(X_{sim}+X_{sim2a}) \quad (6.1)$$

$$Y_a = (Y_{sim}+Y_{sim2a}) \quad (6.2)$$

$$Z_a = -(Z_{sim}+Z_{sim2a}) \quad (6.3)$$

Based on the ACP's position in space (X_a, Y_a, Z_a), the airwake velocity data (U_a, V_a, W_a) is read from the look-up tables, and then the nominal freestream velocity component is subtracted from *x* and *y* total velocity components (Eqns. 6.4 and 6.5), to obtain velocity perturbations from nominal freestream with an Atmospheric Boundary Layer (ABL) correction.

$$U_{pert} = U_a - V_{WOD}*cos(Azi_{WOD}) \quad (6.4)$$

$$V_{pert} = -(V_a + V_{WOD}*sin(Azi_{WOD})) \quad (6.5)$$

where V_{WOD} and Azi_{WOD} are Wind Over Deck (WOD) magnitude and direction, respectively. These data are then passed to the FLIGHTLAB environment.

6.3. Effect of Ship Airwake on an RTF-Class I UA Model

6.3.1. GCS Airwake Test Conditions

The RTF Class I UA model was launched at 45 degrees from the ship's bow to simulate a headwind (relative to the UA) launch for a Green 45 wind at three different speeds 10, 15, and 20 knots. This represents 10, 20, 30 Green 45 WOD conditions. The UA model was also launched into a beam crosswind at 315 degrees (45 degrees to port from the ship's bow), as shown in Figure 6.13, under the same WOD conditions as the headwind launches. The figure also shows the FLIGHTLAB sign convention used for the data formatting. These conditions reflect a combination of the most benign and worst launch directions. The inertial X direction is positive from stern to bow, Y direction from port to starboard and Z direction vertically downwards. Aircraft take-off or launch speeds are referenced to the Indicated Airspeed (IAS), i.e. the speed at which the aircraft is moving through the air. IAS is the combination of groundspeed and wind speed, and a value of was 50 knots was used for all of the tests. The model was launched into a 'clean' freestream as a control to show the differences between

the effects of clean air and turbulent airwake on the model. Table 6.5 provides a summary of the models and test conditions used in the UA testing.

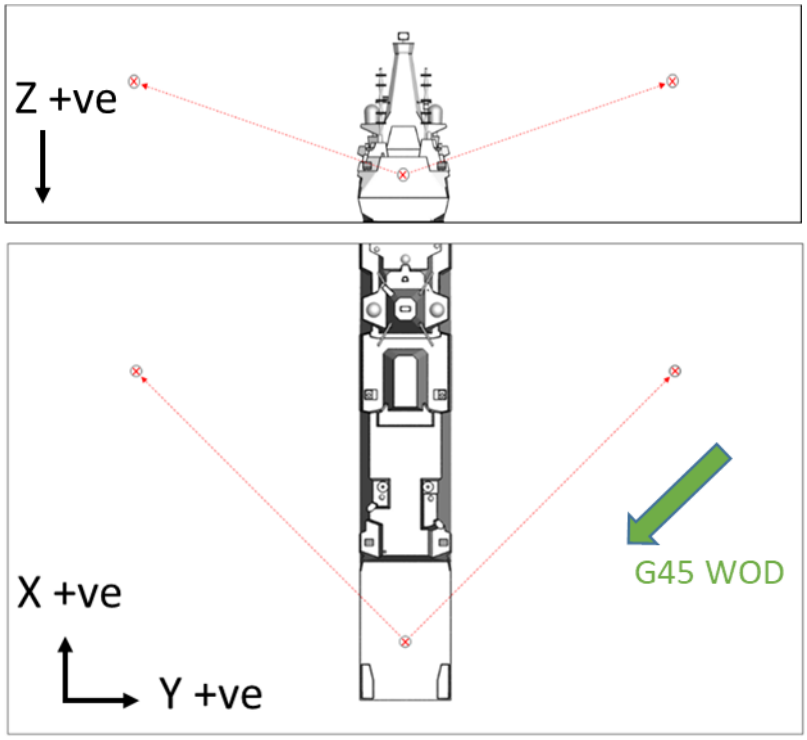

Figure 6.13: UA Launch trajectories and FLIGHTLAB co-ordinate system

Table 6.5: Model launch test conditions

Model	Launch Azimuth (°)	WOD	Airwake
RTFSE_01	45	10 kts G45	N
RTFSE_02	45	15 kts G45	N
RTFSE_03	45	20 kts G45	N
RTFSE_04	315	10 kts G45	N
RTFSE_05	315	15 kts G45	N
RTFSE_06	315	20 kts G45	N
RTFSE_1	45	10 kts G45	Y
RTFSE_2	45	15 kts G45	Y
RTFSE_3	45	20 kts G45	Y
RTFSE_4	315	10 kts G45	Y
RTFSE_5	315	15 kts G45	Y
RTFSE_6	315	20 kts G45	Y

6.3.2. GCS Airwake Virtual AirDyn

In Chapter 3, the Virtual AirDyn (VAD) desktop flight simulation tool was described. Unlike the piloted flight simulation work that has been conducted at UoL with unsteady airwakes [168], the VAD does not require any pilot inputs to stabilise the flight model in the presence of a disturbance. In Chapter 3, a trimmed FLIGHTLAB helicopter model was immersed in an unsteady CFD airwake at fixed positions and the out-of-trim unsteady forces and moments were recorded to give a measure of the impact of the airwake on the vehicle's response. This method has been adopted in this chapter to allow the effect of a ship's airwake on a UA launch to be assessed.

The CFD-generated velocity components of the airwake are imposed onto the UA model via the ACPs, as described in Section 6.2.2.2 (see Figure 6.12). The UA was held stationary in the ship's airwake at the locations shown in Figure 6.14 and the time histories of the unsteady moments and forces at the UA's centre of gravity were recorded over the thirty seconds of airwake data. The VAD analysis was conducted at seven locations (1 – 7) for port side (P) and starboard side (S) launches in a Green 45 wind, Tables 6.6 and 6.7 provide details of the spot locations. For the port launches, the aircraft had a heading of 315° relative to the ship's bow, representing a crosswind launch and a heading of 45° for an into-wind launch, as shown in Figure 6.14.

Table 6.6: Point locations for port side VAD assessment

	P1	**P2**	**P3**	**P4**	**P5**	**P6**
X (ft)	-200	-166	-133	-100	-66	-33
Y (ft)	0	-33	-66	-100	-133	-166
Z (ft)	-30	-40	-50	-60	-70	-80

Table 6.7: Point locations for starboard side VAD assessment

	S1	**S2**	**S3**	**S4**	**S5**	**S6**
X (ft)	-200	-166	-133	-100	-66	-33
Y (ft)	0	33	66	100	133	166
Z (ft)	-30	-40	-50	-60	-70	-80

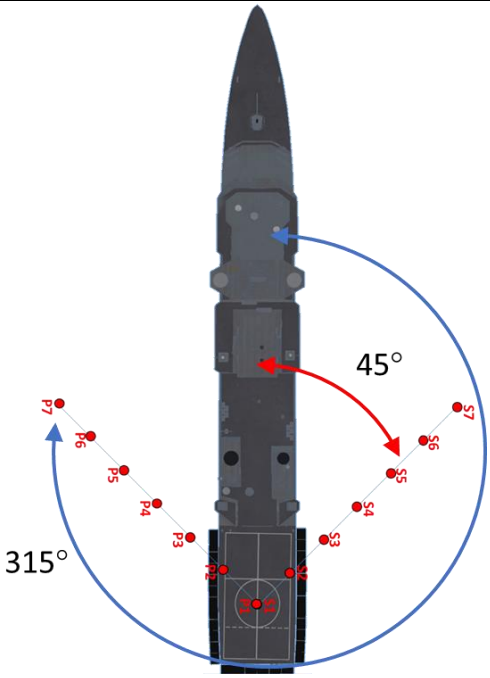

Figure 6.14: VAD locations and UA headings

6.3.3. UA Airwake Encounter Results

In Chapter 3, the VAD technique was used in conjunction with an examination of the CFD flow fields to investigate the airflow in/around the helicopter launch and recovery area prior to future vehicle operations. A similar approach is adopted here to investigate the hazards posed for UA launches. An analysis of the vehicle's response is undertaken first using the VAD technique, followed by an examination of the CFD airwake to identify the causes of the responses. Finally, the simulation model is launched into an airwake environment and its performance assessed.

Figures 6.15 and 6.16 show the VAD time-histories for both the port and starboard launch conditions at sensor locations 1-7 for a 20 knots Green 45 WOD (model RTFSE_6 in Table 6.5). This speed was selected as it was considered to be the most challenging condition that could be tested. The UA model was not able to trim in higher crosswind speeds due to control limits being reached. All aircraft have crosswind limits and this value is in line with a typical UA. It should be remembered that the VAD analysis shows the unsteady moments and forces on the basic airframe i.e. does not include the effect of the flight controller (or pilot if there is one) which will be explored later in this section.

The results show that at locations P1/S1, the centre of the ship's deck, the aircraft is subjected to the largest forces and moments indicating that it is in the region of most disturbed airflow. For the port side locations, there are significant variations in the both the

forces at locations P2 and P3 whilst on the starboard side the variations have dampened out at S2/S3. This suggests that the size of the disturbance region on the port side is larger than on the starboard side. In addition to the disturbed region being larger, the forces and moments on the port side are significantly larger indicating that the airflow there is more highly disturbed than the starboard side.

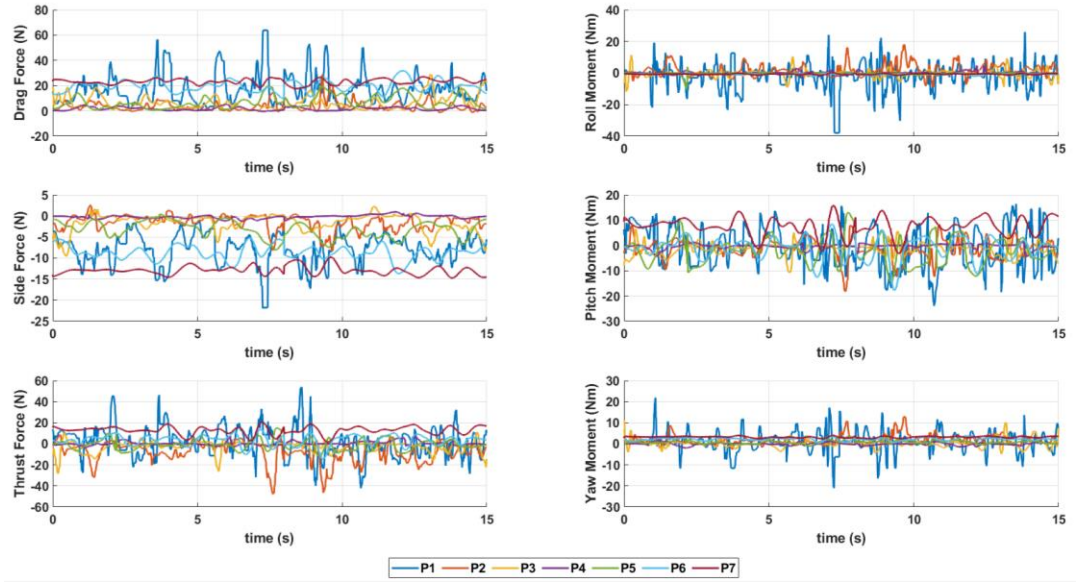

Figure 6.15: Port side force and moment time histories, 20 knot wind

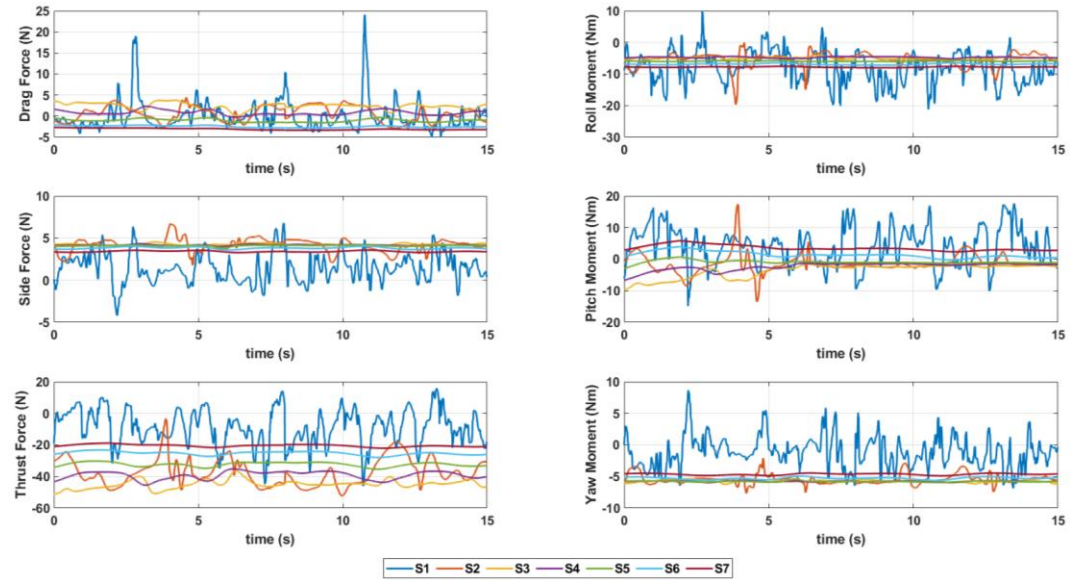

Figure 6.16: Starboard side force and moment time histories, 20 knot wind

The differences in the unsteady forces and moments on the aircraft, produced by variations in the local flow conditions, are captured in the RMS values for each spot location as shown in Figures 6.17 and 6.18. As was seen with the VAD time histories, the effect of the airwake is more significant on the port side compared to the starboard side. This indicates that the aircraft is in much more disturbed airflow on the port side compared with the starboard side with a 50% incease in the moment RMSs in some cases. It also shows that the unsteadiness dampens out more quickly on the starboard side. On the port side there is a significant change in the pitching moment, My, between P4 and P5, suggesting a sudden change in the local flow conditions.

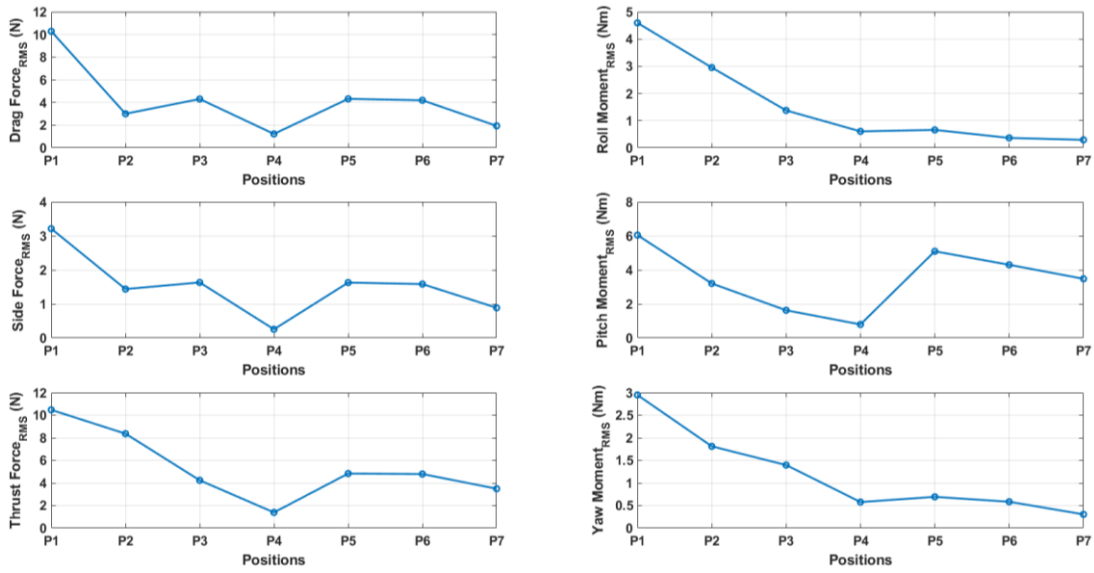

Figure 6.17: VAD RMSs for port side launch, 30 knots groundspeed 20 knots wind

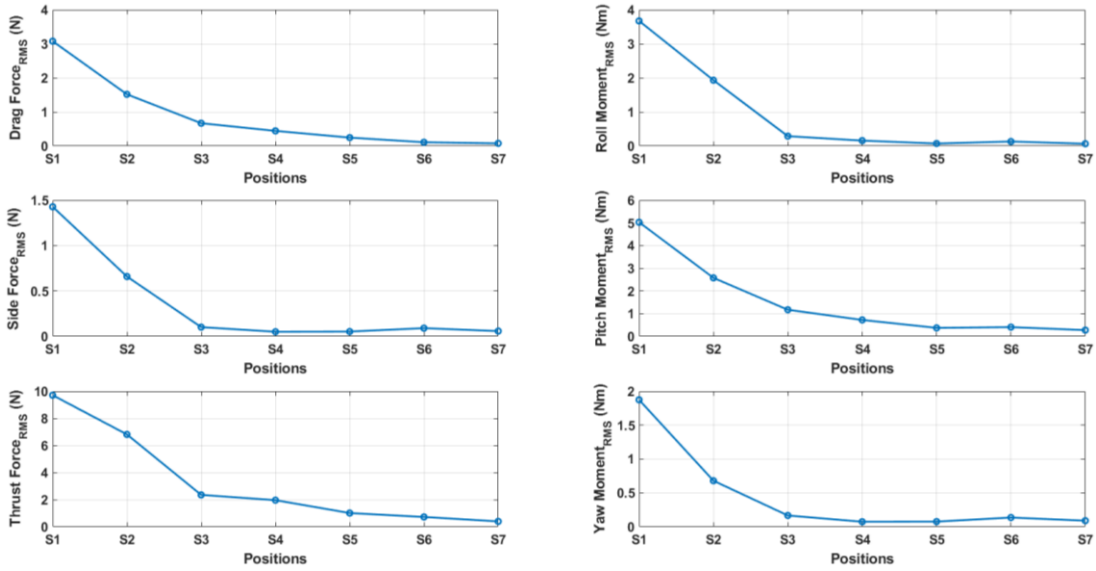

Figure 6.18: VAD RMSs for starboard side launch, 30 knots groundspeed 20 knots wind

To examine the source of the VAD results, CFD contour plots were taken at a plane along the intended flightpath shown by the red line in Figure 6.19. All the CFD images presented below are in plan view from directly above the GCS.

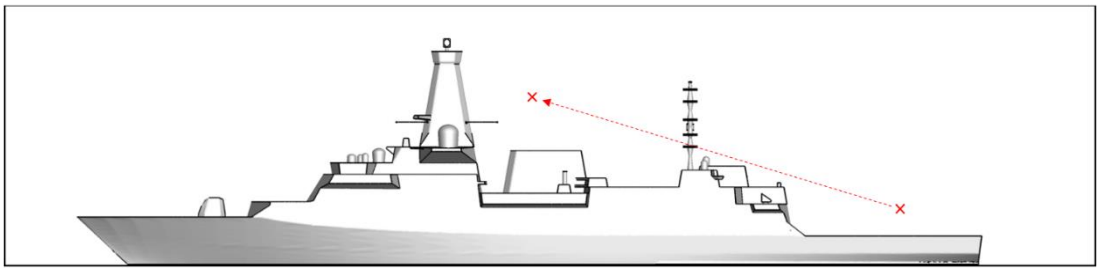

Figure 6.19: Side view of UAV launch trajectory from GCS flight deck

Figure 6.20 shows contours of lateral turbulence intensity along the intended flightpath. The black circles represent the VAD sample locations on the port (P) and starboard (S) intended trajectories. The first point to note is that the co-located launch points P1/S1 are in an area where a highly turbulent shear layer has formed due to the oblique wind separating from the vertical hangar edge. Should the VAD/CFD tools be used for launch planning purposes this area would likely be identified as an area to avoid for launching the UA.

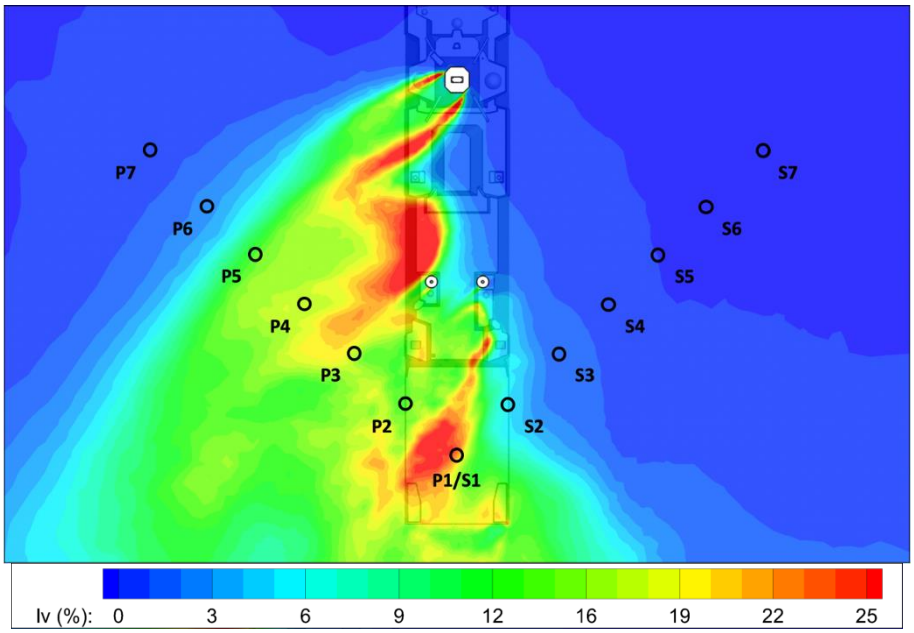

Figure 6.20: Contours of lateral turbulence intensity showing VAD sample locations

When examining the CFD flow field for the starboard launch condition, the turbulence intensity level drops rapidly as the sample points move away from the deck edge. This is not the case for the port launch where the sampling points P3 and P4 are still in areas of disturbed flow in the lee of the ship. As would be expected the data are consistent with the

VAD results. When the UA is flying in areas of disturbed airflow the aircraft will be subject to the larger forces and moments which the flight controller will have to counteract. Whilst it is outside the scope of this thesis, the tools being developed have the potential to be used as part the flight controller design process.

In the VAD analysis, an apparent anomaly in the trend of reducing RMS values moving away from the ship was noted between locations P4 and P5. Figure 6.21 shows contours of longitudinal velocity normalised by the freestream values with the VAD sample locations indicated by black circles. Along the port side trajectory, there is an increase in the longitudinal velocity at location P5 resulting from the upstream flow separation caused by the main mast. This would result in an increase in the velocity disturbances across the UA's wingspan leading to a larger pitching moment RMS value as observed in the VAD results.

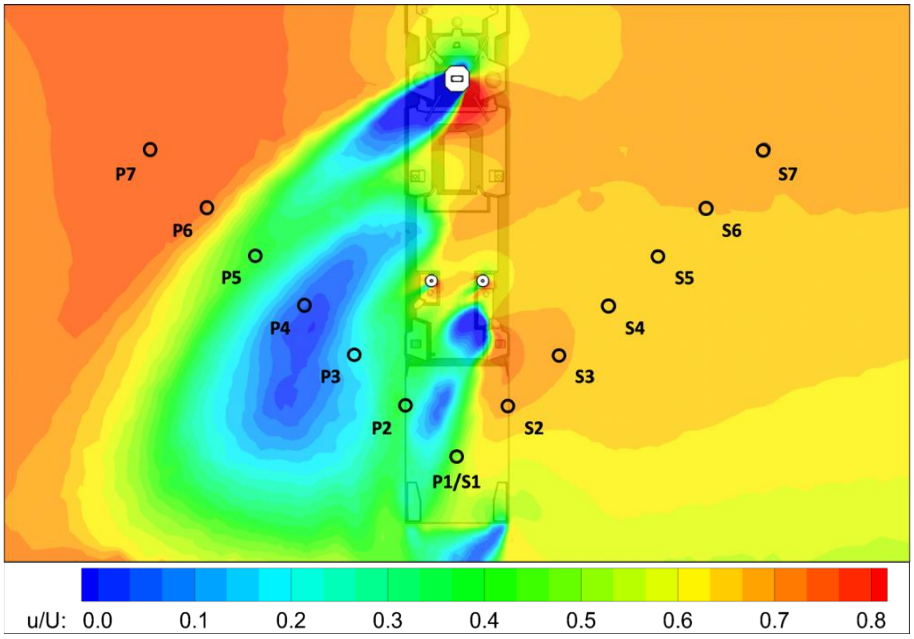

Figure 6.21: Contour of longitudinal velocity normalised by the freestream value

The VAD technique was applied to an aircraft fixed in space subjected to local unsteady flow disturbances. The results from the VAD analysis correlate with the observations made for the CFD plots. However, what is ultimately of interest is the response of the vehicle in free flight following a launch. A study was conducted to examine UA launches, with and without the AFCS active in different wind conditions. The effect of the ship's airwake on a UA without the flight control system active is shown in Figure 6.22 for port and starboard launches at different launch speeds. Whilst launches would typically be conducted with an AFCS active, a control engineer needs to have an idea of the degree of gust rejection that the system requires to optimise their design. Design of the AFCS is outside the scope of this thesis but

previous rotary-wing research [101] showed the importance of observing the 'free response' of a UA for control optimisation; the simulation environment presented in this thesis enables this to be examined for a fixed-wing UA. Under nil wind conditions, the un-controlled UA follows the initial launch trajectory as would be expected. When introducing the unsteady airwake, the lack of a flight control system prevents the UA following the desired launch trajectory when in the presence of an unsteady airwake. At different launch speeds, the UA will not encounter the same unsteady airwake velocity components due to the time varying nature of the wake. At the lowest 35 knots launch speed the UA is immersed longer in the airwake resulting in the largest flightpath deviations. For the 55 knots launch, after initially 'surviving' the launch, examination of the ACP data showed that the UA encountered a downdraft causing it to lose height resulting in contact with the sea's surface.

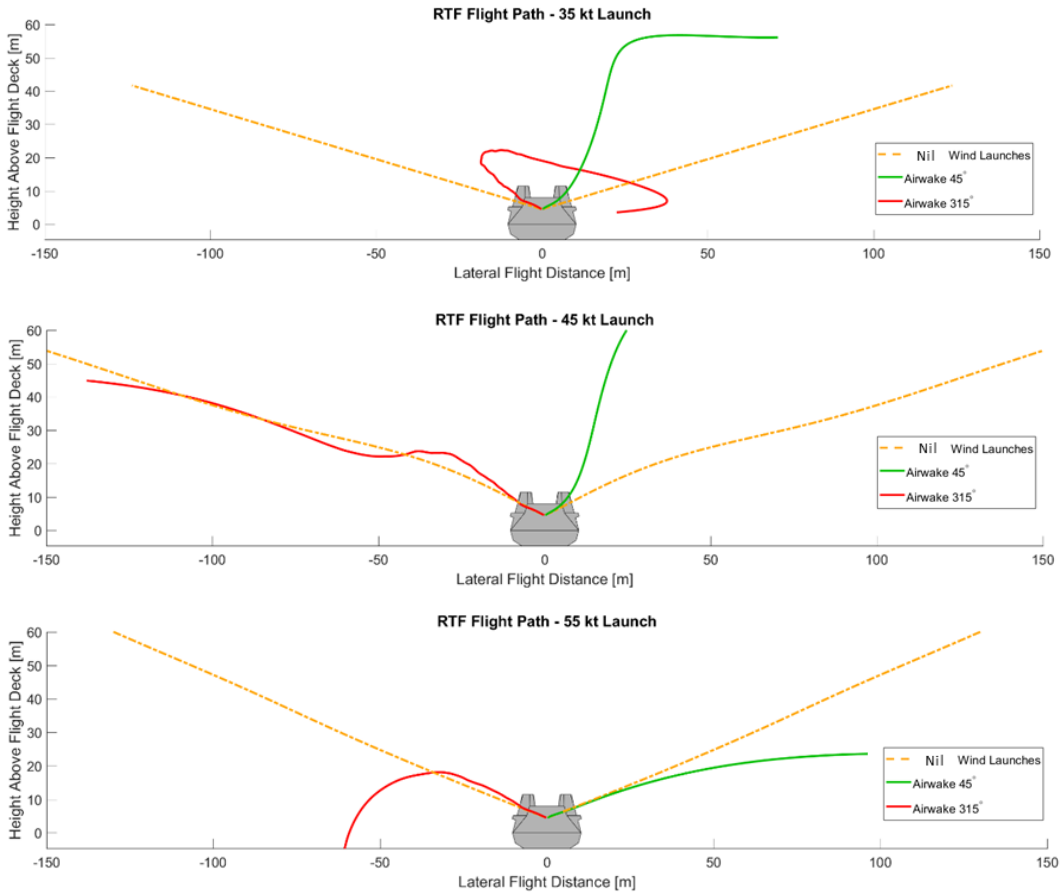

Figure 6.22: Stern views of launches of uncontrolled UA into nil wind, 20 knots 45° and 315° airwakes from the GCS bow

The time-dependent nature of a UA encounter with an unsteady airwake is illustrated in Figure 6.23 for the 35 knot launch condition, comparing this time a uniform wind i.e. freestream value and an unsteady airkwake launch. When an airwake is integrated into the

real-time simulation, a timing signal is used to step the airwake forward in time. For the previous comparison, all the simulations commenced at the same clock time. The launches shown in Figure 6.23 begin at different clock times, allowing the UA to encounter different flow structures within the airwake. For the starboard launches (indicated by the green line) there is little difference in the flightpath due to the launch time; i.e. there is no difference for the uniform wind. As with the launch into the uniform wind, in the airwake cases the UA encounters a headwind which increases the rate of climb of the UA again as expected. For the portside launches, there is a significant difference between the UA's trajectory at different launch times indicating that the UA is encountering time-varying flow conditions. Again, this should be expected due to the flapping shear layer that is present in and around the launch location. This highlights the need to examine the UA's response throughout the airwake time history to ensure the worst-case attitude change is identified and including in any AFCS design.

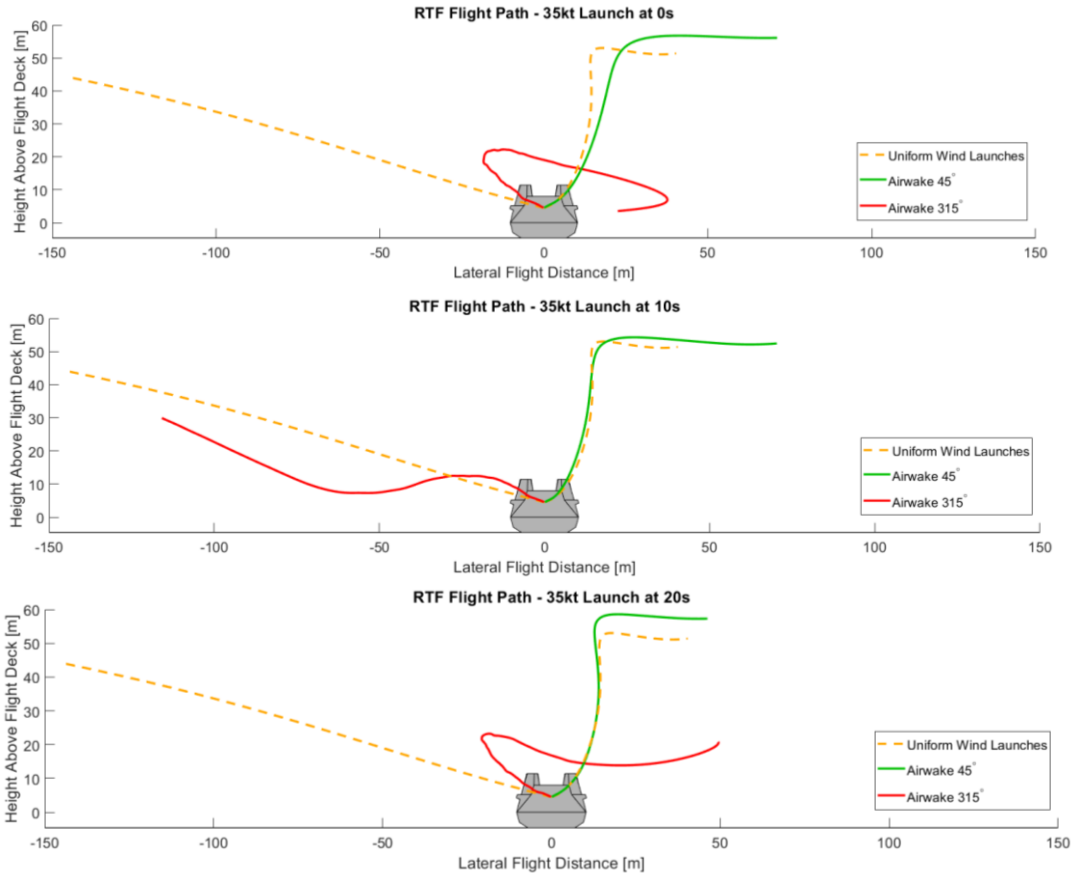

Figure 6.23: Stern views of uncontrolled UA launches at different airwake time intervals

Figure 6.24 shows the impact of a 'basic' ACFS i.e. non-optimised, on UA flight path control in the presence of an airwake.

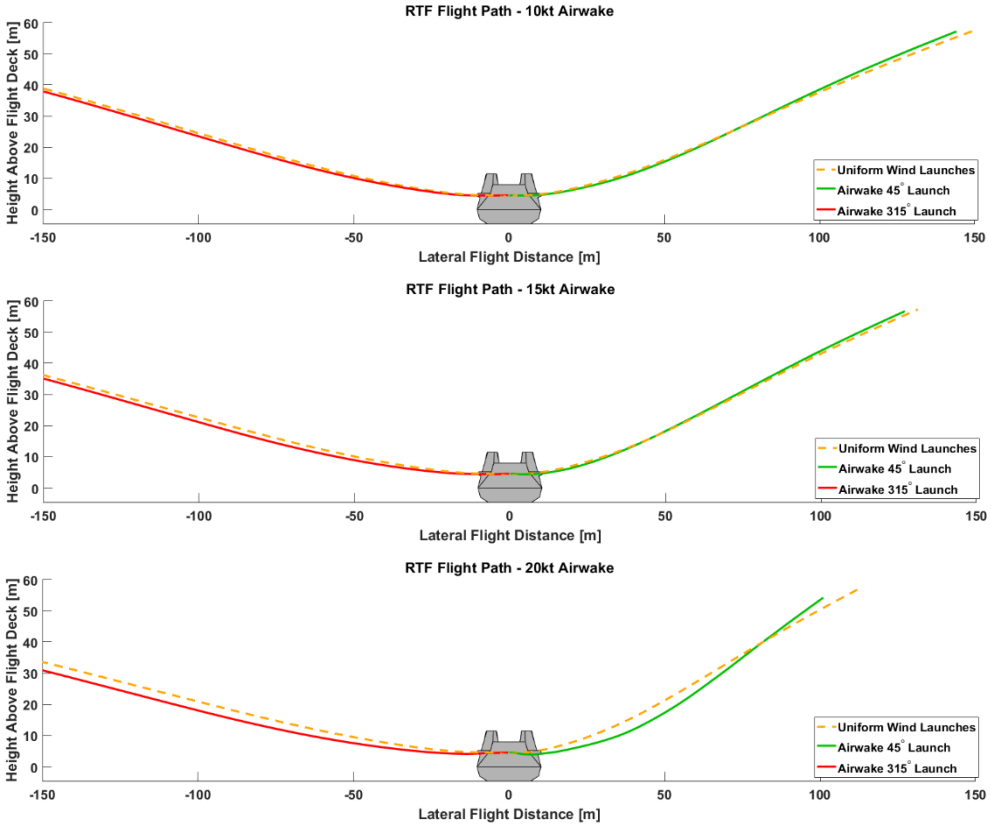

Figure 6.24: Stern view of controlled UAV launch trajectories at 45° and 315° from the GCS bow

The vertical profile flown by each model, with and without the airwake (i.e. in unsteady and steady flow), following a launch with the AFCS active. The vertical climb performance for the 45° headwind launch is much improved compared to 315° crosswind condition as might be expected. For both launch directions, an increase in wind strength causes a larger deviation between the flightpath in the no-wake (uniform wind launch representing the freestream condition) and wake conditions. As previously stated, optimisation of the ACFS is outside the scope of this thesis, however the impact of implementing a basic ACFS is illustrated in Figure 6.25. Without the AFCS, launches in the presence of an airwake could results in loss of the UA and possible collision with the ship.

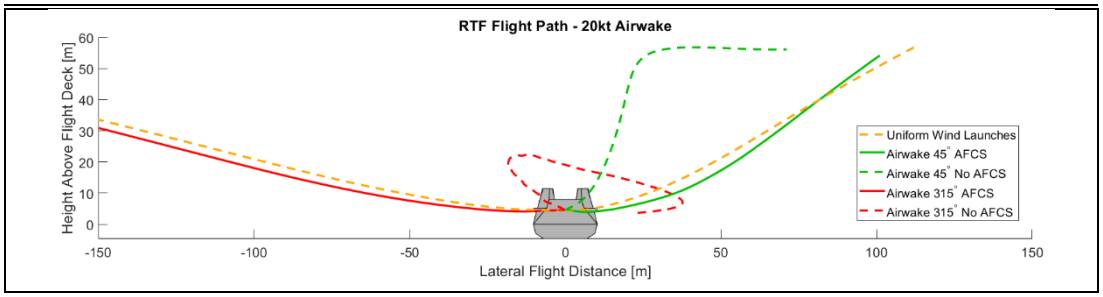

Figure 6.24: Stern view of UAV launch trajectories at 45° and 315° from the GCS bow

6.4. Chapter Summary

The development of a new modelling and simulation environment for UA launches has been presented in this chapter. A Class I type UA flight dynamics model was integrated with a CFD airwake in FLIGHTLAB. Unlike the traditional fixed-wing wake modelling approach, the airwake was applied to the flight dynamics model using Airload Computation Points, allowing velocity gradients across the vehicle to more realistically affect the vehicle's trajectory. Simulated port and starboard launches were examined in the presence of a Green 45 wind. The VAD technique identified that port side launches would be subjected to larger forces and moments compared with starboard side launches. An examination of the CFD flow field showed that this was caused by the large areas of turbulent flow in the lee of the ship's superstructure. The launch spot chosen in the study was found to be in the area of highest disturbed flow and it would be recommended to identify of launch areas for future studies. The time varying nature of the unsteady airwakes needs to be considered when designing an AFCS to control the flightpath of a UA.

The method presented in this Chapter shows that it is possible to investigate the effect of local flow conditions on UA launches, identify launch avoid areas and could be used to test flight control system designs prior to real-world testing.

Chapter 7. Conclusions and Recommendations

Although modern warships routinely operate with on-board helicopters, the effect of the ship superstructure aerodynamics on the flying environment around the ship is generally not considered in the design process. Previously the air flow over the ship has been investigated using wind tunnel studies but these do not give much insight into how the air flow will affect the helicopter. Similarly, the air flow at the anemometer locations have previously been investigated in the wind tunnel, and smoke tests have been used to observe the trajectory of the exhaust plume. These tests seem to be carried out because the relevant Defence Standard, referred to in Chapter 4, requires them, but there is no evidence that the ship design is altered as a result of the tests. The ultimate testing of the flying environment and the anemometer performance comes during sea trials, by which time it is too late to remedy any problems due to the ship's structure. Modern warship superstructure designs are evolving to become more RCS-compliant, and the emerging geometries are having an even greater effect on the ship's aerodynamics. The study reported in this thesis is a major contribution to a project carried out at the University of Liverpool whereby the aerodynamic analysis of the Type 26 City class frigate was carried out solely by CFD, and it was done during the design process and informed many of the design decisions that were made. The research is a major contribution to improving knowledge and understanding of how the ship architecture affects the air flow and, in turn, the ship's helicopter. The major areas of concern for the helicopter are the air flow conditions over and around the flight deck, including the raising of ambient temperatures due to the ship's engine exhaust gas, and the accuracy of the ship's anemometers and their ability to specify the relative wind strength and direction, which is crucial in defining the safe operating limits for the helicopter.

It has been a challenge to convince a very traditional ship building industry that computational modelling and simulation has a role to play in informing ship design from the perspective of the ship's helicopter. However, during the course of this research project, confidence and trust has been developed, so much so that the CFD methodology is currently being applied to the Australian derivative of the Type 26, the Hunter class. Important lessons have been learned during the research, but there is also more work that needs to be done

to improve the analytical support that can be given to the ship designers during the design cycle. The following sections present the main conclusions from the research and recommendations for further work.

7.1. Conclusions

1. CFD has been demonstrated to be an effective tool for predicting the air flow over and around a full-scale warship. Once the solution method has been set up, the ability to test variations in flow conditions and geometry make CFD a very flexible alternative to wind tunnel testing. DES is an effective hybrid formulation of LES and RANS for producing unsteady full-scale airwakes. It has been shown that density boxes, which limit the growth of the computational mesh, are necessary to resolve the turbulent eddies at an appropriate length scale.

2. The GCS-compliant design of the modern warship does affect the air flow over the flight deck and hence the ship's helicopter. This should be acknowledged at the beginning of the design process and should inform design and operational decisions. The differences have been quantified through a CFD analysis of the Type 23 frigate and the GCS, including an assessment of how the different airwakes will affect the aerodynamic loads on a helicopter. The Type 23, with its smaller and more fragmented superstructure, creates a less aggressive airwake than the GCS.

3. The relative smooth unbroken superstructure of the GCS allows the air flow from oblique winds to flow mostly unhindered down the side of the ship and to produce a turbulent air flow over the flight deck. CFD analysis showed that the air flow over the flight deck with and without the Mission Bay doors open did affect the air flow and the predicted unsteady loads on the helicopter; however, it was not clear that this would lead to greater pilot workload during launch and recovery.

4. The more slender main mast and yardarms on the Type 23 frigate have significantly less effect on the ship's anemometers than do the bulky main mast and shorter, less isolated, yardarms of the GCS.

5. The dispersion of the ship engine exhaust gases was conducted for full power from the gas turbines, and therefore the Type 23 was operating on two turbines that were each approximately half of the power output from the GCS. The total mass flow rate and temperature of the turbine exhaust gases was therefore the same for both ships. It was demonstrated that the larger airwake of the GCS was more effective in dispersing and

cooling the exhaust efflux. The exhaust plume from the Type 23 presents a greater threat to the helicopter, in both winds from ahead and from Green 30, due to the plume being slightly hotter and closer to the landing deck.

6. In winds from close to ahead it has been shown that the bulky main mast of the GCS creates a large recirculation zone in its wake that entrains hot exhaust gases from the engine exhausts. The recirculated hot gases have the potential to increase the ship's infra-red signature, unlike the Type 23 where the smaller mast does not entrain the hot engine exhaust gases. Deflectors in the exhaust outlet could remedy this situation.

7. It has been demonstrated that the air flow distortion at the ship's anemometers around the 360° azimuth can be determined using CFD.

8. The bulky main mast of the GCS will inevitably distort the air flow at the ship's anemometer locations. The current practice, and the statements in DEFSTAN 00-133 Part 2, need to be modified, otherwise the anemometers will never be placed in a suitable location. At the very least, the main anemometers should be placed as high up the main mast as possible and mounted on slender yardarms of suitable length.

9. The convention of mounting the anemometers on the main mast should be questioned and alternative locations on the superstructure explored; this can be done using the CFD data.

10. An aft anemometer is a feasible solution to obtaining accurate wind measurements for winds from astern (tailwind ±45°). However, the placement of the anemometer needs careful consideration. For the GCS, the aft anemometer should be placed as high as possible on the rear pole mast, mounted on a short yardarm that is facing directly aftwards.

11. The wealth of knowledge that previously informed the design of a ship's exhaust funnels so they would effectively disperse the ship's engine exhaust gases away from the ship (including the use of deflectors) is not being used. The design of the funnels is mainly driven by RCS, and predictive CFD analysis should be used to investigate the interaction of the hot gases with the ship's superstructure to prevent local surfaces being heated.

12. The hot engine exhaust gases are significantly cooled through mixing with the turbulent airwake. Nevertheless, air temperatures in the flying areas around the flight deck can become elevated and unsteady, which can adversely affect the helicopter. The analysis shows that oblique winds from the starboard, e.g. Green 30, can be the most problematic

as the exhaust gases are deflected into the area off the port side of the ship where the helicopter beings its landing manoeuvre.

13. The inclusion of an eductor in the CFD analysis of the exhaust gas dispersion was successfully implemented. The eductor was effective in improving the cooling of the hot exhaust gases, but elevated air temperatures will still be present.

14. Unlike the CAA, the military authorities do not have safety standards for air temperature elevations over helicopter landing decks. This study has shown how the unsteady air temperatures in the flying area can be calculated and has provided quantified examples. An equivalent military assessment and safety standard should be considered.

15. While there is now a useful body of experimental data to provide confidence in CFD-computed ship airwakes, the same in not true for the computation of hot gas mixing in a turbulent cross flow. The experiment described in this thesis was intended to address that shortfall, and should be pursued.

16. A novel modelling and simulation technique for assessing the flight trajectory of an Unmanned Aircraft in a ship's airwake has been developed and demonstrated. The Virtual AirDyn analysis was used to explain how the loads on the UA were consistent with the CFD airwake. The simulated flight trajectories, into relatively clean headwinds and into turbulent crosswinds, were computed. The simulation method has good potential for developing UA for maritime applications, for developing appropriate flight controllers, and for developing appropriate launch and recovery operational procedures.

17. The unsteady nature of the airwakes means that there is a time dependency on the level of UA upset following an encounter. A significant difference in UA flightpath will occur depending on which part of the airwake the UA is launched into. This needs to be fully examined in any AFCS design activities.

7.2. Recommendations

1. Existing practices for placing the ship's main anemometers are not effective for the modern RCS-compliant warship. A survey of the GCS superstructure should be undertaken, using the already computed CFD airwakes, to identify where, if anywhere, the air flow is least affected and the anemometers will be most effective.

2. The use of traditional anemometers mounted on the ship's superstructure should be challenged, and alternative air flow measurement techniques sought, e.g. LIDAR (Light Imaging Detection and Ranging).

3. The inclusion of aft anemometers should be considered for all future helicopter-enabled ships. The placement of the aft anemometer should be carefully selected to avoid local flow distortion and adjacent equipment.

4. The study into the confidence of CFD for computing the mixing of hot gas jets in a turbulent cross flow should be pursued, both experimentally as recommended in the thesis, and by varying the turbulent Prandtl number in the CFD.

5. In future CFD studies of ship exhaust gas dispersion the inclusion of surface heating should be specified from the outset.

6. Further development of the Unmanned Aircraft simulation method should be undertaken to realise its full potential for designing the vehicle and its control system and for exploring different deployment scenarios.

References

[1] The National Museum, “A brief History of the Royal Navy.” [Online]. Available: http://www.nmrn-portsmouth.org.uk/sites/default/files/styles/homepage_collections_slidshows/public/modules/image/A brief history of the RN.pdf. [Accessed: 14-Feb-2019].

[2] C. N. Longridge, *The Anatomy of Nelson’s Ships*. Hemel Hempstead, UK: Special Interest Model Books, 1955.

[3] J. Fincham, *A History of Naval Architecture*. London, UK: Whittaker & Co, 1851.

[4] Navy Wings, “70th Anniversary of Pioneering Helicopter Landing.” [Online]. Available: https://navywings.org.uk/news-blog/70th-anniversary-pioneering-helicopter-landing/. [Accessed: 15-Feb-2019].

[5] Fleet Air Arm Officers Association, “Fleet Air Arm History.” [Online]. Available: https://www.fleetairarmoa.org/fleet-air-arm-history-timeline. [Accessed: 01-Feb-2019].

[6] L. B. Bryson, F. E. Heenan, and C. A. Johnson, “Helicopters in the Royal Navy,” *Aeronaut. J.*, vol. 76, no. 740, pp. 469–500, 1972.

[7] World Naval Ships, “RN Destroyers: Tribal Class (1936).” [Online]. Available: https://www.worldnavalships.com/forums/showthread.php?t=10926. [Accessed: 10-Jan-2019].

[8] S. Huler, *Defining the Wind: The Beaufort Scale, and How a 19th-Century Admiral Turned Science into Poetry*. Crown Publishers, 2004.

[9] W. E. Knowles Middleton, *Invention of the Meteorological Instruments*. Baltimore: The Johns Hopkins Press, 1969.

[10] PV Performance Modeling Collaborative, “Wind Speed and Direction,” 2018. [Online]. Available: https://pvpmc.sandia.gov/modeling-steps/1-weather-design-inputs/weather-observations/wind-speed-and-direction/. [Accessed: 12-Jan-2019].

[11] Gill Instruments Limited, “WindObserver II Wind Speed Sensor,” 2019. [Online]. Available: http://www.gill.co.uk/products/anemometer/wind-speed-and-direction-sensors.html. [Accessed: 12-Jan-2019].

[12] Biral Industrial and Research Associates Limited, “Ultrasonic Anemometer 3D,” 2019. [Online]. Available: https://www.biral.com/product/ultrasonic-anemometer-3d-4-3830-20-340/. [Accessed: 12-Jan-2019].

[13] W. J. Pierson, “Examples of, reasons for, and consequences of the poor quality of wind data from ships for the marine boundary layer: Implications for remote sensing,” *J. Geophys. Res.*, vol. 95, no. C8, pp. 13313–13340, 1990.

[14] C. Lavers, *Reeds Vol 14: Stealth Warship Technology*, 1st ed. London, UK: Adlard Coles Nautical, 2012.

[15] Anon., “Stealthy Class - The World’s Best Navy Corvettes,” *Arthashastra - Indian Defense & Space*, 2019. [Online]. Available: http://harindrakumar.blogspot.com/2015/01/stealthy-class-worlds-best-navy.html. [Accessed: 15-Jan-2019].

[16] R. O’Rourke, “Navy DDG-51 and DDG-1000 Destroyer Programs : Background and

Issues for Congress," *Congr. Reseach Serv. Rep. Congr.*, 2019.

[17] R. Sisk, "The US Navy's newest stealth destroyer could get nuclear cruise missiles," *Business Insider*, 2018. [Online]. Available: https://www.businessinsider.com/us-navy-stealth-destroyer-nuclear-cruise-missiles-2018-2?r=US&IR=T. [Accessed: 15-Jan-2019].

[18] Anon., "D-92 HMS Liverpool," *Seaforces - Online*, 2019. [Online]. Available: http://www.seaforces.org/marint/Royal-Navy/Destroyer/D-92-HMS-Liverpool.htm. [Accessed: 15-Jan-2019].

[19] Anon., "Improving the Type 45 Destroyer," *UK Defence Journal*, 2019. [Online]. Available: https://ukdefencejournal.org.uk/improving-the-type-45-destroyer/. [Accessed: 09-Apr-2020].

[20] Prism Defence, "Prism Defence." [Online]. Available: http://www.prismdefence.com.

[21] B. Lumsden and G. D. Padfield, "Challenges at the helicopter-ship dynamic interface," in *Military Aerospace Technologies, FITEC '98*, 1998, no. 10, pp. 89–122.

[22] Prism Defence, "Danish Defence MH-60R Seahawk bad weather landing," *Forsvaret*, 2016. [Online]. Available: https://www.youtube.com/watch?v=w3A_noXLzuo. [Accessed: 15-Jan-2019].

[23] S. J. Hodge, J. S. Forrest, G. D. Padfield, and I. Owen, "Simulating the environment at the helicopter-ship dynamic interface: research, development and application," *Aeronaut. J.*, vol. 116, no. 1185, pp. 1155–1184, Nov. 2012.

[24] Research and Technology Organisation (RTO), "RTO AGARDograph 300: Helicopter/Ship Qualification Testing," North Atlantic Treaty Organisation (NATO), 2003.

[25] Ministry of Defence, "Defence Standard 00-133 Aviation Arrangements in Surface Ships Parts 0-4," 2015.

[26] M. Roscoe and C. Wilkinson, "DIMSS - JSHIP's Modelling and Simulation Process for Ship/Helicopter Testing & Training," in *AIAA Modeling and Simulation Technologies Conference and Exhibit*, 2002, no. August, pp. 1–12.

[27] G. Turner, W. Clark, I. Cox, B. Finlay, and J. Duncan, "Project SAIF – assessment of ship helicopter operating limits using the Merlin helicopter simulator," in *American Helicopter Society 62nd Annual Forum*, 2006.

[28] S. Johncock, "F 231 HMS Argyll," *Seaforces - Online*, 2019. .

[29] BAE Systems, "Further 500 UK Maritime Industries jobs sustained by new Type 26 Global Combat Ship Contract Awards," *BAE Systems*, 2017. [Online]. Available: https://www.baesystems.com/en/article/further-500-uk-maritime-industries-jobs-sustained-by-new-type-26-global-combat-ship-contract-awards. [Accessed: 15-Jan-2019].

[30] R. Mateer, S. A. Scott, I. Owen, and M. D. White, "Superstructure Aerodynamics of the Type 26 Global Combat Ship," in *14th International Naval Engineering Conference and Exhibition (INEC)*, 2018.

[31] M. F. Kelly, N. A. Watson, S. J. Hodge, M. D. White, and I. Owen, "The Role of Modelling and Simulation in the Preparations for Flight Trials Aboard the Queen

Elizabeth Class Aircraft Carriers," in *Proceedings of the International Naval Engineering Conference & Exhibition (INEC)*, 2018.

[32] K. R. Reddy, R. Toffoletto, and K. R. W. Jones, "Numerical simulation of ship airwake," *Comput. Fluids*, vol. 29, no. 4, pp. 451–465, 2000.

[33] S. Polsky and C. Bruner, "Time-accurate computational simulations of an LHA ship airwake," in *18th Applied Aerodynamics Conference*, 2000.

[34] J. Zhang, G. Minelli, A. Rao, B. Basara, R. Bensow, and S. Krajnović, "Comparison of PANS and LES of the flow past a generic ship," *Ocean Eng.*, vol. 165, no. July, pp. 221–236, 2018.

[35] S. Polsky, "A computational study of unsteady ship airwake," *40th AIAA Aerosp. Sci. Meet. Exhib.*, Jan. 2002.

[36] S. A. Polsky and T. A. Ghee, "Application and verification of internal boundary conditions for antenna mast wake predictions," *J. Wind Eng. Ind. Aerodyn.*, vol. 96, no. 6–7, pp. 817–830, Jun. 2008.

[37] J. Van Muijden, O. Boelens, J. van der Vorst, and J. Gooden, "Computational ship airwake determination to support helicopter-ship dynamic interface assessment," in *21st AIAA Computational Fluid Dynamics Conference*, 2013, no. August.

[38] C. Crozon, R. Steijl, and G. N. Barakos, "Numerical Study of Helicopter Rotors in a Ship Airwake," *J. Aircr.*, vol. 51, no. 6, pp. 1813–1832, 2014.

[39] W. Yuan, R. Lee, and A. Wall, "Simulation of unsteady ship airwakes using openfoam," in *30th Congress of the International Council of the Aeronautical Sciences, ICAS 2016*, 2016.

[40] W. Yuan, A. Wall, and R. Lee, "Simulations of unsteady airwakes behind ships in motion," in *31st Congress of the International Council of the Aeronautical Sciences, ICAS 2018*, 2018.

[41] W. Yuan, A. Wall, and R. Lee, "Combined numerical and experimental simulations of unsteady ship airwakes," *Comput. Fluids*, vol. 172, pp. 29–53, 2018.

[42] E. W. Quon, P. A. Cross, M. J. Smith, N. C. Rosenfeld, and G. R. Whitehouse, "Investigation of ship airwakes using a hybrid computational methodology," *Annu. Forum Proc. - AHS Int.*, vol. 4, pp. 3001–3014, 2014.

[43] D. M. Roper, I. Owen, and G. D. Padfield, "CFD Investigation of the Helicopter-Ship Dynamic Interface," in *61st Annual Forum Proceedings - AHS International*, 2005, vol. 2, pp. 1985–2002.

[44] S. J. Hodge, S. J. Zan, and D. M. Roper, "Time-Accurate Ship Airwake and Unsteady Aerodynamic Loads Modeling for Maritime Helicopter Simulation," *J. Am. Helicopter Soc.*, vol. 54, no. 2, p. 22005, 2009.

[45] J. S. Forrest and I. Owen, "An investigation of ship airwakes using Detached-Eddy Simulation," *Comput. Fluids*, vol. 39, no. 4, pp. 656–673, 2010.

[46] D. M. Roper, "INTEGRATING COMPUTATIONAL FLUID DYNAMICS AND PILOTED SIMULATION SHIP-HELICOPTER OPERATING LIMITS," University of Liverpool, 2006.

[47] J. S. Forrest, "Predicting Ship-Helicopter Operating Limits using Time-Accurate CFD Ship Airwakes and Piloted Flight Simulation," University of Liverpool, 2009.

[48] C. H. Kääriä, “Investigating the Impact of Ship Superstructure Aerodynamics on Maritime Helicopter Operations,” University of Liverpool, 2012.

[49] P. Scott, “THE APPLICATION OF MODELLING AND SIMULATION TO SHIP DESIGN FOR HELICOPTER OPERATIONS,” University of Liverpool, 2017.

[50] M. F. Kelly, “The Development, Validation, and Integration of Aircraft Carrier Airwakes for Piloted Flight Simulation,” University of Liverpool, 2018.

[51] C. H. Wilkinson, S. J. Zan, N. E. Gilbert, and J. D. Funk, “MODELLING HELICOPTER AND SIMULATION OF SHIP AIR WAKES FOR - A COLLABORATIVE VENTURE,” in *RTO Meeting Proceedings 15: Fluid Dynamics Problems of Vehicles Operating Near or in the Air-Sea Interface*, 1999, no. February, p. Section 8: 1-12.

[52] S. J. Zan, “On Aerodynamic Modelling and Simulation of the Dynamic Interface,” *Proc. Inst. Mech. Eng. Part G J. Aerosp. Eng.*, vol. 219, no. 5, pp. 393–410, May 2005.

[53] S. Shukla, S. S. Sinha, and S. N. Singh, “Ship-helo coupled airwake aerodynamics: A comprehensive review,” *Prog. Aerosp. Sci.*, vol. 106, no. February, pp. 71–107, Apr. 2019.

[54] N. A. Watson, M. F. Kelly, I. Owen, S. J. Hodge, and M. D. White, “Computational and experimental modelling study of the unsteady airflow over the aircraft carrier HMS Queen Elizabeth,” *Ocean Eng.*, vol. 172, no. September 2018, pp. 562–574, Jan. 2019.

[55] ANSYS. Inc., “Fluids - Computational Fluid Dynamics,” *ANSYS. Inc.*, 2020. [Online]. Available: https://www.ansys.com/en-gb/products/fluids. [Accessed: 07-Apr-2020].

[56] J. D. Anderson Jr, *Computational Fluid Dynamics: The Basics with Applications*. McGraw-Hill Education, 1995.

[57] F. R. Menter, “Two-equation eddy-viscosity turbulence models for engineering applications,” *AIAA J.*, vol. 32, no. 8, pp. 1598–1605, 1994.

[58] P. SPALART and S. ALLMARAS, “A one-equation turbulence model for aerodynamic flows,” in *30th Aerospace Sciences Meeting and Exhibit*, 1992, p. 23.

[59] K. Hanjalić and B. E. Launder, “A Reynolds stress model of turbulence and its application to thin shear flows,” *J. Fluid Mech.*, vol. 52, no. 4, pp. 609–638, Apr. 1972.

[60] ANSYS. Inc., “4.10. Detached Eddy Simulation (DES),” *ANSYS FLUENT 12.0 Theory Guide*, 2009. [Online]. Available: http://www.afs.enea.it/project/neptunius/docs/fluent/html/th/node42.htm.

[61] ANSYS. Inc., “Heat Transfer Theory,” *ANSYS FLUENT 12.0 Theory Guide*. [Online]. Available: https://www.afs.enea.it/project/neptunius/docs/fluent/html/th/node107.htm. [Accessed: 05-Mar-2019].

[62] W. M. Kays, “Turbulent Prandtl Number—Where Are We?,” *J. Heat Transfer*, vol. 116, no. 2, pp. 284–295, May 1994.

[63] B. van Leer, “Towards the ultimate conservative difference scheme. V. A second-order sequel to Godunov’s method,” *J. Comput. Phys.*, vol. 32, no. 1, pp. 101–136, Jul. 1979.

[64] BAE Systems, “Type 26 Global Combat Ship - DSEi 2013,” *BAE Systems Flickr*, 2013. [Online]. Available: https://www.flickr.com/photos/bae_systemsplc/. [Accessed: 09-Apr-2020].

[65] R. G. Lee and S. J. Zan, “Wind Tunnel Testing of a Helicopter Fuselage and Rotor in a Ship Airwake,” *J. Am. Helicopter Soc.*, vol. 50, no. 4, pp. 326–337, 2009.

[66] ANSYS. Inc., “4.12.2. Standard Wall Functions,” *ANSYS FLUENT 12.0 Theory Guide*, 2009. .

[67] R. Raghav, “Near wall treatment,” *ANSYS Student Community*, 2018. [Online]. Available: https://studentcommunity.ansys.com/thread/neat-wall-tratment/. [Accessed: 02-Feb-2019].

[68] T. Avraham, “Turbulence Modeling – Near Wall Treatment,” *Tomer’s Blog - All About CFD*, 2019. [Online]. Available: https://allaboutcfd-tomersblog.com/2019/06/21/turbulence-modeling-near-wall-treatment-in-ansys-fluent/. [Accessed: 07-Apr-2020].

[69] ANSYS. Inc., “7.3.15. Symmetry Boundary Conditions,” *ANSYS FLUENT 12.0 User Guide*, 2009. [Online]. Available: http://www.afs.enea.it/project/neptunius/docs/fluent/html/ug/node251.htm.

[70] F. M. White, *Fluid Mechanics*, 7th ed. McGraw-Hill Education, 2009.

[71] J. Counihan, “Adiabatic atmospheric boundary layers: A review and analysis of data from the period 1880–1972,” *Atmos. Environ.*, vol. 9, no. 10, pp. 871–905, Oct. 1975.

[72] Royal Navy, “Duke-Class.” [Online]. Available: https://www.royalnavy.mod.uk/the-equipment/ships/frigates/duke-class. [Accessed: 24-Aug-2019].

[73] J. Allen, “HMS Lancaster,” *Defence Images, Flickr*, 2013. [Online]. Available: https://www.flickr.com/photos/defenceimages/9445625916/. [Accessed: 07-Apr-2020].

[74] BAE Systems, “Global Combat Ship.” [Online]. Available: https://www.baesystems.com/en-uk/product/global-combat-ship. [Accessed: 24-Aug-2019].

[75] Wikipedia, “HMS Sutherland (F81),” *Type 23 frigate*, 2012. [Online]. Available: https://en.wikipedia.org/wiki/Type_23_frigate. [Accessed: 15-Feb-2019].

[76] J. Crawford, “Royal Navy Type 23 Frigate HMS Montrose Navigates the Ice Pack in the South Atlantic,” *Wikimedia Commons*, 2011. [Online]. Available: https://commons.wikimedia.org/wiki/File:Royal_Navy_Type_23_Frigate_HMS_Montrose_Navigates_the_Ice_Pack_in_the_South_Atlantic_MOD_45153600.jpg. [Accessed: 15-Feb-2019].

[77] S. Wood, “Type 26 Frigate,” *Royal Navy’s Type 26 Frigates - new £3.7 billion contract signed*, 2017. [Online]. Available: https://des.mod.uk/royal-navys-type-26-frigates-3-7-billion-contract-signed/. [Accessed: 15-Feb-2019].

[78] V. Kolář, “Vortex identification: New requirements and limitations,” *Int. J. Heat Fluid Flow*, vol. 28, no. 4, pp. 638–652, Aug. 2007.

[79] K. Brown, “Type 26 Global Combat Ship CGI Images.” BAE Systems, Scotstoun, Glasgow, 2017.

[80] Royal Navy, “Type 26 Mission Bay,” *Royal Navy*, 2015. [Online]. Available: https://www.royalnavy.mod.uk/news-and-latest-activity/news/2015/september/16/150916-type-26. [Accessed: 15-Feb-2019].

[81] J. S. Forrest, C. H. Kaaria, and I. Owen, “Evaluating ship superstructure aerodynamics for maritime helicopter operations through CFD and flight simulation,” *Aeronaut. J.*, vol. 120, no. 1232, pp. 1578–1603, Oct. 2016.

[82] Y. Wang, J. Curran, G. D. Padfield, and I. Owen, “AirDyn: an instrumented model-scale helicopter for measuring unsteady aerodynamic loading in airwakes,” *Meas. Sci. Technol.*, vol. 22, no. 4, p. 045901, Apr. 2011.

[83] C. H. Kääriä, Y. Wang, M. D. White, and I. Owen, “An experimental technique for evaluating the aerodynamic impact of ship superstructures on helicopter operations,” *Ocean Eng.*, vol. 61, pp. 97–108, Mar. 2013.

[84] C. H. Kääriä, J. S. Forrest, and I. Owen, “The virtual AirDyn: a simulation technique for evaluating the aerodynamic impact of ship superstructures on helicopter operations,” *Aeronaut. J.*, vol. 117, no. 1198, pp. 1233–1248, Dec. 2013.

[85] Advanced Rotorcraft Technology INC., “FLIGHTLAB.” [Online]. Available: https://www.flightlab.com/flightlab.html. [Accessed: 28-Nov-2019].

[86] Ministry of Defence, “Defence Standard 00-133 Aviation Arrangements in Surface Ships Part 2: Design, Construction and Provision (Aviation Services and Compartments),” 2014.

[87] C. Davies, “Royal Navy Type 23 Frigate HMS Northumberland,” *Wikimedia Commons*, 2010. [Online]. Available: https://commons.wikimedia.org/wiki/File:Royal_Navy_Type_23_Frigate_HMS_Northumberland_MOD_45152174.jpg. [Accessed: 15-Feb-2019].

[88] Anon., “HMS Calliope,” *Naval History and Heritage Command*, 1884. [Online]. Available: https://www.history.navy.mil/content/history/nhhc/our-collections/photography/numerical-list-of-images/nhhc-series/nh-series/NH-75000/NH-75964.html. [Accessed: 28-Mar-2019].

[89] Anon., “HMS Dreadnought,” *Naval History and Heritage Command*, 1906. [Online]. Available: https://www.history.navy.mil/content/history/nhhc/our-collections/photography/numerical-list-of-images/nhhc-series/nh-series/NH-61000/NH-61017.html. [Accessed: 28-Mar-2019].

[90] N. Friedman, *U.S. BATTLESHIPS: AN ILLUSTRATED DESIGN HISTORY*. Annapolis, MD: Naval Institute Press, 1985.

[91] Anon., “USS South Carolina (BB-26),” *Naval History and Heritage Command*, 1910. [Online]. Available: https://www.history.navy.mil/content/history/nhhc/our-collections/photography/us-navy-ships/battleships/south-carolina-bb-26/NH-61225.html. [Accessed: 28-Mar-2019].

[92] Anon., “NRL’s XAF radar on the battleship USS New York,” *U.S. Naval Research Laboratory*, 1938. [Online]. Available: https://www.nrl.navy.mil/news/releases/fleets-first-radar-turns-75.

[93] J. D. Luse, “A Brief History of the Use of Marine Radar,” *Navigation*, vol. 28, no. 3, pp. 199–205, Sep. 1981.

[94] R. Stratchko, “USS Arleigh Burke (DDG-51),” *Defense Visual Information Distribution Service*, 2013. [Online]. Available: https://www.dvidshub.net/image/1023190/phibron-meu-integrated-training. [Accessed: 28-Mar-2019].

[95] C. E. Kane, G. Fixter, and G. Pogson, “The advanced technology mast for HMS Ark Royal,” *Plast. Rubber Compos.*, vol. 39, no. 3–5, pp. 238–243, Jun. 2010.

[96] L. Holden, “R 07 HMS Ark Royal,” *Seaforces - Online*, 2010. [Online]. Available: http://www.seaforces.org/marint/Royal-Navy/Aircraft-Carrier/R-07-HMS-Ark-Royal.htm. [Accessed: 28-Mar-2019].

[97] S. M. Anderson, “At sea with USS Arthur W. Radford (DD 968),” *United States Navy*, 2002. [Online]. Available: https://www.navy.mil/view_image.asp?id=3483. [Accessed: 28-Mar-2019].

[98] Damen, “Holland Class Ocean Going Patrol Vessel 3750,” *Damen*, 2019. [Online]. Available: https://products.damen.com/en/ranges/opv-holland-class/holland-class-ocean-going-patrol-vessel-3750? [Accessed: 28-Mar-2019].

[99] General Dynamics Bath Iron Works, “Future USS Zumwalt’s first underway at sea,” *Official U.S. Navy Page (Flickr)*, 2015. [Online]. Available: https://www.flickr.com/photos/56594044@N06/22965290304/. [Accessed: 28-Mar-2019].

[100] Ministry of Defence, “Defence Standard 08-133 Part 2: Requirements and Guidance for the Aviation Arrangements in Surface Ships - Guidance for the Design and Construction of Aviation Requirements,” 2008.

[101] UK Defence Forum, “HMS Defender,” *UK Defence Forum*, 2015. [Online]. Available: https://ukdefenceforum.net/viewtopic.php?t=35&start=15. [Accessed: 28-Mar-2019].

[102] Aeronautical & General Instruments Ltd., “Naval Products.” [Online]. Available: https://www.agiltd.co.uk/naval-products/. [Accessed: 20-Nov-2019].

[103] Ministry of Defence, “Defence Standard 00-133 Aviation Arrangements in Surface Ships Part 4: Acceptance of Aviation Arrangements,” no. 2, 2015.

[104] S. N. Moore, “Type 45 HMS Daring Air Flow Air Pattern Trial Report,” *UK RESTRICTED 08/01546*. Qinetiq, Farnborough, UK, 2008.

[105] C. Norberg, “Flow around rectangular cylinders: Pressure forces and wake frequencies,” *J. Wind Eng. Ind. Aerodyn.*, vol. 49, no. 1–3, pp. 187–196, 1993.

[106] T. Tamura and T. Miyagi, “The effect of turbulence on aerodynamic forces on a square cylinder with various corner shapes,” *J. Wind Eng. Ind. Aerodyn.*, vol. 83, no. 1–3, pp. 135–145, Nov. 1999.

[107] Y. C. Kim and J. Kanda, “Wind pressures on tapered and set-back tall buildings,” *J. Fluids Struct.*, vol. 39, pp. 306–321, 2013.

[108] Scientific American, “USS Wyoming,” *Scientific American*, 1915. [Online]. Available: https://blogs.scientificamerican.com/anecdotes-from-the-archive/u-s-navy-and-the-arms-race-1915/. [Accessed: 10-May-2019].

[109] O. W. Waterman, “NH 82114 USS California (BB-44),” *Naval History and Heritage Command*, 1921. [Online]. Available: https://www.history.navy.mil/our-

collections/photography/us-navy-ships/battleships/california-bb-44/NH-82114.html. [Accessed: 10-May-2019].

[110] Tyne and Wear Archives and Museums, “HMS Kelly,” *Tyne and Wear Archives and Museums (Flickr)*, 1939. [Online]. Available: https://www.flickr.com/photos/twm_news/9608579072/. [Accessed: 10-May-2019].

[111] H. C. Acker, “Stack Design to Avoid Smoke Nuisance,” *trans SNAME*, vol. 60. pp. 566–594, 1952.

[112] E. Ower and A. D. Third, “Superstructure design in relation to the descent of funnel smoke,” *Trans. Inst. Mar. Eng.*, vol. 1, pp. 109–138, 1959.

[113] G. J. Baham and D. Mccallum, “Stack Design Technology for Naval and Merchant Ships,” *Soc. Nav. Archit. Mar. Eng.*, vol. 85, pp. 324–349, 1977.

[114] Naval Ship Engineering Centre, “Technical Practices Manual for Surface Ship Stack Design NAVSEC Report 6136-76-18.”

[115] P. R. Kulkarni, S. N. Singh, and V. Seshadri, “Flow visualization studies of exhaust smoke-superstructure interaction on naval ships,” *Nav. Eng. J.*, vol. 117, no. 1, pp. 41–56, 2005.

[116] P. R. Kulkarni, S. N. Singh, and V. Seshadri, “Parametric studies of exhaust smoke-superstructure interaction on a naval ship using CFD,” *Comput. Fluids*, vol. 36, no. 4, pp. 794–816, 2007.

[117] R. Vijayakumar, V. Seshadri, S. N. Singh, and P. R. Kulkarni, “A wind tunnel study on the interaction of hot exhaust from the funnel with the superstructure of a naval ship,” *Ocean. MTS/IEEE Kobe-Techno-Ocean’08 - Voyag. Towar. Futur. OTO’08*, pp. 1–6, 2008.

[118] P. R. Kulkarni, S. N. Singh, and V. Seshadri, “The Smoke Nuisance Problem On Ships - A Review,” *Int. J. Marit. Eng.*, vol. 147, no. a2, p. 15, 2009.

[119] D. A. Vaitekunas and Y. Kim, “IR signature management for the modern navy,” in *Infrared Imaging Systems: Design, Analysis, Modeling, and Testing XXIV*, 2013, vol. 8706, p. 87060U.

[120] K. J. Finley, “USS Arleigh Burke (DDG 51) departs Naval Station Norfolk,” *United States Navy*, 2012. [Online]. Available: https://www.navy.mil/view_image.asp?id=114441.

[121] U.S. Navy, “Aerial starboard quarter view of the US Navy (USN) Arleigh Burke Class (Flight IIA) Guided Missile Destroyer (Aegis) USS NITZE (DDG 94) underway in the Atlantic Ocean on the builder’s sea trials,” *National Archives Catalog*, 2005. [Online]. Available: https://catalog.archives.gov/id/6669115. [Accessed: 10-May-2019].

[122] P. Scott, M. White, and I. Owen, “Unsteady CFD modelling of ship engine exhaust gases and over-deck air temperatures, and the implications for maritime helicopter operations,” *Annu. Forum Proc. - AHS Int.*, vol. 3, no. January, pp. 2026–2034, 2015.

[123] Civil Aviation Authority, “CAP 437: Standards for offshore helicopter landing areas,” 2018.

[124] Air Accidents Investigation Branch, “AAIB Bulletin No: 3/96, Sikorsky S61N Sea King, G-AYOM,” Farnborough, UK, 1995.

[125] Irish Aviation Authority, “AAIU Synoptic Report No: 2004-001,” 2004.

[126] BMT Fluid Mechanics Limited, “CAA Paper 99004: Research on Offshore Helideck Environmental Issues,” London, UK, 2000.

[127] X. Vavasseur, “Q&A with BAE Systems on Type 26 Frigate Design Update at Euronaval 2012,” *Navy Recognition*, 2013. .

[128] J. Buckingham, “Geared Electric Propulsion,” in *Shipping in Changing Climates Conference 2016*, 2016, no. 10th-11th November.

[129] J. Thompson and D. Vaitekunas, “IR Signature Suppression of Modern Naval Ships,” in *ASNE 21st Century Combatant Technology Symposium*, 1998, pp. 1–9.

[130] S. Ergin and E. Dobrucalı, “Numerical modeling of exhaust smoke dispersion for a generic frigate and comparisons with experiments,” *J. Mar. Sci. Appl.*, vol. 13, no. 2, pp. 206–211, Jun. 2014.

[131] T. F. Fric and A. Roshko, “Vortical structures in the wake of a transverse jet,” *J. Fluid Mech.*, vol. 279, pp. 1–47, Nov. 1994.

[132] G. A. Davidson, “Dimensionless correlations for bouyant plume behaviour in crossflows and scaling criteria for physical modelling of dispersion processes,” *J. Wind Eng. Ind. Aerodyn.*, vol. 51, no. 2, pp. 135–155, 1994.

[133] P. R. Slawson and G. T. Csanady, “On the mean path of buoyant, bent-over chimney plumes,” *J. Fluid Mech.*, vol. 28, no. 02, p. 311, May 1967.

[134] B. E. Johnson, G. S. Elliott, and K. T. Christensen, “Structural characteristics of a heated jet in cross-flow emanating from a raised, circular stack,” *Exp. Fluids*, vol. 54, no. 1543, Jun. 2013.

[135] M. W. Carbon, H. J. Kutsch, and G. A. Hawkins, “The response of thermocouples to rapid gas-temperature changes,” *Trans. ASME*, vol. 72, no. 5, pp. 655–657, 1950.

[136] J. Chen, D. F. Fletcher, B. S. Haynes, and J. D. Hooper, “Validation of the Cobra probe using turbulence measurements in a fully developed pipe flow,” in *Proceedings of the 13th Australasian Fluid Mechanics Conference, Melbourne, Australia, 13-18 December*, 1998.

[137] Y. Guo and D. H. Wood, “Instantaneous velocity and pressure measurements in turbulent mixing layers,” *Exp. Therm. Fluid Sci.*, vol. 24, no. 3–4, pp. 139–150, May 2001.

[138] Turbulent Flow Instrumentation, “Cobra Probe,” *TFI Catalogue*, 2015. [Online]. Available: http://www.turbulentflow.com.au/Downloads/Cat_CobraProbe.pdf. [Accessed: 07-Apr-2020].

[139] L. P. Chua, Y. F. Li, T. Zhou, and C. M. S. Yu, “Measurements of Turbulent Prandtl Number of a Heated Square Jet,” in *14th Australasian Fluid Mechanics Conference, Adelaide University, 10-14 December*, 2001, no. December, pp. 713–716.

[140] J. Craske, P. Salizzoni, and M. van Reeuwijk, “The turbulent Prandtl number in a pure plume is 3/5,” *J. Fluid Mech.*, vol. 822, pp. 774–790, Jul. 2017.

[141] U.S. Department of Defense, “Unmanned Aircraft Systems (UAS) DoD Purpose and Operational Use.” [Online]. Available: https://dod.defense.gov/UAS/. [Accessed: 26-Dec-2019].

[142] K. Schindler, “110930-N-JQ696-401 An MQ-8B Fire Scout unmanned aerial vehicle (UAV),” *United States Navy*, 2011. [Online]. Available: https://www.navy.mil/view_image.asp?id=108121. [Accessed: 20-Dec-2019].

[143] J. A. Winnefeld and F. Kendall, “Unmanned Systems Integrated Roadmap: FY 2011-2036,” 2011.

[144] Royal Navy, “Royal Navy gets eagle eyes in £30m deal for unmanned planes,” *Royal Navy*, 2013. [Online]. Available: https://www.royalnavy.mod.uk/news-and-latest-activity/news/2013/june/20/130620-royal-navy-gets-eagle-eyes. [Accessed: 20-Dec-2019].

[145] I. Cox, J. Howitt, and J. Duncan, “The Use of Simulation to De-risk Maritime UAV Operations,” in *Platform Innovations and System Integration for Unmanned Air, Land and Sea Vehicles (AVT-SCI Joint Symposium)*, 2007, no. 13, pp. 13-1-13–16.

[146] “The Royal Navy and Unmanned Systems.” [Online]. Available: https://www.thinkdefence.co.uk/2013/08/the-royal-navy-and-unmanned-systems/. [Accessed: 26-Dec-2019].

[147] B. Manimala, “Further Development of Synthetic Environments To Support The Early Evaluation of Unmanned Rotary Wing Vehicles,” in *Rotorcraft Simulation – Trends and Future Applications, RAeS Autumn Conference, 12-13 November*, 2019.

[148] UK Ministry of Defence, “Joint Doctrine Publication 0-30.2: Unmanned Aircraft Systems,” 2017.

[149] T. R. Fell, M. D. White, M. Jump, I. Owen, and S. Manso, “Sensitivity study of a small maritime rotary UAS operating in a turbulent airwake,” in *71st Annual American Helicopter Society International Annual Forum*, 2015, vol. 3, pp. 1989–1997.

[150] M. R. Crump and C. Bil, “Control techniques for autonomous launching of ship-based unmanned air vehicles (UAVs),” *Aeronaut. J.*, vol. 106, no. 1057, pp. 121–128, 2002.

[151] U.S. Department of Defense, “Flying Qualities of Piloted Airplanes,” *MIL-F-8785C*, 1980.

[152] Boeing Defence UK, “Royal Navy’s new ‘eye in the sky,’” *Her Majesty’s Government*, 2013. [Online]. Available: https://www.gov.uk/government/news/royal-navys-new-eye-in-the-sky. [Accessed: 20-Dec-2019].

[153] F. Kendoul, “Survey of advances in guidance, navigation, and control of unmanned rotorcraft systems,” *J. F. Robot.*, vol. 29, no. 2, pp. 315–378, Mar. 2012.

[154] J. L. Sanchez-Lopez, J. Pestana, S. Saripalli, and P. Campoy, “An Approach Toward Visual Autonomous Ship Board Landing of a VTOL UAV,” *J. Intell. Robot. Syst.*, vol. 74, no. 1–2, pp. 113–127, Apr. 2014.

[155] M. R. Snyder, A. Kumar, and P. Ben-Tzvi, “Off Ship Measurement of Ship Air Wakes Using Instrumented Unmanned Aerial Vehicles,” in *32nd AIAA Applied Aerodynamics Conference*, 2014, no. June, pp. 1–9.

[156] B. Ferrier, J. Duncan, J. Nelson, D. Carico, and D. Ludwig, “Further Validation of Simulated Dynamic Interface Testing Techniques as a Tool in the Forecasting of Air Vehicle Deck Limits,” in *American Society of Naval Engineers Launch & Recovery Symposium 2010, “Launch, Recovery & Operations of Manned and Unmanned Vehicles from Marine Platforms”, December 8-9*, 2010.

[157] T. R. Fell, M. D. White, M. Jump, and I. Owen, “Towards establishing flying qualities requirements for maritime unmanned aircraft systems,” in *71st American Helicopter Society International Annual Forum*, 2015, vol. 2, pp. 1465–1474.

[158] T. R. Fell, M. Jump, M. D. White, and I. Owen, “Initial progress to establish flying qualities requirements for maritime unmanned aircraft systems,” *40th Eur. Rotorcr. Forum 2014*, vol. 2, pp. 809–820, 2014.

[159] P. W. Mullen, “An unmanned aerial vehicle (UAV) called the ‘Scan Eagle’ lands in the skyhook for recovery on the flight deck aboard the U.S. Navy Tarawa Class Amphibious Assault Ship USS SAIPAN (LHA 2) during operations in the Atlantic Ocean,” *National Archives Catalog*, 2006. [Online]. Available: https://catalog.archives.gov/id/6700834. [Accessed: 20-Dec-2019].

[160] United States Coast Guard, “SCANEAGLE (SE) UNMANNED AIRCRAFT SYSTEM (UAS) STANDARD OPERATING PROCEDURE (SOP),” 2013.

[161] R. W. Du Val and C. He, “Validation of the FLIGHTLAB virtual engineering toolset,” *Aeronaut. J.*, vol. 122, no. 1250, pp. 519–555, Apr. 2018.

[162] 3DR, “3DR.” [Online]. Available: http://www.3dr.com. [Accessed: 26-Dec-2019].

[163] L. Lu, “Modelling of DA42 TWIN STAR and RTF Aero UAV in FLIGHTLAB,” *Virtual Eng. Cent. Rep.*, 2015.

[164] M. Drela, “XFOIL Subsonic Aerofoil Development System,” 2013. [Online]. Available: http://web.mit.edu/drela/Public/web/xfoil/. [Accessed: 26-Dec-2019].

[165] 3D Robotics, “Introducing 3DR’s Aero Fixed-Wing,” *DIY Drones: The Leading Community for Personal UAVs*, 2014. [Online]. Available: https://diydrones.com/profiles/blogs/introducing-3dr-s-aero-fixed-wing. [Accessed: 20-Dec-2020].

[166] L. T. Ngyuen, M. E. Ogburn, W. P. Gilbert, K. S. Kibler, P. W. Brown, and P. L. Deal, “Simulator Study of Stall/Post-Stall Characteristics of a Fighter Airplane with Relaxed Longitudinal Stability,” *NASA Tech. Pap. 1538*, no. December, 1979.

[167] W. A. Memon, “The Development of High-Fidelity Modelling & Simulation for the Helicopter Ship Dynamic Interface,” University of Liverpool, 2019.

[168] I. Owen, M. D. White, G. D. Padfield, and S. J. Hodge, “A virtual engineering approach to the ship-helicopter dynamic interface – a decade of modelling and simulation research at the University of Liverpool,” *Aeronaut. J.*, vol. 121, no. 1246, pp. 1833–1857, Dec. 2017.

Appendix A: Published Papers

The following papers have been published by the author as part of this research project:

[1] R. Mateer, P. Scott, M. D. White, and I. Owen, "A CFD Study of the Aerodynamics of a Ship's Bulky Enclosed Mast," *in proceedings of American Society of Naval Engineers Launch and Recovery Symposium, 16-17th November*, 2016, Linthicum Heights, MD

[2] I. Owen, M. D. White, P. Scott, R. Mateer, M. F. Kelly, "*Modelling and Simulation at The University of Liverpool in Support of UK Naval Aviation*," *in proceedings of American Society of Naval Engineers Launch and Recovery Symposium, 16-17th November*, 2016, Linthicum Heights, MD

[3] R. Mateer, S. A. Scott, I. Owen, and M. D. White, "Superstructure Aerodynamics of the Type 26 Global Combat Ship," *in proceedings of 14th International Naval Engineering Conference and Exhibition (INEC), 2nd-4th October,* 2018, Glasgow, UK.